
NOVAE, THE SUPER-REMNANT
PHENOMENON, AND THE LINK TO TYPE IA
SUPERNOVAE

Michael William Healy

A thesis submitted in partial fulfilment of the requirements of
Liverpool John Moores University
for the degree of
Doctor of Philosophy

September 2021

Declaration

The work presented in this thesis was carried out at the Astrophysics Research Institute, Liverpool John Moores University. Unless otherwise stated, it is the original work of the author.

While registered as a candidate for the degree of Doctor of Philosophy, for which submission is now made, the author has not been registered as a candidate for any other award. This thesis has not been submitted in whole, or in part, for any other degree.

Michael William Healy
Astrophysics Research Institute
Liverpool John Moores University
IC2, Liverpool Science Park
146 Brownlow Hill
Liverpool
L3 5RF
UK

Abstract

A classical nova describes the sudden brightening of a star in the night sky, before it fades away to quiescence. As systems exhibiting nova outbursts are binary, this steep increase in luminosity is attributed to a thermonuclear runaway on the surface of a white dwarf (WD), resulting in the violent ejection of material previously accreted from a non-degenerate companion. After the system has experienced a nova outburst, both the WD and companion remain intact, allowing for further accretion and subsequent eruptions. Though all nova systems can theoretically experience repeated outbursts, only those systems that have been observed to erupt more than once are known as recurrent novae (RNe). Recent theoretical studies have demonstrated that the WD in a RN system can grow in mass, due to retaining a proportion of the ejected material, up to the Chandrasekhar limit. Consequently, some novae are considered to be single-degenerate progenitors of type Ia supernovae (SNIa).

With novae being progenitor candidates of SNIa, it is vital to understand how the underlying system is affected by its environment. Galactic, Magellanic Cloud and M31 novae are routinely studied, yet those in other Local Group galaxies are not. We address this by conducting a multiwavelength observational campaign of a classical nova observed in the Local Group irregular dwarf galaxy, NGC 6822. This consisted of determining the photometric evolution of the system; identifying lines in the spectra at various epochs, including the nebular phase, and their associated velocities; attempting to detect X-ray emission and searching for a progenitor system within archival *Hubble Space Telescope* images. Even though displaying many characteristics seen in regular classical novae, AT2017fvz did reveal tentative evidence for belonging to the ‘faint and fast’ group of novae, and possibly as being a recurrent nova.

Currently, the system with the shortest recurrence period known is M 31N 2008-12a. A WD close to the Chandrasekhar limit and a very high accretion rate combine to ensure an outburst once every year. As well as being the most rapidly recurring nova we know of, 12a is surrounded by a vast unique nova super-remnant (NSR), at least two orders of magnitude larger than any other nova shell. We show, through Strömngren sphere analysis, that this enormous structure could not be formed solely through photoionisation from the RN system, giving further credence to the dynamical formation of the structure through many previous outbursts.

Similar to M 31N 2008-12a, any recurrent nova system with a massive WD and high accretion rate should also be surrounded by a vast dynamic remnant. Even so, the characteristics of the underlying nova system will influence its scale and structure. To test this, we employ a large suite of hydrodynamical simulations to model the growth of many NSRs. Each simulation incorporates a growing WD, and has various combinations of mass accretion rate, local interstellar medium (ISM) density, initial WD mass and WD temperature in order to capture parameter dependencies. These models reveal that the higher the ISM density and accretion rate, the smaller the resulting NSR, whereas the temperature and initial mass of the WD have little impact on the final structure.

If the NSR around M 31N 2008-12a is actually commonplace, then finding more of these phenomena would present a vital new method for not only locating previously unknown recurrent nova systems, but also for finding once active systems (before depleting their donor) as well as the sites for upcoming SNIa. With this motive in mind, we use the suite of simulations employed to model NSRs in order to predict the radial sizes and emission characteristics of other remnants, utilised in the first ever targeted search for these vast structures around a number of Galactic RNe.

Finally, we look at two post-nova evolutionary scenarios, one involving the complete depletion of the donor and the other incorporating a SNIa, to determine observational signatures of these events. We find that the NSR would change very little from the fully formed version after the companion ceases donating material, whereas the SNIa ejecta colliding with the already formed remnant would trigger extreme X-ray emission a few thousand years after the explosion takes place; likely detectable with current X-ray missions.

Publications

The work presented in this thesis, the contents of Chapter 2, has been submitted and accepted for publication in a refereed journal:

Healy M. W., Darnley M. J., Copperwheat C. M., James P. A., Filippenko A. V., Henze M., Hestenes J. C., Page K. L., Williams S. C. and Zheng, W., 2019, “AT 2017fvz: a nova in the dwarf irregular galaxy NGC 6822”, *Monthly Notices of the Royal Astronomical Society*, 486, 433.

The work presented in this thesis, the contents of Chapter 3, has been submitted and accepted for publication in a refereed journal:

Darnley M. J., Hounsell R., O’Brien T. J., Henze M., Rodríguez-Gil P., Shafter A. W., Shara M. M., Vaytet N. M. H., Bode M. F., Ciardullo R., Davis B. D., Galera-Rosillo R., Harman D. J., Harvey E. J., **Healy M. W.**, Ness J.-U., Ribeiro V. A. R. M. and Williams S. C., 2019, “A Recurrent Nova Super-Remnant in the Andromeda Galaxy”, *Nature*, 565, 460-463.

The work presented in this thesis, the contents of Chapter 4, Chapter 5, Chapter 6 and Chapter 7, is being prepared to be submitted to a refereed journal:

Healy M. W., and Darnley M. J., in preparation – *Searching for Recurrent Nova Super-Remnants*

The author was involved in the following published astronomy telegrams:

Williams S. C., Darnley M. J., **Healy M. W.**, Murphy-Glaysher F. J. and Ransome C. L., 2020, ATel, 14145 – *Spectroscopic confirmation of the 2020 eruption of recurrent nova M31N 1963-09c*

Williams S. C., Darnley M. J., **Healy M. W.**, Murphy-Glaysher F. J., Ransome C. L., Zhang M. and Gao, X., 2020, ATel, 14121 – *Spectroscopic classification of three M31 novae with the Liverpool Telescope*

Williams S. C., Darnley M. J., **Healy M. W.**, Murphy-Glaysher F. J. and Ransome C. L., 2020, ATel, 14053 – *Spectroscopic classification of AT2020ubx as a nova in M31*

Williams S. C., Darnley M. J., **Healy M. W.**, Murphy-Glaysher F. J. and Ransome C. L., 2020, ATel, 13795 – *Spectroscopic classification of AT2020lye as a nova in M31*

Williams S. C., Darnley M. J., **Healy M. W.**, Murphy-Glaysher F. J. and Ransome C. L., 2020, ATel, 13384 – *Classification of AT2019wlo and AT2019wvf as M31 novae*

Darnley M. J., Oksanen A., Henze M., Shafter A. W., Williams S. C., **Healy M. W.**, Murphy-Glaysher F. J., Ransome C. L. and Kafka S., 2019, ATel, 13273 – *Recurrent Nova M31N 2008-12a: spectroscopic confirmation of the 2019 eruption*

Williams S. C., Darnley M. J., **Healy M. W.**, Murphy-Glaysher F. J. and Ransome C. L., 2019, ATel, 13241 – *Spectroscopic classification of AT2019tpb/ASASSN-19aad as a Galactic Nova*

Williams S. C., Darnley M. J., **Healy M. W.**, Murphy-Glaysher F. J. and Ransome C. L., 2019, ATel, 13228 – *Spectroscopic classification of AT2019sxc as a nova in M31*

Williams S. C., Darnley M. J., **Healy M. W.**, Murphy-Glaysher F. J. and Ransome C. L., 2019, ATel, 13078 – *Spectroscopic classification of AT2019pih and M31N 2019-09a as a novae in M31*

Williams S. C., Hornoch K., Darnley M. J., **Healy M. W.**, Murphy-Glaysher F. J. and Ransome C. L., 2019, ATel, 12999 – *Spectroscopic classification of M31N 2019-08a as a nova in M31*

Williams S. C., Darnley M. J., **Healy M. W.**, Murphy-Glasyher F. J. and Ransome C. L., 2019, ATel, 12953 – *Spectroscopic classification of AT2019lcg as a nova in M31*

Williams S. C., Darnley M. J. and **Healy M. W.**, 2019, ATel, 12349 – *Liverpool Telescope spectroscopy of six nova candidates*

Darnley M. J., Carey G., **Healy M. W.** and Williams S. C., 2018, ATel, 12245 – *Spectroscopic classification of AT2018jas as a classical nova in M31*

Williams S. C., Darnley M. J. and **Healy M. W.**, 2018, ATel, 12138 – *Liverpool Telescope classification of optical transients*

Darnley M. J., **Healy M. W.** and Williams S. C., 2018, ATel, 12017 – *Liverpool Telescope observations of AT2018fsy*

Darnley M. J., **Healy M. W.** and Williams S. C., 2018, ATel, 11983 – *Liverpool Telescope observations of five Local Group nova candidates*

Williams S. C., Darnley M. J. and **Healy M. W.**, 2018, ATel, 11928 – *Spectroscopic classification of PNV J17422408-2053088 as a Galactic nova*

Sitaram M., **Healy M. W.** and Darnley M. J., 2018, ATel, 11765 – *Spectroscopic classification of AT2018bto and AT2018cmi as nova eruptions in M31*

Darnley M. J., Copperwheat C. M., Harvey E. J. and **Healy M. W.**, 2018, ATel, 11601 – *Liverpool Telescope Spectroscopy of the Nova Eruption from V392 Persei*

Darnley M. J., **Healy M. W.** and Williams S. C., 2018, ATel, 11472 – *ASASSN-18gb: Spectroscopic confirmation as a nova eruption in NGC 3109*

Williams S. C., Darnley M. J. and **Healy M. W.**, 2018, ATel, 11398 – *Spectroscopic classification of TCP J17140253-2849233 as a Galactic nova*

Darnley M. J., **Healy M. W.**, Henze M. and Williams S. C., 2018, ATel, 11149 – *Recurrent Nova M31N 2008-12a: Liverpool Telescope observation of the waning 2017 eruption*

Darnley M. J., **Healy M. W.**, Henze M. and Williams S. C., 2017, ATel, 11117 – *Recurrent Nova M31N 2008-12a: Liverpool Telescope spectroscopic confirmation of the 2017 eruption*

Acknowledgements

First and foremost, I would like to sincerely thank my PhD supervisor, Dr Matt Darnley. Your enthusiasm, your seemingly endless motivation, your insight and your continuous support has guided me immensely throughout the past three and half years. I would also like to thank my co-supervisors, Dr Chris Copperwheat and Professor Phil James for your input and recommendations, both with research and with career progression.

Next, there are too many people to name without missing someone out, so I simply want to thank everyone from the Astrophysics Research Institute who have helped me along the way and for always making me feel welcomed within the department.

I want to thank my parents immensely, Madeline and James, for supporting me, not only throughout my PhD, but for all of my academic journey. You always back my decisions, offer alleviating advice during difficult periods to give a sense of perspective, and never discourage my true ambitions - thank you. And a special mention to Piper for sitting (and mostly sleeping) next to me all through the writing process.

I want to say “ありがとうございました” to my brother and sister-in-law, Daniel and Hana, for being there to talk to, listening to the progression of my PhD as well as allowing me to air frustrations that sometimes cropped up along the journey, even though you are both over five thousand miles away in Japan.

To end, I wish to thank my partner, Shikha, whom I only met because of this PhD. You have motivated me and have given me the confidence that I needed at just the right time that I needed it. I have learnt much from you and I am so thankful that I will have you by my side for my postdoctoral adventures and beyond.

എനിക്ക് നിന്നെ ഇഷ്ടമാണ്

“It’s hard to choose what to do next if you don’t know where you’re trying to get to. But if you have some sort of long-term goal in mind, then it puts things more in context and in focus for the choices that you’re making right now.”

- Col. Chris Hadfield,
Commander, CSA & NASA Colonel, RCAF fighter pilot (retired)

Contents

Declaration	ii
Abstract	iii
Publications	v
Acknowledgements	viii
List of Figures	xi
List of Tables	xii
1 Introduction*	1
1.1 A brief history of novae	1
1.2 Classical novae	2
1.2.1 Nova outburst	3
1.2.2 Lithium production	4
1.2.3 X-ray and γ -ray production	5
1.2.4 Photometric properties	7
1.2.5 Spectroscopic properties	9
1.2.6 Nova shells	12
1.3 Extragalactic novae and nova rates	14
1.4 Recurrent novae	15
1.4.1 Potential type Ia supernova progenitors	17
1.4.2 ‘Faint and fast’ novae and the ‘Bolometric MMRD’	18
1.4.3 Rapid recurrent novae	19
1.4.4 M31 N 2008-12a – the rapid recurrent nova prototype	19
1.4.5 M31 N 2008-12a nova super-remnant	21
1.5 Hydrodynamical simulations of novae	26
1.5.1 Introduction to hydrodynamics	26
1.5.2 Examples	28
1.6 Facilities	29
1.6.1 The Liverpool Telescope (LT)	30
1.6.2 Katzman Automatic Imaging Telescope (KAIT)	30
1.6.3 Asteroid Terrestrial-impact Last Alert System (ATLAS)	31
1.6.4 All-Sky Automated Survey for Supernovae (ASAS-SN)	32
1.6.5 <i>Hubble Space Telescope (HST)</i>	32

1.6.6	<i>The Neil Gehrels Swift Observatory (Swift)</i>	33
1.7	Summary and Thesis Outline	33
2	Multiwavelength Study of the Classical Nova AT 2017fvz*	35
2.1	Introduction	35
2.2	Discovery of AT 2017fvz	36
2.3	Observations and data analysis	36
2.3.1	Ground-based photometry	36
2.3.2	Spectroscopy	37
2.3.3	UV and X-ray observations	38
2.4	Results	40
2.4.1	Reddening	40
2.4.2	Photometric evolution	40
2.4.3	Spectroscopic evolution	46
2.4.3.1	Early Decline	50
2.4.3.2	'Plateau' Phase	54
2.4.3.3	Nebular Phase	54
2.4.3.4	H α evolution	55
2.4.4	X-rays	55
2.4.5	The nova progenitor	57
2.4.5.1	Obtaining data	57
2.4.5.2	Positional transformation	58
2.4.5.3	Position of source	58
2.4.5.4	SED of the source	59
2.5	Discussion	62
2.5.1	The previous nova in NGC 6822	62
2.5.2	Comparison to novae in other galaxies	64
2.5.2.1	IC 1613	66
2.5.2.2	The Magellanic Clouds	67
2.5.2.3	M 31 and M 32	68
2.5.2.4	M 33	69
2.5.3	Nova rate in NGC 6822 and IC 1613	69
2.5.4	The lack of X-rays	70
2.5.5	A possibly 'faint and fast' or recurrent nova?	72
2.6	Summary and Conclusions	73
3	Photoionisation Analysis of Nova Super-remnant	75
3.1	Introduction	75
3.2	A supernova remnant	75
3.3	A superbubble	77
3.4	A fossil H II region	77
3.5	Summary	83
4	Hydrodynamical Simulations of Recurrent Nova Super-Remnants	84
4.1	Introduction	84
4.2	Hydrodynamical Simulations with Morpheus	85
4.2.1	Are simulations required?	86

4.2.2	Testing resolution of simulations	90
4.2.3	Testing changing grid size	92
4.2.4	Amending timestep computation within Morpheus	94
4.3	Tests prior to main simulations	96
4.3.1	Eruptions timescales	96
4.3.2	Intra-eruption shocks	97
4.4	Parameter space for main simulations	99
4.4.1	System parameters	99
4.4.2	Growing a white dwarf	103
4.5	Main simulations	105
4.5.1	Run 1 (reference simulation)	105
4.5.2	Run 2 and Run 3	114
4.5.3	Run 4, Run 5 and Run 6	117
4.5.4	Run 7, Run 8 and Run 9	120
4.5.5	Run 1, Run 10 and Run 11	123
4.6	Main simulations with radiative cooling	123
4.6.1	Run 12 (reference simulation with radiative cooling)	126
4.6.2	Run 12, Run 13 and Run 14	131
4.6.3	Run 15, Run 16 and Run 17	131
4.6.4	Run 18, Run 19 and Run 20	134
4.7	Diagnostics of Runs 1, 2, 3 and Runs 12, 13, 14	134
4.8	Comparing simulations to M 31N 2008-12a NSR	141
4.9	Tests post main simulations	143
4.9.1	Varying Mass Accumulation Efficiency	143
4.9.2	Fitting a power law to find system parameters	144
4.9.3	Varying the initial WD mass	153
4.9.4	Changing accretion rate within simulation	156
4.10	Summary	160
5	Searching for Recurrent Nova Super-Remnants	162
5.1	Introduction	162
5.2	Preliminary radial size equation	163
5.3	Estimating the local ISM density	165
5.3.1	Method 1	165
5.3.2	Method 2	166
5.4	First search for Galactic nova super-remnants	167
5.5	Refinement of radial size equation	169
5.6	Predictions of NSR emission at $P_{\text{rec}} = 1$ year epoch	175
5.6.1	Fraction of ionisation within NSR	176
5.6.2	Emission measure and X-ray emission within NSR	180
5.6.3	Recombination time within NSR	182
5.7	Evolution of NSR emission	185
5.7.1	Evolution of the ionisation fraction and emission measure	186
5.7.2	Evolution of X-ray luminosity	189
5.8	Replicating the M 31N 2008-12a NSR	196
5.8.1	Parameter space of NSR radial size equation	196
5.8.2	Photoionisation regions of NSR at $P_{\text{rec}} = 1$ year epoch	198

5.8.3	Synthetic sky images of NSR at $P_{\text{rec}} = 1$ year epoch	203
5.9	Summary	206
6	Post-Nova Evolution of Nova Super-Remnants	208
6.1	Donor material depletion	208
6.1.1	Dynamical evolution of remnant after donor depletion	209
6.1.2	X-ray luminosity of remnant after donor depletion	212
6.2	SNIa explosion within the NSR	213
6.2.1	Dynamical evolution of remnant after SNIa	214
6.2.2	X-ray luminosity evolution of remnant after SNIa	216
6.3	Summary	221
7	Summary, Future Work and Recent Developments	223
7.1	Summary	223
7.1.1	AT2017fvz - an extragalactic classical nova	223
7.1.2	Photoionisation analysis of M31N 2008-12a NSR	224
7.1.3	Simulations of NSRs	224
7.1.4	Searching for NSRs	225
7.1.5	Post-nova evolution of NSRs	226
7.2	Future Work	226
7.2.1	Simulations	227
7.2.1.1	Helium flashes	227
7.2.1.2	Donor and disk interaction	227
7.2.1.3	Varying the mass accretion rate	228
7.2.1.4	ISM density gradient	228
7.2.2	Observables	228
7.2.2.1	Galactic search continuation	228
7.2.2.2	Extragalactic search	229
7.2.2.3	Predicting X-ray observations using XSPEC	229
7.2.2.4	Infrared emission from NSRs	230
7.3	Observations around T Coronae Borealis	230
7.4	A possible super-remnant surrounding RS Ophuichi?	230
7.5	The Big Picture	233
A	Hydrodynamics Derivations	235
A.1	Fluid flow equations	235
A.1.1	Continuity Equation	235
A.1.2	Euler Equation	236
A.1.3	Energy Equation	237
A.1.4	Equation of state	238
A.1.5	Shocks	239
A.2	Solving the fluid flow equations with Morpheus	239
B	Derivation of Strömgren sphere	241
C	Determining boundary locations of the simulated NSRs	243

Contents	xiv
D Machines	245
E Morpheus code alteration	246
F Colouring Scheme	247
Bibliography	248

List of Figures

1.1	Classical nova illustration	2
1.2	Light curve classes	4
1.3	X-ray spectra from a Galactic and extragalactic nova	6
1.4	Nova light curve	7
1.5	Light curve classes	8
1.6	Maximum magnitude-rate of decline relations	9
1.7	Spectroscopic classes of novae	10
1.8	Examples of spatially resolved nova shells	13
1.9	Observations of M 31N 2008-12a nova super-remnant	23
1.10	M 31N 2008-12a nova super-remnant	24
1.11	M 31N 2008-12a NSR simulation dynamics	25
1.12	Full hydrodynamical simulation of 100,000 identical eruptions.	26
1.13	Additional results of M 31N 2008-12a NSR simulations	27
1.14	The Liverpool Telescope	30
1.15	Asteroid Terrestrial-impact Last Alert System	31
1.16	<i>Hubble Space Telescope</i>	32
2.1	AT 2017fvz light curve (Optical and near-UV)	42
2.2	AT 2017fvz light curve in <i>uvw1</i> and <i>u'</i> -band	43
2.3	AT 2017fvz light curve in <i>B</i> - and <i>V</i> -band	44
2.4	AT 2017fvz light curve in <i>i'</i> - and <i>r'</i> -band	45
2.5	Exponential fit to <i>V</i> -band photometry	47
2.6	Power law fit to <i>V</i> -band photometry	50
2.7	AT 2017fvz spectroscopy	51
2.8	Balmer emission line evolution	53
2.9	H α emission line evolution	56
2.10	<i>HST</i> coordinates of AT 2017fvz derived from LT images	59
2.11	Position of source near to AT 2017fvz	60
2.12	Hertzsprung-Russell diagram of <i>HST</i> image and Hipparcos stars	61
2.13	SED of source near AT 2017fvz	63
2.14	Spectra of AT 2017fvz, NGC 6822 1999 nova and Nova IC 1613 2015	65
2.15	Luminosity specific nova rates	71
3.1	Spectroscopy of the nova super-remnant shell	76
3.2	Sulphur vs H α ratio of supernova remnants	76
3.3	Superbubble Henize 70 in the Large Magellanic Cloud	78
3.4	Strömgen sphere radii	81

4.1	NSR evolution from identical eruptions with analytic solution fit . . .	87
4.2	Resolution comparison with 0.01, 0.1 & 1 AU/cell after 4 eruptions . .	90
4.3	Resolution comparison with 0.1 & 1 AU/cell after 23 eruptions	91
4.4	Resolution comparison with 1 & 10 AU/cell after 728 eruptions	91
4.5	Varying growth factor in Morpheus	92
4.6	Changing the grid size in Morpheus	93
4.7	Amending timestep computation within Morpheus	95
4.8	Changing eruption timescale and inter-ejecta shocks	98
4.9	Relations between M_{WD} and $m_{\text{ig}}, P_{\text{rec}}, t_{\text{ml}}, v_{\text{ej}}$	102
4.10	Evolution of system parameters wrt M_{WD}	106
4.11	Evolution of system parameters wrt P_{rec}	107
4.12	Evolution of system parameters wrt total time	108
4.13	Evolution of system parameters wrt number of eruptions	109
4.14	Run 1 in full (reference simulation)	110
4.15	Run 1 in full (reference simulation) compared to full 12a eruptions . .	111
4.16	Dynamics of run 1 with 10 AU/cell and 100 AU/cell	113
4.17	Comparing shell evolution from identical vs non-identical eruptions . .	114
4.18	Run 1, Run 2 and Run 3 in full ($1 \times 10^{-7} M_{\odot} \text{ yr}^{-1}$ comparison)	115
4.19	Run 1 – 9 shell width evolution	116
4.20	Run 1 – 9 shell temperature evolution	117
4.21	Run 4, Run 5 and Run 6 in full ($1 \times 10^{-8} M_{\odot} \text{ yr}^{-1}$ comparison)	119
4.22	Comparison of KE evolution from nova eruptions and red giant wind .	120
4.23	Run 7, Run 8 and Run 9 in full ($1 \times 10^{-9} M_{\odot} \text{ yr}^{-1}$ comparison)	121
4.24	Run 1, Run 10 and Run 11 in full (T_{WD} comparison)	124
4.25	Run 1, Run 10 and Run 11 shell width evolution	125
4.26	Run 1, 4, 7, 10 and 11 recurrence period vs radial size	126
4.27	Run 1, 4, 7, 10 and 11 cumulative kinetic energy vs radial size	127
4.28	Effect of radiative cooling in identical vs non-identical eruptions	128
4.29	Effect of radiative cooling in full reference simulation	129
4.30	Run 1, 4 & 7 and Run 12, 15 & 18 shell width evolution comparison . .	130
4.31	Run 12, Run 13 and Run 14 in full (cool $1 \times 10^{-7} M_{\odot} \text{ yr}^{-1}$ comparison) 132	
4.32	Run 15, Run 16 and Run 17 in full (cool $1 \times 10^{-8} M_{\odot} \text{ yr}^{-1}$ comparison) 133	
4.33	Run 18, Run 19 and Run 20 in full (cool $1 \times 10^{-9} M_{\odot} \text{ yr}^{-1}$ comparison) 135	
4.34	Run 1 – 9 and Run 12 – 20	136
4.35	Density evolution for Runs 1, 2, 3 and Runs 12, 13, 14	137
4.36	Pressure evolution for Runs 1, 2, 3 and Runs 12, 13, 14	138
4.37	Temperature evolution for Runs 1, 2, 3 and Runs 12, 13, 14	139
4.38	Velocity evolution for Runs 1, 2, 3 and Runs 12, 13, 14	140
4.39	Mass evolution for Runs 1, 2, 3 and Runs 12, 13, 14	141
4.40	Dynamics of the NSR from Run 12, 13 and 14 when $P_{\text{rec}} = 1 \text{ yr}$	142
4.41	Total kinetic energy with varying mass accumulation efficiency	144
4.42	Power law relations between M_{WD} and $m_{\text{ig}}, P_{\text{rec}}, t_{\text{ml}}, v_{\text{ej}}$	145
4.43	Evolution of system parameters wrt M_{WD} (power law)	146
4.44	Evolution of system parameters wrt P_{rec} (power law)	147
4.45	Evolution of system parameters wrt total time (power law)	148
4.46	Evolution of system parameters wrt number of eruptions (power law) .	149
4.47	Run 1 – 3 and Run 21 – 23 (power law comparison)	151

4.48	Run 12 and Run 24 (cool power law comparison)	152
4.49	Run 1 and Run 25 – 27 (initial M_{WD} comparison)	154
4.50	Run 1 and Run 25 – 27 (initial M_{WD} shell width evolution)	155
4.51	Run 1, 4, 7, 21, 25, 26 and 27 recurrence period vs radial size	156
4.52	Run 1, 4, 7, 21, 25, 26 and 27 cumulative kinetic energy vs radial size	157
4.53	Run 12 and Run 28 (cool initial M_{WD} comparison)	158
4.54	Changing the accretion rate during the evolution	159
5.1	Six Galactic recurrent novae	170
5.2	Run 1, Run 2 and Run 3 in full with power law fits	172
5.3	Run 4, Run 5 and Run 6 in full with power law fits	173
5.4	Recurrence period vs cumulative time for different accretion rates	175
5.5	Ionisation fraction of reference simulation NSR when $P_{\text{rec}} = 1$ year	177
5.6	Ionised mass of reference simulation NSR when $P_{\text{rec}} = 1$ year	178
5.7	Emission from NSR of reference simulation when $P_{\text{rec}} = 1$ year	179
5.8	Emission measure ordered by temperature when $P_{\text{rec}} = 1$ year	181
5.9	NSR X-ray luminosity when $P_{\text{rec}} = 1$ year	182
5.10	Synthetic X-ray spectra from APEC & VAPEC model	183
5.11	Recombination time of reference simulation NSR when $P_{\text{rec}} = 1$ year	184
5.12	Evolution of ionisation fraction & emission measure for four regions	187
5.13	Evolution of $\bar{\rho}$, \bar{T} , \bar{f} and emission measure for three regions	188
5.14	Evolution of ionised mass in NSR	189
5.15	Evolution of recombination time in NSR	190
5.16	Evolution of emission measure with identical eruption comparison	191
5.17	Evolution of emission measure in different regions of Run 1	192
5.18	X-ray evolution models with eruptions	194
5.19	X-ray evolution models comparison with M 31N 2008-12a models	195
5.20	Parameter space to form 12a remnant	197
5.21	Photoionisation regions for the reference simulation	200
5.22	Photoionisation regions as a function of ISM density	202
5.23	Synthetic sky images compared to 12a NSR	204
5.24	Synthetic sky images with radiative cooling compared to 12a NSR	205
6.1	Dynamics and evolution of NSR after donor depletion	210
6.2	Evolution of shell velocity after donor depletion	211
6.3	Emission measure evolution of NSR post donor-depletion	212
6.4	X-ray luminosity of NSR ~ 3000 years after donor depletion	213
6.5	Dynamics of NSR after SNIa	215
6.6	Evolution of SNIa ejecta	216
6.7	X-ray luminosity evolution of the NSR after SNIa	217
6.8	X-ray luminosity of NSR ~ 2000 years after SNIa	218
6.9	X-ray luminosity of NSR at epoch of SNIa impact	219
6.10	Synthetic X-ray spectra from APEC & VAPEC model at impact	220
6.11	Synthetic sky image of NSR X-ray luminosity at SNIa impact	221
7.1	Liverpool Telescope Observations of the vicinity around T CrB	231
7.2	Possible NSR around RS Ophiuchi	232

A.1 Schematic of second order Godunov scheme	240
C.1 Schematic to illustrate determining boundary locations of NSRs	243
F.1 Colour scheme	247

List of Tables

1.1	Speed classes of novae	6
1.2	Collection of all recurrent novae	16
1.3	Key parameters of M 31N 2008-12a	19
1.4	The eruption history of M31N 2008-12a	20
2.1	Spectroscopic observations of AT 2017fvz	38
2.2	UV and X-ray observations of AT 2017fvz	39
2.3	AT 2017fvz decline times in each filter	46
2.4	Evolution of emission line fluxes	48
2.5	Evolution of emission line velocities	49
2.6	<i>HST</i> /WFPC2 photometry of the source near to AT 2017fvz	62
2.7	Emission line velocities of NGC 6822 1999 nova and AT 2017fvz	66
3.1	Radii of Strömgren spheres from a non-continuous ionising flux	82
3.2	Radii of Strömgren spheres from a continuous ionising flux	82
3.3	M 31N 2008-12a luminosity derived from a Strömgren sphere	83
4.1	Example of inflow file for <i>Morpheus</i>	94
4.2	Nova envelope parameters from Yaron et al. (2005)	100
4.3	Comparing parameters from simple model to observations	104
4.4	Each run with associated parameters	112
4.5	Each power law run with associated parameters	150
4.6	Each run with different initial M_{WD} with associated parameters	153
5.1	Ten Galactic recurrent novae	168
D.1	Six machines used for hydrodynamical simulations	245

To my Mum and Dad

Chapter 1

Introduction[★]

1.1 A brief history of novae

Since antiquity, the ancients around the world would gaze up into the night sky for guidance, prophecy and wonder. Transient objects such as novae, from *stella nova* (Latin for ‘new star’), animated the darkness with their sudden appearance in the night sky from apparently nothing to naked eye brightness and, as a consequence, were duly recorded. The earliest recorded pre-telescopic example of a nova comes from China during the 14th century BC (Li, 1988, also see Duerbeck (2008) for a catalogue of pre-telescopic Galactic novae and supernovae up to 1604). One of the best located novae to occur before telescopic aid erupted on 11 March 1437 – the fast-declining Galactic classical nova, Nova Scorpii AD 1437. Other interesting observations of potential novae include the *Star of Bethlehem* most likely being a bright nova recorded by the Chinese and Koreans around 5 BC (Clark et al., 1977) as well as CK Vul, until recently believed to be the first recorded nova, observed during 1670 (Shara et al., 1985), which is now thought to be a white dwarf-brown dwarf merger (Eyres et al., 2018) or a member of the Intermediate Luminosity Optical Transients (ILOTs; see Banerjee et al. 2020).

The sporadic noting of novae ended with “the beginning of systematic monitoring of the sky by photographic means” (Duerbeck, 2008) with T Aur being discovered around 1892 (Campbell, 1893). The binary nature of these ‘new stars’ was then revealed with the discovery of eclipses in DQ Her (Nova Her 1934; Walker, 1954; Kraft, 1964). Since then, approximately 300 Galactic novae and over 1100 extragalactic novae have been recorded (see Section § 1.3).

[★]Parts of this chapter are published within the article with the title “AT 2017fvz: a nova in the dwarf irregular galaxy NGC 6822” in *Monthly Notices of the Royal Astronomical Society*, 2019, 486, 4334 – 4347 and is reproduced with permission from MNRAS.

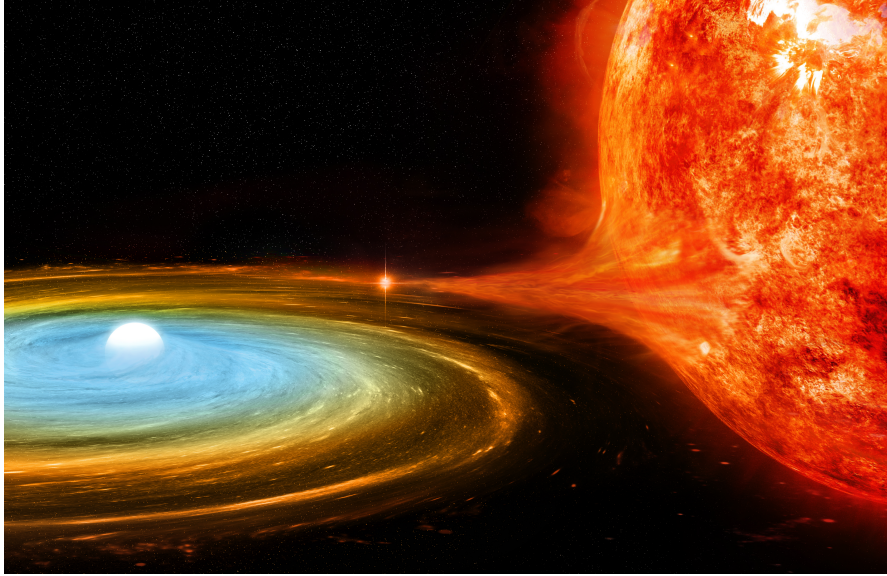


FIGURE 1.1: An artist's impression of a classical nova system. The white dwarf can be seen at the centre of an accretion disk with material streaming from the companion star. Image credit: NASA/CXC/M.Weiss.

1.2 Classical novae

Classical novae (CNe) are the result of a thermonuclear eruption on the surface of a white dwarf (WD) triggered by the accretion of hydrogen-rich material from a non-degenerate companion. They take their place in the class of accreting binaries known as cataclysmic variables, first proposed by [Walker \(1954\)](#) to be closely interacting binary systems consisting of a WD, later found to be of carbon-oxygen (CO) or oxygen-neon (ONe) composition, accreting material from either a main sequence, sub-giant, or red giant companion star (see [Darnley et al., 2012](#)). This accretion usually results in the formation of an accretion disk around the degenerate object, as shown in [Figure 1.1](#). If the mass accretion rate of the system is between approximately $1 \times 10^{-6} M_{\odot} \text{ yr}^{-1}$ and $1 \times 10^{-11} M_{\odot} \text{ yr}^{-1}$, the stage is set for a luminous outburst. As well as CNe, this configuration can give rise to a number of other strongly related astrophysical phenomenon such as dwarf novae (DNe) and recurrent novae (RNe; see [Section § 1.4](#)). Furthermore, depending on the orbital period of the system, and therefore variation in accretion rate, cataclysmic variable systems such as this may go through cycles of mild or deep hibernation ([Hillman et al., 2020a](#)). The quiescent state of mild hibernating systems leads to appearing as a novalike binary, then as DNe and back to a novalike between successive nova eruptions, whereas deep hibernating systems can appear as detached binaries for millions of years between nova outbursts ([Hillman et al., 2020a](#)).

1.2.1 Nova outburst

But how does matter funnelling onto the WD create the third most luminous stellar explosion currently known, rivalled only by gamma-ray bursts and supernovae (Bode et al., 2004)? As discussed, the WD within the binary system accretes material from a cooler companion; through a stellar wind emanating from the evolved donor, the Roche lobe shrinking due to gravitational radiation if the system is below the period gap or Roche lobe overflow from evolutionary processes of the donor if above the period gap. This material then streams through the inner Lagrangian point into an accretion disk surrounding the WD (Starrfield et al., 1976, 2016).

On the surface of the WD, the accreted material is increasingly subjected to extremely high temperatures and pressures, leading to degeneracy. Once an ignition temperature is reached (Starrfield et al., 1972), the envelope of material bordering the WD undergoes a thermonuclear runaway (TNR) with the unstable burning of hydrogen (H). The resulting high temperatures recouple the dependency with pressure, leading to a violent expansion of the accreted layer from the surface of the WD. Those ejecta accelerated to velocities greater than the escape velocity of the degenerate host will produce a pseudo-photosphere, appearing at various wavelengths to distant observers as the nova eruption (Starrfield et al., 1976, 2020). The amount of material retained on the WD's surface over this eruption cycle has recently been shown, through theoretical studies, to be greater than zero (see, for e.g. Prialnik & Kovetz, 1995; Yaron et al., 2005; Kato et al., 2015; Hillman et al., 2015, 2016; Starrfield et al., 2021), clearly indicating mass retention on the WD and the possibility for a future SNIa (see Section § 1.4.1).

Recent γ -ray and optical observations of the Galactic nova ASASSN-16ma indicates that a portion of the optical light seen from a nova arises from shocks in the ejecta reprocessing light (Li et al., 2017). This is supported by high-cadence monitoring of a sample novae (V1369 Cen, V5855 Sgr, V549 Vel, ASASSN-17pf, FM Cir, V906 Car, V435 CMa, V613 Sct, V1706 Sco, ASASSN-19qv, LMCN-2019-07a and V1707 Sco) by Aydi et al. (2020b) whom concur that nova outbursts are not one single ballistic event, but are a combination of two (or possibly three) components. The material ejected during the outburst as described above is the slow component of the event, with the fast component being the radiation-driven wind from the WD following afterwards (Aydi et al., 2020b). This eventually collides with the earlier ejecta, leading to shocks and γ -ray emission (see Section § 1.2.3), heavily influencing the visual event we see as in Nova V906 Car (Aydi et al., 2020a, and see Figure 1.2).

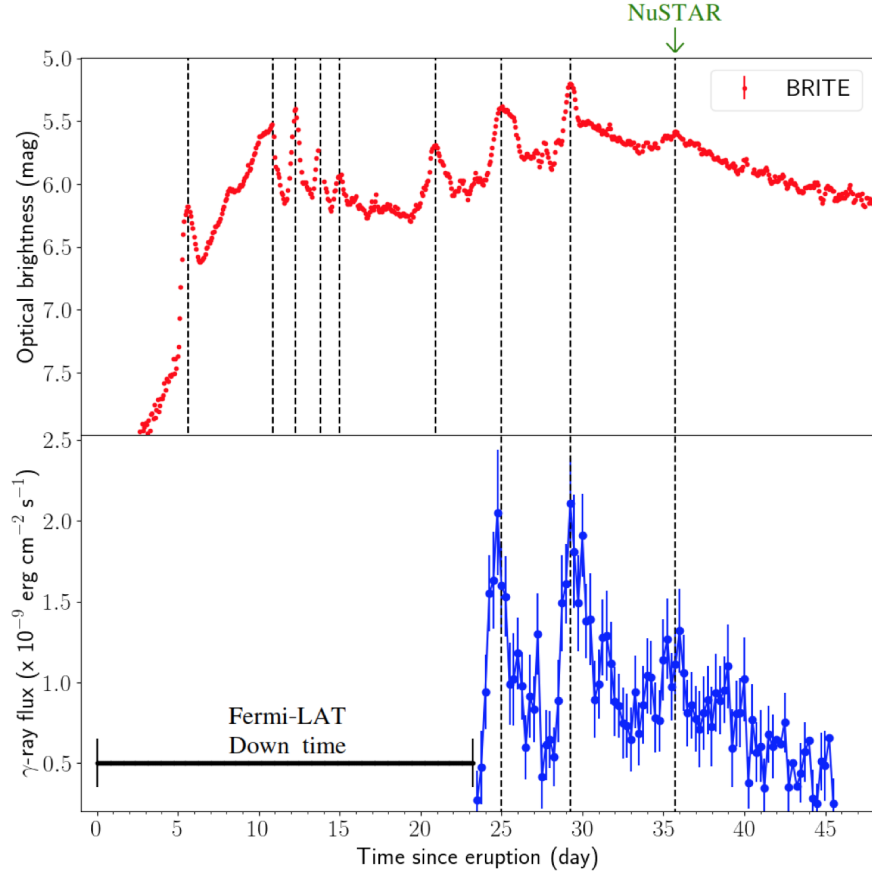
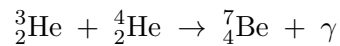


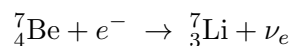
FIGURE 1.2: The top panel shows a high-cadence optical light curve of Nova V906 Car with flares associated with shocks. These optical flares correlate with the coincident flaring seen in the γ -ray light curve in the bottom panel. Reprinted by permission from Springer Nature Customer Service Centre GmbH: Springer Nature, Nature Astronomy “Direct evidence for shock-powered optical emission in a nova”, Elias Aydi et al. © 2020 (Aydi et al., 2020a).

1.2.2 Lithium production

The thermonuclear runaway within the WD envelope can form substantial amounts of beryllium-7 (${}^7\text{Be}$) with a half-life ~ 53 days (Giraud et al., 2007) through the following proton-proton chain reaction:



where γ represents gamma-ray radiation. This was first proposed by Cameron & Fowler (1971) to occur during the advanced stages of red giant stars, and afterwards implemented in nova research (Arnould & Norgaard, 1975). The ${}^7\text{Be}$ is then ejected during the nova outburst before decaying through electron capture (Izzo et al., 2018):



and enriching the interstellar medium with lithium-7 (${}^7\text{Li}$; [Arnould & Norgaard, 1975](#); [Starrfield et al., 1978](#)), with e^- representing an electron and ν_e representing an electron neutrino. Even though the rate of ${}^7\text{Be}$ decaying to ${}^7\text{Li}$ is dependent on electron density, the number of electrons never drops too low to impede this reaction, neither through the ejecta thinning nor through recombination as the ejecta is always too hot (S. Starrfield, private communication).

Recent observational evidence from a number of novae such as V382 Velorum ([Della Valle et al., 2002](#)), V1369 Centauri ([Izzo et al., 2015](#)), V339 Delphini ([Tajitsu et al., 2015](#)), V2944 Ophiuchi ([Tajitsu et al., 2016](#)), V5668 Sagittarii ([Tajitsu et al., 2016](#); [Molaro et al., 2016](#)), and V407 Lupi ([Izzo et al., 2018](#); [Aydi et al., 2018b](#)) all reinforce this idea, making novae one of the most plausible stellar candidates for the production of this element ([Izzo et al., 2018](#)), contributing substantially to the total ${}^7\text{Li}$ in the Galaxy. This is significant for trying to reconcile overabundances of lithium observed ([Spite, 1990](#)) with the multitude of depletion mechanisms of Li (see, for e.g. [Spite, 1990](#); [D’Antona & Matteucci, 1991](#)).

1.2.3 X-ray and γ -ray production

Following the TNR, quasi-stable hydrogen burning continues within the material remaining on the WD surface. This results in the emission of a large amount of X-rays typically peaking between 30–50 eV – the so-called super-soft X-ray source (SSS; see, [van den Heuvel et al., 1992](#); [Osborne, 2015](#)). GQ Muscae was the first classical nova from which X-ray emission was detected during outburst ([Oegelman et al., 1984](#)) along with other X-ray sources such as CAL83 and RX J0527.8-6954 ([Greiner et al., 1991](#)). The SSS is initially obscured by the optically thick ejecta surrounding the nova, however, once the optical depth has decreased sufficiently, the SSS is unveiled. The time at which this occurs is used to define the ‘turn-on’ time (t_{on} ; [Henze et al., 2014a](#)). The SSS ‘turn-off’ time (t_{off}) is defined as the cessation of nuclear burning on the surface of the WD, resulting in a marked decline in the super-soft X-ray emission (see, e.g., [Hachisu & Kato, 2006](#); [Kato & Hachisu, 2020](#)). Alternatively, the ‘turn-off’ time can be defined observationally as when the SSS drops below the detection limit ([Henze et al., 2014a](#)), however this is more relevant for extragalactic systems. X-ray observations and X-ray spectra such as the examples given in [Figure 1.3](#) allow the study of the WD’s effective temperature and therefore the WD’s mass, the luminosity, the duration of hydrogen burning on the surface as well as studying the WD’s atmosphere to estimate chemical abundances, with the possibility of differentiating between a CO and an ONe WD ([Orio, 2020](#); [Ness, 2020](#)).

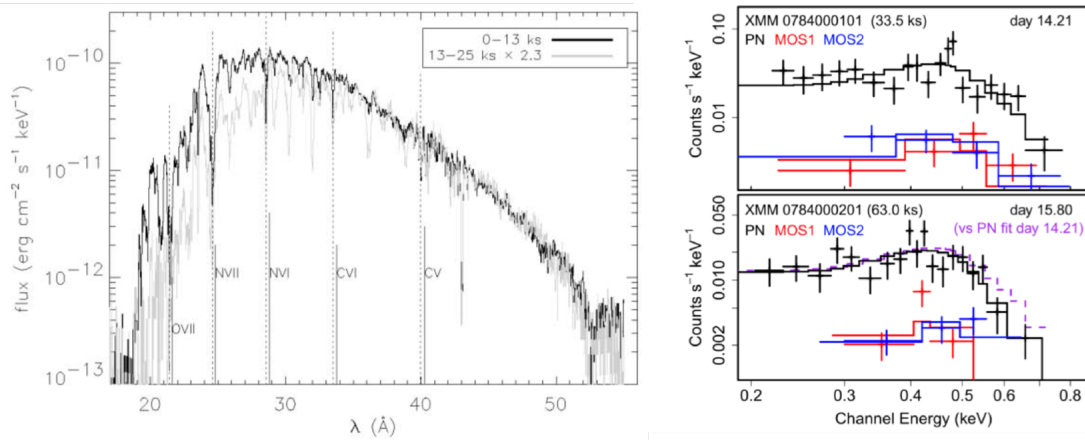


FIGURE 1.3: Two examples of X-ray spectra from a Galactic nova and an extragalactic nova. **Left:** Chandra-LETGS spectrum of V4743 Sgr with the strongest absorption lines indicated. Taken from [Ness et al. 2003](#) © AAS. Reproduced with permission. **Right:** *XMM-Newton* EPIC spectra of the recurrent nova M31 2008-12a. Taken from [Henze et al. 2018a](#) © AAS. Reproduced with permission.

As well as emitting soft X-rays, novae can produce hard X-ray emission with temperatures up to several keV ([Krautter, 2008](#)). This emission can be produced from the accretion stream; shocks within the nova wind; shocks from the collision between a fast wind with a pre-existing slow wind from the WD and shocks within the region where the nova ejecta collides with a red giant (RG) wind or an old nova shell ([Balman et al., 1998](#); [Krautter, 2008](#)).

Additionally, ejecta from the nova outburst expanding within the circumstellar wind of a RG companion can give rise to γ -ray emission (see [Ackermann et al., 2014](#), for more details). This can be through the high-energy particles being accelerated to produce π^0 decay γ -rays from proton-proton interactions or inverse Compton scattering of the RG radiation, as was the case for V407 Cygni 2010, the first γ -ray detected nova ([Cheung et al., 2010](#); [Abdo et al., 2010](#)). However, significantly in 2012 and 2013, three classical novae were detected in γ -rays by the *Fermi*/Large Area Telescope – V959 Mon, V1324 Sco and V339 Del ([Ackermann et al., 2014](#)). These gamma-ray novae have different speed classes (see Table 1.1) and different companion types ([Hachisu & Kato, 2018](#)) meaning that all novae could be potential gamma-ray emitters, possibly arising from the collisional shocks between a slow and fast component of the nova system ([Metzger et al., 2014](#); [Aydi et al., 2020a,b](#)). Detection of γ -rays in these novae may then be due to their close proximity ([Ackermann et al., 2014](#)).

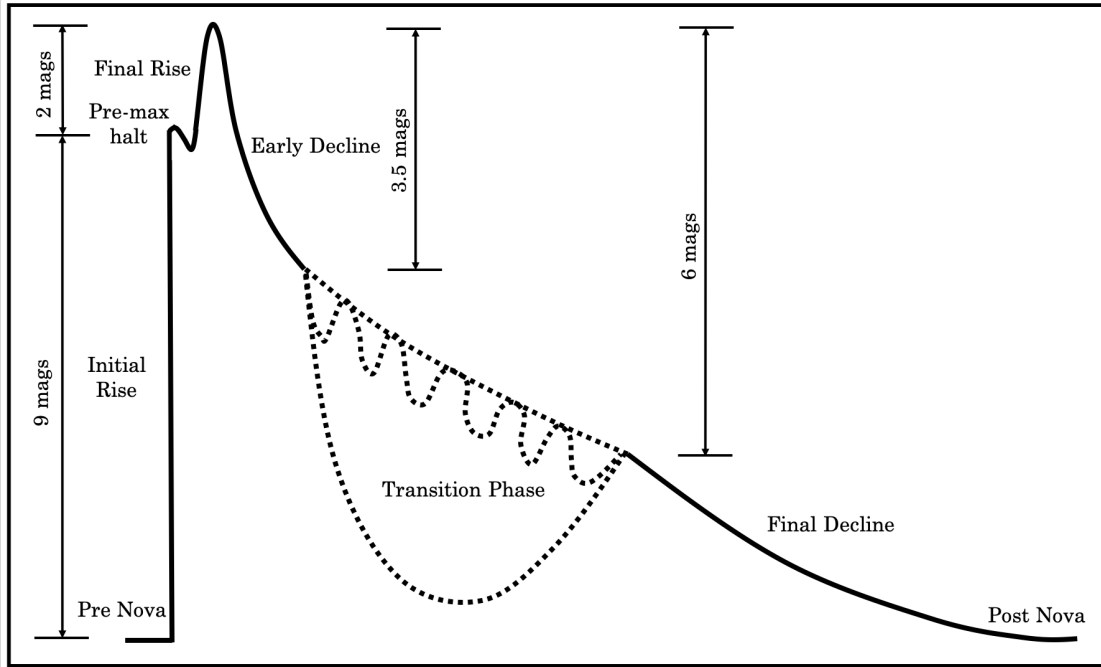


FIGURE 1.4: A reproduction by the author of the morphology of a nova light curve showing the rise in luminosity from quiescence followed by varying types of decline (McLaughlin, 1939, 1960).

1.2.4 Photometric properties

The luminosity of novae typically increases to a few tens of thousands of solar luminosities (see, e.g., Bode, 2010) with peak absolute magnitudes reaching $M_V \simeq -10.5$ in extreme cases (Shafter et al., 2009; Aydi et al., 2018a), before fading away to quiescence (see Figure 1.4). Observationally, one can categorise novae into different speed classes based on their decline times, t_2 and t_3 (Payne-Gaposchkin, 1957). These denote the time taken to decay by 2 or 3 magnitudes from maximum light, respectively, and range from ‘very-fast’ for novae with $t_2 < 10$ d to ‘very-slow’ for $t_2 > 150$ d, and similarly for t_3 (see Table 1.1). However, difficulties arise in assigning novae to a

TABLE 1.1: Classification of nova light curves by their speed class including the change in magnitude over time (Payne-Gaposchkin, 1957).

Speed class	t_2 (days)	\dot{m}_V (mag d ⁻¹)
Very fast	< 10	> 0.20
Fast	11 – 25	0.18 – 0.08
Moderately fast	26 – 80	0.07 – 0.025
Slow	81 – 150	0.024 – 0.013
Very slow	151 – 250	0.013 – 0.008

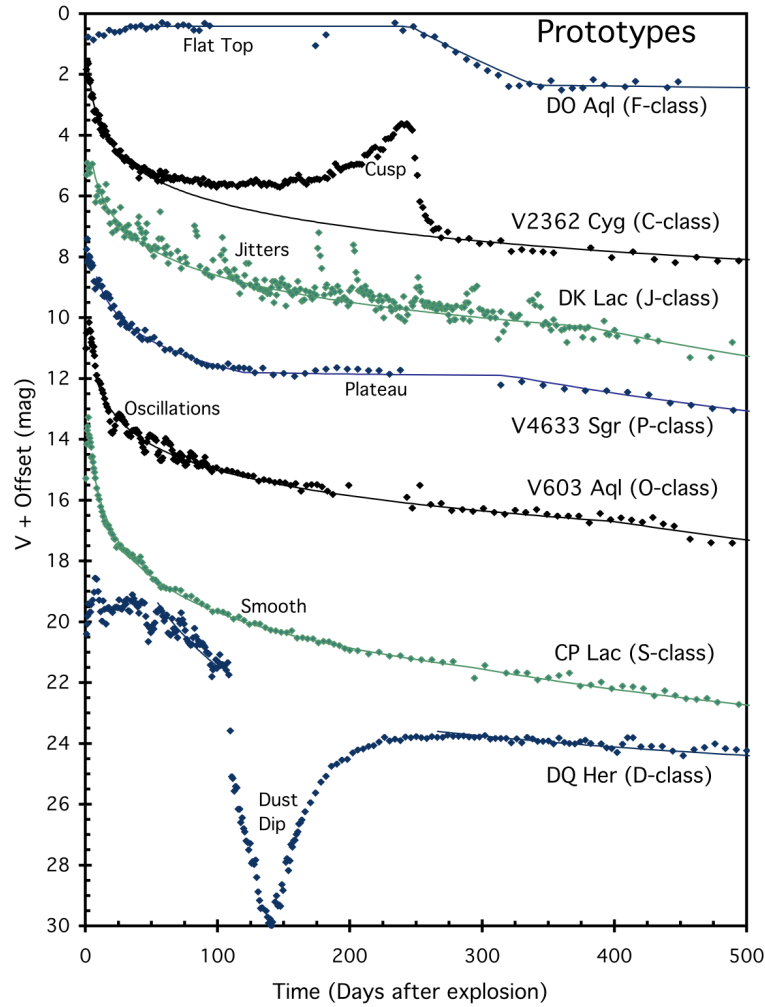


FIGURE 1.5: Light curve classes and the name of the prototype as outlined in Strope et al. (2010) © AAS. Reproduced with permission.

speed class due to nova light curves also showing variability (see Figure 1.5) during their decline from peak magnitude. Instead, categorising light curves based on their prominent features, as given in Strope et al. (2010), is possibly a more useful endeavour.

Could there be a connection between a nova’s peak brightness and the time taken to fade? Zwicky (1936) was the first to propose such a relation between this decline time and the maximum absolute visual magnitude of a nova. McLaughlin (1945) and Arp (1956) developed this idea further into the ‘maximum magnitude – rate of decline’ relation (MMRD; see, e.g., Downes & Duerbeck, 2000, and the top left and top right panel of Figure 1.6), with the potential to use novae to estimate distances. However, the MMRD suffers from a large scatter and recently the relation has been diluted by the discovery of both ‘faint and fast’ novae (see Section § 1.4.2 and the bottom left and bottom right panel of Figure 1.6) in M 31 (Kasliwal et al., 2011) and M 87

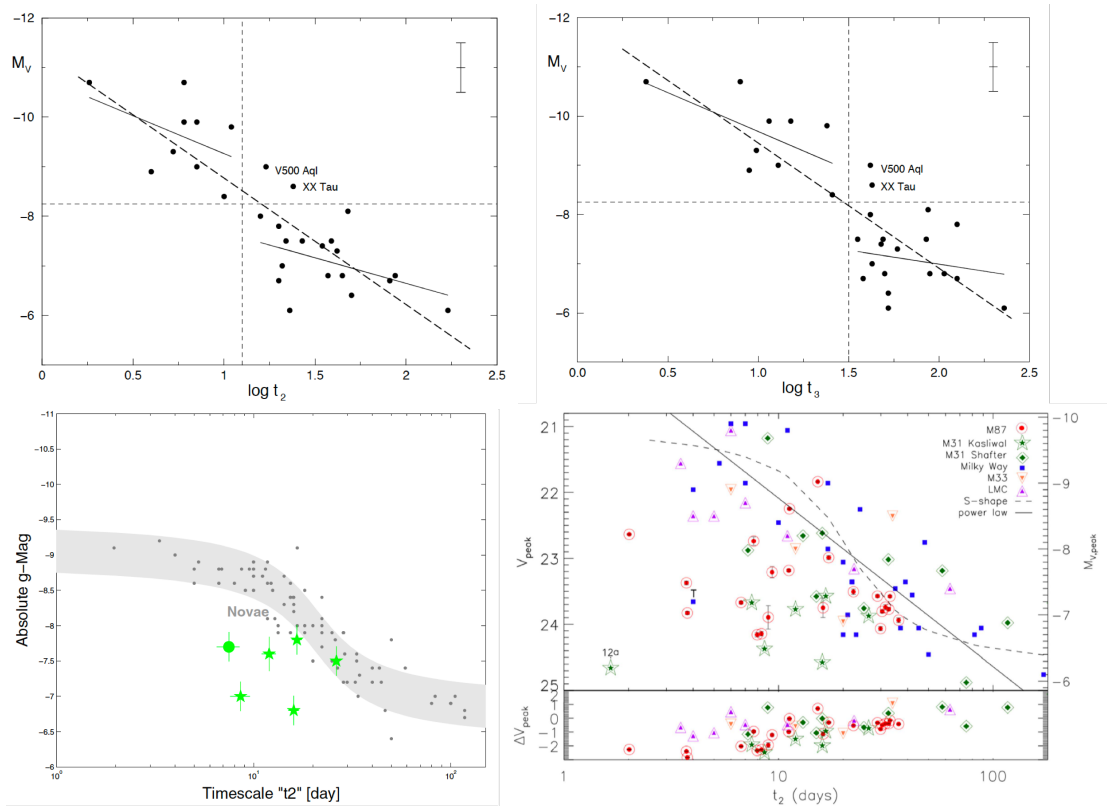


FIGURE 1.6: Maximum magnitude – rate of decline relations. **Top left:** Peak absolute visual magnitude versus t_2 decline time with MMRD relation from Downes & Duerbeck (2000) © AAS. Reproduced with permission. **Top right:** Peak absolute visual magnitude versus t_3 decline time with MMRD relation from Downes & Duerbeck (2000) © AAS. Reproduced with permission. **Bottom left:** Peak absolute g magnitude versus t_2 decline time with MMRD relation from Kasliwal et al. (2011) © AAS. Reproduced with permission. The six green points are the ‘faint and fast’ novae (see Section § 1.4.2). **Bottom right:** Peak V magnitude vs the t_2 decline time given in Shara et al. (2017b) © AAS. Reproduced with permission. This illustrates the large scatter in the MMRD from new novae that sit in the earlier empty areas of the peak magnitude-decline time plot.

(Shara et al., 2016, 2017b), and the, possibly related, short-cycle RNe ($P_{\text{rec}} < 10$ yr; Darnley & Henze 2020 and see Section § 1.4.3). Figure 1.6 demonstrates how earlier and deeper observations with recent surveys, have begun to populate parts of the MMRD plots that were otherwise empty and in doing so, seemingly terminating the MMRD relation, though the debate (see Schaefer, 2018; Selvelli & Gilmozzi, 2019; Della Valle & Izzo, 2020) for its validity in Galactic novae still exists despite Gaia DR2 (Gaia Collaboration et al., 2018). Perhaps the MMRD relation can be revived by accounting for bolometric luminosity instead of considering only optical, as discussed by Darnley & Henze (2020, and see Section § 1.4.2).

Buscombe & de Vaucouleurs (1955) suggested that novae could be utilised as standard candles. They noted that the absolute magnitudes of novae converge to the same value 14–16 d after maximum light – a relation now bearing their name.

For example, the absolute magnitude 15 days after maximum of novae in M 49 is $M_{V,15} = -6.36 \pm 0.19$ from a recalibrated Buscombe–de Vaucouleurs relation (Ferrarese et al., 2003). Similarly, novae in M 87 display $M_{606W,15} = -6.37 \pm 0.46$ and $M_{814W,15} = -6.11 \pm 0.43$ (Shara et al., 2018). However, Darnley et al. (2006) found no evidence for such a convergence in the more complex stellar population of M 31.

1.2.5 Spectroscopic properties

Novae can be divided into two different classes based on the prominent non-Balmer emission lines in their spectra: He/N (helium-nitrogen) and Fe II (singly ionised iron) novae (see Williams, 1992, 1994; Shore, 2012, and Figure 1.7). Williams (2012) proposed that these two populations occur due to differing gaseous components of the binary systems. Williams (2012) suggested that the high velocity He- and N-enhanced ejecta from the surface of the WD should produce an initial spectrum dominated by He and N in every nova. These lines will be optically thick or thin depending on the mass ejected during the eruption, ejecta that will ultimately impact the donor star. The donor’s radiation field may then, depending on the binary separation, be stimulated by the TNR leading to an ejection of mass from the donor (see Figueira et al., 2018, for related hydrodynamic simulations). If the subsequent donor mass loss is not significant then the He/N lines will remain dominant post-maximum producing a He/N novae. However, if the mass loss from the companion star is significant then this additional circumbinary material can be excited giving rise to an Fe II nova spectrum (Williams, 2012). If we observe Fe II lines before the He/N lines become dominant then we classify this as a “hybrid” nova (Williams, 1992). Williams (1992) presented Nova LMC 1988 No. 2 as an example of a hybrid nova as its spectrum evolved from being dominated by Balmer and Fe II emission lines a few days after eruption to a spectrum with many H, He and N lines.

The proportion of novae belonging to each spectral class has been observed to vary between different galaxies. This may be due to differences in the dominant stellar population and metallicity of a given host (Shafter, 2013) so studying novae in extragalactic environments provides the only way to explore how the local environment, e.g., the metallicity and star-formation rate, can affect the nova rate and characteristics of nova eruptions (Shara et al., 2016). Novae arising from the younger stellar populations within the disk components of galaxies will generally have higher WD masses and hence systems that eject less material at higher velocities – the He/N spectral class (Shafter, 2013). Older stellar populations, typically associated with the bulge component of galaxies, will have more Fe II novae as the mean nova WD

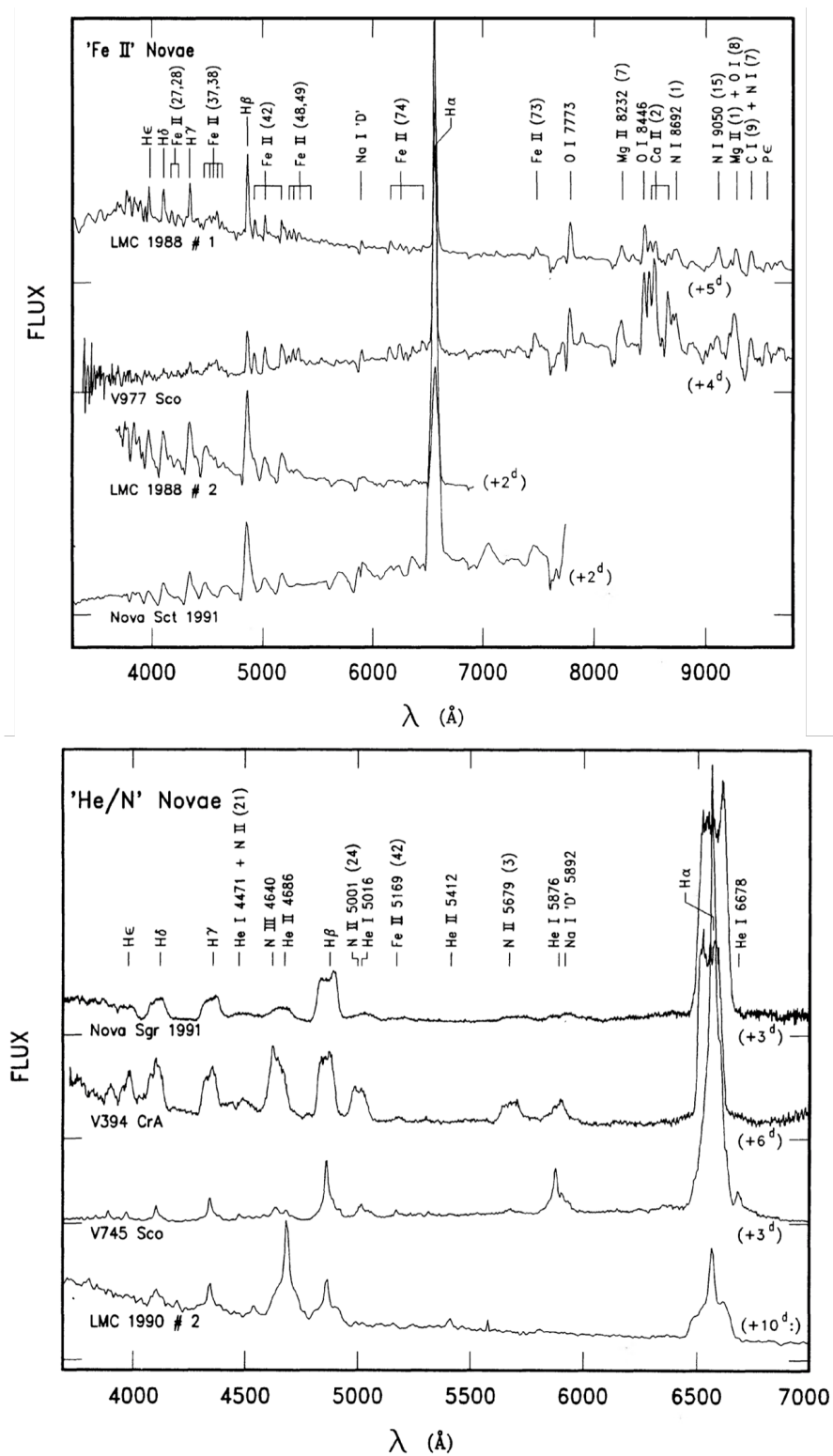


FIGURE 1.7: Spectroscopic classes of novae given in Williams (1992) © AAS. Reproduced with permission. **Top:** Novae with features indicative of the Fe II spectroscopic class. **Bottom:** Novae with features indicative of the He/N spectroscopic class.

mass will be lower, leading to more material being ejected more slowly. For example, [Della Valle & Livio \(1998\)](#) and [Della Valle & Izzo \(2020\)](#) found that novae in the Galactic disk tend to belong to the He/N spectroscopic class whereas those in the thick-disk/bulge form the majority of Fe II novae. However, [Özdönmez et al. \(2018\)](#) recently suggested that this may be a selection effect. Similarly, M 31, a galaxy with a disk and a bulge component, has a nova population that is dominated by Fe II novae with 82% belonging to this spectral class ([Shafter et al., 2011, 2014](#)) and the rest belonging to the He/N or “hybrid” spectral class. [Shafter et al. \(2011\)](#) also reported that the spectral class of novae had no spatial dependence although the inclination of M 31 may have affected study of the scale height distribution.

Bulge-less galaxies have similar numbers of each spectral type of nova. For example, 5 of the 10 spectroscopically classified novae in M 33 belong to the Fe II spectral class and, to the 98% confidence level, this indicates that the M 33 nova spectral type distribution differs from that of M 31 ([Shafter et al., 2014](#)). Likewise, the fraction of Fe II novae in the LMC, which also lacks a bulge, is $\sim 50\%$ ([Shafter, 2013](#)).

Another subclass of classical novae identified from their spectra are the neon (Ne) novae, an example of such being V1974 Cyg ([Collins et al., 1992](#)). These CNe show stronger Ne emission lines than the permitted lines during the nebular phase, and if the Ne abundances computed from their spectra are much greater than solar Ne abundances, the Ne within the ejecta may have originated from an ONe WD ([Hachisu & Kato, 2016](#)).

1.2.6 Nova shells

A nova eruption will eject approximately $\sim 10^{-4} M_{\odot}$ of material into its surroundings with typical velocities ranging from a few hundred to several thousands of kilometres per second ([O’Brien, 2008](#)), with the interaction of ejecta travelling at different velocities shock heating the gas leading to X-ray and radio emission such as that seen in RS Ophuichi ([Bode & Kahn, 1985](#); [O’Brien et al., 1992](#)) and V838 Her ([O’Brien et al., 1994](#)). This ejected material then goes on to form a nova shell (see for e.g. [Cohen, 1985](#); [Gill & O’Brien, 1998](#); [Slavin et al., 1995](#); [Gill & O’Brien, 2000](#); [Ribeiro et al., 2009](#); [Santamaría et al., 2020](#); [Harvey et al., 2020](#)). Figure 1.8 shows a few examples of these spatially resolved shells.

[Hutchings \(1972\)](#) introduced the idea that a nova shell is structured with an equatorial waist and polar cones of emission resulting from the originally spherically symmetrical ejecta interacting with the companion. Crucially these nova shells can tell us a great deal about the underlying system. For example, the rotation of the

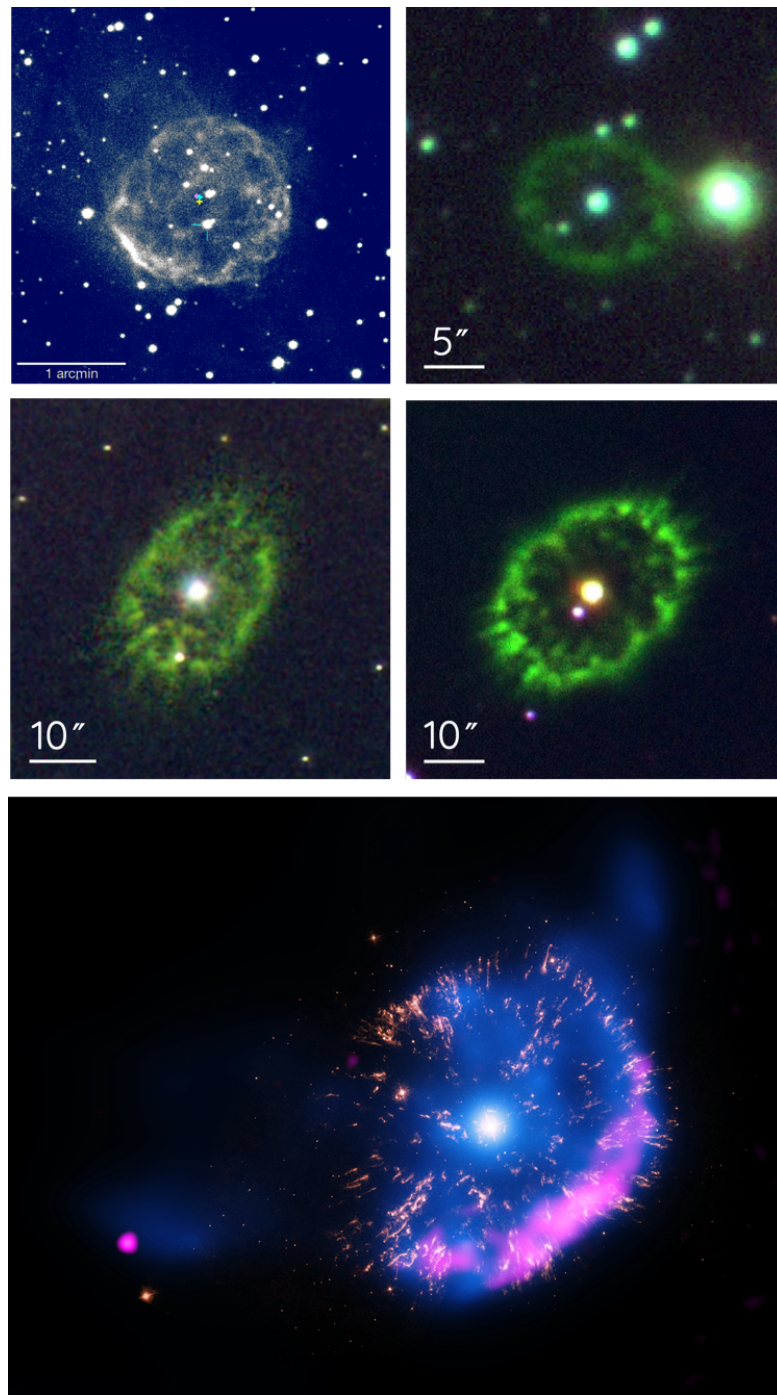


FIGURE 1.8: Five examples of spatially resolved nova shells. **Top left:** False colour $H\alpha$ image of the shell ejected by Nova Scorpii AD 1437 from [Shara et al. \(2017a\)](#). Reprinted with permission from K. Ilkiewicz & J. Mikolajewska. Reprinted by permission from Springer Nature Customer Service Centre GmbH: Springer Nature, Nature “Proper-motion age dating of the progeny of Nova Scorpii AD 1437”, M. M. Shara et al © 2017. **Top right, middle left, middle right:** *RGB* composite images of FH Ser, T Aur and DQ Her, respectively, from [Santamaría et al. \(2020\)](#) © AAS. Reproduced with permission. **Bottom:** A composite image made from X-ray (blue), optical (red) and radio images (purple) of the nova shell surrounding GK Per (image credit: X-ray: NASA/CXC/RIKEN/D.Takei et al; Optical: NASA/STScI; Radio: NRAO/VLA).

WD envelope can be ascertained from the asphericity of the nova remnant (Porter et al., 1998) and the orbital inclination of the binary can be determined from the orientation of the equatorial rings (Slavin et al., 1995; Harvey et al., 2020).

Additionally, the shaping of these structures can be linked with the speed class of the nova (Slavin et al., 1995). Remnants with structure and evidence of polar blobs or equatorial rings are common to slow novae whereas faster novae exhibit approximately circular shells with bright knots of emission (Slavin et al., 1995), although in another study, this was found not to be the case (Ribeiro, 2011). From simple geometries that incorporate expanding ellipsoidal shells encircled by equatorial and tropical rings or polar caps at various inclinations, emission line profiles can be calculated (Gill & O'Brien, 1999) and used to reveal different components of the nova shell. This is demonstrated in Ribeiro et al. (2009) with the remnant surrounding RS Ophiuchi being modelled as a bipolar structure with two co-aligned components as well as the shell around V5668 Sagittarii being modelled as having an equatorial-ring-waist in Harvey et al. (2018). Furthermore, X-ray and radio observations of the recurrent nova RS Ophiuchi reveal an asymmetric collimated ejection of material in the form of a jet-like structure (Sokoloski et al., 2006; O'Brien et al., 2006).

We can also derive kinematical information such as expansion velocities (Vaytet et al., 2007a; Harvey et al., 2016), use the expansion parallax method with these shells to determine distances to their associated novae (O'Brien, 2008) as well as studying a plethora of other important physics such as thermonuclear reactions, formation of dust, clumping and mixing mechanisms, radiation-driven winds and astrophysical chemistry as stated in Gill & O'Brien (2000).

1.3 Extragalactic novae and nova rates

Approximately 250 novae have been discovered within the Galaxy from 1900 to 2015 (Shafter, 2017) with a further 66 being discovered after this up to September 2021 (see, e.g. <https://asd.gsfc.nasa.gov/Koji.Mukai/novae/novae.html>). Extragalactic novae, in contrast, are found in far greater numbers, with over 1100 nova candidates being discovered in M31 alone (see Pietsch et al., 2007; Pietsch, 2010). Consequently, extragalactic novae prove to be very useful when it comes to population studies as we can build up a large sample of novae from the same galaxy and assume that they are at similar distances. Galactic novae, on the other hand, suffer from differing levels of extinction. This results in reliable estimates of the Galactic nova rate being difficult to obtain, with the current most plausible estimate being $50_{-23}^{+31} \text{ yr}^{-1}$ (Shafter, 2017).

It is important to study extragalactic novae in dwarf galaxies as well as larger galaxies. This is to determine how the environment of the host system, such as the differing metallicities and star formation rates can affect not only the nova rate but their characteristics (Shara et al., 2016). For example, the large spiral galaxies M 31 and M 81 have nova rates of $65_{-15}^{+16} \text{ yr}^{-1}$ (Darnley et al., 2006) and $33_{-8}^{+13} \text{ yr}^{-1}$ (Neill & Shara, 2004), respectively. The ellipticals, M 49 and M 84 have much larger rates of $189_{-22}^{+26} \text{ yr}^{-1}$ and $95_{-14}^{+15} \text{ yr}^{-1}$ (Curtin et al., 2015), respectively. The elliptical galaxy M 87 has a nova rate of $363_{-45}^{+33} \text{ yr}^{-1}$ (Shara et al., 2016), however, it has been argued that this may instead be an upper limit (Shafter et al., 2017).

Small spiral galaxies such as M 33 and dwarf galaxies such as the Large Magellanic Cloud (LMC) and Small Magellanic Cloud (SMC) have much lower nova rates of $2.5_{-0.7}^{+1.0} \text{ yr}^{-1}$ (Williams & Shafter, 2004), $2.4 \pm 0.8 \text{ yr}^{-1}$ and $0.9 \pm 0.4 \text{ yr}^{-1}$, respectively (Mróz et al., 2016). Shafter et al. (2014) determined that there is a linear relation between the nova rate of a galaxy and its K -band luminosity, used as a direct tracer of the stellar mass, in the form $R = \nu_K L_K$, where R is the nova rate of a galaxy (per year), L_K is the K -band luminosity of the galaxy in units of $10^{10} L_{\odot,K}$ and $\nu_K = 2.25 \text{ yr}^{-1} [10^{10} L_{\odot,K}]^{-1}$ — the ‘luminosity specific nova rate’ (LSNR). With reference to this relationship, Mróz et al. (2016) stated that the LSNR in the LMC and the SMC are 2–3 times higher than in other galaxies, they proposed that this may be due to the re-ignition of the star formation a few Gyr ago.

1.4 Recurrent novae

A classical nova eruption is not the end of the binary’s activity. Even though the accretion disk surrounding the WD can be altered (Henze et al., 2018a) to the point of removal in many cases (Drake & Orlando, 2010; Figueira et al., 2018), it will re-establish after the nova outburst (Worters et al., 2007) in preparation for future eruptions. It is predicted that all novae follow such a recurrent cycle, however the broad range of times between consecutive eruptions, which, from theory, can be as brief as 50 days (Kato et al., 2014), to longer than 1000 years (Yaron et al., 2005), means that novae are split into separate categories based on their recurrence period (P_{rec}), influenced by observational bias.

Classical novae have been observed to erupt just once. Recurrent novae (RNe), on the other hand, are systems that have been recorded erupting multiple times throughout observational history, stemming from the underlying binary (in the majority of cases) containing a high mass WD and a high accretion rate. The combination of less material needed to trigger the burning of hydrogen on a WD with an

increased surface gravity, along with a higher delivery of this material, creates the conditions for recurrent nova outbursts (Darnley, 2021).

Such an example is the Galactic recurrent nova RS Ophiuchi, having erupted at least seven¹ times since 1898 (Evans et al., 2008; Adamakis et al., 2011). This is one of the ten currently known RNe residing in the Galaxy and lends its name to one of the three subclasses (Anupama, 2008). The *RS Ophiuchi-class* (or symbiotic RNe) are defined by having red giant donors and includes RS Ophiuchi, T Coronae Borealis, V3890 Sagittarii, V745 Scorpii and V2487 Ophiuchi (suspected to belong to this class through quiescent NIR photometry; Darnley et al. 2012). The *U Scorpii-class* includes U Scorpii, CI Aquillae and V394 Coronae Australis, grouped together by their sub-giant companions leaving the last two Galactic RNe we know of, T Pyxidis and IM Normae, being placed in a separate class known as the *T Pyxidis-class* on account of their short orbital periods (as well as main sequence companions and lower mass WDs). As both have orbital periods below the period gap, these systems should have a low accretion rate driven by gravitational radiation loss, but instead are observed to have high accretion rates (Schaefer et al., 2010), so can be named the “recurrent unusual novae” (Darnley, 2021).

In total, there are 32 currently known recurrent novae (with potentially many more masquerading as a classical cousin, see Pagnotta & Schaefer, 2014), with recurrence periods ranging from 1 year (Darnley et al., 2014) up to 98 years (Pagnotta et al., 2009), clearly outlining our current observational constraints. As mentioned, ten RNe reside in the Galaxy, with the others being found in the Large Magellanic Cloud (four RNe) and M 31 (nineteen RNe). Using Darnley (2021) and Darnley & Henze (2020), we have collated all of these recurrent novae in Table 1.2 along with their recurrence period and number of (confirmed) known eruptions. For the RNe in the Galaxy, we have included the type of donor: red giant (RG), sub-giant (SG) or main sequence (MS) (Darnley et al., 2012).

1.4.1 Potential type Ia supernova progenitors

A type Ia supernova (SNIa) is the result of a carbon-oxygen WD evolving to the Chandrasekhar mass (M_{Ch} ; Chandrasekhar 1931), at which point a thermonuclear disruption takes place and the WD explodes (see for e.g. Hillebrandt & Niemeyer, 2000)². The two leading hypotheses to explain how this threshold is reached are

¹RS Ophiuchi experienced an outburst in August 2021. See the following for the first report: (<http://www.cbat.eps.harvard.edu/iau/cbet/005000/CBET005013.txt>).

²The author is aware that the double detonation of sub-Chandrasekhar mass WDs with surface helium shells is also a proposed SN Ia progenitor (see e.g. Gronow et al., 2021, and references therein).

TABLE 1.2: Collection of all recurrent novae grouped into their respective host galaxy with number of known (confirmed) eruptions and recurrence period. Taken from Darnley & Henze (2020) and Darnley (2021) with references therein. The type of donor is given for the Galactic RNe with red giant, sub-giant and main sequence indicated with RG, SG or MS, respectively. See Section § 1.4.4 for a more detailed discussion of the most rapidly recurring nova, M 31N 2008-12a. [✱] M31N 2017-01e was determined to be a recurrent nova after the publication of Darnley & Henze (2020) and Darnley (2021). [†] The first eruption is taken from Williams & Darnley (2017a) and the second eruption (and therefore recurrence period) is from Steven Williams (private communication).

Nova (donor type)	Known eruptions	P_{rec} (years)
Milky Way		
U Scorpii (SG)	10	10 ± 1
RS Ophiuchi (RG)	7	15 ± 6
T Pyxidis (MS)	6	24 ± 12
V745 Scorpii (RG)	3	26 ± 1
CI Aquillae (SG)	3	27 ± 4
V3890 Sagittarii (RG)	3	29 ± 1
V394 Coronae Australis (SG)	2	~ 38
T Coronae Borealis (RG)	2	~ 80
IM Normae (MS)	2	~ 82
V2487 Ophiuchi (RG)	2	~ 98
LMC		
LMCN 1968-12a	4	6.7 ± 1.2
LMCN 1996	2	~ 22
LMCN 1971-08a	2	~ 38
YY Doradus	2	~ 67
M 31		
M31N 2008-12a	14	0.99 ± 0.2
M31N 2017-01e [*]	2 [†]	~ 2.7
M31N 1997-11k	3	~ 4
M31N 1963-09c	4	~ 5
M31N 1960-12a	3	~ 6
M31N 1984-07a	3	~ 8
M31N 2006-11c	2	~ 8
M31N 1990-10a	3	~ 9
M31N 2007-11f	2	~ 9
M31N 2007-10b	2	~ 10
M31N 1926-07c	3	~ 11
M31N 1982-08b	2	~ 14
M31N 1945-09c	2	~ 27
M31N 1926-06a	2	~ 37
M31N 1966-09e	2	~ 41
M31N 1961-11a	2	~ 44
M31N 1953-09b	2	~ 51
M31N 1919-09a	2	~ 79
M31N 1923-12c	2	~ 88

the double WD merger scenario (the double degenerate pathway; [Iben & Tutukov, 1984](#); [Webbink, 1984](#)) and the single degenerate case, whereby the WD grows in mass by accreting material from a non-degenerate companion ([Whelan & Iben, 1973](#); [Hachisu et al., 1999a,b](#); [Hillebrandt & Niemeyer, 2000](#)) – the same underlying system that produces RNe.

There are two possible barriers preventing a WD in a single degenerate binary to lead to a SNIa: He-flashes and donor depletion. Unlike *hydrogen* flashes (nova outbursts) that retain matter, *helium* flashes, which occur once a sufficiently large He-layer has accumulated from the by-products of previous H-flashes, were predicted to eject all accreted material ([Idan et al., 2013](#)). However, recent studies have shown that the repeating nature of RNe *can* provide a mechanism for the net accumulation of material on the WD following the nova eruption ([Yaron et al., 2005](#); [Hillman et al., 2015, 2016](#); [Starrfield et al., 2020](#)). Specifically, after the first few tens of He-flashes ([Hillman et al., 2020b](#)), the WD core temperature increases sufficiently to remove degeneracy of the He-layer, leading to less explosive He-flashes and the resumption of mass retention ([Hillman et al., 2016, 2020b](#)). Ultimately, this retained material will grow the WD to the Chandrasekhar limit in a reasonable time ($\sim 10^7 - 10^8$ years; [Hillman et al., 2016](#)) and rip it apart in a SNIa ([Whelan & Iben, 1973](#)). Alternatively, if the companion evolves such that no donatable material remains in the envelope, then the WD will cease growing and thereby never reach the M_{Ch} , resulting in an extinct RN (a former RN with a depleted donor; [Darnley, 2021](#)).

We should see a relation between the progenitors of SNe Ia and redshift as the single degenerate and double degenerate pathways clearly have unique timescales. Double degenerate SNeIa would not be seen at high redshifts as they take an exceedingly long time to coalesce ([Webbink, 1984](#)), whereas SNeIa from RNe (the single degenerate pathway), could be observed at higher redshifts owing to their reasonable evolutionary time ([Hillman et al., 2016](#)).

1.4.2 ‘Faint and fast’ novae and the ‘Bolometric MMRD’

A new sub-class of classical novae, possibly related to the rapid recurrent novae (RRNe; see Section § 1.4.3), was identified from observations of M 31 ([Kasliwal et al., 2011](#)) and M 87 ([Shara et al., 2016](#)), located in a previously empty region of the luminosity-timescale phase space – the ‘faint and fast’ novae (see bottom left panel of Figure 1.6). First predicted by [Yaron et al. \(2005\)](#) from their nova grid models, and as their name suggests, these objects are much fainter in comparison to similar novae and rapidly decline from peak magnitude ([Kasliwal et al., 2011](#)). [Kasliwal](#)

[et al. 2011](#) explain that if the binary system contains a hot and massive WD then the TNR would not be as explosive and so the peak luminosity of the nova outburst would be fainter. Additionally, a smaller portion of the accreted envelope would be sufficient to trigger the TNR because of the hotter WD, resulting in a much shorter timescale ([Kasliwal et al., 2011](#)).

The MMRD phase space was originally made up of novae diagonally distributed from top left to bottom right coupled with empty quadrants on the bottom left and top right (see top left panel of Figure 1.6). This distribution represented the bright-fast novae with high mass WDs and a low accretion rate, detected because of their increased luminosity, through to the faint-slow novae containing low mass WDs accreting at a high rate being observed due to their longevity in the sky ([Darnley, 2021](#)). Effectively, these are classical novae that have been observed optically. The faint-fast novae, situated in the bottom left quadrant of the MMRD phase space as a consequence of having a high mass WD and a high \dot{M} ([Darnley & Henze, 2020](#)), are more difficult to find (optically) as they require deeper and higher cadence observations, something only recently attainable with the Fast Transients In Nearest Galaxies (P60-FasTING) survey ([Kasliwal et al., 2011](#)). Instead, these systems would emit most of their energy in the FUV or EUV due to the higher effective temperature of a faint-fast nova pseudo-photosphere ([Darnley et al., 2016](#); [Darnley & Henze, 2020](#)).

This led [Darnley & Henze \(2020\)](#) to suggest that the empty region of the MMRD may be occupied with bright-slow novae containing a low mass WD and a low \dot{M} that are optically-faint but infrared-bright as a result of a massive, slowing evolving, ejecta, in a similar manner to that suggested by [Shara et al. \(2010\)](#) with regards to old classical novae. [Darnley & Henze \(2020\)](#) initiated the idea that eSPecially Red Intermediate-luminosity Transient Events (SPRITES; [Kasliwal et al., 2017](#)), with their infrared luminosity bridging the gap between novae and supernovae, may be these elusive bright-slow novae. They went on further to propose that instead of an optical MMRD relation, we should be considering the viability of a ‘maximum bolometric magnitude–rate of decline’ relationship, or possibly the MMRD concept in various energy bands.

1.4.3 Rapid recurrent novae

In addition to the classical and recurrent, a third category of novae has recently been proposed in order to extract those systems that we have a chance to observe and study much more frequently – “a phenomenological ‘watch list’ of RNe” ([Darnley](#)

TABLE 1.3: The key parameters of the M31N 2008-12a system taken from [Darnley & Henze \(2020\)](#) with references therein.

Parameter	Value
P_{rec}	347 ± 10 days
M_{WD}	$\simeq 1.38 M_{\odot}$
\dot{M}_{SSS}	$1.6 \times 10^{-7} M_{\odot} \text{ yr}^{-1}$
\dot{M}_{disk}	$(6 - 14) \times 10^{-7} M_{\odot} \text{ yr}^{-1}$
$\dot{M}_{\text{ejected,H}}$	$(0.26 \pm 0.04) \times 10^{-7} M_{\odot}$
η	+63%
L_{donor}	$103_{-11}^{+12} L_{\odot}$
R_{donor}	$14.14_{-0.47}^{+0.46} R_{\odot}$
$T_{\text{eff,donor}}$	4890 ± 110 K
P_{orb}	$\gtrsim 5$ days
d	752 ± 17 kpc
$E(B - V)$	0.10 ± 0.03

[& Henze, 2020](#)). Dubbed the ‘rapid recurrent novae’ (RRNe) by [Darnley & Henze \(2020\)](#), this group contains all novae with $P_{\text{rec}} < 10$ yrs, of which there are currently ten members: U Sco (see for e.g. [Pagnotta et al., 2015](#)) in the Galaxy, LMCN 1968-12a (see for e.g. [Kuin et al., 2020](#)) within the Large Magellanic Cloud and ten in M 31 (see [Henze et al., 2018a](#), and Table 1.2 for a brief summary).

It is surprising that out of ten RN in our Galaxy, we only see one example of a RRN, yet one of the four LMC RNe and over half of the M 31 RN belongs to this group. Similar to the ‘faint and fast’ novae (see Section § 1.4.2), RRNe must harbour high mass WDs with a high mass accretion rate from the donor in order to generate such frequent low luminosity outbursts ([Yaron et al., 2005](#)). As a result of producing frequent low amplitude eruptions, it is suggested by [Darnley & Henze \(2020\)](#) that Galactic RRNe may have been previously misidentified as other types of transients that are not followed up and spectroscopically confirmed, such as DNe, possibly neglecting many RRNe in the Milky Way, a similar motive behind the recent study of DNe to compare with CNe ([Kawash et al., 2021](#)).

1.4.4 M31 N 2008-12a – the rapid recurrent nova prototype

M31N 2008-12a (or simply 12a) is the fastest RRN currently known with an average recurrence period of $\bar{P}_{\text{rec}} = 0.99 \pm 0.02$ years ([Darnley & Henze, 2020](#)). This unique object (see Table 1.3) is the prototype RRN having erupted each year (see Table 1.4) since its discovery in 2008 by [Nishiyama & Kabashima³](#). Taking into account the

³http://www.cbat.eps.harvard.edu/iau/CBAT_M31.html#2008-12a

archival X-ray observations of this object recovered from 1992, 1993 and 2001 (Tang et al., 2014; Henze et al., 2014b) then the system could potentially have a shorter recurrence period of 174 ± 10 days (Henze et al., 2015b; Darnley et al., 2016), although more recent data indicates that this is unlikely to be the case (Darnley et al. in prep).

These extremely frequent nova outbursts occur because of a combination of the most massive WD known ($M_{\text{WD}} \simeq 1.38 M_{\odot}$; Kato et al., 2015) along with a substantial accretion rate of $(0.6 \lesssim \dot{M} \lesssim 1.4) \times 10^{-6} M_{\odot} \text{ yr}^{-1}$ (Darnley et al., 2017b) provided by the only example of a proposed Roche lobe overflowing red giant companion (Darnley et al., 2017b). Darnley et al. (2014) first identified the progenitor of M 31N 2008-12a from *Hubble Space Telescope (HST)* archival images allowing for the characteristics of the donor star, an M 31 red clump donor, to be determined (Darnley et al., 2017b).

The high mass WD and high \dot{M} results in a low optical luminosity as a low amount of mass is ejected (ejected hydrogen mass $M_{\text{ej,H}} = (2.6 \pm 0.4) \times 10^{-8} M_{\odot}$; Henze et al., 2015a) during outburst (Yaron et al., 2005; Kato et al., 2015) that interacts and shocks the disk and donor wind already existing within the system (Darnley et al., 2016, 2017b). Such a low mass ejecta rapidly reveals the highest effective temperature SSS X-ray emission known in novae ($T_{\text{eff}} \sim 120$ eV; Darnley et al., 2016) in just six days (Henze et al., 2018a) which then proceeds to emit for a further 13 days ($t_{\text{off}} \simeq 19$ days; Henze et al., 2015b). However, the unusual 2016 eruption of M 31N 2008-12a exhibited a much shorter SSS, ‘turning off’ after only ~ 15 days ($t_{\text{on}} = 4.9 \pm 1.1$ days and $t_{\text{off}} = 14.9 \pm 1.2$ days; Henze et al., 2018a). This is proposed to be a consequence of the 2016 eruption being very late (see Table 1.4). As the outburst was late, the accretion rate must have been lower and so the disk was less massive, leading to more disruption during the nova event (Henze et al., 2018a). This in turn would mean less or no refuelling of the SSS (also see Aydi et al., 2018b), therefore it ‘turned off’ earlier than in previous outbursts, and furthermore, due to this refuelling, the WD must be more massive than previous studies with no refuelling predicted (Henze et al., 2018a).

Significantly, it has been predicted from models that this system has a mass accumulation efficiency of $\eta = 0.63$ (Kato et al., 2015) meaning that the already massive WD in this system is growing and could reach the Chandrasekhar mass (M_{Ch}) in less than 20,000 years (Darnley et al., 2017b). The fate of this WD, when it does eventually reach the M_{Ch} , will completely depend on its composition. If it is an ONe WD then it will undergo accretion-induced collapse to a neutron star (Gutierrez et al., 1996), but if it is a CO WD it will explode as a SNIa – in which case this system is an excellent SNIa progenitor candidate (Darnley et al., 2017a). Rapid FUV spectroscopy using the *Hubble Space Telescope (HST)* only 3 days after the 2015 eruption

TABLE 1.4: The Eruption History of M31N 2008-12a.

Date of eruption ^a (UT)	Date of SSS-on ^b (UT)	Days since last eruption ^c	Day of the year	References
(1992 Jan 28)	1992 Feb 03	...	392	1, 2
(1993 Jan 03)	1993 Jan 09	341	368	1, 2
(2001 Aug 27)	2001 Sep 02	...	238	2, 3
2008 Dec 25	359	4
2009 Dec 02	...	342	335	5
2010 Nov 19	...	352	322	2
2011 Oct 22.5	...	337.5	294.5	5–8
2012 Oct 18.7	< 2012 Nov 06.45	362.2	291.7	8–11
2013 Nov 26.95 ± 0.25	≤ 2013 Dec 03.03	403.5	329.95	5, 8, 11–14
2014 Oct 02.69 ± 0.21	2014 Oct 08.6 ± 0.5	309.8 ± 0.3	274.69	8, 15
2015 Aug 28.28 ± 0.12	2015 Sep 02.9 ± 0.7	329.6 ± 0.3	239.28	14, 16–18
2016 Dec 12.32 ± 0.17	2016 Dec 17.2 ± 1.1	471.7 ± 0.2	346.32	19–23
2017 Dec 31.3 ± 0.1	2018 Jan 05.48	384.0 ± 0.2	364.3	24–28
2018 Nov 06.8 ± 0.1	2018 Nov 12.5 ± 0.5	310.5 ± 0.1	309.8	28–30
2019 Nov 06.6 ± 0.2	2019 Nov 11.8 ± 0.5	364.8 ± 0.2	309.6	31–33
2020 Oct 30.7 ± 0.2	2020 Nov 04.9 ± 0.4	359.1 ± 0.3	303.7	34–36
2021 Oct 1 ≤ Based on mean date ≤ 2021 Dec 28				
2021 Sep 12 ≤ Based on 2020 date ≤ 2021 Dec 7				

This is an updated version of a table first compiled by [Tang et al. \(2014\)](#), subsequently updated by [Darnley et al. \(2015a\)](#), [Henze et al. \(2015b\)](#), [Darnley et al. \(2016\)](#), presented in shortened form in [Darnley et al. \(2017a,b\)](#), and most recently [Henze et al. \(2018a\)](#).

^a Eruption onset times estimated from data immediately pre- and post-eruption. Dates within parentheses are extrapolated from X-ray data (see [Henze et al., 2015b](#)). The rapid eruption evolution constrains associated uncertainties to just a few days.

^b Turn-on time of the SSS emission. See [Henze et al. \(2015b\)](#) for details of the 1992 and 1993 *ROSAT* detections and the 2001 *Chandra* data.

^c The time since last eruption is quoted when consecutive detections are assumed to be consecutive eruptions; the time is the interval between estimated eruption dates.

References. – (1) [White et al. \(1995\)](#), (2) [Henze et al. \(2015b\)](#), (3) [Williams et al. \(2004\)](#), (4) [Nishiyama & Kabashima \(2008\)](#), (5) [Tang et al. \(2014\)](#), (6) [Korotkiy & Elenin \(2011\)](#), (7) [Barsukova et al. \(2011\)](#), (8) [Darnley et al. \(2015a\)](#), (9) [Nishiyama & Kabashima \(2012\)](#), (10) [Shafter et al. \(2012b\)](#), (11) [Henze et al. \(2014b\)](#), (12) [Tang, Cao & Kasliwal \(2013\)](#), (13) [Darnley et al. \(2014\)](#), (14) [Darnley et al. \(2016\)](#), (15) [Henze et al. \(2015a\)](#), (16) [Darnley et al. \(2015b\)](#), (17) [Darnley et al. \(2015c\)](#), (18) [Henze et al. \(2015c\)](#), (19) [Henze et al. \(2018a\)](#), (20) [Itagaki \(2016\)](#), (21) [Itagaki et al. \(2016\)](#), (22) [Henze et al. \(2016a\)](#), (23) [Henze et al. \(2016b\)](#), (24) [Boyd et al. \(2017\)](#), (25) [Henze et al. \(2018b\)](#), (26) [Henze et al. \(2018c\)](#), (27) [Darnley et al. \(2018a\)](#), (28) [Darnley et al. \(2018b\)](#), (29) [Henze et al. \(2018d\)](#), (30) [Henze et al. \(2018e\)](#), (31) [Oksanen et al. \(2019\)](#), (32) [Darnley et al. \(2019b\)](#), (33) [Darnley et al. \(2019c\)](#), (34) [Darnley et al. \(2020a\)](#), (35) [Darnley & Page \(2020\)](#), (36) [Darnley, Page & Henze \(2020b\)](#).

determined that there was no Ne within the ejecta, implying that the WD is a CO variant (Darnley et al., 2017a), but unfortunately, the composition of 12a’s WD is still not confirmed. The same spectra also revealed a very high velocity N v line with a profile consistent with a short-lived high velocity collimated outflow analogous to a jet (Darnley et al., 2017b; Darnley & Henze, 2020).

1.4.5 M31 N 2008-12a nova super-remnant

First associated with M31 N 2008-12a in Darnley et al. (2015a), this RRN is uniquely surrounded by a vastly extended nebulosity. The nebulosity (designated object 787) was first identified as a ‘ring’-like structure (see top left panel of Figure 1.9) in a narrow-band survey of M31 in 1987 (Walterbos & Braun, 1992), a couple of decades before the discovery of the first eruption from the rapidly recurring nova in 2008. However, after the 2015 eruption, H α data of this region taken with the Steward 2.3m Bok Telescope in 2005 and 2006 as part of an M 31 nova survey (Coelho et al., 2008; Franck et al., 2012) was examined alongside narrow-band imaging data from the LGGs (Massey et al., 2007), leading to the ‘rediscovery’ of the vast remnant and its association with M 31N 2008-12a (Darnley et al., 2015a).

Follow up narrow-band H α + [N II] observations made with the Liverpool Telescope’s (LT) IO:O camera (Steele et al., 2014) revealed the structure to be elliptical in nature (see top right and bottom left panel of Figure 1.9 and lower left of Figure 1.10), the southwest part of the structure being much brighter than the northeast, with a semi-major axis of $\sim 0'.3$ and a semi-minor axis of $\sim 0'.2$, corresponding to 67 pc and 45 pc at the distance of M 31, respectively (Darnley et al., 2019a). Comparing the dimensions of this structure to some of the previously largest Galactic nova shells known such as GK Persei (~ 0.02 pc; Bode et al., 2004), Z Camelopardalis (~ 0.7 pc; Shara et al., 2007) and AT Cancri (0.2 pc; Shara et al., 2012), a nova *super*-remnant (NSR; Darnley et al., 2019a) status is justified. It was determined from measuring the projected semi-major axes of the inner and outer edge of the remnant, that it had a shell thickness of 22%. Along with LT imaging of the super-remnant shell, *Hubble Space Telescope* H α + [N II] imaging presented in Darnley et al. (2019a) showed clear edges of the shell towards the south and west as well as displaying potential knots and filamentary formations (see bottom right panel of Figure 1.9 and upper right of Figure 1.10), similar to the interacting shells seen in T Pyxidis (Shara et al., 1997; Toraskar et al., 2013).

Darnley et al. (2019a) ruled out the possibility of the shell being a SN remnant, a superbubble or a fossil H II region with high-spatial resolution *Hubble Space Telescope*

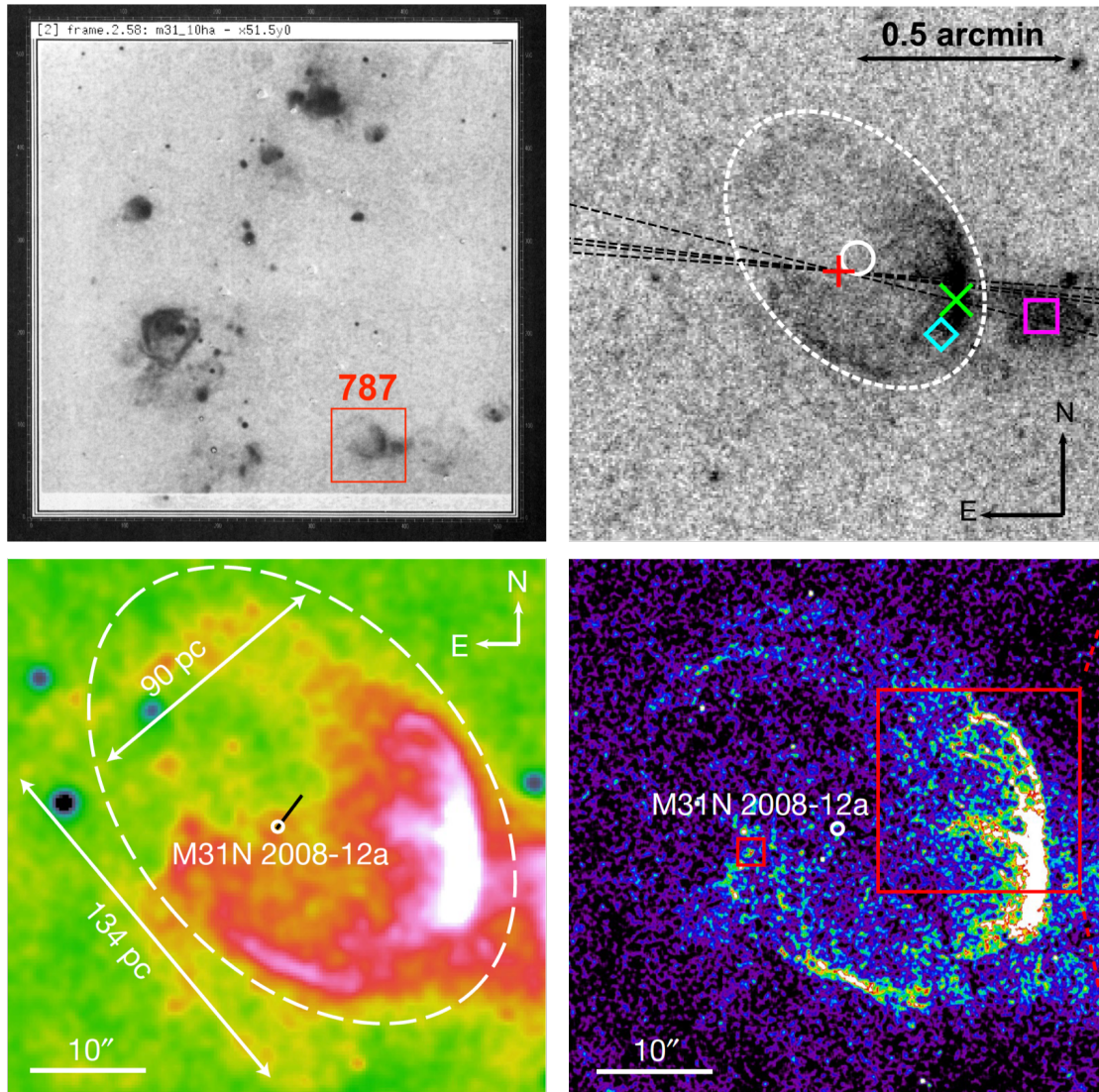


FIGURE 1.9: **Top left:** Narrow-band $H\alpha$ image taken and edited from [Walterbos & Braun \(1992\)](#). The nova super-remnant, designated as 787 in this work, is indicated with a red box by the author. Credit: Walterbos & Braun, *A&AS*, 92, 625, 1992, reproduced with permission © ESO. **Top right:** Liverpool Telescope $H\alpha$ image taken from [Darnley et al. \(2015a\)](#) indicating the remnant with a white dashed-line ellipse and the position of M 31N 2008-12a with a red cross. The white circle indicates the location of the ring structure 787 in ([Walterbos & Braun, 1992](#)), the green cross is the south-western knot $H\text{II}$ 3556 detailed in [Azimlu et al. \(2011\)](#), the magenta box is a feature identified as a SNR (their object 857) by [Dodorico et al. \(1980\)](#) and the blue diamond is identified as a cluster of stars in [Johnson et al. \(2012\)](#) (their PC 167). Credit: Darnley et al., *A&A*, 580, A45, 2015, reproduced with permission © ESO. **Bottom left:** Liverpool Telescope narrow-band $H\alpha + [\text{N II}]$ image of the nova super-remnant from [Darnley et al. \(2019a\)](#) with the dimensions indicated. **Bottom right:** Also from [Darnley et al. \(2019a\)](#), a high resolution *Hubble Space Telescope* narrow-band $H\alpha + [\text{N II}]$ image of the same region as the bottom left panel revealing a filamentary structure.

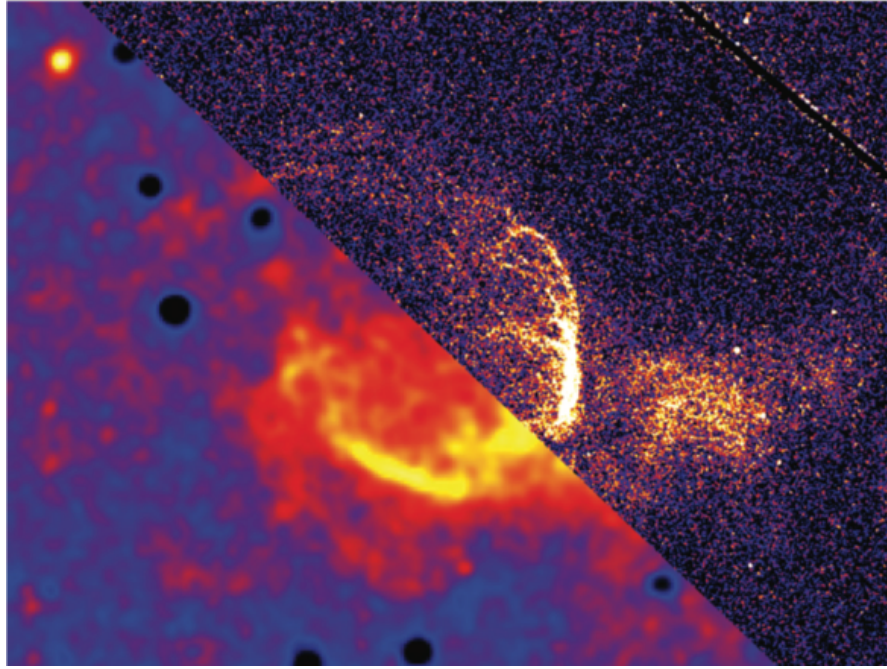


FIGURE 1.10: The nova super-remnant surrounding the RRN M 31N 2008-12a. The lower left part of the image is a narrow band $H\alpha$ observation using the Liverpool Telescope. The top right part of the image is a high spatial $H\alpha+[NII]$ observation using *Hubble Space Telescope*. Reprinted from *Advances in Space Research*, 66, Matthew J. Darnley, Martin Henze, “On a century of extragalactic novae and the rise of the rapid recurrent novae”, 1147-1168, 2020, with permission from Elsevier (Darnley & Henze, 2020).

$H\alpha+[NII]$ imaging, Liverpool Telescope $H\alpha+[NII]$ imaging and deep low-resolution spectroscopy from the Gran Telescopio Canarias and Hobby-Eberly Telescope (see Chapter 3 for a detailed discussion). Instead the NSR’s existence was attributed to the continual sweeping up of $\sim 10^{5-6} M_{\odot}$ (Darnley et al., 2019a) of local interstellar medium (ISM) from many previous nova eruptions.

In order to test the viability of 12a’s NSR being produced by many past RN eruptions, Darnley et al. (2019a) utilised the Morpheus program (Vaytet et al., 2007b) to perform a one-dimensional hydrodynamical simulation (see Section 1.5.1) of 100,000 identical 12a eruptions. Self- and ISM-interaction by each wave of ejecta did indeed sweep up a huge cavity surrounded by a moving shell with a thickness of $\sim 22\%$, found to be consistent with observations of the NSR (see top left, top middle and top right panels of Figure 1.11 and Figure 1.12). Unlike single eruption events around CNe, a unique feature of a structure being formed from repeatedly interacting eruptions is the continuously shock-heated region located within the outer shell referred to as the ejecta pile-up region (Darnley et al., 2019a, and see top right panel of Figure 1.12).

Darnley et al. (2019a) details that the cavity within the simulated NSR consists of

adiabatically cooling ejecta in free high velocity expansion. This expanding material collides into the previous eruptions that have been slowed by interaction with earlier eruptions, and eventually the ISM, resulting in high velocity inter-ejecta shocks and substantial heating as the gas dramatically decelerates. After 100,000 eruptions, the high density shell at the outskirts of the remnant, is made up of $17M_{\odot}$ of swept up ISM (see left panel of Figure 1.13), 3,000 times the mass ejected by the nova over this period of time. Once established, this shell maintains a peak shell over-density approximately four times that of the surrounding ISM and slowly moves outwards as more eruptions collide with the inner shell (Darnley et al., 2019a).

Extrapolating the growth rate from these simulations to the observed size of the super-remnant, Darnley et al. (2019a) suggested an age of 6×10^6 yrs for the NSR associated with 12a (see bottom left panel of Figure 1.11), in which time the total mass swept up would be about $3 \times 10^4 M_{\odot}$ (see left panel of Figure 1.13). After this same period of time, the super-remnant outer shell would be expanding at 5 km s^{-1}

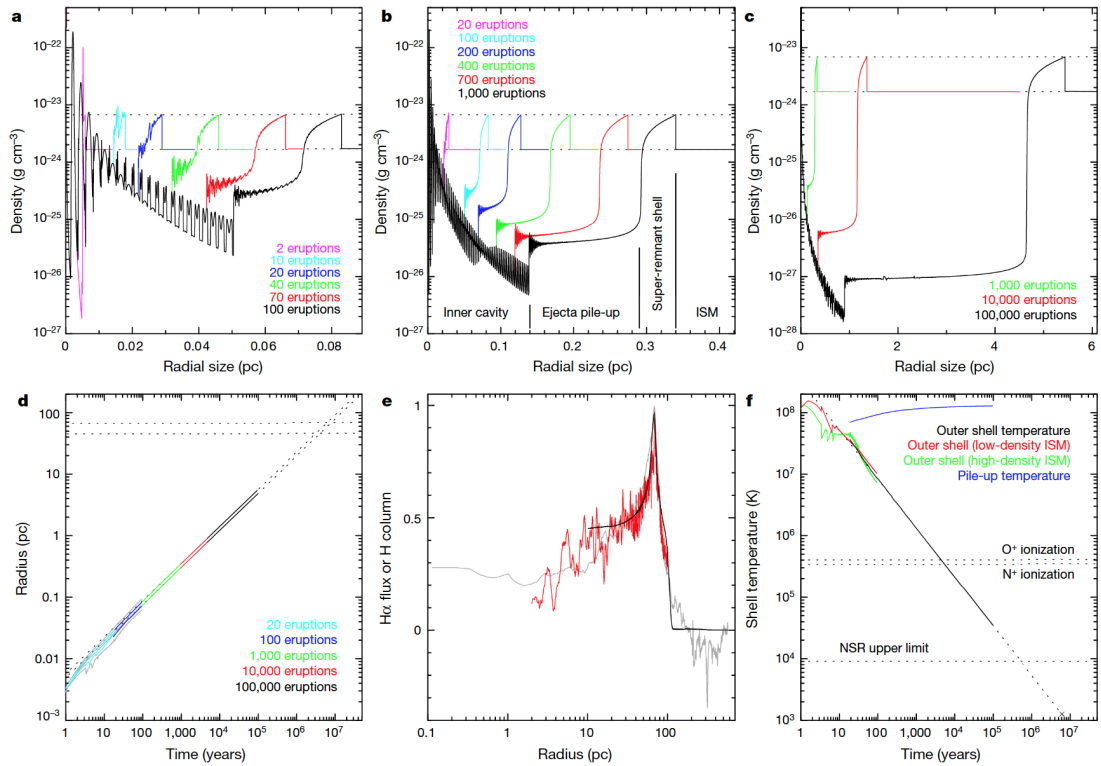


FIGURE 1.11: The results of the hydrodynamic simulations of M 31N 2008-12a recurrent eruptions. **Top left, top middle and top right:** The radial density profiles of the NSR around 12a from 2 – 100,000 eruptions with the inner cavity, ejecta pile-up and super-remnant shell indicated. **Bottom left:** Radial growth curves extrapolated (dotted lines) to the current size of the NSR. **Bottom middle:** The radial $H\alpha$ + $[N II]$ flux the LT (grey) and *HST* (red) imaging compared to the simulated NSR, rescaled from 100,000 eruptions to the size of the remnant. **Bottom right:** The temperature evolution of the super-remnant. Taken from Darnley et al. (2019a).

(see middle panel of Figure 1.13) dropping to less than 10^4 K (see bottom right panel of Figure 1.11). Darnley et al. (2019a) also conducted a simulation of 1000 eruptions to determine the effects of radiative cooling and found that it had a negligible effect, meaning that energy lost through radiation is minimal, and therefore has little effect on the evolving dynamics of this system (see left panel of Figure 4.28). This is due to the radiative cooling being inefficient at temperatures above $10^{6.5}$ K as well as at low densities (Darnley et al., 2019a), and this is the case for all of the material in the ejecta pile-up region and remnant shell because of the frequent nature of these eruptions. The same mechanism shaping the NSR surrounding 12a is also growing the CO WD, predicted to surpass the Chandrasekhar limit and explode as a SN Ia in less than 20,000 years (Darnley et al., 2017b). Finally, to quote Darnley et al. (2019a), “the size and mass of this super-remnant demonstrate that 12a has not just been erupting frequently for a decade as observed, but for millions of years”.

In Chapter 4, we carry out a thorough exploration of various characteristics that

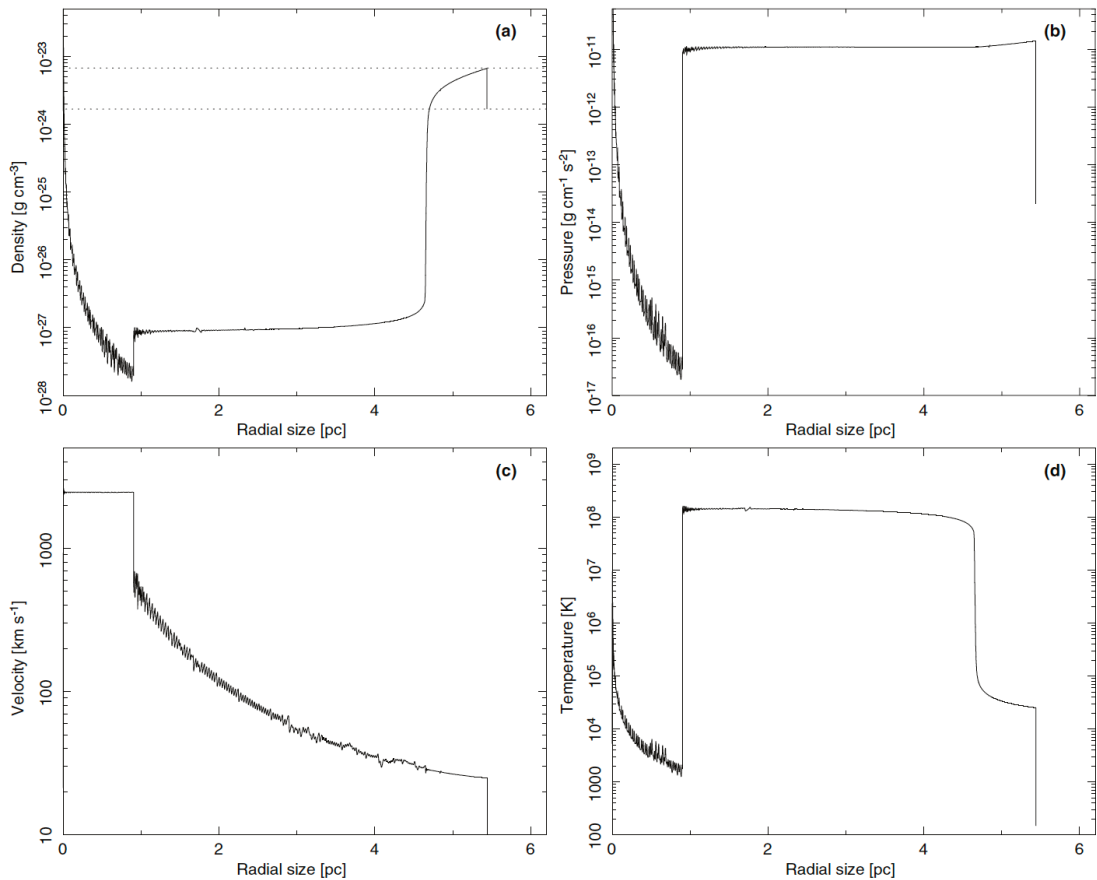


FIGURE 1.12: The full simulation of 100,000 identical recurrent nova eruptions without radiative cooling. Panel (a) is the radial density profile, panel (b) is the pressure radial profile, panel (c) is the velocity radial profile and panel (d) is the temperature radial profile. Taken from Darnley et al. (2019a).

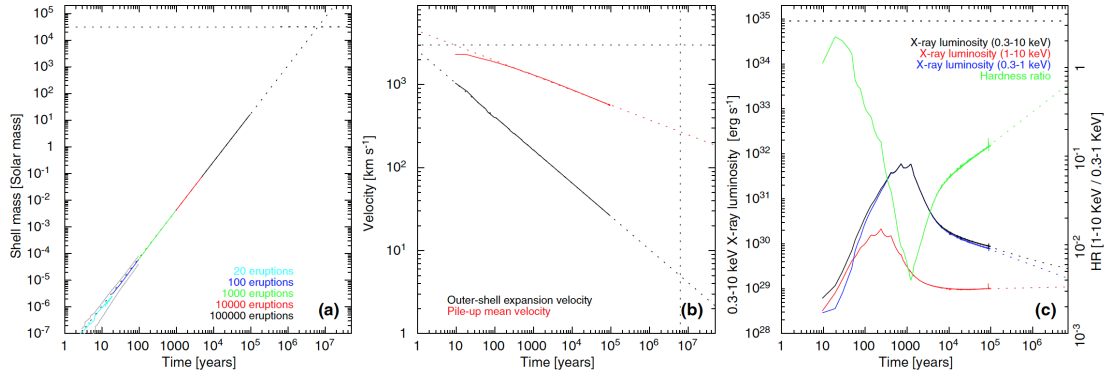


FIGURE 1.13: Additional results of the hydrodynamic simulations of M 31N 2008-12a recurrent eruptions. **Left:** The evolution of shell mass for 20 – 100,000 eruptions with the extrapolated growth shown (dotted line). **Middle:** The evolution of the outer shell expansion velocity (black) and the mean velocity within the ejecta pile-up region (red). **Right:** The evolution of the hard (1 – 10 keV; red), soft (0.3 – 10 keV; blue) and total (0.3 – 10 keV; black) X-ray luminosity of the NSR with the hardness ratio (hard/soft) shown in green). Taken from [Darnley et al. \(2019a\)](#).

could effect a NSR’s evolution in order to aid the search for more of these vast remnants. This will be the first attempt to determine if the NSR associated with M 31N 2008-12a is unique or whether it is simply the first of the phenomena to be found.

1.5 Hydrodynamical simulations of novae

1.5.1 Introduction to hydrodynamics

Observations are essential in astronomy to classify and understand objects in the Universe. However, observations may only give us a partial understanding of the underlying system. Theoretical models are used within astrophysics to study inaccessible objects in order to predict and compare key observational traits, and are therefore crucial in confirming suggested theories that we use to describe processes within astrophysics.

Theoretical modelling comprises a set of mathematical equations governing a number of physical parameters confined by boundary conditions. The outcome of the modelling is then compared to observational data to determine validity and if a discrepancy is found, parameters are readjusted until the model and data are consistent. If exact solutions are used for the governing mathematical equations, we have an analytical model. On the other hand, numerical modelling involves solving the governing equations by turning them into discrete equations and approximating the solutions. Typically, this involves dividing the object to be modelled into smaller components and solving the discrete equations numerically in each component.

The two main methods for numerical gas dynamics are the Eulerian approach and the Lagrangian approach. The Eulerian description splits space up into a stationary grid with each cell having a constant volume and containing gas with a particular mass, momentum and energy. Each cell is then evolved using the hydrodynamical equations to determine quantities such as density and velocity. The Lagrangian approach, on the other hand, attaches properties to all particles within the fluid and follows these particles as they vary along a certain trajectory, with an example of this method being Smoothed Particle Hydrodynamics (SPH).

Many astrophysical phenomena can be approximated by a fluid (a liquid, a gas or a plasma), and as such, can be modelled with hydrodynamics. For example, a star can be treated as a fluid under gravity because it is a (mostly) homogeneous gas creating its own gravitational field (Shore, 1992). A stellar wind interacting with a local ISM can mimic a fluid, as well as the Universe on a cosmological scale. Consequently, the equations of fluid mechanics⁴ can be used to model these processes, known as hydrodynamical modelling. This approximation is only valid when the mean free path of components within the system are much shorter than any scale length within the medium and so are negligible, so that the structure can be described as continuous (Shore, 1992; Vaytet, 2009).

These equations of fluid dynamics are solved numerically using a finite difference method. This involves converting the differential equations into linear equations through a Taylor series expansion and solving these equations at points nearby to the discretised points of the divided grid. Within this thesis, we will be utilising an Eulerian code.

1.5.2 Examples

Like other fields of astrophysics, hydrodynamical simulations have been utilised extensively in nova research covering many processes including the TNR on the surface of the WD, the nova outburst, ejecta-accretion disk interaction, nova shell evolution and recently, to model a unique nova super-remnant (see Section § 1.4.5 for more detail). In this section, I will provide brief details of a number of these studies.

Prior to the nova outburst and the formation of a shell, an accretion phase takes place within the binary system. This, along with the nova explosion itself, has been modelled for the Galactic recurrent nova RS Ophiuchi using 3D hydrodynamical simulations in Walder et al. (2008). The 3D structure of the blast wave emanating

⁴A derivation of these equations is given in Appendix A.

from the 2006 nova outburst of this same system has also been modelled, revealing information about the morphology of the nova remnant as well as providing constraints on system parameters such as ejecta mass (Orlando et al., 2009). A similar study involving 3D hydrodynamic simulations was conducted for another Galactic recurrent nova, U Scorpii, to model the early blast wave from the system (Drake & Orlando, 2010). The accretion disk in the system was completely destroyed in this simulation; with a bow shock forming from interaction with the secondary star. Additionally, a particular disk gas density gave rise to a collimated blast wave alongside a bipolar shell emitting in the X-ray regime. Meanwhile, Figueira et al. (2018) performed a suite of 3D SPH simulations to simulate the companion, the accretion disk and the nova outburst to determine how the ejected material interacts with both the secondary and the disk.

The evolution of the shell surrounding RS Ophuichi from the 1985 outburst was presented in Bode & Kahn (1985, Paper I) as a spherically symmetric model with a high velocity ejecta and a slow velocity wind. This allowed for the phase of evolution to be determined from radio and X-ray observations. A cooling parameter was then added to this model in O'Brien & Kahn (1987, Paper II) in order to account for radiative cooling within the dynamics. X-ray emission was then predicted by this model in O'Brien et al. (1992, Paper III) to compare with EXOSAT observations of the outburst to obtain model parameters such as outburst energy, ejecta mass, mass loss rate and the evolution the subsequent X-ray emission. A numerical hydrodynamics code was developed in O'Brien & Lloyd (1994) and used in O'Brien et al. (1994) to present a spherically symmetric model of V838 Her, with interaction between a slower wind followed by a faster wind, expanding into a low-density environment. Vaytet et al. (2007b) then created a hydrodynamical model of RS Ophuichi with an updated version of the code given in O'Brien et al. (1994), which included an ejection of mass from the nova in the form of a wind. The interaction of winds being ejected at different velocities led to forward and reverse shocks as well as contact discontinuities.

As well as the accretion phase and nova outburst phase, hydrodynamical simulations have been used to explore the mixing processes of the accreted material with the outer layers of the white dwarf. Starrfield et al. (1972) utilised hydrodynamical models to follow the TNR process taking place in the hydrogen-rich envelopes on the surface of the underlying WD to create a nova eruption. They found that the abundance of CNO nuclei must be strongly enhanced to produce the outburst we see in actual novae with the degree of enhancement affecting the outburst's observable features. Prialnik & Kovetz (1984) and Kovetz & Prialnik (1985) also used

hydrodynamical models to study the effects of diffusion and convection for enhancing the abundances of CNO in the nova envelope. Simulations were performed by [Casanova et al. \(2016\)](#) of the mixing process that occurs during a nova outburst at the interface between the WD and the accreted envelope, finding that this naturally recreates the self-enrichment of this envelope with the material from the underlying core. More recently, hydrodynamical simulations have been used to evolve a broad range of white dwarf masses with incorporation of different compositions of accreted material to find that the TNR takes place in all scenarios (see [Starrfield et al., 2021](#), and references therein).

Furthermore, nova systems have been modelled and followed through multiple cycles of eruptions with broad ranges of underlying parameters, including white dwarf mass, white dwarf temperature and mass accretion rate in order to reproduce nova outburst characteristics ([Prialnik & Kovetz, 1995](#); [Yaron et al., 2005](#)). As mentioned in Section § 1.4.1, these studies have also been used to illustrate that the white dwarfs in nova systems can grow in mass, even with the inclusion of helium flashes, and reach the critical mass for a SNIa explosion (see, for example, [Yaron et al., 2005](#); [Hillman et al., 2015, 2016](#); [Starrfield et al., 2020](#); [Hillman et al., 2020b](#)).

1.6 Facilities

In this section, I will give a very brief description of a number of facilities that have been utilised for the research of this thesis.

1.6.1 The Liverpool Telescope (LT)

The Liverpool Telescope (LT; [Steele et al., 2004](#)) is a fully autonomous 2m Ritchey-Chrétien Cassegrain telescope with an altitude-azimuth mount sited at the Observatorio del Roque de los Muchachos on La Palma⁵ (see Figure 1.14). A number of instruments are mounted to the LT including the Optical Wide Field Camera (IO:O) and the SPectrograph for the Rapid Acquisition of Transients (SPRAT; [Piascik et al., 2014](#)) which we utilised to study the nova AT 2017fvz (see Section § 2.3.2 and § 2.4.3).

The LT concentrates on meeting specific scientific goals: (i) rapid robotic reaction to unpredictable phenomena and their systematic follow-up; (ii) small scale surveys and serendipitous source follow-up; (iii) monitoring of variable objects on all timescales from seconds to years, and (iv) simultaneous coordinated observations

⁵<http://telescope.livjm.ac.uk/About/>



FIGURE 1.14: The Liverpool Telescope. Image credit: Daniel López/IAC 2016.

with other ground and space based facilities. Novae are one of the predominant areas of research carried out using the LT with its fast slewing speed giving it the ability to rapidly respond to targets of opportunity. The current on-going nova programmes on the LT include detecting eruptions of the RRN, M31 N 2008-12a (see Section § 1.4.4) and following-up these detections. The LT is also involved in observing and classifying Galactic and extragalactic novae as well as γ -ray novae.

1.6.2 Katzman Automatic Imaging Telescope (KAIT)

The Katzman Automatic Imaging Telescope is a fully robotic 0.76m Ritchey-Chrétien reflecting telescope located at Lick Observatory in California⁶. KAIT is equipped with a filter wheel (including *UBVRI* filters), a CCD camera and an automatic guider, allowing for the detection of stars at $R \approx 20$ from a five minute guided exposure when the seeing is favourable ($\leq 2''$; Filippenko et al., 2001).

The main goal of this facility is to discover SNe with redshifts generally less than 5000 km s^{-1} for further study (Filippenko et al., 2001). However, owing to the nature of the instrument, KAIT can detect nearby celestial objects such as comets and asteroids as well as novae and cataclysmic variables in the Local Group such as AT2017fvz (see Chapter 2).

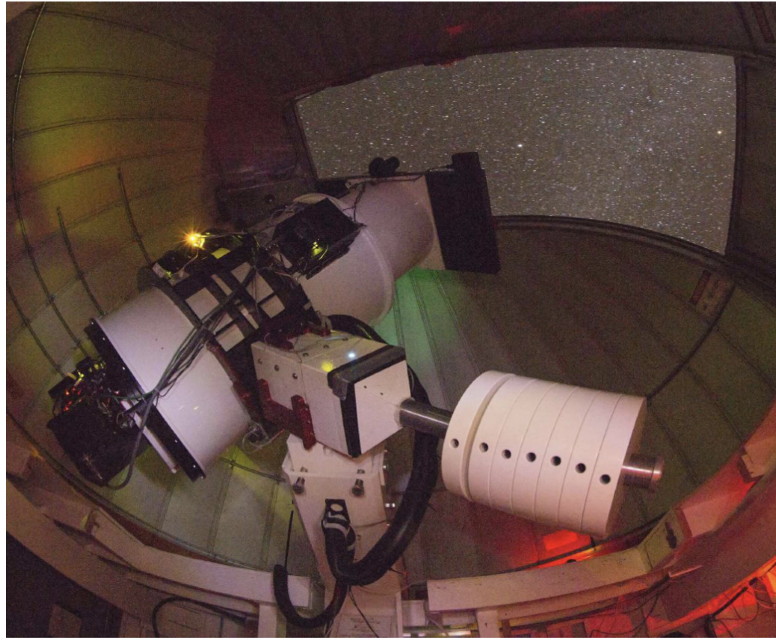


FIGURE 1.15: An Asteroid Terrestrial-impact Last Alert System unit on Haleakala from inside the dome. Taken from [Tonry et al. \(2018\)](#) © AAS. Reproduced with permission.

1.6.3 Asteroid Terrestrial-impact Last Alert System (ATLAS)

The Asteroid Terrestrial-impact Last Alert System (ATLAS; see [Figure 1.15](#)) is an automatic early warning system dedicated to finding near-Earth asteroids, consisting of two telescopes 100 miles apart, one at Haleakala (Hawaii) and one at Mauna Loa (Hawaii), automatically scanning the whole sky several times every night⁷.

Alongside monitoring the sky for potentially threatening asteroids, ATLAS also (i) reports supernovae candidates, (ii) detects numerous types of transients, (iii) finds counterparts of gravitational wave sources, (iv) provides limits on the rate of kilonovae, (v) detects variability in innumerable objects ([Heinze et al., 2018](#)), (vi) characterises asteroids as well as accurately determining 3D positions and velocities of satellites in geosynchronous orbit ([Tonry et al., 2018](#)).

1.6.4 All-Sky Automated Survey for Supernovae (ASAS-SN)

The All-Sky Automated Survey for Supernova (ASAS-SN) currently consists of twenty four telescopes located around the globe scanning the entire sky every night in the V -band down to $V \approx 18$ ([Shappee et al., 2014](#)). This “Small Synoptic Survey Telescope”

⁶<http://w.astro.berkeley.edu/bait/kait.html>

⁷<https://atlas.fallingstar.com/home.php>

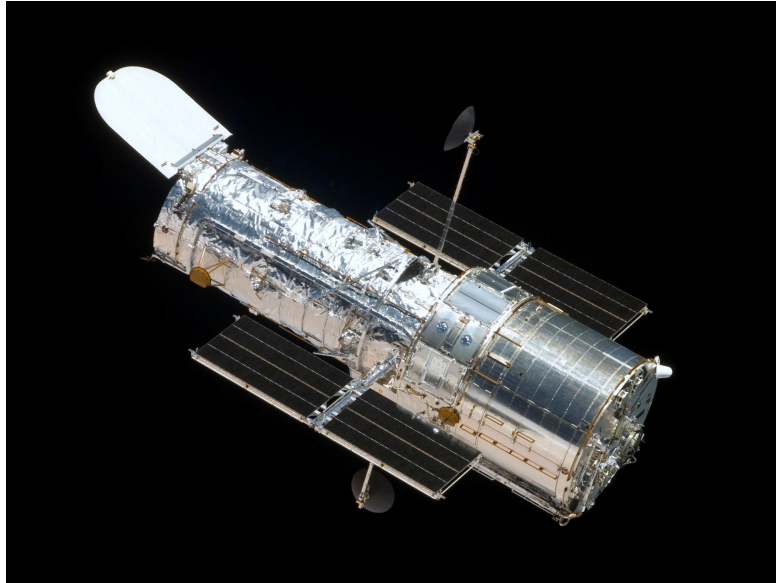


FIGURE 1.16: *Hubble Space Telescope* in 2009. Image credit: NASA.

complements other time-domain projects as well as discovering bright Galactic and extragalactic transients with its high-cadence survey⁸.

1.6.5 *Hubble Space Telescope (HST)*

The *Hubble Space Telescope (HST)* is a large, space based, observatory in Low Earth orbit (an altitude of 547 km) unhindered by the effects of light pollution and atmospheric distortions that ground based facilities must deal with (see Figure 1.16). Deployed in 1990 by the space shuttle *Discovery*, this 2.4m telescope is sensitive to light with wavelengths ranging from the ultraviolet to the infrared (115 – 2500 nanometers)⁹.

The Wide Field and Planetary Camera 2 (WFPC2), known as “the camera that saved Hubble”¹⁰ was a camera installed in 1993 replacing the original Wide Field and Planetary Camera. The CCDs in the WFPC2 were sensitive to the near-infrared, the visible spectrum as well as the near ultraviolet, and so archival images taken with the F170W, F255W, F336W, F439W, F555W, and F814W filters were used to search for a progenitor for the nova, AT 2017fvz (see Section § 2.4.5).

⁸<http://www.astronomy.ohio-state.edu/~assassin/index.shtml>

⁹<https://www.nasa.gov/content/about-hubble-facts>

¹⁰<https://www.jpl.nasa.gov/missions/wide-field-and-planetary-camera-2-wfpc2>

1.6.6 *The Neil Gehrels Swift Observatory (Swift)*

The Neil Gehrels Swift Observatory (Swift) is another space based observatory in Low Earth orbit dedicated to studying gamma-ray bursts (GRB) with its three telescopes (Gehrels et al., 2004). The Burst Alert Telescope (BAT) is a wide-field gamma-ray (15 – 150 keV) detector and so detects GRBs for rapid ground based follow up. The narrow-field X-ray Telescope (XRT; Burrows et al., 2005) then provides a more precise location and performs spectroscopy of the detected GRB working within the X-ray regime (0.2 – 10 keV). The GRB will then be followed up with the third *Swift* telescope, the narrow-field Ultraviolet/Optical Telescope (UVOT; Roming et al., 2005) operating within the range of 170 – 600 nm.

The main objectives of *Swift* from the beginning of the mission were to determine the origin of GRBs alongside particular focus on classification and outflows (Gehrels et al., 2004). Owing to the observatory's rapid slew speed and range of detectors, it is also utilised for a variety of other time-domain astrophysics, including nova research (see Section § 2.3.3).

1.7 Summary and Thesis Outline

Before outlining the contents of this thesis, we will briefly highlight the key points from this chapter. To summarise:

1. Novae are the result of a thermonuclear explosion on the surface of an accreting white dwarf.
2. Recurrent novae are systems that have been observed in eruption more than once.
3. Ejecta from the nova outburst can form resolvable nova shells.
4. The white dwarfs in nova systems can grow in mass towards the Chandrasekhar limit, making them a single degenerate progenitor of type Ia supernovae.
5. M 31N 2008-12a is the most rapidly recurring nova known, with the average time between outbursts being approximately one year.
6. M 31N 2008-12a is surrounded by a unique nova super-remnant, tens of parsecs in size, created from many past eruptions.

My thesis looks at the time domain field of novae by focussing on individual systems in great detail. Firstly, I outline in Chapter 2 the extensive observational study I carried out on a classical nova in Barnard's Galaxy, one of only a few extragalactic novae studied in such detail. In Chapter 3, I present the contribution I made towards removing an alternative origin of the nova super-remnant surrounding the rapidly recurrent nova, M 31N 2008-12a. I then move into the theoretical study I undertook in Chapter 4 using hydrodynamical simulations to explore the parameter space that contributes towards the evolution of nova super-remnants belonging to other recurrent novae, before predicting observables associated with these systems in order to find more examples in Chapter 5. In Chapter 6, I use simulations to explore two different scenarios for the post-nova evolutionary stage of nova super-remnants. Lastly, I finish this thesis by concluding, in Chapter 7, what I have found before suggesting ways to refine our hydrodynamical simulations further to aid the hunt for more of these vast shells.

Chapter 2

Multiwavelength Study of the Classical Nova AT 2017fvz[★]

M. W. Healy,¹ M. J. Darnley,¹ C. M. Copperwheat,¹ A. V. Filippenko,^{2,3}
M. Henze,⁴ J. C. Hestenes,² P. A. James,¹ K. L. Page,⁵ S. C. Williams,⁶
and W. Zheng²

¹Astrophysics Research Institute, Liverpool John Moores University, Liverpool, L3 5RF, UK

²Department of Astronomy, University of California, Berkeley, CA 94720-3411, USA

³Miller Senior Fellow, Miller Institute for Basic Research in Science,
University of California, Berkeley, CA 94720, USA

⁴Department of Astronomy, San Diego State University, San Diego, CA 92182, USA

⁵X-Ray and Observational Astronomy Group, Department of Physics & Astronomy,
University of Leicester, LE1 7RH, UK

⁶Physics Department, Lancaster University, Lancaster, LA1 4YB, UK

2.1 Introduction

In this Chapter, I detail the extensive multiwavelength observational campaign I conducted to study a classical nova in a Local Group galaxy. First, in Section § 2.2 I describe the discovery of the nova and the galaxy it resides in. The observations and data analysis of the nova will be then be described in Section § 2.3. In Section § 2.4, I present the results of the photometry, spectroscopy, and X-ray analysis, and I discuss these in Section § 2.5, before summarising these findings in Section § 2.6.

[★]A version of this chapter is published with the title “AT2017fvz: a nova in the dwarf irregular galaxy NGC 6822” in *Monthly Notices of the Royal Astronomical Society*, 2019, 486, 4334 – 4347 and is reproduced with permission from MNRAS.

2.2 Discovery of AT 2017fvz

The transient AT 2017fvz, also categorised as kait-17bm, is only the second spectroscopically confirmed nova to be discovered within NGC 6822¹, a dark matter dominated (Weldrake et al., 2003) dwarf irregular galaxy in the Local Group. At a distance 476 ± 44 kpc (Rich et al., 2014), Barnard’s Galaxy, as it is otherwise known, was initially identified as “an excessively faint nebula” when first observed by Barnard (1884) and later determined to be “a very faint cluster of stars and nebulae, about $20' \times 10'$, resembling the Magellanic Clouds” (Hubble, 1925). It has had an average star-formation rate of $1.4 \times 10^{-2} M_{\odot} \text{yr}^{-1}$ over the past 100 Myr, and around $1.0 \times 10^{-2} M_{\odot} \text{yr}^{-1}$ in the last 10 Myr, similar to the Large Magellanic Cloud (LMC) however, unlike the LMC and the majority of Local Group, it exhibits a low metallicity environment $[\text{Fe}/\text{H}] \approx -0.5$ (Larsen et al., 2018).

AT 2017fvz was discovered on 2017 Aug 2.384 UT with an unfiltered magnitude of 17.6 at $\alpha = 19^{\text{h}}45^{\text{m}}1^{\text{s}}.03$, $\delta = -146^{\circ}50'74''$ (J2000; Hestenes, Zheng & Filippenko, 2017) by the Katzman Automatic Imaging Telescope (KAIT; see Filippenko et al., 2001) of the Lick Observatory Supernova Search (LOSS). It was also observed by the All-Sky Automated Survey for Supernovae (ASAS-SN; see Shappee et al., 2014) on Aug 3.190, with the Asteroid Terrestrial-impact Last Alert System (ATLAS; Tonry et al., 2018; Heinze et al., 2018) on Aug 3.386² before being classified as an extragalactic nova by Williams & Darnley (2017b) with the Liverpool Telescope (LT) approximately 7 days after discovery.

2.3 Observations and data analysis

2.3.1 Ground-based photometry

We initially had photometric data from KAIT and ATLAS, both of which discovered the nova, alongside observations later taken with the LT. However, this available data was sparse (only one data point from both KAIT and ATLAS) and did not include photometry from before the nova outburst. Therefore, once it was clear that we were limited to the analysis we could make with this data, such as accurately determining the time of eruption and decline times in multiple bands, we searched for and identified more photometric data taken with KAIT and ATLAS.

¹See Section § 2.5.1 for further discussion of the first nova.

²<https://wis-tns.weizmann.ac.il/object/2017fvz>

After contacting Dr WeiKang Zheng (who became a co-author of [Healy et al., 2019](#)) from the KAIT facility, we were notified that the field containing the nova had been monitored by KAIT using its clear filter since 2017 July 15.404 without any associated detections until the discovery on Aug 2.384, after which the nova was followed until Aug 31.284. Similarly, after contacting Professor Stephen Smartt to enquire over further ATLAS photometry, we were informed that ATLAS monitored a similar field from July 5.477 using its ‘orange’ filter, approximately covering r' and i' (5600–8200 Å³), without any associated detections until the first observation on Aug 3.386. Like KAIT, the nova was monitored after discovery by ATLAS for the next 47 days until Sep 19.317 using the orange filter and also a ‘cyan’ filter which approximately covers V and r' (4200–6500 Å). A few hours before the ATLAS detection, the nova was detected a single time by ASAS-SN on 2017 Aug 3.190 with a V -band filter. An LT follow-up campaign then began 7.53 d post-discovery; observations were taken with IO:O⁴ through $u'BVr'i'$ filters.

Debiasing and flatfielding of the LT images were performed using the automatic LT reduction pipeline. Aperture photometry was calculated from these LT data using standard tools within PyRAF and calibrated against stars from the Local Group Galaxies Survey (LGGS; [Massey et al., 2007](#)). The $u'r'i'$ magnitudes of the LGGS stars were calculated using the transformations from [Jester et al. \(2005, their Table 1\)](#).

Each time spectra were obtained with SPRAT (see Section § 2.3.2) mounted on the LT, acquisition images were also taken using the SPRAT detector. These acquisition images were reduced using the same procedure as used for the IO:O data. The acquisition images were unfiltered, but the photometry was calibrated relative to the r' filter.

We were informed by Dr WeiKang Zheng that the KAIT data were reduced using a custom pipeline ([Ganeshalingam et al., 2010](#)). Point-spread-function (PSF) photometry was then obtained using DAOPHOT ([Stetson, 1987](#)) from the IDL Astronomy User’s Library ([Landsman, 1993](#)). Several nearby stars from the APASS catalog ([Henden et al., 2009](#)) were used to calibrate the KAIT clear-band data, with their magnitudes converted to the Landolt R -band system using the empirical prescription presented by Robert Lupton⁵.

³<http://www.fallingstar.com/specifications.php>

⁴<http://telescope.livjm.ac.uk/TelInst/Inst/I00>

⁵<http://www.sdss.org/dr7/algorithms/sdssUBVRITransform.html#Lupton2005>

TABLE 2.1: Summary of spectroscopic observations of AT2017fvz with SPRAT on the Liverpool Telescope.

UT Date ^a	MJD (d)	$t - t_0(d)$	Exposure time (s)
2017-08-09.900	57974.900	8.016	3×600
2017-08-15.924	57980.924	14.040	3×600
2017-08-19.894	57984.894	18.010	3×600
2017-08-25.885	57990.885	24.001	3×600
2017-09-12.879	58008.879	41.995	3×900
2017-10-10.848	58036.848	69.964	3×900

^a The date refers to the mid-point of each observation.

ATLAS carries out difference imaging of every frame with respect to a reference sky and the photometry reported here is from those images. The photometry was carried out as described by [Tonry et al. \(2018\)](#) and [Stalder et al. \(2017\)](#).

2.3.2 Spectroscopy

The optical spectra of this nova were taken with SPRAT mounted on the LT. SPRAT is a spectrograph with a slit $95''$ long and $1''8$ wide giving a resolution of 18 \AA per pixel corresponding to $R \sim 350$ at the centre of the spectrum. It covers visible wavelengths between $4000\text{--}8000 \text{ \AA}$. The details of the spectra, which were all taken using SPRAT's blue-optimised mode, are summarised in [Table 2.1](#). All spectra were extracted, wavelength calibrated and flux calibrated automatically by the SPRAT pipeline ([Piascik et al., 2014](#)). The spectrum taken on 2017 Aug 25 was not flux calibrated due to poor sky transparency (clouds). The spectra were then analysed using routines with PyRAF.

2.3.3 UV and X-ray observations

We were granted a total of five Neil Gehrels *Swift* Observatory ([Gehrels et al., 2004](#)) target of opportunity (ToO) observations (Target ID: 10268), totalling 20.0 ks, in order to follow any UV and X-ray emission during the evolution of the nova. We initially obtained four observations, however a fifth was requested after determining the spectral energy distribution of a source located near to the nova's location (see [Section § 2.4.5.4](#)). This source had consistent luminosities to the nova in the u' -band at $t = 103 \text{ d}$ and the $uvw1$ filter. This may have indicated that we serendipitously performed photometry on a *HST* image of the same nova during an outburst in 2007, thus a recurrent nova. However, we could see from that fifth observation that the

luminosity of the nova in the *uvw1* filter was still consistent with the source ~ 120 days after the fourth *Swift* observation. This tells us that the latest photometric points we have of AT 2017fvz derived from in the u' -band and *uvw1* filter are most likely photometry of this nearby source.

Dr Kim Page (a co-author from [Healy et al., 2019](#)) carried out the X-ray analysis procedure to obtain the results which we summarise in Table 2.2. We carried out the procedure to determine the UV magnitudes of AT 2017fvz with guidance from Kim and these are what we present in Table 2.2.

NUV data were obtained with the UV/Optical Telescope (UVOT; [Roming et al., 2005](#)) through the *uvw1* filter. X-ray data were collected by the X-ray Telescope (XRT; [Burrows et al., 2005](#)) in photon-counting mode. The NUV data were processed with HEASoft tools (v6.24; [Blackburn, 1995](#)) and using the most recent calibration files. We extracted the count-rate upper limits from the X-ray data using the online *Swift* XRT tool⁶ ([Evans et al., 2009](#)).

2.4 Results

2.4.1 Reddening

NGC 6822 has a Galactic longitude and latitude of $\ell = 25.4^\circ$ and $b = -18.4^\circ$, respectively ([Mateo, 1998](#)). This results in the galaxy being affected by a modest amount of foreground extinction due to the Milky Way. [Kayser \(1967\)](#) found the Galactic reddening toward the outer regions of NGC 6822 to be $E(B - V) = 0.27 \pm 0.03$ mag, as did [Massey et al. \(1995\)](#) with $E(B - V) = 0.26$ mag. These are consistent with [Gallart et al. \(1996\)](#) and [Massey et al. \(2007\)](#) who found $E(B - V) = 0.24 \pm 0.03$ mag and $E(B - V) = 0.25$ mag, respectively. The online dust-mapping tool⁷ ([Green et al., 2018](#)) returns a Galactic reddening toward NGC 6822 of $E(B - V) = 0.22 \pm 0.02$ mag.

Cepheid variables within NGC 6822 have been employed to estimate the internal reddening. [McAlary et al. \(1983\)](#) found $E(B - V) = 0.36$ mag, [Gieren et al. \(2006\)](#) reported a similar average reddening of $E(B - V) = 0.356 \pm 0.013$ mag. [Rich et al. \(2014\)](#) used optical and infrared data for Cepheids to determine that the foreground reddening along the line of sight to NGC 6822 is $E(B - V) = 0.35 \pm 0.04$ mag.

⁶http://www.swift.ac.uk/user_objects/

⁷<http://argonaut.skymaps.info>

TABLE 2.2: Neil Gehrels *Swift* Observatory UVOT magnitude and X-ray.

Exp ^a (ks)	Date ^b (UT)	MJD (d)	$t - t_0^c$ (d)	$uvw1^d$ (mag)	X-ray rate (0.3–1 keV) (10^{-3} ct s $^{-1}$)	$L_{0.3-1\text{keV}}^e$ (10^{37} erg s $^{-1}$)	X-ray rate (0.3–10 keV) (10^{-3} ct s $^{-1}$)	$L_{0.3-10\text{keV}}^e$ (10^{37} erg s $^{-1}$)
3.9	2017-09-09	58005	38.12	18.6 ± 0.1	< 1.9	< 0.8	< 1.9	< 0.8
3.7	2017-10-08	58034	67.12	19.4 ± 0.2	< 3.5	< 1.4	< 3.3	< 1.3
3.4	2017-11-07	58064	97.12	19.6 ± 0.3	< 2.5	< 1.0	< 3.2	< 1.3
3.7	2018-04-27	58235	268.12	20.2 ± 0.3	< 3.4	< 1.3	< 3.2	< 1.3
4.0	2018-08-25	58355	388.12	19.9 ± 0.2	< 2.5	< 1.0	< 3.0	< 1.2

^aDead-time corrected XRT exposure time.

^bStart date of the observation.

^cTime since day of eruption on 2017 Aug. 1.884.

^dVega magnitudes for the *uvw1* filter (central wavelength: 2600 Å).

^eX-ray luminosity upper limits (unabsorbed, blackbody fit, 0.3–1 keV or 0.3–10 keV, as indicated).

We have no knowledge of the radial displacement of AT 2017fvz within NGC 6822 so we adopt the two most extreme values of reddening. The foreground reddening toward NGC 6822 gives the lower limit, the addition of reddening internal to NGC 6822 gives the upper limit.

2.4.2 Photometric evolution

The photometry from the LT, KAIT, ASAS-SN, ATLAS, and *Swift* data are presented in the form of a light curve in Figure 2.1, which illustrates that the nova was discovered prior to peak optical magnitude. We have also split the light curve into different filters for clarity in Figure 2.2, Figure 2.3 and Figure 2.4. From the data provided on the Transient Name Server webpage, we initially calculated the time of eruption of this nova to be 2017 Aug 1.897 ± 0.470 which was between the last non-detection of the nova by ATLAS and the first detection by KAIT. However, with the new photometric data we obtained from WeiKang Zheng and Stephen Smartt, we were able to calculate the time of eruption to be 2017 Aug 1.9 ± 0.5 , which is the midpoint between the last non-detection by KAIT with $m_{\text{clear}} > 18.1$ on 2017 Aug 1.384 and the discovery on Aug 2.384. This is very close to the original value so even though it is more accurate, it is still stated as the same value of 2017 Aug 1.9 ± 0.5 throughout, which we refer to the time of eruption as t_0 .

We can see from the lower limiting magnitudes before t_0 on the light curve that KAIT and ATLAS monitored this portion of the sky before the nova eruption. After this pre-nova period, we observe a steep rise but no evidence for a pre-maximum halt. However, with this being a very-fast nova (see Table 2.3) such a halt would be expected to persist for only a few hours (Hounsell et al., 2010), and the cadence of these observations is not high enough to resolve such a short stage.

The photometry calculated from the KAIT observations, the ‘orange’ filter from ATLAS, and the unfiltered SPRAT acquisition images (labelled as r' in Figure 2.1) is broadly consistent with the r' -band magnitudes from the LT observations from peak to around 20 d after eruption, therefore we will assume that these data are equivalent to the r' -band. The u' , B , and V bands all fade at the same uniform rate from peak until around 40 d, while i' fades more slowly and r' even slower due to the strong influence of the $H\alpha$ emission line on the broad-band photometry. The evolution of the $H\alpha$ emission line of AT 2017fvz is shown in Figure 2.9.

There is evidence for a ‘plateau’ in the u' , B , V , and i' -band light curves around $t = 25$ d. As such, this nova could belong to the ‘plateau’ class (P-class) as described in Strobe et al. (2010) where we observe a smoothly declining light curve interrupted

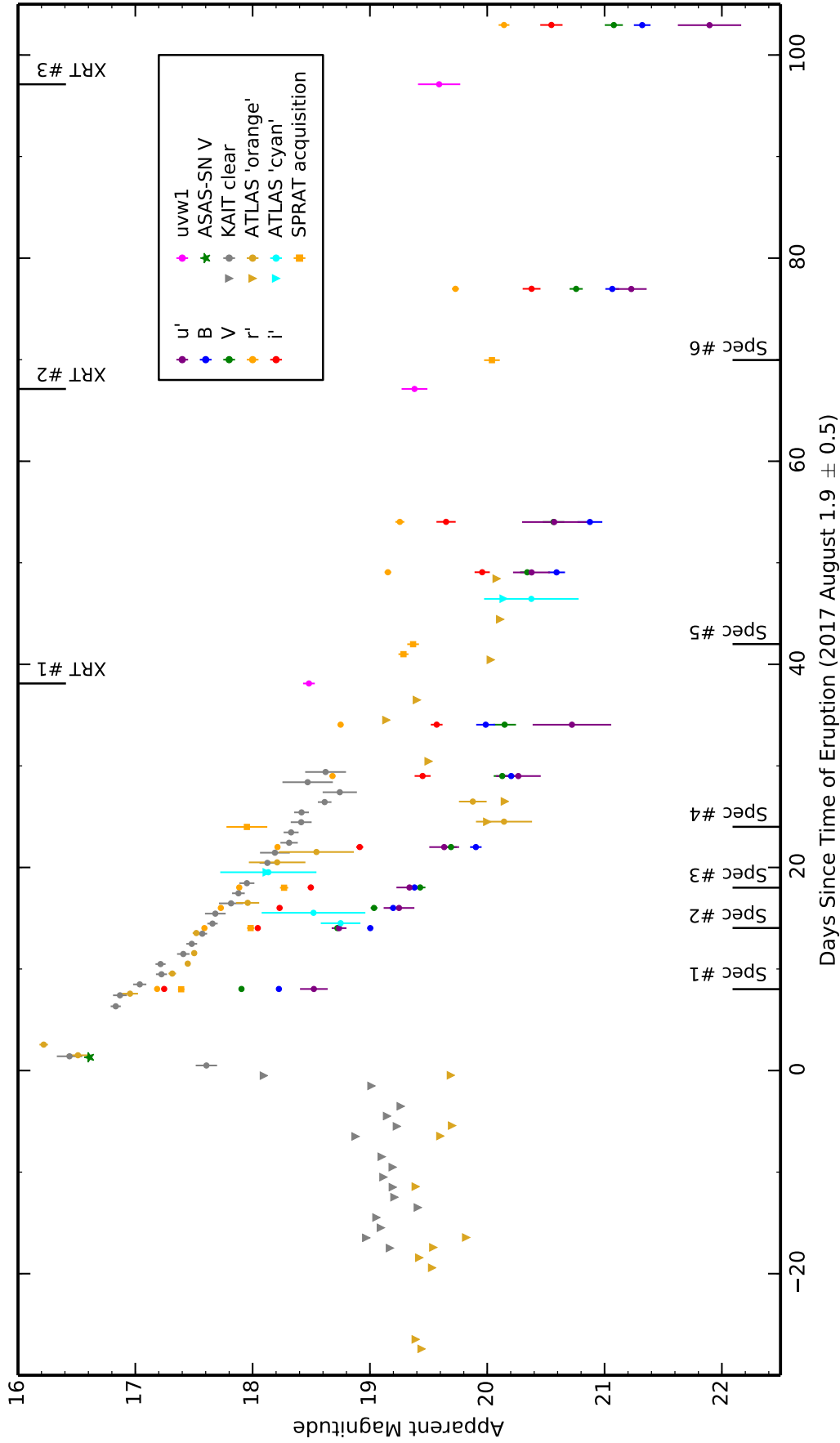


FIGURE 2.1: Optical and near-UV light curve of AT2017fz. The colours represent different filters: *Swift uvw1* (pink); LT *u'* (purple); LT *B* (blue); LT *V* (green); LT *i'* (red); LT *r'* (orange); KAIT clear (grey); ATLAS orange (gold) and ATLAS cyan (cyan). The green star close to peak is the *V* magnitude from ASAS-SN. The orange squares are the *r'* magnitudes from the LT SPRAT acquisition images. The grey, gold and cyan triangles are the upper limits in KAIT clear, ATLAS orange and ATLAS cyan filters, respectively. We have also indicated the times of the six SPRAT spectra along the bottom axis and the times of the first three *Swift XRT* observations along the top axis; the fourth and fifth *Swift XRT* visits occurred at $t = 268.12$ d and $t = 388.12$ d, respectively.

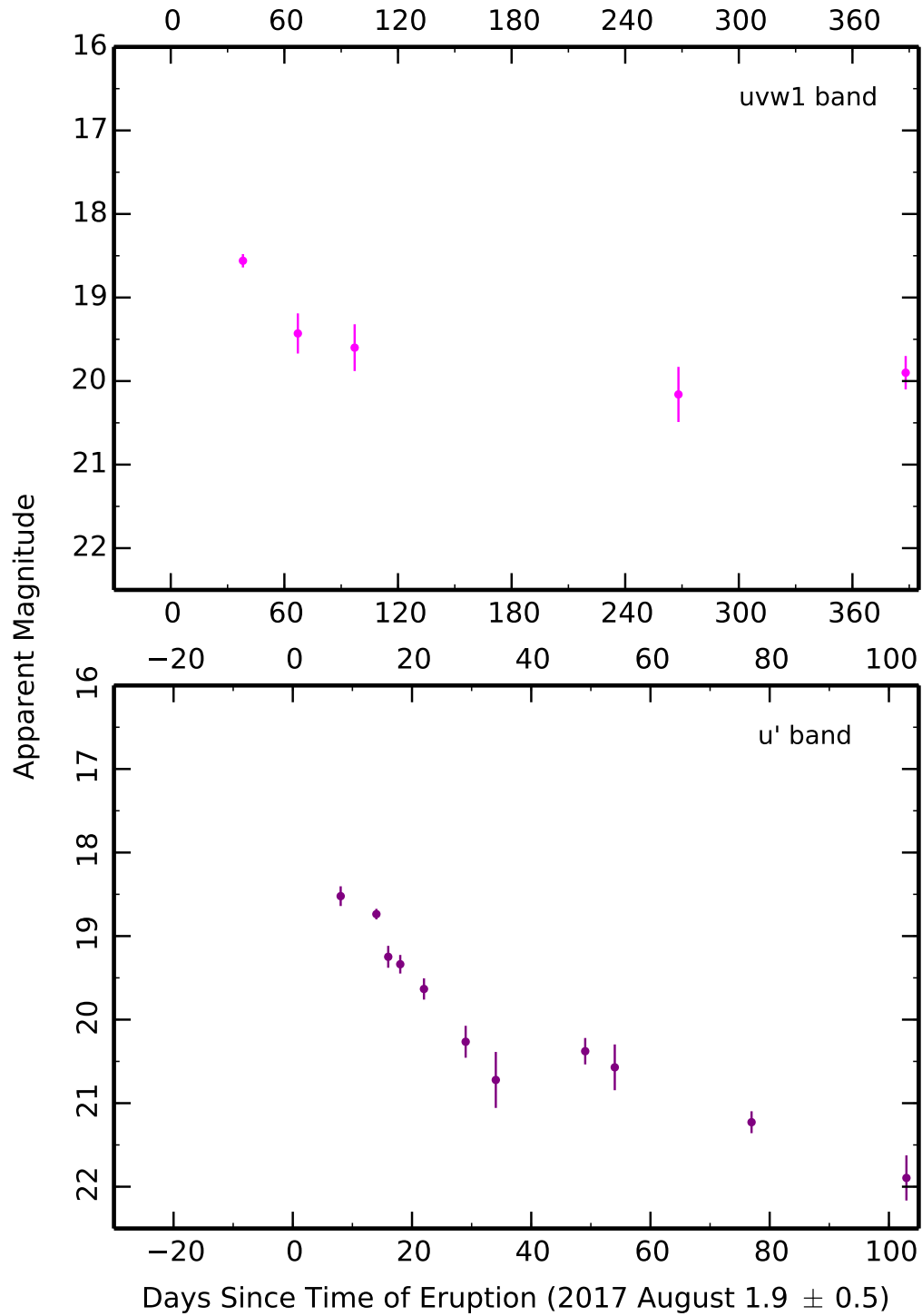


FIGURE 2.2: Optical and NUV light curves of AT2017fvz. As in Figure 2.1, the colours represent different filters: *Swift uvw1* (pink) and LT *u'* (purple). Note that the *uvw1* plot covers ~ 420 days.

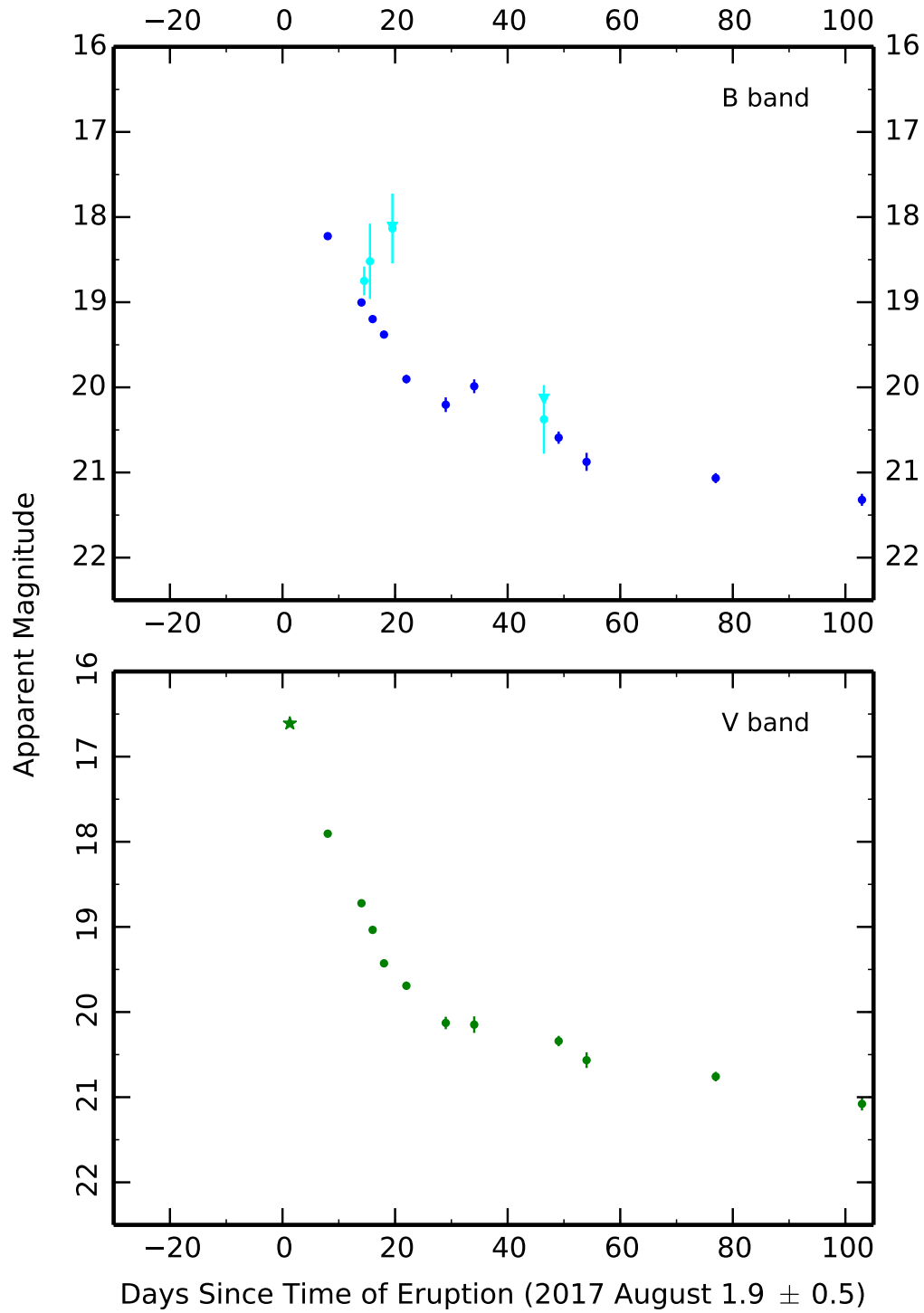


FIGURE 2.3: Optical light curves of AT 2017fvz. As in Figure 2.1, the colours represent different filters: LT *B* (blue); LT *V* (green) and ATLAS cyan (cyan). The green star close to peak is the *V* magnitude from ASAS-SN. The cyan triangles are the upper limits in the ATLAS cyan filter.

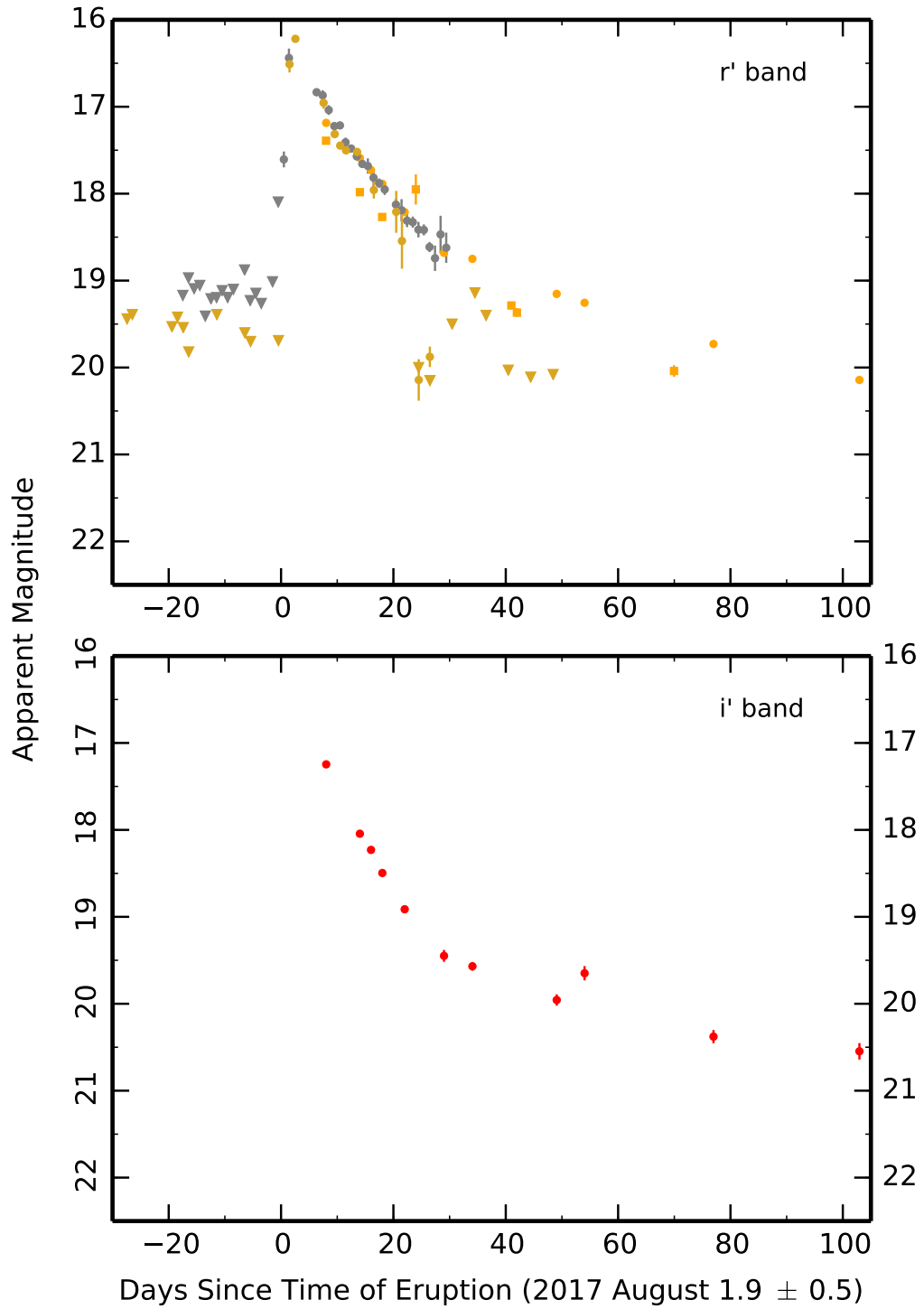


FIGURE 2.4: Optical light curves of AT2017fyz. As in Figure 2.1, the colours represent different filters: LT i' (red); LT r' (orange); KAIT clear (grey) and ATLAS orange (gold). The orange squares are the r' magnitudes from the SPRAT acquisition images. The grey and gold triangles are the upper limits in KAIT clear and ATLAS orange filters, respectively.

by a short period when the apparent optical magnitude remains approximately constant. It has been proposed that such plateaus are produced by the SSS irradiating a re-formed, or surviving, accretion disk and the donor. The subsequent reprocessed optical light then dominates the light emitted by the nova ejecta, temporarily halting the decline of light curve (Hachisu et al., 2000; Evans et al., 2008; Pagnotta & Schaefer, 2014; Darnley et al., 2016). Given the large proportion of RNe that belong to the P-class (in comparison to those that are CNe), Pagnotta & Schaefer (2014) proposed that a light curve plateau is a reasonable indicator of a RN. However, it does not provide strong evidence in isolation.

Taking the distance modulus to NGC 6822 as $\mu_0 = 23.38 \pm 0.02$ (Rich et al., 2014), correcting for reddening using $E(B - V) = 0.22 \pm 0.02$ (see Section § 2.4.1), and assuming the extinction law $R_V = 3.1$ (Cardelli et al., 1989), we derive an absolute magnitude for the peak of the eruption in the V -band of $M_V = -7.45 \pm 0.07$. For this absolute magnitude we have used the ASAS-SN photometry as this is the closest observation to the peak through this filter.

The peak r' -band magnitude of AT 2017fvz was derived using the orange filter on ATLAS ($m_{r'} = 16.22 \pm 0.04$). Finding the extinction for the r' -band ($\lambda \sim 0.658 \mu\text{m}$) using Cardelli et al. (1989, their equations 2a–3c) to be $A_{r'} = 0.815A_V$ gives a peak absolute magnitude of $M_{r'} = -7.72 \pm 0.06$. The r' -band absolute magnitude of the nova 15 d after peak is $M_{r',15} = -5.60 \pm 0.05$.

We have estimated the decline times t_2 and t_3 of the nova by taking the brightest data point as the peak of the eruption and fitting an exponential function of the form $M = a + b \exp(ct)$ to the data for each filter. An example of such is given in Figure 2.5 which shows the exponential function fitted to the V -band photometric points. Figure 2.6 shows a power law function fitted to the same V -band photometric points. These decline times are summarised in Table 2.3. In addition, we fitted an exponential function and power law function to only the photometry up to the apparent plateau to determine if the plateau significantly impacts the estimate (shown as blue lines in Figure 2.5 and Figure 2.6) and found the V -band t_2 decline time changes by $\sim 15\%$ for the exponential and $\sim 1\%$ for the power law.

If we use t_2 and t_3 with the corresponding MMRD relations in Downes & Duerbeck (2000) then we predict peak absolute magnitudes of $M_V = -9.01 \pm 0.53$ for t_2 and $M_V = -8.99 \pm 0.70$ for t_3 . However, these relations were derived from Galactic novae and so may produce incorrect magnitudes for AT 2017fvz as it is located in a different environment (also see Section § 2.5.5).

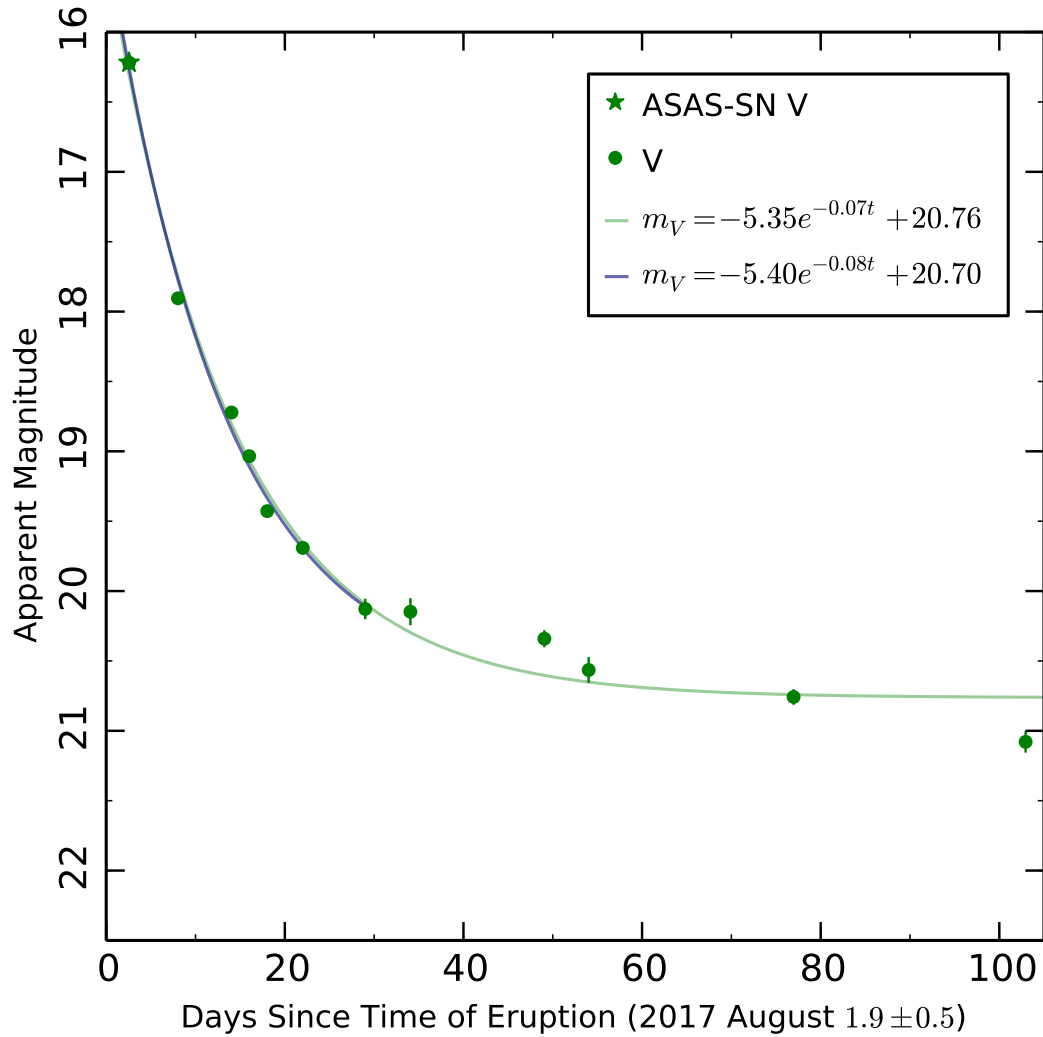


FIGURE 2.5: The green line is the exponential function fitted to the V -band photometry. The blue line is the exponential function fitted to the V -band photometry up to $t \approx 30$ d (excluding the apparent plateau).

TABLE 2.3: Summary of decline times of AT 2017fvz in each filter.

Filter	t_2 (days)	t_3 (days)
u'	7.1 ± 0.2	13.8 ± 0.3
B	6.8 ± 0.2	13.3 ± 0.3
V	8.1 ± 0.2	15.2 ± 0.3
r'	15.5 ± 0.4	33.0 ± 1
i'	13.0 ± 0.3	25.3 ± 0.6

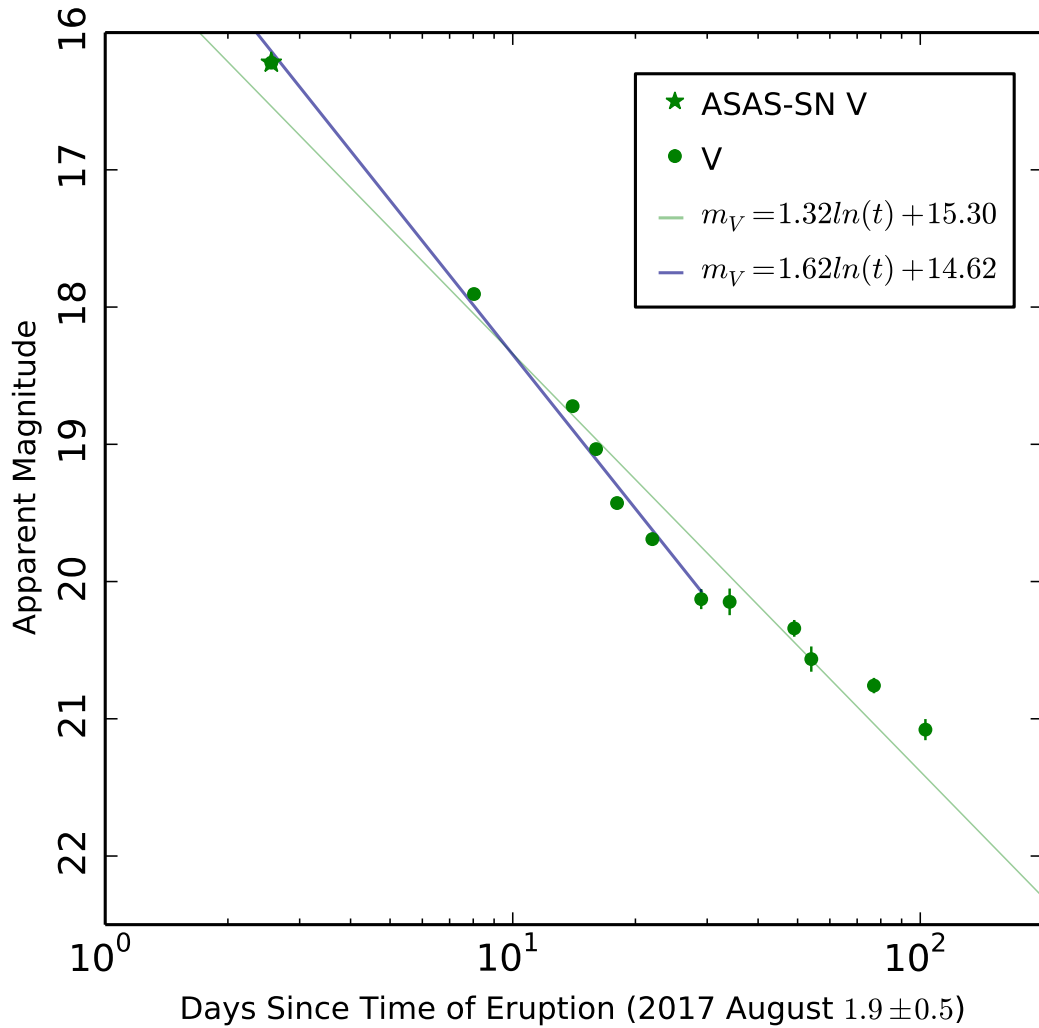


FIGURE 2.6: The green line is the power law function fitted to the V -band photometry. The blue line is the power law function fitted to the V -band photometry up to $t \approx 30$ d (excluding the apparent plateau).

2.4.3 Spectroscopic evolution

To aid the analysis of the spectra taken of AT2017fvz, we made extensive use of the multiplet table in Moore (1945) and the nova emission line table from Williams (2012). All of the spectra of AT2017fvz are plotted in Figure 2.7. These spectra can be broadly split into three groups: the first contains the first four spectra which are within an approximately 16 day-long period when the nova light curve was in the early decline; the fifth spectrum was then taken around $t = 42$ d when the nova light curve began to plateau and then the sixth spectrum was taken around $t = 70$ d during the nova’s nebular phase.

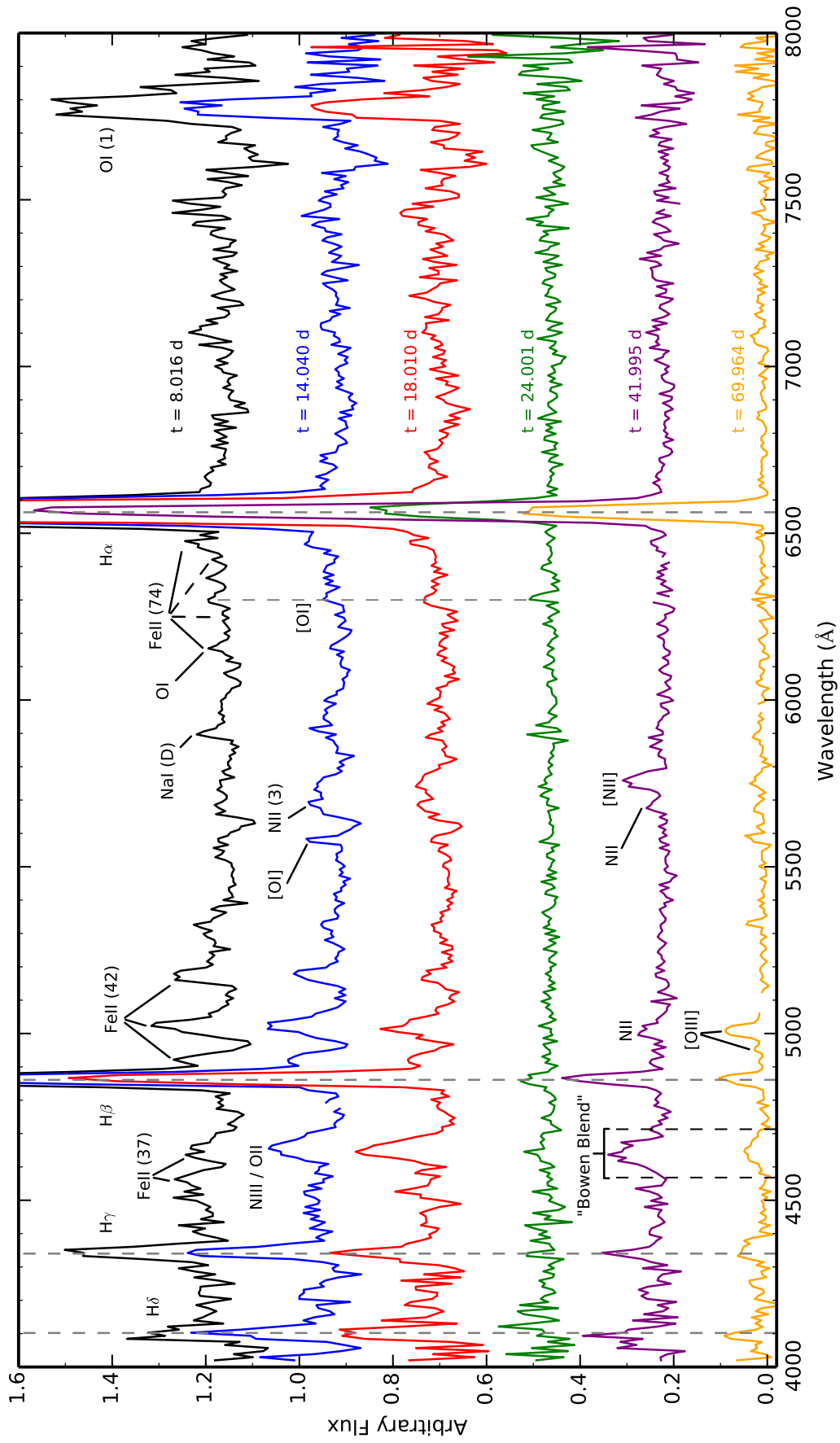


FIGURE 2.7: The six SPRAT spectra of AT 2017fvz. We have given the time after eruption for each spectrum, and have labeled the prominent emission lines including the Balmer lines. The gaps in $t = 14.040$ d, $t = 41.995$ d and $t = 69.964$ d were the locations of cosmic rays.

All of these spectra are shown in the frame of the observer, but for line identification we have quoted the rest wavelength. The average radial velocity of NGC 6822 is -57 km s^{-1} (Koribalski et al., 2004). The flux and FWHM velocity were calculated by fitting Gaussian profiles to the emission lines using the SPLAT package in STARLINK; these are reported in Table 2.4 and Table 2.5, respectively.

2.4.3.1 Early Decline

Our first spectrum was taken at $t = 8.016 \text{ d}$ when the nova was in the early decline⁸. By this time, we have missed the optically thick ‘fireball’ stage which occurs on the rise until around peak, which is characterised by a black-body-like continuum punctuated with blue-shifted absorption lines (Shore, 2012). The transition out of the fireball stage results in emission lines becoming the dominant features of the spectrum with associated P Cygni absorptions diminishing over time. We may have caught the very end of this transition with some of the Fe II lines and the H δ emission line still showing tentative signs of P Cygni profiles. The H δ emission line has a small blue-shifted absorption component with a midpoint of $4052.4 \pm 7.6 \text{ \AA}$ and an equivalent width of $29.3 \pm 5.7 \text{ \AA}$. Also, the emission component may have a different profile than the other Balmer lines with a FWHM of $\sim 2400 \text{ km s}^{-1}$. In Figure 2.8 we have plotted the Balmer lines for $t = 8.016 \text{ d}$, $t = 14.040 \text{ d}$ and $t = 18.010 \text{ d}$ in order to illustrate the evidence for a H δ P Cygni versus a ‘drop-off’ at the edge of the spectrograph.

The other prominent features of this first spectrum are the H α , H β and H γ emission lines and the double peaked O I (1) emission line at 7773 \AA , which all have FWHM velocities of $\sim 2400 \text{ km s}^{-1}$. There is an Fe II (42) triplet redward of H β at 4924 , 5018 , and 5169 \AA , as well as a fairly strong Na I (D) emission line at approximately 5892 \AA . There may be a weak Fe II (74) multiplet blueward of H α , however, we only see this at 6148 \AA and 6456 \AA (even this is made more prominent by the ‘wing’ of the H α line) with the 6248 \AA and 6417 \AA lines clearly absent. Another explanation for this line at 6148 \AA could be that it is O I (6158 \AA). Between these lines, there is a feature at around 6300 \AA which may be [O I], that persists through the spectra until the ‘plateau’ phase. We also see tentative evidence for Fe II (37) lines at 4556 \AA and 4629 \AA .

We can compare this spectrum to that of Nova IC 1613 2015 (Williams et al., 2017, see their Figure 4) at $t = 6.59 \text{ d}$ as it is a similar time after eruption. In Figure 2.14,

⁸This spectrum was used by Williams & Darnley (2017b) to classify AT 2017fvz as an extragalactic nova.

TABLE 2.4: The evolution of emission line fluxes from the spectra of AT2017fvz in units of $10^{-15} \text{ erg cm}^{-2} \text{ s}^{-1}$.

Line identification (rest wavelength [Å])	t = 8.016 d	t = 14.040 d	t = 18.010 d	t = 41.995 d	t = 69.964 d
H δ (4102)	6.3 \pm 2.9	7.8 \pm 1.6	6.7 \pm 2.5	1.9 \pm 1.3	1.7 \pm 0.4
H γ (4341)	12.3 \pm 1.4	9.4 \pm 1.2	6.7 \pm 1.3	2.4 \pm 0.5	2.0 \pm 0.6
H β (4861)	30.4 \pm 2.5	31.0 \pm 4.2	26.7 \pm 1.8	6.8 \pm 0.5	2.4 \pm 0.5
[O III] (5007)	–	–	–	–	2.6 \pm 0.4
[Fe II] (5018)	4.6 \pm 0.7	5.0 \pm 1.3	–	–	–
H α (6563)	139.2 \pm 5.5	212.8 \pm 12.1	230.0 \pm 10.6	61.4 \pm 2.8	24.3 \pm 1.7
[O I] (7773)	27.7 \pm 3.8	21.5 \pm 3.2	16.4 \pm 2.2	–	–

We have not included the spectrum from 24.001 days after eruption because the fluxes are not reliable due to poor weather (see Section 2.3.2).

TABLE 2.5: The evolution of emission line velocities from the spectra of AT 2017fvz in units km s^{-1} .

Line identification (rest wavelength [Å])	t = 8.016 d	t = 14.040 d	t = 18.010 d	t = 24.001 d	t = 41.995 d	t = 69.964 d
H δ (4102)	2600 \pm 900	2100 \pm 340	2100 \pm 610	–	900 \pm 460	1500 \pm 260
H γ (4341)	2500 \pm 220	2000 \pm 200	2200 \pm 330	–	1400 \pm 210	3500 \pm 820
H β (4861)	2300 \pm 150	2100 \pm 210	1900 \pm 100	–	1800 \pm 110	1600 \pm 240
[O III] (5007)	–	–	–	–	–	1900 \pm 200
[Fe II] (5018)	1900 \pm 220	2200 \pm 230	–	–	–	–
H α (6563)	2430 \pm 70	2300 \pm 100	2070 \pm 70	2000 \pm 90	1840 \pm 60	1900 \pm 100
[O I] (7773)	2800 \pm 290	2200 \pm 240	2000 \pm 210	–	–	–

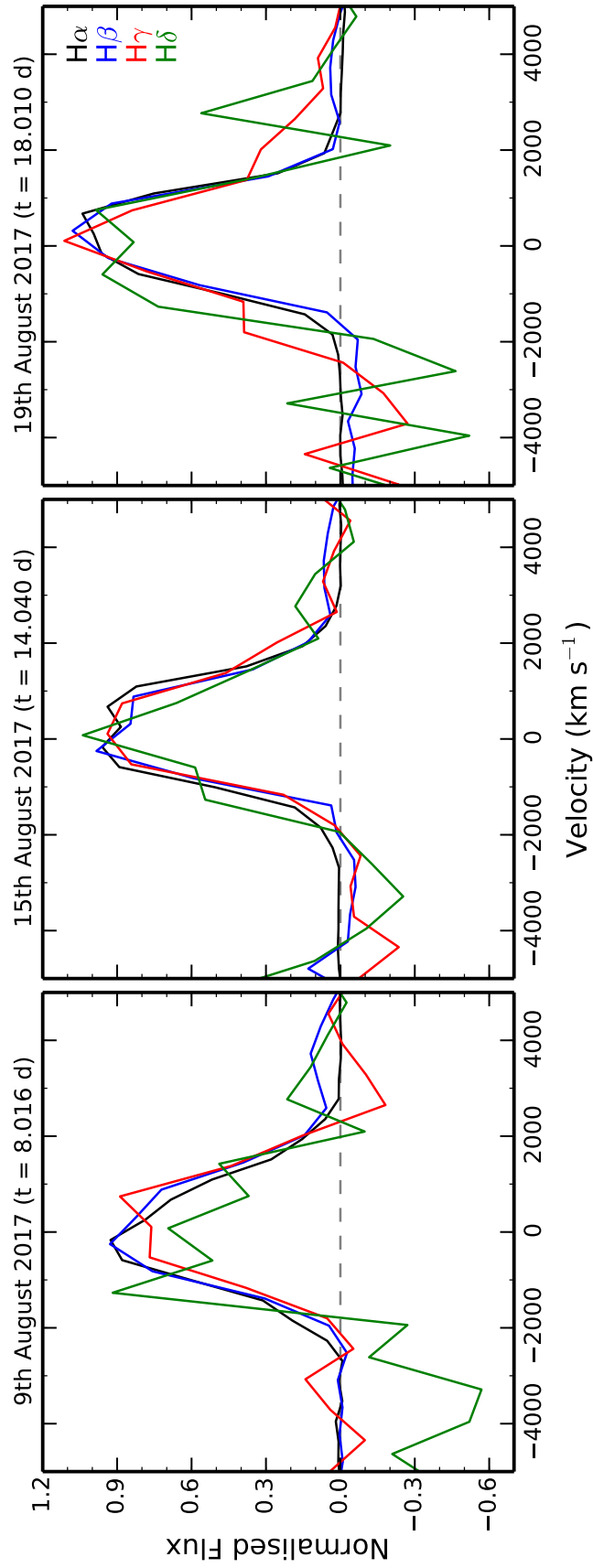


FIGURE 2.8: The evolution of the H α , H β , H γ and H δ emission lines from the spectra of AT 2017fvz over approximately 10 days, shown with a normalised peak strength. All of the Balmer lines fall to the same continuum on the blue side, except for H δ which shows blue-shifted absorption at $t = 8.016$ d. This is evidence of a P Cygni profile associated with this emission line at that time.

we can see the same dominant Balmer lines and the double peaked O I (1) emission line in both. However in Nova IC 1613, there are He I emission lines at 5900 Å and potentially 5048 Å (Williams et al., 2017, suggest this is more likely to be N II) as well as a number of other nitrogen lines that the spectrum of AT 2017fvz clearly lacks.

The second spectrum of AT 2017fvz, taken 14.040 days post-eruption, maintains all of the aforementioned emission lines including the Balmer lines, with slightly lower FWHM velocities of $\sim 2100 \text{ km s}^{-1}$, and many Fe II lines. In addition, there is a prominent feature that has developed at around 4640 Å which may be a blending of the N III and O II emission lines at 4631 Å and 4638 Å, respectively. Other emission lines could be present at this location including C IV (4658 Å), the forbidden [Fe III] (4658 Å) or O I (18) at 4655 Å. The [O I] (5577 Å) line can be seen alongside the N II (3) line at 5679 Å which is similar to the same line found in V1494 Aquilæ (Nova Aql 1999) around 14 days after maximum light (Iijima & Esenoglu, 2003, see their Figure 6) and found in the spectrum of an Fe II nova, SN 2010U⁹, 15.3 days after maximum (Czekala et al., 2013, see their Figure 11).

The third spectrum, $t = 18.010 \text{ d}$, has the same emission lines as the previous two spectra with all of the lines except H α , H β , H γ and the blend of lines at $\sim 4640 \text{ Å}$ having become weaker. See Section § 2.4.3.4 for a more in-depth look at the evolution of the H α emission line. Unfortunately, the fourth spectrum ($t = 24.001 \text{ d}$) has low signal to noise due to the conditions in which this spectrum was taken so we only see Balmer lines and [O I] at 6300 Å but little else.

2.4.3.2 ‘Plateau’ Phase

The fifth spectrum was taken during the apparent plateau phase 41.995 days post-eruption. The Balmer emission lines still dominate but there are now many nitrogen emission lines such as N II (24) at 5001 Å, N II (3) at 5679 Å and [N II] (5755 Å). The nitrogen lines at 5679 Å and 5755 Å can clearly be seen in Nova IC 1613 2015 at $t = 57.51 \text{ d}$ (Williams et al., 2017, see their Figure 5).

Many nitrogen lines are expected during this phase of the evolution of a nova when we should begin to see a considerable enhancement of nitrogen lines – the so-called ‘nitrogen flaring’ – which is caused by the Bowen fluorescence mechanism whereby N III is ‘pumped’ by the UV resonance lines of O III (Bowen, 1934, 1935). This ‘flaring’ of nitrogen has long been known with Wright (1940) noticing this in the spectrum of DN Geminorum (Nova Gem 1912) near 4600 Å, stating that “it appears at first

⁹Not a supernova (Czekala et al., 2013)!

sight hopeless to try to interpret” as well as in the RN T Coronae Borealis at 4097 Å and 4103 Å (Herbig & Neubauer, 1946). In the case of V5668 Sgr (Nova Sgr 2015b), Harvey et al. (2018) indicated that this ‘Bowen Blend’ around 4640 Å may be more naturally explained by ‘oxygen flaring’ whereby there is flaring of the O II multiplet (V1) from 4638–4696 Å.

Such ‘oxygen/nitrogen flaring’ also manifests itself in the spectrum of AT 2017fvz through a broad amalgamation of lines at approximately 4640 Å where it is difficult to determine the individual lines due to the low spectral resolution. We can assume that they are the N II (5) multiplet at 4614 Å, 4621 Å and 4630 Å, and the C III (1) multiplet at 4647 Å, 4650 Å and 4651 Å as well as other nitrogen species.

2.4.3.3 Nebular Phase

The final spectrum was taken 69.964 days after the time of eruption coinciding with the nova’s nebular phase. There have not been many extragalactic novae beyond the Magellanic Clouds observed spectroscopically during their nebular phase (Williams et al., 2017).

At this stage, the spectrum is totally dominated by emission lines as the spectrum changes its appearance to be more akin to that of a planetary nebula (Popper, 1940). The ‘Bowen Blend’ from the previous spectrum is still visible and has broadened to cover and incorporate more wavelengths taking on a ‘dome-like’ appearance.

There is also evidence for the [O III] nebular lines at 4959 and 5007 Å. The appearance of [O III] often roughly coincides with the beginning of the SSS phase when the ejecta from the nova are becoming optically thin to UV radiation and collisions are still occurring due to the high enough density providing a cooling mechanism (Mason et al., 2018). At this time, the density of the ejecta must be less than the critical density ($n_e = 6.8 \times 10^5 \text{ cm}^{-3}$) for the collisional de-excitation of [O III]. We would also expect an [O III] nebular line at 4363 Å. However, with this being a relatively weak line, it is most likely hidden by the neutral mercury (Hg I) sky line at 4358 Å (Osterbrock & Ferland, 2006). Even so, we can use the ratio of these three emission lines (Osterbrock & Ferland, 2006, see their Figure 5.1; assuming 4363 Å is weak) to estimate that the electron temperature within this part of the ejecta could be as low as 5000 K.

Additionally, the ratio of [O III] 5007/4959 Å ~ 3.5 and, as in Williams et al. (2017), this ratio is larger than the expected (~ 3) which suggests that these nebular lines may still be blended with other emission lines such as N II.

2.4.3.4 H α evolution

The evolution of the H α emission line profile is shown in the left panel of Figure 2.9. After the first spectrum at $t = 8.016$ d, when the line has a FWHM of 2430 ± 70 km s $^{-1}$, the line progressively narrows from 2300 ± 100 km s $^{-1}$ to 2070 ± 70 km s $^{-1}$ and then to 1840 ± 60 km s $^{-1}$ at $t = 14.040$ d, $t = 18.010$ d and $t = 41.995$ d respectively. The line width then remains constant between the fifth and sixth spectra with the FWHM being 1900 ± 100 km s $^{-1}$ at $t = 69.964$ d.

In the right image of Figure 2.9, we have zoomed into the base of the H α emission line in order to show the faint asymmetric line to the blue. Taking an average of the H α line over the six spectra highlights this emission and illustrates that it is unlikely to be a feature of the H α line because it is not seen on both sides of the base. As mentioned in Section § 2.4.3.1, this feature is most likely a weak Fe II (74) emission line at 6456 Å.

2.4.4 X-rays

Utilising the r' -band decline time ($t_2 \approx 15$ d; see Table 2.3), we used the correlations presented by Henze et al. (2014a) to estimate the SSS properties of AT 2017fvz. We predict that a SSS with blackbody temperature $kT \approx 50$ eV should have appeared at $t_{\text{on}} \approx 72$ d and turned off at $t_{\text{off}} \approx 243$ d.

A Galactic foreground column density of $N_{\text{H}} = 10^{21}$ cm $^{-2}$ toward AT 2017fvz was derived from the HEASARC N_{H} tool based on the Galactic neutral hydrogen map by Kalberla et al. (2005). We used the PIMMS software (v4.8f) with this column and the estimated SSS temperature to convert from counts to unabsorbed flux. We then derived X-ray luminosities by assuming a distance of 476 kpc to NGC 6822; these are presented in Table 2.2.

We do not detect any X-ray emission from this system between 38 and 388 days after the time of eruption. The luminosity upper limits, calculated from the X-ray count limits (0.3–1 keV), assuming a blackbody temperature of $kT \sim 50$ eV in Table 2.2 are all below 1.4×10^{37} erg s $^{-1}$. As this blackbody temperature is relatively low compared in particular to fast RNe such as M31N 2008-12a (~ 120 eV; Darnley et al., 2016) and RS Oph (~ 90 eV; Osborne et al., 2011), we can conclude that this system did not have a bright SSS phase during our observational window. This is similar to Nova IC 1613 2015 (Williams et al., 2017) where a bright SSS was also absent.

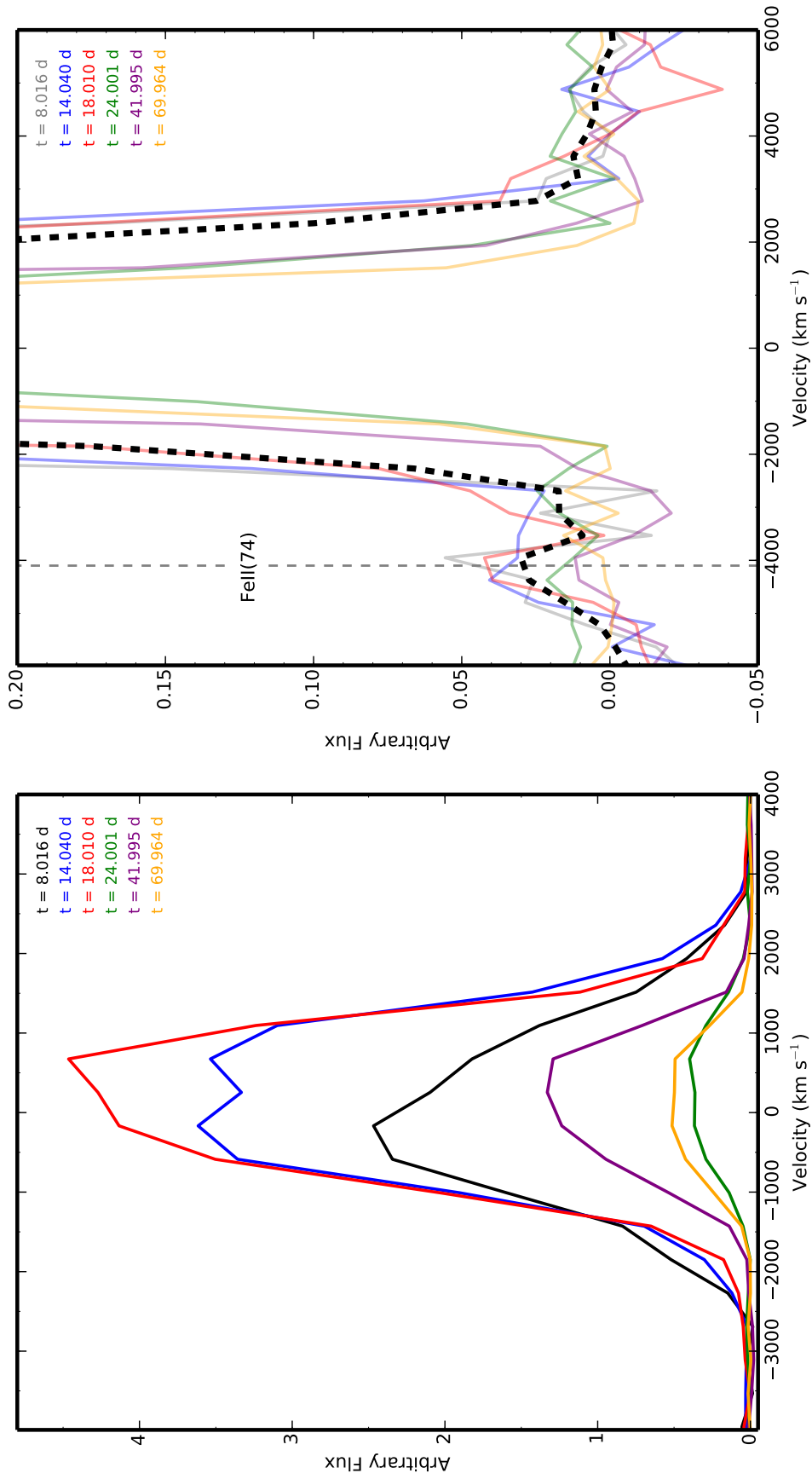


FIGURE 2.9: **Left:** $H\alpha$ emission line evolution from $t = 8.016$ d to $t = 69.964$ d in terms of relative flux with respect to velocity. The $t = 24.001$ d spectrum is significantly lower than expected as this is spectrum was not flux calibrated. **Right:** A closer look at the base of the $H\alpha$ emission line throughout its evolution from $t = 8.016$ d to $t = 69.964$ d in terms of relative flux with respect to velocity. The black dashed line is an average of the six spectra. This average highlights the faint asymmetric emission to the blue side of the $H\alpha$ line, identified here with a grey dashed line, most likely to be a weak Fe II (74) emission line at 6456 \AA .

The upper limit from the five combined observations (0.3–1 keV) is $9 \times 10^{-3} \text{ ct s}^{-1}$. Under the assumption that a SSS would have been present for all five observations, this corresponds to a luminosity $< 4 \times 10^{36} \text{ erg s}^{-1}$. This limit is similar to the luminosity of a number of faint nova SSSs in M31. M31N 2003-08c had a luminosity $3.5 \times 10^{36} \text{ erg s}^{-1}$ when it was first detected around 1540 days post-eruption (Henze et al., 2011) and M31N 2006-09c (also an Fe II nova) had a luminosity $\leq 4.0 \times 10^{36} \text{ erg s}^{-1}$ around 426 days after eruption (Henze et al., 2011). Even though both lack photometric data to use for decline times, we can determine that they are slow novae due to their low ejecta velocities. The FWHM of the H α emission line in M31N 2003-08c is 900 km s^{-1} (di Mille et al., 2003) and M31N 2006-09c has an expansion velocity of $570 \pm 45 \text{ km s}^{-1}$ (Henze et al., 2011). Given their low ejection velocities, the observed turn-on times for these novae are fairly consistent with estimates determined from Figure 8 of Henze et al. (2014a) for t_{on} . We would not expect such a late t_{on} for AT 2017fvz.

2.4.5 The nova progenitor

2.4.5.1 Obtaining data

The WD in the nova system may have had either a main sequence, sub-giant or red giant companion. If the system contains a red giant then it may be detectable with the *Hubble Space Telescope* (*HST*) due to the proximity of NGC 6822. The position of AT 2017fvz is located within archival *HST* Wide-Field Planetary Camera 2 (WFPC2) images (GO:11079) taken in April 2007 using the F170W, F255W, F336W, F439W, F555W, and F814W filters.

2.4.5.2 Positional transformation

As described in Bode et al. (2009), Darnley et al. (2014), and in detail in Williams et al. (2014), we used reference stars in the LT images and one of the F814W *HST* images to align the two and used the resultant plate solution to transform between the two native coordinate systems. We extended the original technique by employing all of the i' -band and r' -band LT images of the nova eruption. The PyRAF package `imcen` converged on the nova's position for all 11 of the r' -band LT images however only converged on the nova in 7 of the 11 i' -band LT images. We used the average nova position and subsequent scatter (in terms of standard deviation σ) in these 18 LT images (shown in Figure 2.10) to more precisely and accurately determine the nova position in the *HST* data – shown in Figure 2.11.

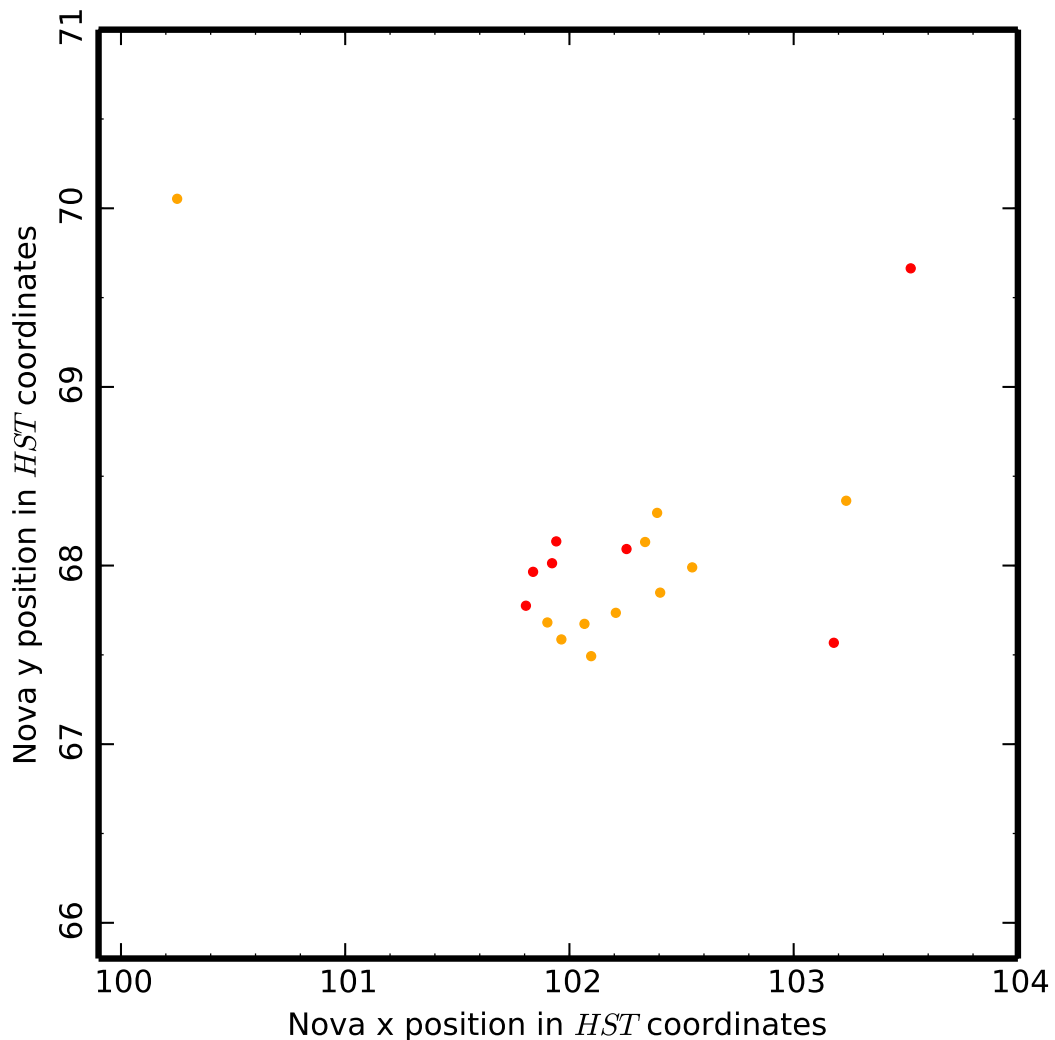


FIGURE 2.10: Position of the nova in *HST* coordinates from the 18 LT images. The red points are the nova’s position from the 7 *i'*-band LT images converted into *HST* coordinates. and the orange points are from the nova’s position in the 11 *r'*-band images converted into *HST* coordinates.

2.4.5.3 Position of source

We performed crowded-field point-spread function fitting photometry using the stellar photometry package DOLPHOT (v2.0; [Dolphin, 2000](#), using standard parameters as given in the manual) on all detected objects in the *HST* image and found a source that is within $5.14\sigma^{10}$ (2.05 WFPC2/PC pixels) of the nova’s location corresponding to an angular separation of $0''.0931$ relating to a projected distance of 0.21 pc (see Figure 2.11 for its position and Table 2.6 for the photometry of the source). While seemingly close, we have no knowledge of the line-of-sight separation of the two objects.

¹⁰This is the standard deviation introduced in Section § 2.4.5.2.

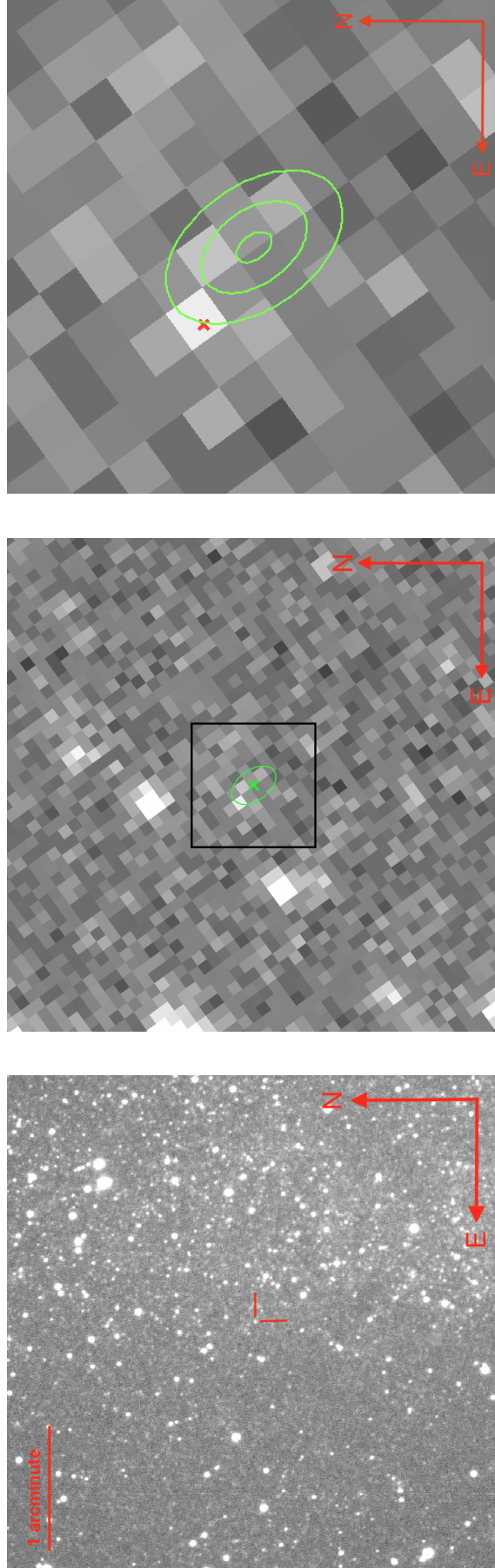


FIGURE 2.11: The location of the nova in an LT image and in archival HST images before the eruption. **Left:** Image of nova AT 2017fvz taken through a V-band filter with IO:O on the LT on 2017 Sep. 19.912. The dimensions of the image are approximately $4' \times 4'$. The position of the nova is indicated by the two red lines. **Middle:** Archival HST image from April 2007 of the nova field taken with the F814W filter. This image has dimensions $2'' \times 2''$ and the black box refers to the zoomed-in region in the right image. The green ellipse is the 5σ error on the location of the nova and the green cross is the location of the nova. **Right:** Zoomed-in region from the left image with dimensions $0.5'' \times 0.5''$. The green ellipses are 1σ , 3σ and 5σ errors centred on the location of the nova. The red cross is a nearby resolved source.

TABLE 2.6: *Hubble Space Telescope*/WFPC2 apparent magnitudes (Vega) of the nearby source. No source was detected in the F225W or F429W data.

Filter	Photometry
F170W	18.481 ± 0.480
F255W	–
F336W	20.982 ± 0.392
F439W	–
F555W	23.372 ± 0.201
F814W	22.259 ± 0.137

Additionally, a colour-magnitude diagram (shown Figure 2.12), based on the *HST* (ESA, 1997a,b) data was used to determine a limiting magnitude of the *HST* image of $m_{F814W} \simeq 23.5$. From the total number of sources found with DOLPHOT in the *HST* image, we removed any sources that were defined by DOLPHOT as not being a ‘bright star’ including ‘faint sources’, ‘elongated sources’, ‘hot pixels’ and ‘extended sources’. We also removed all sources with magnitude uncertainties > 0.3 . Using this, we computed the probability of a coincidental alignment to this limiting magnitude between the nova and the source within 5.14σ to be 18%, using the method described in Williams et al. (2016). This does not pass the criterion used by Williams et al. (2016) to determine if a source was the likely nova progenitor (probability of a chance alignment $\leq 5\%$). So, even though the resolved source is near the position of the nova, the uncertainties on the positional transformation and the coincidence probability indicate with high confidence that this is indeed a chance alignment.

2.4.5.4 SED of the source

Despite this low probability, we determined this source’s luminosity in the F814W, F555W, F336W and F170W filters and plotted a spectral energy distribution (SED) as shown in Figure 2.13 to explore whether this source could be a system capable of a nova eruption. The source is very bright in the NUV indicating that it is most likely to be an O or B star on a similar line of sight to the nova’s location and not the progenitor system. We have also presented SEDs from the multi-band photometry for a number of epochs throughout the nova’s decline which clearly illustrates the influence that the $H\alpha$ emission line has on the r' -band photometry. The last u' -band magnitude we have of the nova (approximately 103 days post-eruption) is consistent with the *HST* F336W filter (at around the same wavelength) so our late-time u' -band photometry is contaminated by this nearby (but blended from the ground) source. The late-time *Swift*/UVOT $uvw1$ photometry is similarly affected.

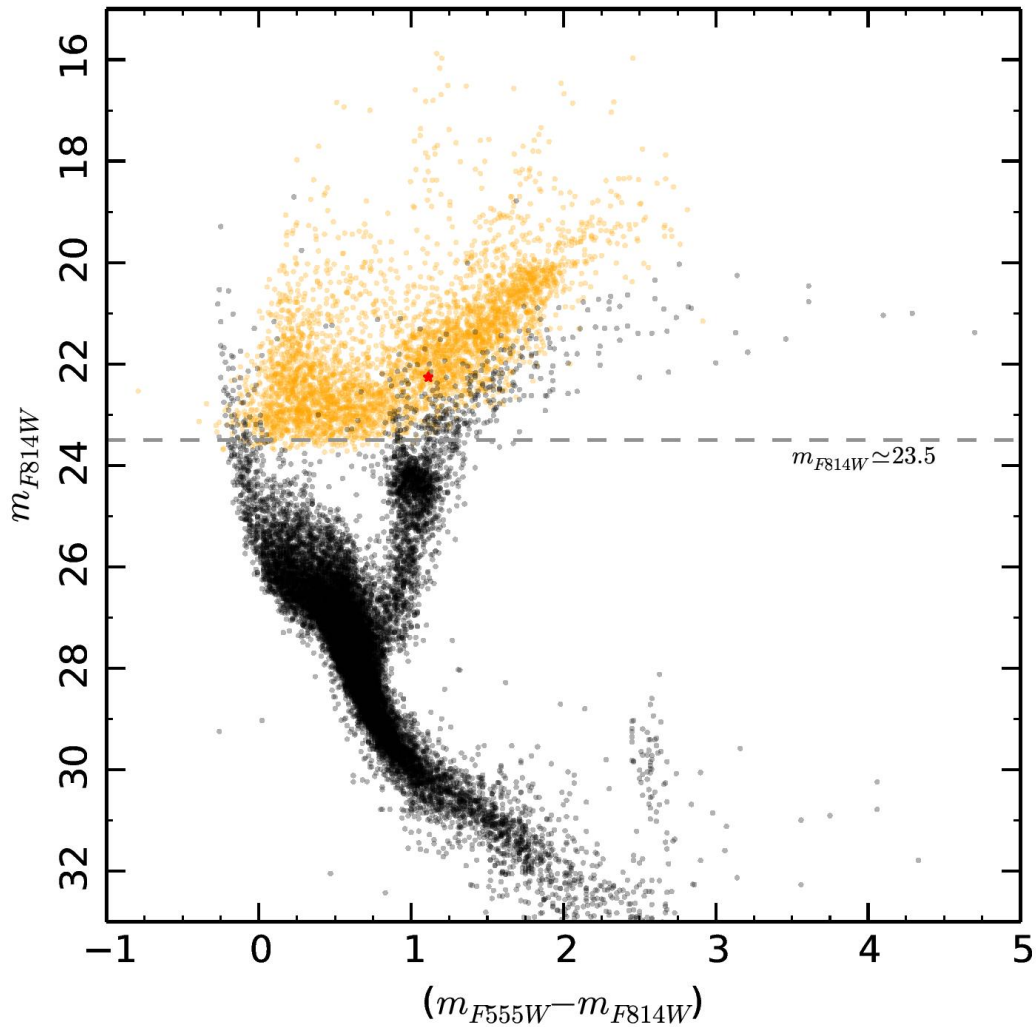


FIGURE 2.12: The orange points are all of the sources detected in the *HST* image (after we made the cuts as described in Section § 2.4.5.3) with their F814W absolute magnitude plotted against their (F555W – F814W). The black points are the stars from the Hipparcos catalogue shifted to the same distance as NGC 6822 and allowing for extinction. We have plotted the source’s position with a red star. We can see that the faintest objects detected in this image have apparent magnitudes of $m_{F814W} \simeq 23.5$ and therefore absolute magnitudes of $M_{F814W} \simeq -1$. The orange *HST* points between the main sequence and red giant branch (above the gap in the black Hipparcos points) are faint field stars in the line of sight towards NGC 6822.

A black-body fit to the SED (*HST* plus *Swift* data) of this source was carried out by Dr Matt Darnley (a co-author from [Healy et al., 2019](#)) and is consistent with the Rayleigh-Jeans tail of a black-body with $T_{\text{eff}} = 40000 \pm 8000$ K and $M \approx -10.1$ ($\chi_{\text{red}}^2 = 1.68$), at the distance of NGC 6822 and assuming $E(B - V) = 0.22$. Such a temperature and luminosity is consistent with an O-star within NGC 6822. However, the F814W photometry is significantly brighter than would be expected from such a star. This may indicate that there is additional redder source also on the same line of sight as the nova. We also cannot rule out an association with the nova other than the relatively high coincidence probability.

2.5 Discussion

2.5.1 The previous nova in NGC 6822

There has been one nova previously reported in NGC 6822, which was discovered independently by both [King & Li \(1999\)](#) with KAIT and [Wei et al. \(1999\)](#) with the Beijing Astronomical Observatory (BAO) Supernova Survey. That nova, located at $\alpha = 19^{\text{h}}45^{\text{m}}0^{\text{s}}.31$, $\delta = -140'10''.3$ (J2000), was discovered by KAIT in unfiltered images taken on 1999 June 23.40 and June 23.44 with $m \approx 17.3$, and by BAO on June 23.69 and June 24.72 with an unfiltered magnitude of 18. The nova was then followed up on June 24.38 by LOSS with an unfiltered apparent magnitude of approximately 17.0 and by the Space Telescope Science Institute on June 26.08 and June 28.07 with *V*-band apparent magnitudes of 19.0 ± 0.1 and 19.6 ± 0.1 respectively ([Bakos & PLANET Collaboration, 1999](#)).

The 1999 nova was spectroscopically confirmed on July 9 using the Kast spectrograph on the 3m Shane telescope at Lick Observatory ([Filippenko, 1999](#)). If we assume that this nova's optical peak occurred on the day of discovery then this spectrum was taken on $t \sim 16$ d, comparable to $t = 14.040$ d and $t = 18.010$ d for our spectra of AT2017fvz. Therefore this spectrum is plotted in [Figure 2.14](#) alongside a combined spectrum of AT2017fvz from $t = 8.016$ d, $t = 14.040$ d and $t = 18.010$ d for comparative purposes.

Just as we see in the spectra of AT2017fvz, there are prominent Balmer lines and many of the same Fe II lines. Blueward of H β there is Fe II (37) at 4629 Å and 4666 Å and redward there is Fe II (42) at 4924 Å, 5018 Å and 5169 Å. The Fe II (74) multiplet is located to the blue of H α at 6148 Å, 6248 Å, 6417 Å and 6456 Å and again the emission line at 6156 Å is most likely to be O I (6158 Å). The Na I (D) and [O I]

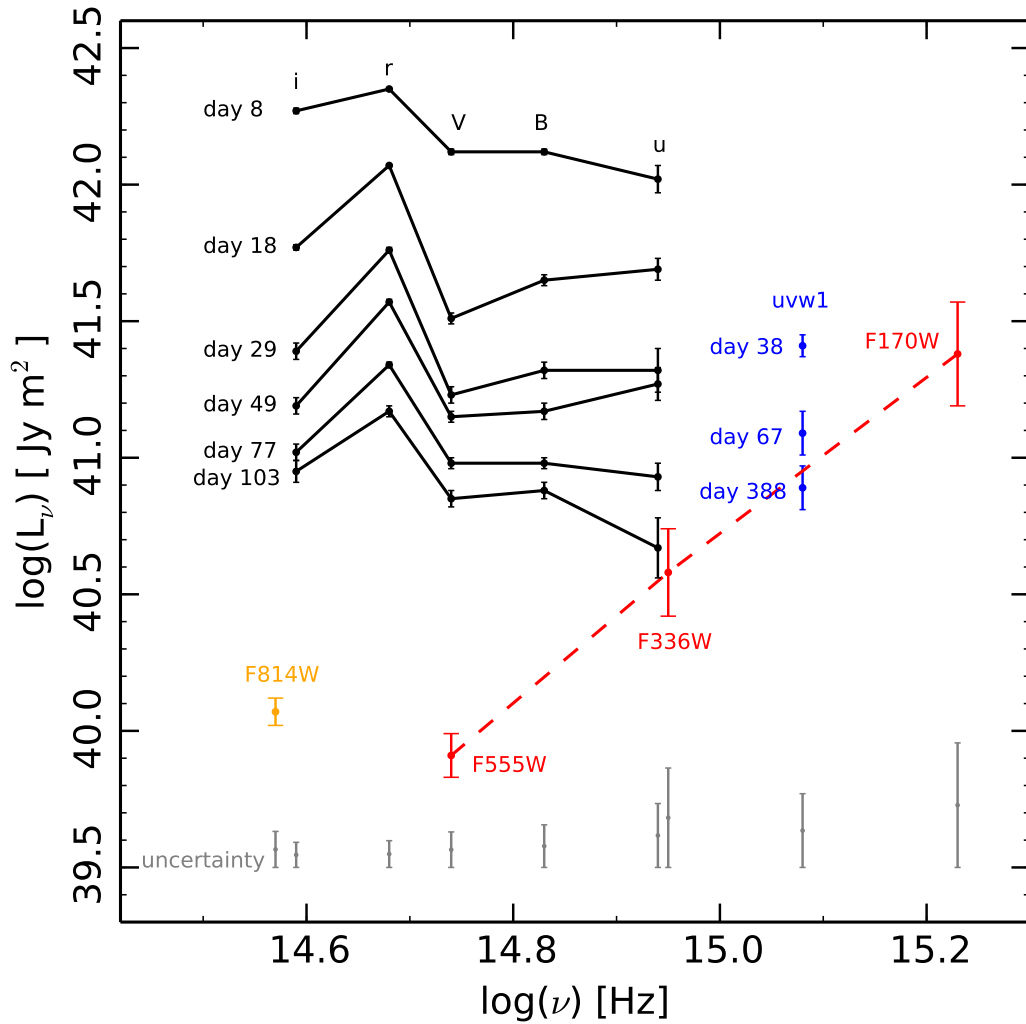


FIGURE 2.13: SED of AT2017fvz from 8 days to 103 days after the time of eruption and SED of the source within 5.14σ of the location of AT2017fvz. The black points are the SEDs of AT2017fvz in the $u'BVr'i'$ filters from LT observations. The blue points are from the *Swift* *uvw1* photometry of AT2017fvz. The red points are luminosities potentially associated with an O or B star derived from the *HST* F555W, F336W and F170W filters and the orange point is a luminosity from potentially another source derived from the *HST* F814W filter, with both being near the nova's location. The grey bars are the combined systematic uncertainties from the distance to NGC 6822 and the extinction in each filter below the associated filter.

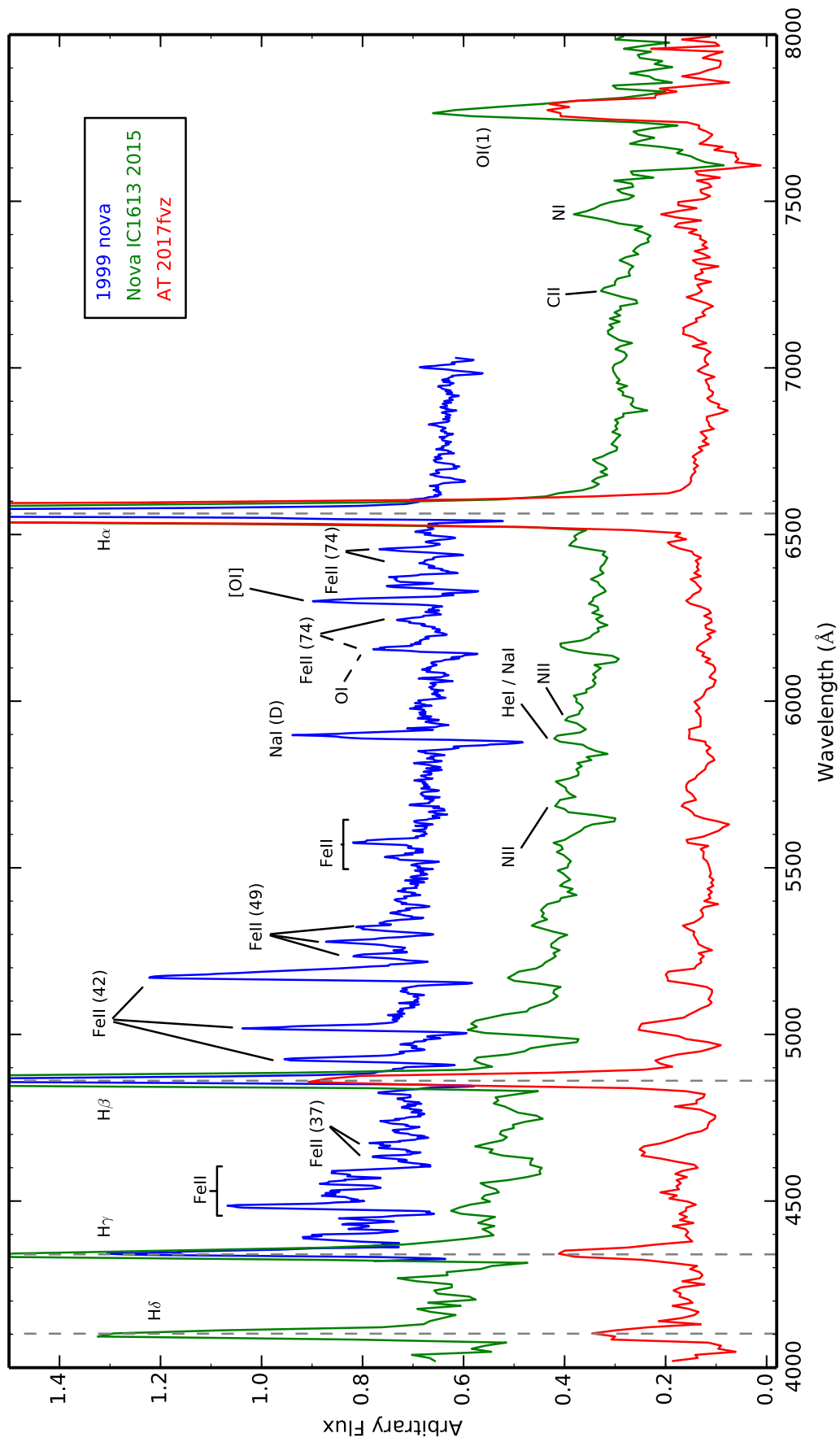


FIGURE 2.14: Combined spectrum of AT 2017fvz from $t = 8.016$ d, $t = 14.040$ d and $t = 18.010$ d for comparison with the spectrum of the 1999 nova taken on 1999 July 9 (~ 16 d after discovery) and a spectrum of Nova IC 1613 2015 taken 6.59 days after discovery.

TABLE 2.7: The emission line velocities in km s^{-1} from the spectra of the 1999 nova in NGC 6822 compared to the same emission lines as AT 2017fvz at $t = 14.040$ d.

Line identification	Wavelength [Å]	1999 nova	AT 2017fvz
H γ	4341	900 ± 120	2000 ± 200
Fe II (37)	4491	910 ± 60	–
H β	4861	970 ± 50	2100 ± 210
Fe II (42)	4924	840 ± 50	–
Fe II (42)	5018	840 ± 80	2200 ± 230
Fe II (42)	5169	1500 ± 110	–
Fe II(49)	5235	860 ± 30	–
Fe II (49)	5276	1120 ± 50	–
Fe II (49)	5326	1600 ± 150	–
Fe II	5533	840 ± 90	–
Fe II	5573	850 ± 60	–
Na I (D)	5892	800 ± 130	–
[O I]	6300	650 ± 40	–
H α	6563	830 ± 20	2300 ± 100

emission lines at 5892 \AA and 6300 \AA , respectively, are also present and much more apparent.

As well as the large number of Fe II lines between H β and H γ that were not clearly visible in the AT 2017fvz spectrum, we see the Fe II (49) multiplet at 5235 \AA , 5276 \AA and 5326 \AA to the red of the Fe II (42) multiplet. There are features in the spectrum at approximately 5533 \AA and 5573 \AA which may also be Fe II.

Many of the lines, such as Na I (D), Fe II (42) and the Balmer lines have P Cygni profiles indicating that this spectrum was taken as the nova transitioned from the fireball stage. Comparing this directly to the evolution of AT 2017fvz tells us that this 1999 nova was relatively slow which is also consistent with the much narrower emission lines created through slower ejecta velocities. See Table 2.7 for the emission line velocities of many of the prominent emission lines with the corresponding velocity for AT 2017fvz.

2.5.2 Comparison to novae in other galaxies

In addition to the comparison of the 1999 nova in NGC 6822, we can make comparisons with novae that have been found in other Local Group dwarf galaxies as well as with other relatively well studied Local Group galaxies such as M 31 and M 33.

2.5.2.1 IC 1613

Comparison to Nova IC 1613 2015 (Williams et al., 2017) is relevant as not only is AT2017fvz in a similar environment (a dwarf irregular galaxy) and has a similar peak absolute magnitude but the spectra were obtained with the same spectrograph, SPRAT. This removes any differences occurring in the spectra due to apparatus differences so a direct comparison of spectral lines can be made.

Though similar, AT2017fvz is a faster but dimmer nova than Nova IC 1613 2015 with a shorter V -band decline time (~ 8 d) than $t_2 \sim 13 \pm 2$ days and a fainter V -band absolute magnitude (-7.45) than $M_V = -7.93 \pm 0.08$. So as expected from a faster system, the nova in NGC 6822 has greater line velocities corresponding to faster ejecta velocities.

Each nova belongs to a different spectroscopic class as illustrated in Figure 2.14. Nova IC 1613 2015 was classified as a “hybrid” as it presents both He I and N II emission lines in its early decline spectra as well as a wealth of Fe II lines. These helium and nitrogen lines are absent in the spectra of the Fe II nova, AT2017fvz. We have one example of a “hybrid” nova in IC 1613 and two examples of Fe II novae in NGC 6822. Even though this is only a small sample, it illustrates that novae from different spectroscopic classes have been found in dwarf irregular galaxies.

2.5.2.2 The Magellanic Clouds

The LMC contains many novae (see, Shafter, 2013) and the SMC one (Mróz et al., 2016) that have similar characteristics to AT2017fvz. These are:

LMCN 1977-03a: This nova has similar characteristics to AT2017fvz as it is an Fe II nova with $t_{2,V} = 11$ d (compared to ~ 8 d) and with peak $M_V = -8.2$ (compared to -7.45 ; Canterna & Schwartz, 1977). However, it has an expansion velocity of 1400 km s^{-1} , from the mean value of the $H\alpha$ (FWHM = 1600 km s^{-1}) and [O I] (6300 \AA) emission lines (Canterna & Thompson, 1981), which is much slower than AT2017fvz.

LMCN 1995-02a: With a decline time of $t_{2,V} = 11.0 \pm 3.0$ d (Hearnshaw et al., 2004) and a peak absolute magnitude of $M_V = -8.5$, LMCN 1995-02a is a brighter Fe II nova than AT2017fvz even though it belongs to the same speed class (again with a much slower $H\alpha$ FWHM = 1500 km s^{-1} ; Shafter, 2013) – further validation that AT2017fvz may be a ‘faint and fast’ nova. It also appears to show a plateau in its optical light curve, similar to AT2017fvz, around 12 days after maximum (see

Figure 3 in [Hearnshaw et al., 2004](#)). Unlike AT 2017fvz which shows no evidence for a SSS phase, this nova was rediscovered as the third supersoft X-ray nova with an effective temperature of around 30 eV ([Orio & Greiner, 1999](#)) after originally being discovered by [Liller \(1995\)](#).

LMCN 2000-07a: [Greiner et al. \(2003\)](#) found, from an estimated time of maximum, that Nova LMCN 2000-07a had an absolute magnitude of $M_V = -8.2$. This is another example of a nova with a decline time similar to AT 2017fvz ($t_{2,V} = 8.0_{-3.5}^{+4.5}$ d; [Hearnshaw et al., 2004](#)) being much brighter at peak. [Duerbeck & Pompei \(2000\)](#) reported that the spectrum taken around a week after maximum showed Balmer emission lines with $\text{FWHM} = 1700 \text{ km s}^{-1}$, a Na I (D) emission line and a number of Fe II multiplets also seen in the early spectrum of AT 2017fvz such as 42, 37 and 74 as well as 38, indicative of a Fe II nova. Just like AT 2017fvz, there was no supersoft X-ray phase found for this nova ([Greiner et al., 2003](#)). It is therefore suggested that the SSS phase must have been shorter than 7 weeks or the effective temperature of the WD was below ~ 10 eV in order for the SSS to not be observable.

LMCN 2002-02a: Nova LMCN 2002-02a was found to have a V -band decline time of $t_{2,V} = 12.0$ d by [Mason et al. \(2005b\)](#) which they then used with a MMRD relation to find an peak absolute magnitude of $M_V = -8.6$. The early spectra (6 and 11 days past maximum) indicate that this is another Fe II nova. They show prominent Balmer lines and strong Fe II multiplets such as 42, 49, 37 and 38 as well as the Na I (D) emission line at 5892 \AA (see Figure 4 in [Mason et al., 2005b](#)). The late spectrum taken 161 days post-maximum shows the same nebular [O III] emission lines as AT 2017fvz at 4959 and 5007 \AA but much stronger. Along with a high expansion velocity of 2150 km s^{-1} , this nova stands out as being the closest to AT 2017fvz with respect to all of its properties.

SMCN 2005-08a: With an I -band decline time of $t_2 = 14 \pm 2$ d ([Mróz et al., 2016](#)), this nova is similar to AT 2017fvz which has $t_{2,i'} \sim 13$ d. This nova had a peak V -band apparent magnitude of 10.4 ([Schwarz et al., 2011](#)) which we used with $\mu_0 = 18.95 \pm 0.07$ ([Graczyk et al., 2014](#)) and $A_V = 0.11 \pm 0.06$ ([Aydi et al., 2018a](#)) to determine a peak V -band absolute magnitude of -8.66 ± 0.09 , much brighter than AT 2017fvz. SMCN 2005-08a is an Fe II nova with the usual spectrum dominated by Balmer lines, Fe II (42) and Fe II (74) multiplets and Na I (D) emission lines ([Mason et al., 2005a](#)). Its Balmer lines were very broad with an average $\text{FWHM} \sim 3200 \text{ km s}^{-1}$ with [Mason et al. \(2005a\)](#) also noting marginal evidence of a P Cygni absorption component to the blue of the $\text{H}\beta$ emission line possibly indicating an expansion velocity of 2100 km s^{-1} . As with AT 2017fvz, there were no X-rays detected 219 days post-maximum ([Schwarz et al., 2011](#)).

2.5.2.3 M 31 and M 32

As previously mentioned, most (82%) of the novae in M 31 belong to the Fe II spectral class. Using the cumulative t_2 distribution plot of M 31 novae from Williams et al. (2016), we can say that AT 2017fvz would belong to the fastest 10 per cent of novae. It is therefore a relatively fast Fe II nova with respect to those in M 31, backed-up by the collection of M 31 nova properties in Shafter et al. (2011). All of the other novae in M 31 from Williams et al. (2016) that are faster belong to the He/N or “hybrid” class placing this nova at the edge of the classification scheme. The few novae belonging to the Fe II spectroscopic class with decline times similar to AT 2017fvz are:

M31N 2004-11a: This nova has a peak absolute R -band magnitude $M_R = -8.04 \pm 0.25$ (compared to $M_{r'} = -7.72 \pm 0.06$) and an R -band decline time of $t_{2,R} = 19.1 \pm 1.9$ (compared to $M_{r'} = 15.5 \pm 0.4$). However, the FWHM of the $H\alpha$ and $H\beta$ emission lines are significantly smaller: 1580 km s^{-1} and 1230 km s^{-1} , respectively (Shafter et al., 2011).

M31N 2006-10b: M31N 2006-10b has $M_V = -7.98 \pm 0.11$ and a V -band decline time $t_{2,V} = 5.8 \pm 0.3$ – similar to AT 2017fvz. However, it does not belong to the Fe II spectral class but is a “hybrid”. Its spectrum changed from showing many Fe II lines ~ 1 day post-discovery to a typical He/N nova spectrum ~ 3 weeks later (Shafter et al., 2011). This difference in spectroscopic class to AT 2017fvz may be the result of the much larger ejecta velocities ($H\alpha$ and $H\beta$ emission lines had $\text{FWHM} > 3000 \text{ km s}^{-1}$).

M31N 2007-11d: This is a much brighter nova than AT 2017fvz with $M_V \simeq -9.5$ even though it has a similar decline time, $t_{2,V} \sim 9.5$ days (Shafter et al., 2009). Other similarities include its early spectrum showing the $H\alpha$, $H\beta$, $H\gamma$ and Fe II (42) emission lines indicative of a Fe II nova with $\text{FWHM} \sim 2300 \text{ km s}^{-1}$ and some P Cygni profiles.

M31N 2009-10b: The nova M31N 2009-10b has spectral type Fe II with $t_{2,B} = 8.0 \pm 0.2 \text{ d}$ and $t_{2,V} = 8.9 \pm 0.2 \text{ d}$, comparable to AT 2017fvz. However, it was much brighter with a peak $M_V = -9.68 \pm 0.11$. As discussed in Section § 2.5.5, this is close to the absolute magnitude we would have expected AT 2017fvz to have with its associated decline time (Shafter et al., 2011).

M32N 2004-01a: Neill & Shara (2005) found ‘M 32 nova 1’ in the dwarf galaxy M 32, a satellite of M 31, and found it to have a V -band decline rate, $t_2 \sim 31$ days. Their Figure 6 (a spectrum taken eight days post-discovery), shows the same Fe II lines alongside the $H\beta$ line as the spectrum of AT 2017fvz in Figure 2.7, which is also eight days after the time of eruption.

2.5.2.4 M 33

There are a number of novae that reside in M 33 (Shafter et al., 2012a) with which we can make comparisons to AT 2017fvz as they belong to the same spectroscopic class. Unfortunately, only one of these has light curve properties which would enable a direct comparison:

M33N 2007-09a: This nova belongs to the ‘very fast’ fading speed class with $t_{2,B} = 11.0 \pm 0.3$ and $t_{2,V} = 5.9 \pm 0.2$ but has a brighter peak absolute magnitude of $M_V = -8.93 \pm 0.15$. Its spectrum includes Balmer emission lines and a number of He I and N II lines placing it in the He/N category. The FWHM of the H α and H β lines are 4800 km s^{-1} and 4260 km s^{-1} , respectively, which as expected for a He/N nova are much larger than the Fe II nova AT 2017fvz (Shafter et al., 2012a).

From these examples of novae in other dwarf irregular galaxies, we can build up an argument for AT 2017fvz being atypical. Of all the fast Fe II novae we have identified, AT 2017fvz is the only one that has relatively high velocity ejecta *and* is substantially ‘under-luminous’. However, the lack of an X-ray detection may be a common theme among novae in dwarf irregular galaxies.

2.5.3 Nova rate in NGC 6822 and IC 1613

From the LSNR relationship given in Section § 1.3, we would expect the nova rate for NGC 6822 to be 0.0855 yr^{-1} by using $L_K = 3.8 \times 10^8 L_\odot$ (Weldrake et al., 2003) and the nova rate for IC 1613 to be $0.027 \pm 0.001 \text{ yr}^{-1}$ by using the K -band magnitude of 7.43 (Karachentsev et al., 2013). These have been plotted on Fig 2.15, which is a reproduced Figure 1 from Shafter et al. (2014), showing the dependence of a galaxy’s nova rate on its K -band luminosity¹¹. As mentioned previously, two novae have been observed in NGC 6822 (King & Li 1999 and this work) and three novae have been observed in IC 1613 (see Williams et al. 2017 for more details), therefore we cannot produce a meaningful nova rate to compare this prediction to.

2.5.4 The lack of X-rays

We do not detect X-ray emission from AT 2017fvz with any of the five *Swift* observations. This gives us two scenarios; either the emission was not detectable, or it was detectable but we did not observe the system at the correct time.

¹¹An modified version of Fig 2.15 with updated nova rates is presented in Darnley & Henze (2020).

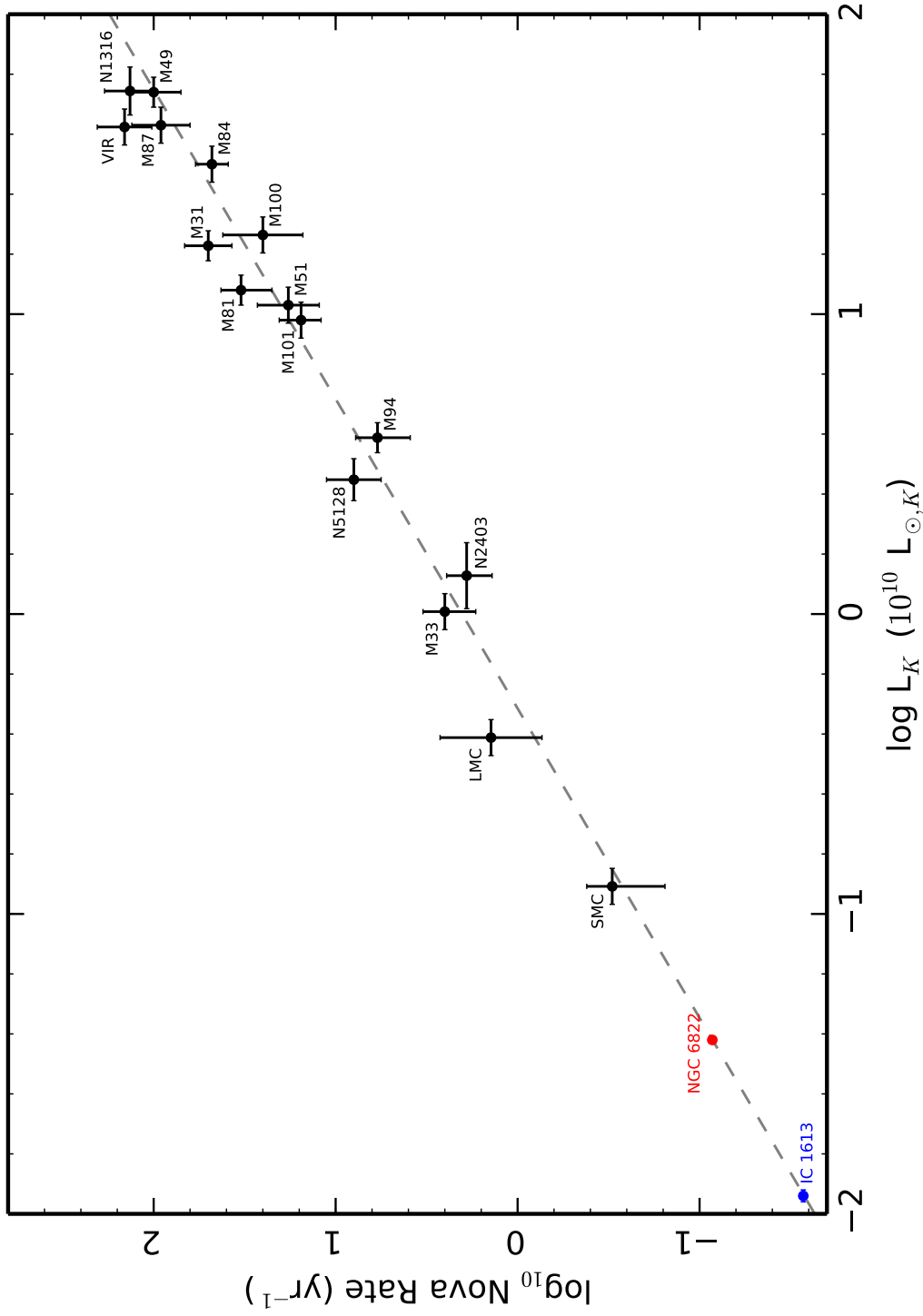


FIGURE 2.15: This is a reproduced plot of Figure 1 from Shafter et al. 2014 which shows the dependence of a galaxy's nova rate on its K -band luminosity. NGC 6822 and IC 1613 are shown in red and blue respectively. The nova rate of these two galaxies have been derived from the LSNR relation.

There are a number of reasons why the X-rays emanating from the surface of the WD may not have been detectable. One option is that the X-ray emission may have ceased before the ejecta surrounding the nova were optically thin enough to permit observation, i.e. $t_{\text{off}} < t_{\text{on}}$.

The other option is that the SSS may have been too faint to be detected, with an upper limit of the X-ray luminosity being $4 \times 10^{36} \text{ erg s}^{-1}$. This is potentially explained by the low metallicity environment of NGC 6822. Depending upon the amount of mixing between the accreted envelope and the underlying WD, the metallicity of the accreted shell will either only weakly (strong mixing) or strongly (little mixing) depend upon the metallicity of the donor. As the TNR operates via the hot-CNO cycle, a lower metallicity shell might therefore be expected to produce a lower luminosity, but longer lived SSS phase. In such a scenario, low metallicity alone might explain the lack of any X-ray detection.

Alternatively, if the X-ray emission was in principle detectable, then the reasons for not observing this SSS phase revolve around the timing of the observations. It may also indicate that the [Henze et al. \(2014a\)](#) correlations used to predict t_{on} and t_{off} (derived from CNe in M 31) are not valid in the lower metallicity environment of NGC 6822 (see, e.g., [Williams et al., 2017](#)). Firstly, the supersoft X-ray source may occur after 388 days (our last *Swift* observation) so we have simply observed too early, indicative of a high mass ejecta and also a low mass WD. Secondly, the whole SSS phase may have taken place within one of the observing gaps, either between 38 d and 67 d, between 67 d and 97 d, between 97 d and 268 d, or between 243 d and 388 d. Though unlikely, there are examples of very short SSS phases in fast novae such as M31N 2007-12d with an extremely short SSS phase of < 20 d ([Henze et al., 2011](#)). Finally, the most tantalising option is that the entire SSS took place before our first *Swift* observation, 38 days post-eruption. This would tell us that we had low mass ejecta and a high mass WD and are potentially dealing with a recurrent nova.

2.5.5 A possibly ‘faint and fast’ or recurrent nova?

With $t_{2,V} = 8.1 \pm 0.2$ d, AT 2017fvz is a ‘very fast’ fading nova. We calculated from the MMRD relations in [Downes & Duerbeck \(2000\)](#) an expected peak V -band absolute magnitude of $M_V \approx -9$, but with a peak absolute magnitude in the range $-7.41 > M_V > -8.33$ mag, AT 2017fvz may be substantially fainter than ‘expected’. Given this range, and after accounting for expected differences between the V -band and g

filters (see, [Shafter et al., 2009](#)), AT 2017fvz would lie below the MMRD (broadly consistent with the position of M 31N 2008-11a) as presented by [Kasliwal et al. \(2011\)](#) (see their Figure 12 in the bottom left panel of Figure 1.6), which plots six ‘faint and fast’ novae by their t_2 and their peak absolute g -band magnitude. Here we suggest caution, as the upper end of this range (high internal extinction contribution and missed light-curve peak) is marginally consistent with the MMRD. We also note that [Kasliwal et al. \(2011\)](#) employed the Balmer decrement to correct for extinction towards many of their M 31 novae; however Case B recombination is not valid in the early stages of nova evolution (see, [Williams et al., 2017](#), for a discussion).

The ‘faint and fast’ region of the MMRD phase space is populated by a number of Galactic (see Figure 13 in [Kasliwal et al., 2011](#)) and M 31 RNe. [Pagnotta & Schaefer \(2014\)](#) defined a number of key indicators for a RN masquerading as a CN (i.e., only one observed eruption). AT 2017fvz satisfies some of these; for example the short t_2 implies the presence of a high-mass WD. The high ejecta velocities (for an Fe II nova) inferred from the H α emission line ($2430 \pm 70 \text{ km s}^{-1}$) further reinforce this suggestion.

Additionally, there is a plateau in the optical light curve from around day 25 to day 45. It has been proposed that such plateaus are produced by the SSS irradiating a reformed, or surviving, accretion disc and the donor. The subsequent reprocessed optical light then dominates the light emitted by the nova ejecta, temporarily halting the decline of the light curve ([Hachisu et al., 2000](#); [Evans et al., 2008](#); [Darnley et al., 2016](#)). This could indicate that the accretion disc survived the eruption, pointing to a high accretion rate and/or low ejected mass – a reasonable indicator of an RN. However, it does not provide strong evidence in isolation. Additionally, the spectrum obtained during the plateau shows no evidence for narrow (or any) He II lines, a key signature of a hot disc (as is seen during the plateau phase of known RNe; e.g. [Henze et al., 2018a](#)).

The other criteria suggested by [Pagnotta & Schaefer \(2014\)](#) require either far superior spectroscopy or identification of the quiescent system. AT 2017fvz matches all their RN indicators that we can reasonably test. The lack of a detected progenitor also indicates the absence of a luminous accretion disc, therefore at most only a modest accretion rate. Even if this system were a RN, it certainly would not be a short-cycle recurrence system.

2.6 Summary and Conclusions

In this chapter, we have presented observations and analysis of AT 2017fvz, the second spectroscopically confirmed nova to be observed within the Local Group dwarf irregular galaxy NGC 6822. We carried out detailed photometric and spectroscopic observations of the nova from its initial rise through to the nebular phase. To summarise as follows:

1. We conducted observations of the nova AT 2017fvz with ground-based photometry with ASAS-SN, ATLAS, KAIT, and the LT, spectroscopy with the LT, and NUV and X-ray observations with *Swift*.
2. AT 2017fvz has peak absolute magnitudes of $M_V = -7.45 \pm 0.07$ and $M_{r'} = -7.72 \pm 0.06$.
3. With $t_{2(V)} = 8.1 \pm 0.2$ d and $t_{3(V)} = 15.2 \pm 0.3$ d, AT 2017fvz is a ‘very fast’ nova.
4. AT 2017fvz belongs to the Fe II spectroscopic class. We also see the usual Balmer lines throughout as well as nebular lines such as [O III] developing in the final spectrum.
5. Tentative evidence for a H δ P Cygni profile is seen in the first spectrum taken 8 days post-eruption, possibly indicating the end of the fireball stage.
6. The FWHM of the H α emission line progressively narrows from 2430 km s^{-1} to 1840 km s^{-1} over ~ 35 d and then remains constant in the final nebular spectrum at ~ 70 days.
7. We see a plateau in the optical light curve from around day 25 to day 45 which may indicate the presence of a surviving or re-formed accretion disk.
8. We did not detect any X-rays between days 38 and 388 indicating that the SSS may have occurred within the first ~ 40 days, or that it was obscured by the ejecta, or was simply too faint to be detectable.
9. There is a source near to the location of AT 2017fvz seen in archival *HST* data. However, it is probably an unassociated O-star.
10. The low luminosity and rapid decline indicate that AT 2017fvz may be a ‘faint and fast’ nova.
11. Additionally, the low luminosity, rapid decline, plateau phase, and potentially short (but unconfirmed) SSS phase are all pointers to a potential RN. Any recurrent nature can only be confirmed by a second eruption.

With AT 2017fvz being the second nova to be spectroscopically confirmed within NGC 6822, we have been able to study another object within a dwarf irregular galaxy – not a typical environment compared to the majority of novae observed within the Local Group. Focusing on novae in other less studied environments such as this will allow us to build up a picture of how they can affect the properties of novae.

Chapter 3

Photoionisation Analysis of Nova Super-remnant

3.1 Introduction

There were a number of alternate sources for the vast nebulosity surrounding the most rapidly recurring nova, M 31N 2008-12a (see Section § 1.4.5). These include a supernova remnant (SNR), a superbubble or a fossil H II region. In order to rule out these other possibilities and thus justify the proposed shaping mechanism coming from many past eruptions, [Darnley et al. \(2019a\)](#) took each scenario in turn. Here I will describe each of the alternatives and explain in detail the possible source in which I contributed towards excluding in [Darnley et al. \(2019a\)](#): a fossil H II region.

3.2 A supernova remnant

One consideration is that the nova super-remnant visible around 12a is a supernova remnant, the remaining ejected material from a previous stellar explosion. An important class of SNR, which are referred to as ‘forbidden-line SNR’ in [Braun & Walterbos \(1993\)](#), can be identified from the ratio of the [S II] (forbidden singly ionised sulphur) emission lines at 6716 Å and 6731 Å to H α being greater than approximately 0.4.

As can be derived from the spectroscopy of the NSR’s outer shell, given in Figure 3.1, the ratio of [S II]/H α > 0.5. This is marginally consistent with that of a supernova remnant candidate (see Figure 3.2 from [Kniazev et al. 2008](#) as well as [Sasaki et al. 2012](#) and [Long et al. 1990](#)) however the absence of strong emission from [O I] and

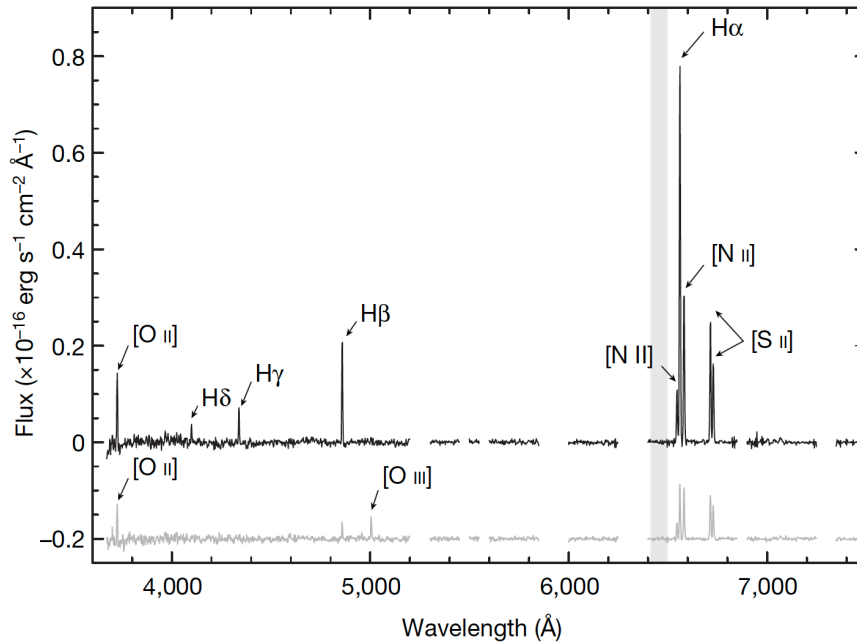


FIGURE 3.1: Spectroscopy of the outer shell of the nova super-remnant surrounding M 31N 2008-12a. The top (black) spectrum is from the bright western part of the NSR and the bottom (grey) spectrum is from the inner eastern knot, both taken with the Gran Telescopio Canarias (GTC). Taken from [Darnley et al. \(2019a\)](#).

[O III] ([Darnley et al., 2015a, 2019a](#)), associated with collisional ionisation ([Braun & Walterbos, 1993](#)), suggests that the outer shell seen around 12a is not a SNR.

Additionally, the spherically expanding blast-wave from the supernova excavates the surrounding interstellar medium; creating a cavity containing a very low-density and high temperature environment that emits soft X-ray radiation ([Sasaki et al., 2012](#)). Synchrotron radiation from relativistic electrons and heavier particles, in the form of radio and X-ray emission, can also be detected from these SNRs ([Sasaki et al., 2012](#)). Utilising the *XMM-Newton* large programme survey of M 31; archival radio surveys; *UBVRI* band images of the LGGS ([Massey et al., 2006](#)) as well as H α , [S II] and [O III] emission-line images, [Sasaki et al. \(2012\)](#) obtained a list of 26 X-ray SNRs and an additional 20 candidates belonging to M 31 and did not suggest that the NSR surrounding 12a was a supernova remnant, even though it was located within their survey area. [Walterbos & Braun \(1992\)](#) also identify the region where the NSR is located to be a region of diffuse emission.

Finally, there is no significant X-ray emission detected from the NSR in available *XMM-Newton* archival observations. The count-rate upper limit of 6.74×10^{-4} counts per second ([Darnley et al., 2019a](#)) is three times fainter than the typical count-rates from detected M 31 SNRs in [Sasaki et al. \(2012\)](#), leading to the conclusion that the nebulosity spatially coincident with M 31N 2008-12a is not a supernova remnant.

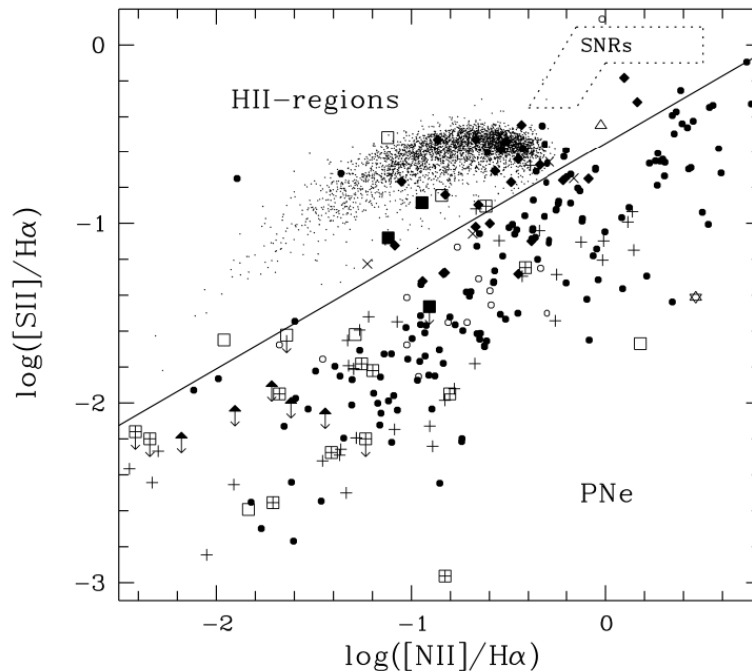


FIGURE 3.2: $[\text{S II}]/\text{H}\alpha$ ratio vs $[\text{N II}]/\text{H}\alpha$ ratio. Supernova remnants inhabit the region as indicated with the dashed line. The $[\text{S II}]/\text{H}\alpha$ ratio from the outer shell of the 12a’s NSR is marginally consistent with this. Taken from Figure 4, “Spectroscopy of two PN candidates in IC 10” (Kniazev et al., 2008).

3.3 A superbubble

A superbubble, also known as a supershell or ISM bubble, is a cavity created within the local ISM by the stellar winds from the most massive stars with spectral types of O and B, as well as supernova explosions (Tomisaka & Ikeuchi, 1986; McCray, 1988). These massive stars usually belong to groups named OB associations, leading to the merging of individually created wind bubbles. Fuel is then rapidly depleted in these massive stars with the resulting supernova adding to the expansion of the already formed superbubble. An example of this type of phenomena, known as Henize 70 (a.k.a N70 or DEM301), residing in the LMC, is shown in Figure 3.3.

Ultraviolet imaging of the NSR with the *HST* would be able to easily detect OB stars responsible for growing a superbubble. However, there is an absence of these within the nebulosity with the accretion disk surrounding 12a remaining the brightest UV source, thereby straightforwardly ruling out this possibility (Darnley et al., 2019a).

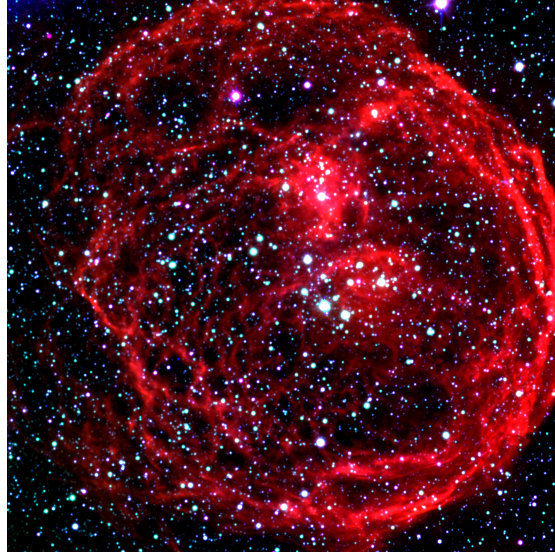


FIGURE 3.3: Composite image of Henize 70, a superbubble in the Large Magellanic Cloud, approximately 300 light years in diameter. Image credit: ESO.

3.4 A fossil H II region

A typical H II region is a region of interstellar hydrogen that has been ionised by early type stars, with surface temperatures of $\sim 50,000$ K (Kahn, 1974), emitting huge amounts of ultraviolet radiation. However, after the ionising source has ceased and thus loses influence over the surrounding gas, the atomic hydrogen within this H II region begins to recombine. This once ionised region becomes a fossil H II region (Nagakura & Omukai, 2005).

Clearly, the recurrent nova eruptions emanating from 12a will form a dynamic remnant from the ejected material and a photoionisation region from the copious amounts of X-ray emission. But, in order to determine if the NSR is either a previously formed H II region no longer being ionised or a dynamically expanding shell being swept up by many previous nova eruptions, we should calculate the size of a fully ionised sphere that would grow from the radiation of the system's nova eruptions. This Strömgren sphere (Strömgren, 1939) would grow until the recombination rate equals the ionisation rate and becomes static. Strömgren analysis is only valid when the recurrence period is much less than the recombination time ($P_{\text{rec}} \ll T_{\text{recomb}}$) as in this scenario, the nova is acting as a source of constant ionising radiation. On the other hand, if $P_{\text{rec}} > T_{\text{recomb}}$, all of the medium surrounding the nova would have sufficient time to recombine before the next nova eruption, so we would observe the effects of a single flash ionisation.

Before considering this Strömgren sphere, we will briefly outline when it is valid to use Case A or Case B recombination. Case A recombination describes a scenario

where a nebula is optically thin to ionising radiation such that recombination to the ground state results in ionising photons escaping the nebula. Case B recombination describes a scenario where a nebula is optically thick to ionising radiation, such that when recombination to the ground state occurs, the resultant ionising photons are immediately absorbed and remain confined to the nebula, with the effective recombination rate being zero. Even though Case B recombination is not considered to be valid for the evolution of novae in their early stages due to the environment of collisional excitation (Case A and B recombination are assumed to be collisionless), as discussed in [Williams et al. \(2017\)](#), we will use it for this derivation as an approximation because it is the closest scenario we have from the two cases.

We begin with the radius of a Strömgren sphere¹ given as:

$$R_s = \left(\frac{3 S_\star}{4\pi n^2 \beta} \right)^{\frac{1}{3}}, \quad (3.1)$$

where S_\star is the ionising luminosity from the source in photons s^{-1} , n is the number of nucleons per m^3 (assumed to be all protons within the surrounding ISM) and β is the total recombination rate for Case B recombination (see discussion above) given as $\beta \approx 2 \times 10^{-16} \times T_{\text{ISM}}^{-0.75} \text{m}^3 \text{s}^{-1}$ (see, for example, [Dyson & Williams, 1980](#)), and T_{ISM} is the effective temperature of the ISM.

We will assume that the ionising radiation predominantly comes from the nova eruptions and therefore the UV radiation from the system's accretion disk and white dwarf make a negligible contribution. If we take the peak nova luminosity as $10^4 L_\odot$ ([Shara, 1989](#); [Yaron et al., 2005](#)), assume that the nova only emits ionising photons for two weeks of the year (the SSS timescale of each eruption; [Henze et al., 2018a](#)), and assume a spectrum of 15 eV photons (this is an overestimate as the blackbody effective temperature of M 31N 2008-12a is 120 eV), then this leads to an ionising luminosity of:

$$S_\star = \frac{10^4 L_\odot}{15 \text{ eV}} \times \frac{2}{52} = \frac{3.8 \times 10^{37} \text{ erg s}^{-1}}{2.4 \times 10^{-11} \text{ erg}} \times \frac{2}{52}$$

$$\therefore S_\star = 6.2 \times 10^{46} \text{ photons s}^{-1}.$$

Setting the ISM to be low density ($n = 1 \text{ cm}^{-3}$) and cold ($T = 90 \text{ K}$) leads to a recombination rate of:

$$\beta \approx 2 \times 10^{-16} \times T_{\text{ISM}}^{-0.75} \text{m}^3 \text{s}^{-1} = 2 \times 10^{-16} \times (90)^{-0.75} \text{m}^3 \text{s}^{-1}$$

$$\therefore \beta = 6.84 \times 10^{-18} \text{m}^3 \text{s}^{-1}.$$

¹See Appendix B for the derivation of this equation.

Substituting these values into equation 3.1 above:

$$R_s = \left(\frac{3}{4\pi} \frac{6.2 \times 10^{46} \text{ s}^{-1}}{(1 \times 10^6 \text{ m}^{-3})^2 (6.84 \times 10^{-18} \text{ m}^3 \text{ s}^{-1})} \right)^{\frac{1}{3}} = 1.29 \times 10^{17} \text{ m},$$

gives us a Strömgen radius of $R_s = 4.2 \text{ pc}$, much smaller than the NSR seen around M 31N 2008-12a. The time taken to ionise the volume of this sphere can be calculated by taking the inverse of the product of number density n and recombination rate β :

$$\tau_{\text{ion}} = \frac{1}{n\beta} = \frac{1}{(1 \times 10^6 \text{ m}^{-3}) \times (6.84 \times 10^{-18} \text{ m}^3 \text{ s}^{-1})} \approx 4600 \text{ years}.$$

We have initially considered a cold low density ISM, however if we were to consider that the NSR has formed from the nova eruptions, then the temperature of the surrounding ISM might be more akin to that seen around O-B stars, typically $\sim 10^4 \text{ K}$ (Anderson et al., 2009), and so:

$$\beta = 2 \times 10^{-16} \times (10^4)^{-0.75} \text{ m}^3 \text{ s}^{-1} = 2 \times 10^{-19} \text{ m}^3 \text{ s}^{-1}.$$

The resulting Strömgen radius in this case would be:

$$R_s = \left(\frac{3}{4\pi} \frac{6.2 \times 10^{46} \text{ s}^{-1}}{(1 \times 10^6 \text{ m}^{-3})^2 (2 \times 10^{-19} \text{ m}^3 \text{ s}^{-1})} \right)^{\frac{1}{3}} = 4.18 \times 10^{17} \text{ m},$$

or $R_s = 13.6 \text{ pc}$, within the same order of magnitude as the 67 pc radius of the NSR. The time taken to ionise this volume will be:

$$\tau_{\text{ion}} = \frac{1}{n\beta} = \frac{1}{(1 \times 10^6 \text{ m}^{-3}) \times (2 \times 10^{-19} \text{ m}^3 \text{ s}^{-1})} \approx 160,000 \text{ years}.$$

However, the ISM density considered so far is much lower than we might expect as 12a appears to be located in a star forming region of M 31, where n will be higher. Therefore, if we were to increase this to a more realistic $n = 100 \text{ cm}^{-3}$, we would create much smaller sub-parsec Strömgen spheres (see Table 3.1).

Next, even though we know that the SSS isn't continuously on, we could also derive an upper limit on the size of a photoionised region by assuming a continuous luminosity of $10^4 L_{\odot}$ from the nova. Similar to the earlier calculation, this would give us an ionising luminosity of $1.6 \times 10^{48} \text{ photons s}^{-1}$. For a high density ISM, the Strömgen sphere is on the order of 1 parsec (see Table 3.2), however for a very low density ($n = 0.1 \text{ cm}^{-3}$), cold ($T = 90 \text{ K}$) ISM, the region begins to reach the size of the observed NSR ($R_s = 57.4 \text{ pc}$). Evidently, the remnant we see is similar in size to

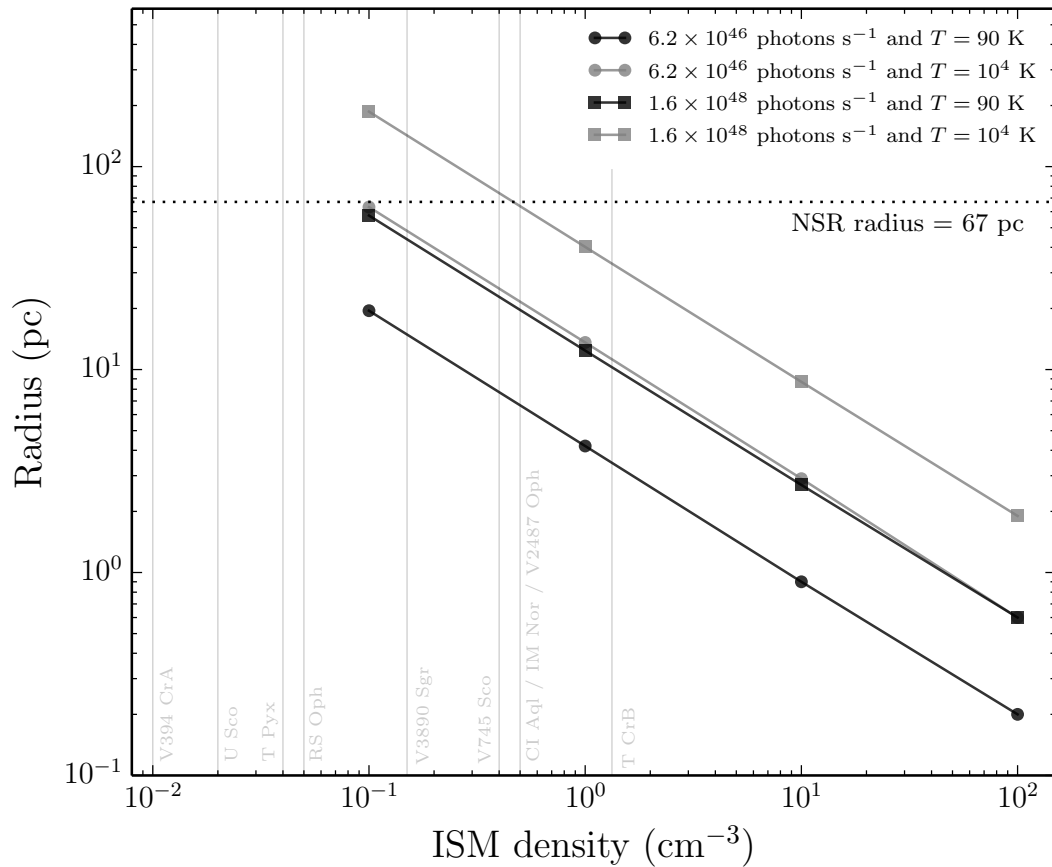


FIGURE 3.4: Radii of Strömgen spheres calculated with varying density ($n = 0.1 \text{ cm}^{-3}$, $n = 1 \text{ cm}^{-3}$, $n = 10 \text{ cm}^{-3}$ and $n = 100 \text{ cm}^{-3}$) and temperature of ISM ($T = 90 \text{ K}$ and $T = 10^4 \text{ K}$) for an ionising flux of $S_* = 6.2 \times 10^{46} \text{ photons s}^{-1}$ (circles) and as a continuous ionising flux from the nova of $S_* = 1.6 \times 10^{48} \text{ photons s}^{-1}$ (squares). The radius of the NSR is indicated with a dashed line. The estimated ISM density surrounding ten Galactic recurrent novae are indicated with vertical grey lines. These densities were estimated during a study (see Section § 5.3 for more detail) by the author, conducted after the work in [Darnley et al. \(2019a\)](#), to help with finding more examples of nova super-remnants.

a couple of these derived photoionised spheres, however we are using an unrealistic setup involving a nova continuously emitting ionising photons (see Figure 3.4). The only combination of parameters that result in a remnant approximately this size, given the lower ionising flux, requires an extremely low density ($n = 0.1 \text{ cm}^{-3}$) and hot ($T = 10^4 \text{ K}$) environment, possibly consistent with the pre-nova ISM density being less than $n = 50 \text{ cm}^{-3}$ ([Darnley et al., 2019a](#)).

Alternatively, as we know that the maximum radius of the NSR is 67 pc, we can derive a luminosity (assuming continuous ionising flux) of the nova needed in order for the sphere to grow this large. As before, we consider various densities of the ISM ($n = 0.1 \text{ cm}^{-3}$, $n = 1 \text{ cm}^{-3}$, $n = 10 \text{ cm}^{-3}$ and $n = 100 \text{ cm}^{-3}$) as well as cold ($T = 90 \text{ K}$) and warm ($T = 10^4 \text{ K}$) ISM. For example, starting with a Strömgen radius of

$R_s = 67 \text{ pc} = 2.1 \times 10^{18} \text{ m}$, with the characteristics of the local ISM being $n = 1 \text{ cm}^{-3}$ and $T = 90 \text{ K}$, we find the following luminosity:

$$S_\star = \frac{4\pi n^2 \beta R_s^3}{3} = \frac{4\pi}{3} (1 \times 10^6 \text{ m}^{-3})^2 (6.84 \times 10^{-18} \text{ m}^3 \text{ s}^{-1}) (2.1 \times 10^{18} \text{ m})^3$$

$$\Rightarrow S_\star = 2.7 \times 10^{50} \text{ photons s}^{-1} \times \left(\frac{2.4 \times 10^{-11} \text{ erg}}{15 \text{ eV photon}} \right) = 6.4 \times 10^{39} \text{ erg s}^{-1}$$

$$\therefore S_\star = 1.7 \times 10^6 L_\odot$$

From Table 3.3 we can see that the nova would need a luminosity ranging from $4.8 \times 10^2 L_\odot$ for a very low density ($n = 0.1 \text{ cm}^{-3}$) warm ($T = 10^4 \text{ K}$) ISM up to $1.7 \times 10^{10} L_\odot$ for a high density ($n = 100 \text{ cm}^{-3}$) cold ($T = 90 \text{ K}$) ISM to produce the remnant seen around 12a. Constraining these parameters from spectroscopy of the remnant such that $T < 9000 \text{ K}$ and $n = 50 \text{ cm}^{-3}$ (Darnley et al., 2019a), we find that the nova luminosity would have to be $1.3 \times 10^8 L_\odot$.

Furthermore, we can look at the overall morphology of the super-remnant. If we were solely seeing the fossilised result of a previously ionised Strömgen sphere, then we would expect to see a spherical structure, even with some irregularities taken into consideration. However, the nova super-remnant we see around 12a is an elliptical structure and it is unlikely that the surrounding ISM would act so preferentially to aid in growing a photoionised sphere into this shape.

TABLE 3.1: Radii of Strömgen spheres calculated with varying density and temperature of ISM with an ionising flux of $S_\star = 6.2 \times 10^{46} \text{ photons s}^{-1}$ to replicate the ionising photons being only produced for two weeks of the year.

	$n = 0.1 \text{ cm}^{-3}$	$n = 1 \text{ cm}^{-3}$	$n = 10 \text{ cm}^{-3}$	$n = 100 \text{ cm}^{-3}$
$T = 90 \text{ K}$	19.5 pc	4.2 pc	0.9 pc	0.2 pc
$T = 10^4 \text{ K}$	63.2 pc	13.6 pc	2.9 pc	0.6 pc

TABLE 3.2: Radii of Strömgen spheres calculated with varying density and temperature of ISM with a continuous ionising flux from the nova of $S_\star = 1.6 \times 10^{48} \text{ photons s}^{-1}$.

	$n = 0.1 \text{ cm}^{-3}$	$n = 1 \text{ cm}^{-3}$	$n = 10 \text{ cm}^{-3}$	$n = 100 \text{ cm}^{-3}$
$T = 90 \text{ K}$	57.4 pc	12.4 pc	2.7 pc	0.6 pc
$T = 10^4 \text{ K}$	186.6 pc	40.2 pc	8.7 pc	1.9 pc

TABLE 3.3: Nova luminosity (assuming continuous ionising flux) calculated with varying density and temperature of ISM with a Strömgen radius equal to the maximum radius of the NSR ($R_s = 67 \text{ pc} = 2.1 \times 10^{18} \text{ m}$).

	$n = 0.1 \text{ cm}^{-3}$	$n = 1 \text{ cm}^{-3}$	$n = 10 \text{ cm}^{-3}$	$n = 100 \text{ cm}^{-3}$
$T = 90 \text{ K}$	$1.7 \times 10^4 L_\odot$	$1.7 \times 10^6 L_\odot$	$1.7 \times 10^8 L_\odot$	$1.7 \times 10^{10} L_\odot$
$T = 10^4 \text{ K}$	$4.8 \times 10^2 L_\odot$	$4.8 \times 10^4 L_\odot$	$4.8 \times 10^6 L_\odot$	$4.8 \times 10^8 L_\odot$
$T < 9000 \text{ K}$	$5.3 \times 10^2 L_\odot$	$5.3 \times 10^4 L_\odot$	$5.3 \times 10^6 L_\odot$	$5.3 \times 10^8 L_\odot$

Of course, the photoionising radiation being emitted from the nova eruptions would have initially dominated and grown an early Strömgen sphere into the ISM. However, the calculations presented above alongside the current size of the NSR suggest that the *growth* of the NSR is now being dominated by the dynamics of the interacting ejecta. In other words, this nova super-remnant has been grown dynamically from the ISM being swept up by many millions of past recurrent nova eruptions into the structure we observe today.

Even so, further work by the author conducted after the study in [Darnley et al. \(2019a\)](#) shows that photoionisation still plays a role within these vast structures (see Section § 5.6). The radiation from the WD itself will influence the internal regions of the remnant and the high velocity shocks within the ejecta pile-up region will lead to highly ionising X-ray radiation, possibly aiding observation (see Section § 5.6).

3.5 Summary

We will finish this chapter by summarising the key points:

1. The nova super-remnant (NSR) around M 31N 2008-12a resembles a number of astrophysical phenomena.
2. An absence of strong emission from [O I] or [O III] and a lack of significant X-ray emission suggests that the NSR is not a supernova remnant.
3. A superbubble (or ISM bubble) would have a detectable OB star association so an absence of this type of system within the NSR ruled out this possibility.
4. Strömgen sphere analysis with characteristics of the local ISM and underlying nova system illustrated that photoionisation cannot be solely responsible for the creation of the NSR, but instead would require additional dynamical growth from many past eruptions colliding with the forming shell.

Chapter 4

Hydrodynamical Simulations of Recurrent Nova Super-Remnants

4.1 Introduction

The nova super-remnant surrounding M 31N 2008-12a owes its existence to the characteristics of the system with the high mass WD and high \dot{M} contributing to the rapidly recurring eruptions. It is therefore clear that we should see vast structures around other RNe with similarly short inter-eruption times (Darnley & Henze, 2020; Darnley, 2021). These remnants also offer another opportunity to find previously unknown RNe and rapidly recurring novae (RRNe), as well as finding ‘extinct’ nova systems in which the companion has ran out of material to donate (Darnley, 2021). Additionally, with the WD in these systems being close to the Chandrasekhar limit with the real possibility to explode as a SNIa, these phenomena also provide “a clear and *persistent signpost* to the progenitor-type of that SNIa” (Darnley, 2021), and deliver reasoning behind the absence of hydrogen in SNIa spectra through removing $\sim 10^6 M_{\odot}$ of mostly hydrogen away from the location of the upcoming event (Darnley, 2021).

Clearly, finding another nova super-remnant would have huge implications. However, the extent to which these shells grow will depend on underlying properties of the binary such as WD temperature, M_{WD} and \dot{M} , as well as density of the surrounding interstellar medium. Other factors will play a role in the observability of NSRs, such as metallicity, donor type, and line-of-sight inclination (Darnley, 2021), but these will not be addressed in this work.

In this chapter, we employ the same method as that in [Darnley et al. \(2019a\)](#) using hydrodynamical simulations to determine the growth of NSRs, but with a more realistic recreation of the evolution of the nova system. In Section § 4.2 we will describe in more detail the Morpheus code used to run the hydrodynamical simulations employed in this study and Section § 4.3 will detail the tests we performed before running our main simulations. We will describe the simple model used to generate simulation parameters in Section § 4.4, outline each of the separate runs in Section § 4.5 before presenting the results of these simulations with radiative cooling in Section § 4.6. We look closely at diagnostics of the reference simulation without and with radiative cooling in Section § 4.7 and compare our simulations to observations of the NSR surrounding M 31N 2008-12a in Section § 4.8. A number of post main simulation tests are described in Section § 4.9 before we finish the chapter by presenting a summary in Section § 4.10.

4.2 Hydrodynamical Simulations with Morpheus

As in [Darnley et al. \(2019a\)](#), the hydrodynamical simulations in this work were performed with the Morpheus program. This is an MPI-OpenMP Eulerian second-order Godunov simulation code with options of Cartesian, spherical and cylindrical coordinates, and includes radiative cooling and gravity¹. Morpheus combines well-established one-dimensional (Asphere; see [Vaytet et al., 2007b](#)), two-dimensional (Novarot; see [Lloyd et al., 1997](#)) and three-dimensional (CubeMPI; see [Wareing et al., 2006](#)) codes written by the Manchester-LJMU astrophysics groups into a single-framework. Additionally, we know that novae ejecta are not spherically symmetric (see Section § 1.2.6), however largely for computational reasons, we have assumed one-dimensional spherical symmetry for the purposes of these simulations, effectively modelling the bulk equatorial ejecta.

The systems are modelled in the same manner as given in [Darnley et al. \(2019a\)](#) with a red giant donor blowing a wind² interspersed with nova eruptions in the style of a top-hat function. Specifically, the characteristics of the blowing wind represents the base level for the majority of output from the underlying system, is instantaneously changed to represent the nova eruption before instantaneously lowering to the base level again after the outburst. Due to the spatial resolution of the simulations being larger than the expected orbital separation of the WD and the donor, we assume

¹We do not make use of gravity in our simulations as we start the ejected material outside of the Hill sphere such that it is already at terminal velocity.

²Although this is realistic for the 12a system (see Section § 1.4.4), it also has a useful computational side effect of not creating completely evacuated cavities between eruptions.

that they are spatially coincident at the origin and therefore interaction between the ejecta and the donor or accretion disk is ignored. The mass donor was assumed to be a red giant blowing continuously, except during nova eruptions, with a wind mass loss rate of $2.6 \times 10^{-8} M_{\odot}$ per year and a terminal velocity of 20 km s^{-1} , consistent with the companion star in the RS Ophiuchi system (Bode & Kahn, 1985). The ejecta from the nova eruptions we are simulating here, unless otherwise stated, are modelled as a wind with incrementally increasing mass-loss rates and velocities governed by the relationships determined from Yaron et al. (2005) models (see Section § 4.4.1 for more detail).

4.2.1 Are simulations required?

A simulation of 1,000 identical nova eruptions with a resolution of ~ 4 AU/cell determines how the density, pressure, velocity and temperature change throughout the whole shell over time. An example is shown in the left panel of Figure 4.1 illustrating shell structure after the 1,000 eruptions, along with the defined boundary locations and their names.

Crucially, with each simulation, we have thousands of snapshots showing the evolution of the nova shell. However, we can find a relationship analytically between the radius of the nova shell and time by implementing conservation of momentum as well as conservation of energy with each identical eruption that takes place.

Firstly, we know that the rate of momentum input from the nova outburst equals the rate of momentum increase of the shell. Also, the mass loss from the system, \dot{m} , is found simply by differentiating the input mass with respect to time. Therefore, we can state:

$$\dot{m}v = \text{constant} = (\dot{m}v)_{\text{shell}} = \frac{d}{dt} \left(\frac{4\pi}{3} r^3 \rho \dot{r} \right),$$

where \dot{m} is mass loss, v is ejection velocity, r is the radius of the shell and ρ is the density of the local ISM. The mass of the shell remains a constant as it grows as a result of being made up exclusively of the swept up material. Assuming that the rate of mass ejection of the system remains unchanged ($\dot{m} = \text{const}$) we find:

$$\int \dot{m}v dt = \dot{m}vt = \frac{4\pi}{3} r^3 \rho \dot{r} + A.$$

Setting the outer radius of the shell to be $r = 0$ when $t = 0$ sets $A = 0$. From here,

$$\dot{m}vt = \frac{4\pi}{3} r^3 \rho \dot{r} = \frac{4\pi}{3} r^3 \rho \frac{dr}{dt}$$

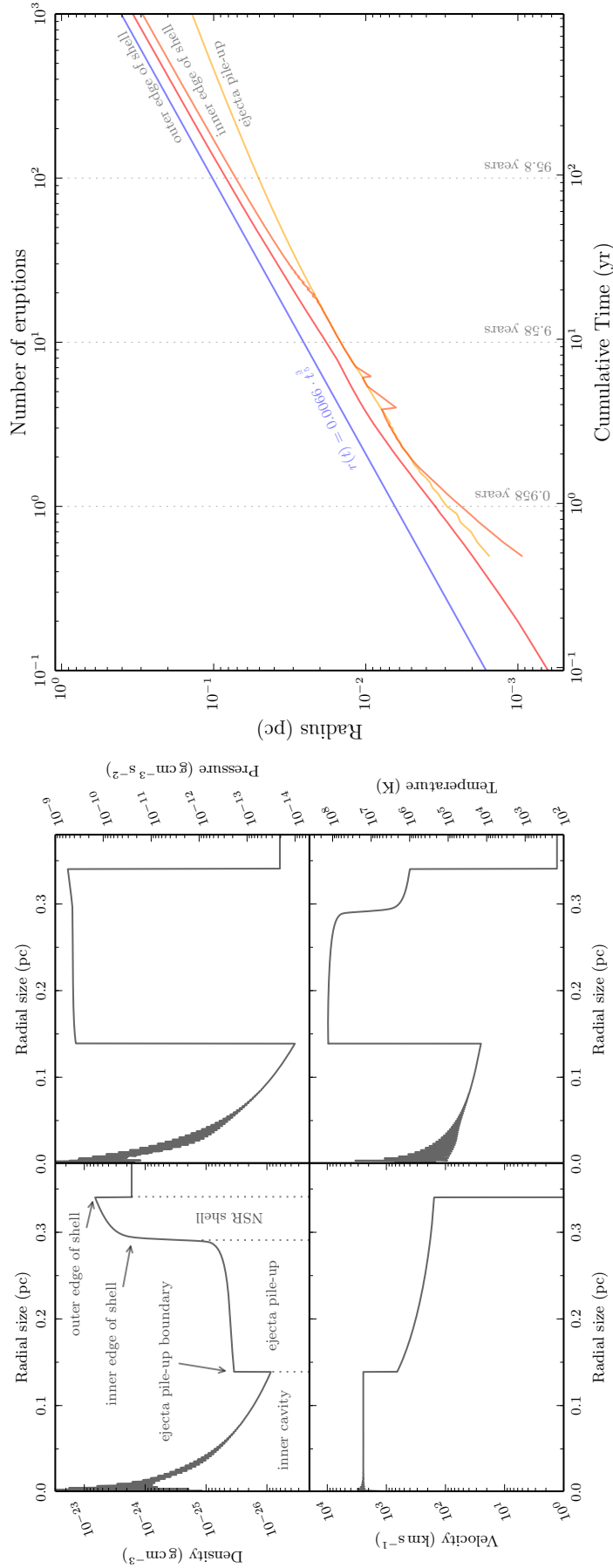


FIGURE 4.1: Left: Nova shell dynamics from 1,000 identical nova eruptions with shell boundaries defined. **Right:** The radial growth curve of the outer edge, inner edge and ejecta pile-up of the nova shell from 1,000 identical nova eruptions. The plotted power law is an analytical fit that is derived in the text.

$$\begin{aligned}\implies \dot{m}v \int t \, dt &= \frac{4\pi}{3}\rho \int r^3 \, dr \\ \implies \frac{\dot{m}vt^2}{2} &= \frac{4\pi\rho}{3} \frac{r^4}{4} + B.\end{aligned}$$

Again setting the outer radius of the shell to be $r = 0$ when $t = 0$ sets $B = 0$. This leads to the power law relation between radius (r) and time (t):

$$r = \left(\frac{3\dot{m}v}{2\pi\rho}\right)^{\frac{1}{4}} t^{\frac{1}{2}}. \quad (4.1)$$

Similar to earlier, we know that the rate of kinetic energy input from the nova outburst equals the rate of kinetic energy increase of the shell. Therefore, we can state:

$$\frac{1}{2}\dot{m}v^2 = \text{constant} = \left(\frac{1}{2}\dot{m}v^2\right)_{\text{shell}} = \frac{d}{dt} \left(\frac{1}{2} \cdot \frac{4\pi}{3} r^3 \rho \dot{r}^2\right) = \frac{d}{dt} \left(\frac{2\pi}{3} r^3 \rho \left(\frac{dr}{dt}\right)^2\right),$$

where \dot{m} is mass loss, v is ejection velocity, r is the radius of the shell and ρ is the density of the local ISM. Assuming that the rate of mass ejection of the system remains unchanged ($\dot{m} = \text{const}$) and the velocity of the ejecta remains the same ($v = \text{const}$) leads to:

$$\begin{aligned}\frac{1}{2}\dot{m}v^2 \int dt &= \frac{\dot{m}v^2 t}{2} = \frac{2\pi}{3} r^3 \rho \left(\frac{dr}{dt}\right)^2 \\ \implies \frac{3\dot{m}v^2 t}{4\pi\rho} &= r^3 \left(\frac{dr}{dt}\right)^2 \\ \implies \left(\frac{3\dot{m}v^2}{4\pi\rho}\right)^{\frac{1}{2}} t^{\frac{1}{2}} &= r^{\frac{3}{2}} \frac{dr}{dt} \\ \implies \left(\frac{3\dot{m}v^2}{4\pi\rho}\right)^{\frac{1}{2}} \int t^{\frac{1}{2}} dt &= \int r^{\frac{3}{2}} dr \\ \implies \left(\frac{3\dot{m}v^2}{4\pi\rho}\right)^{\frac{1}{2}} \frac{2}{3} t^{\frac{3}{2}} &= \frac{2}{5} r^{\frac{5}{2}} + C.\end{aligned}$$

Again setting the outer radius of the shell to be $r = 0$ when $t = 0$ sets $C = 0$:

$$\begin{aligned}\left(\frac{3\dot{m}v^2}{4\pi\rho}\right)^{\frac{1}{2}} \left(\frac{4}{9}\right)^{\frac{1}{2}} t^{\frac{3}{2}} &= \left(\frac{4}{25}\right)^{\frac{1}{2}} r^{\frac{5}{2}} \\ \implies \left(\frac{3\dot{m}v^2}{4\pi\rho} \cdot \frac{4}{9} \cdot \frac{25}{4}\right)^{\frac{1}{2}} t^{\frac{3}{2}} &= \left(\frac{25\dot{m}v^2}{12\pi\rho}\right)^{\frac{1}{2}} t^{\frac{3}{2}} = r^{\frac{5}{2}} \\ \implies r &= \left(\frac{25\dot{m}v^2}{12\pi\rho}\right)^{\frac{1}{2} \cdot \frac{2}{5}} t^{\frac{3}{2} \cdot \frac{2}{5}}.\end{aligned}$$

This leads to the kinetic energy conservation derived power law relation between radius (r) and time (t):

$$r \approx \left(\frac{2\dot{m}v^2}{\pi\rho} \right)^{\frac{1}{5}} t^{\frac{3}{5}}. \quad (4.2)$$

We now have two power law equations to determine the radial size of the shell after an amount of time, one from conservation of momentum (equation 4.1) and one from conservation of kinetic energy (equation 4.2). However, only one of these equations can hold at any given time. In order for momentum to remain constant as the ejecta sweeps up the surrounding ISM, we would need an isothermal regime such that momentum is not lost through other forces. However, as the scenario we are considering is not an isothermal system, equation 4.1 does not hold. As we are simulating a growing shell being formed from the continual sweeping up of the local ISM environment by the ejecta from nova eruptions and have no radiative cooling, we are in the adiabatic regime. The whole system does not transfer heat with its surroundings as the ISM becomes part of the system. We only have a transfer of kinetic energy as the collisions of ejecta take place with the formed outer shell and so kinetic energy is conserved. Therefore, equation 4.2 is valid in this system.

Additionally, we made the assumption that \dot{m} is constant, however if this was not the case, and the total mass within the system changing throughout the simulation, then these equations would also not hold.

In order to fit the power law derived from conservation of kinetic energy (equation 4.2) to the simulated evolution of the nova shell, we will use the input values used to start the simulation. Setting $\dot{m} = (2.6 \times 10^{-6} \text{ M}_{\odot} \text{ yr}^{-1})/50 = 5.2 \times 10^{-8} \text{ M}_{\odot} \text{ yr}^{-1}$ (here, we are dividing by 50 to illustrate a 7 day eruption within an approximate year of 350 days), $v = 3000 \text{ km s}^{-1}$ and $\rho = 1.67 \times 10^{-24} \text{ g cm}^{-3}$ and substituting these values into equation 4.2 above gives:

$$r(t) \approx 0.0066 t^{\frac{3}{5}},$$

where r is the radius of the nova shell in parsecs after an amount of time, t , measured in years. We plot this power law over the shell width evolution³ in the right panel of Figure 4.1 and can see it closely matches. If we were to fit a similar power law ‘by eye’ such that $r(t) \approx 0.0055 t^{3/5}$, we could align the power law and simulated shell width better still. From this fit we can fix all variables except for the ejecta velocity to determine the velocity needed to replicate the simulated nova shell evolution, found to be $v \sim 1890 \text{ km s}^{-1}$. This deficit in velocity compared to the initial

³See Appendix C for more details about how we determined the boundary locations of specific regions utilised throughout this chapter and Chapter 5.

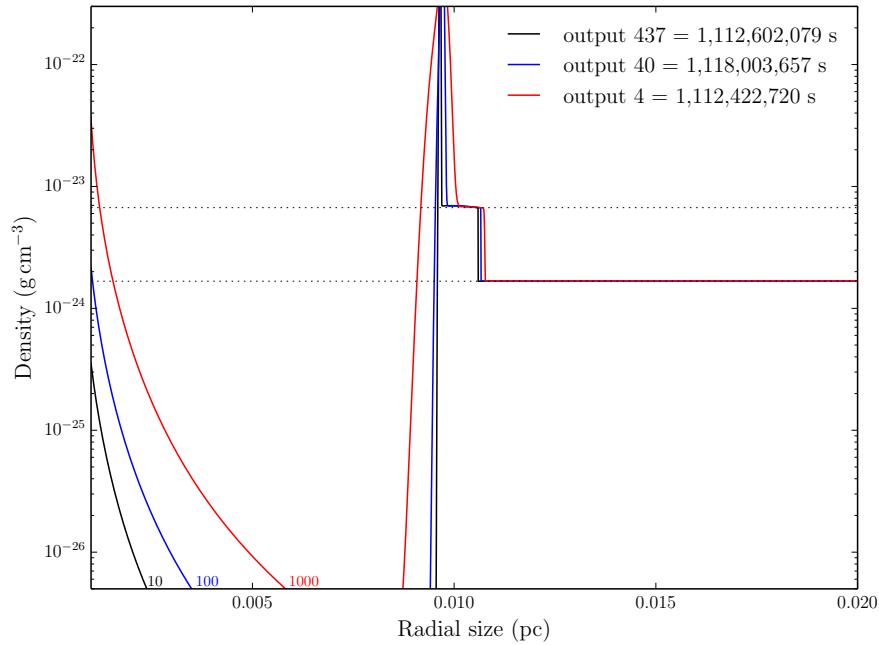


FIGURE 4.2: Preliminary simulation comparing different resolutions at the same time (after first 4 eruptions). The black line is from the run with the first 10 eruptions at 0.01 AU/cell, the blue line is from the run with the first 100 eruptions at 0.1 AU/cell and the red line is from the run with the first 1,000 eruptions at 1 AU/cell.

ejecta velocity can be explained by the deceleration of ejecta due to interaction with previously ejected material (ejecta-ejecta interaction), a direct effect of \dot{m} not being constant throughout (the ejecta intersperses a red giant wind). We can use this relationship to tell us about the size of the remnant at any given time, but not about the overall structure. Therefore, a power law relationship solution takes much less time to acquire, however a full hydrodynamical simulation is a necessity if we are to understand the whole NSR and its emission characteristics.

4.2.2 Testing resolution of simulations

Ideally, we would want to run each full hydrodynamical simulation at a very high spatial resolution, however this is not feasible with temporal and computing constraints. Therefore, we ran the reference simulation (which would have a total of 819,565 eruptions, see Section § 4.5.1) with the first 10 eruptions at a high resolution of 0.01 AU/cell, after which we ran the first 100 eruptions at 0.1 AU/cell. We then ran the first 1,000 eruptions at 1 AU/cell, the first 10,000 eruptions at 10 AU/cell, and lastly, the full 819,565 eruptions at 100 AU/cell. For each new run that had more eruptions but a lower spatial resolution, we compared the simulations at equivalent times including after 4 eruptions (Figure 4.2), 23 eruptions (see Figure 4.3) and 728 eruptions (see Figure 4.4). From these tests, we found that running

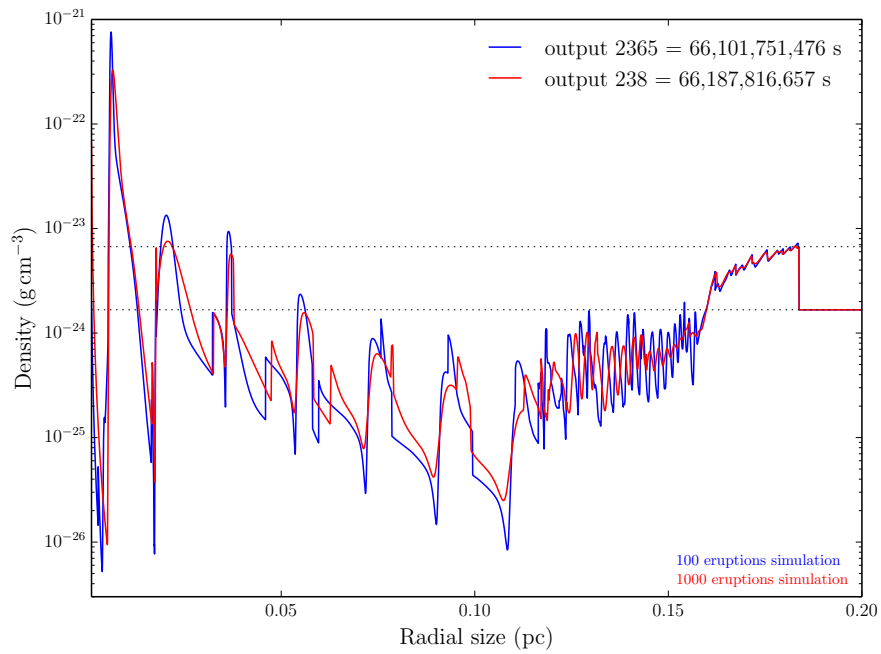


FIGURE 4.3: Preliminary simulation comparing different resolutions at the same time (after first 23 eruptions). The blue line is from the run with the first 100 eruptions at 0.1 AU/cell and the red line is from the run with the first 1,000 eruptions at 1 AU/cell.

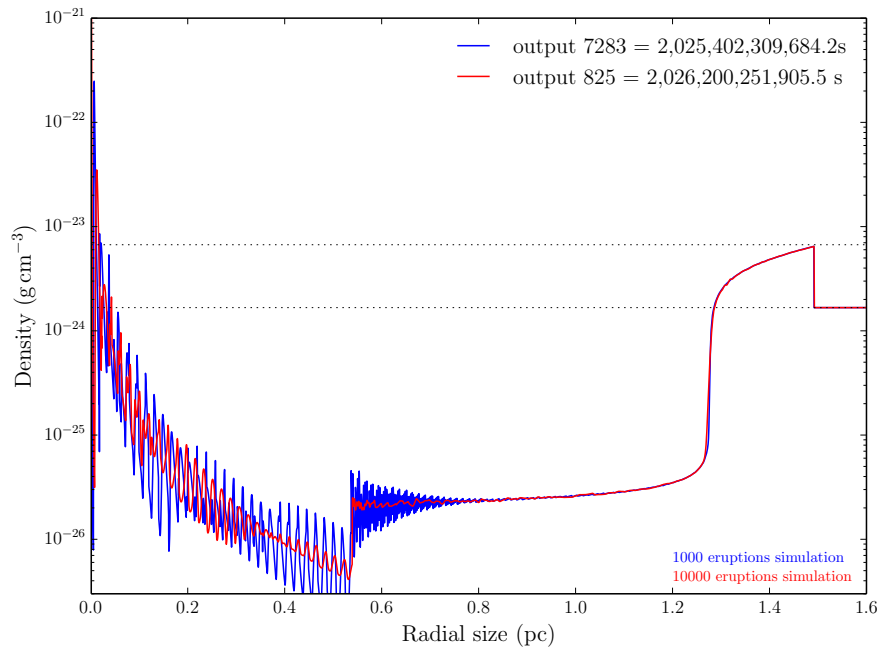


FIGURE 4.4: Preliminary simulation comparing different resolutions at the same time (after first 728 eruptions). The blue line here is from the run with the first 1000 eruptions at 1 AU/cell and the red line here is from the run with the first 10,000 eruptions at 10 AU/cell.

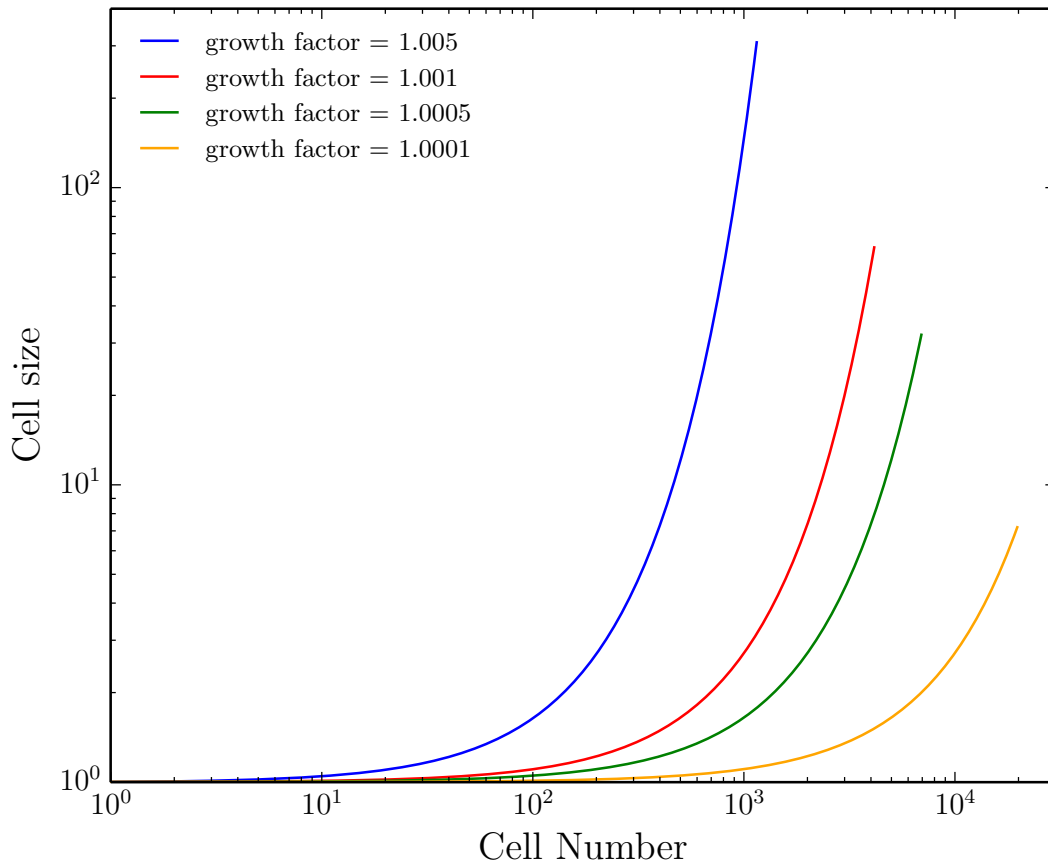


FIGURE 4.5: Varying the ‘growth factor’ within the Morpheus code changes the successive cell sizes within the box of the simulation. Approaching a value of 1 (constant cell size throughout) results in a less dramatic increase in successive cell size.

the full 819,565 eruptions at 100 AU/cell would have the same long term structure as if it had a resolution of 0.01 AU/cell (the resolution of the 10 eruption run).

4.2.3 Testing changing grid size

A further test we carried out after running our first full simulation (see Section § 4.5.1) was focussed on the length of time required to run the full simulations. Even on multiple cores of high performance computing clusters, the length of time for a full simulation to finish was on the order of weeks to months. We therefore wanted to test the Morpheus code’s ability to continuously change grid size as the simulation progresses, reducing the number of iterations needed and thus shortening computing time. This involved changing the ‘growth factor’ of the simulation’s grid size such that each successive cell progressively increases its size as a multiple of the growth factor. For example, leaving this factor unchanged as 1 results in the cells of the simulation remaining constant throughout. However, changing this

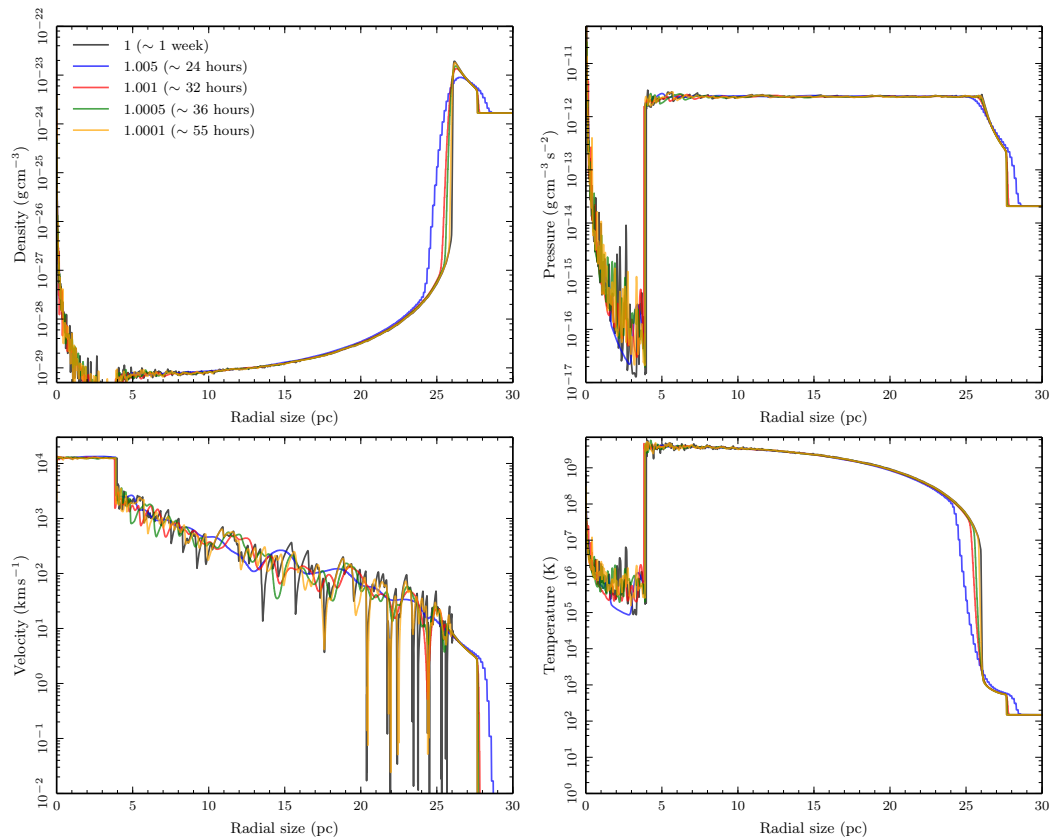


FIGURE 4.6: Changing the ‘growth factor’ within the Morpheus code shortens the time needed to run a full simulation however results in inconsistency with the full simulations with details becoming washed out.

factor to 1.005 would mean that the first cell would have a size of 1, the second cell would have a size of 1.005, the third cell would have a size of 1.005^2 , with the n th cell having a size of $1.005^{(n-1)}$. Figure 4.5 illustrates how the cell size grows throughout the simulation by tuning the growth factor.

From a previous full simulation, we found that it takes approximately one week to run. We then ran the same simulation a number of times whilst changing the growth factor, with the results shown in Figure 4.6. As can be seen, using a growth factor of 1.005 (0.5%) leads to a dramatic reduction in simulation time to ~ 24 hours, however the detail of the structure is considerably washed out (blue line compared to original black line), such that this wouldn’t be useful. In other words, increasing the growth factor reduces the resolution on the larger scales, at the outer edges of the simulation. Furthermore, by approaching a growth factor of 1, the time taken to run the full simulation does increase, however not significantly. The most extreme case trialed used a growth factor of 1.0001 (0.01%), yet the simulation time is again modestly reduced from 1 week to ~ 55 hours, and the simulation is consistent with the original run.

TABLE 4.1: An example showing the contents of an inflow file used to feed into Morpheus. The first column is the cumulative time in days, the second column is the velocity of the ejecta in km s^{-1} and the third column is the mass of the ejecta in units of $M_{\odot} \text{ yr}^{-1}$. The issue arose from interpretation of time by Morpheus.

time [days]	Vel [km/sec]	mdot [Msun/yr]
0.0	271.9632875	5.14266598557e-06
209.995600488	20.0	2.6e-8
32724.346534	271.96815897	5.14261196416e-06
32934.3377352	20.0	2.6e-8
65447.6664278	271.973030415	5.14255967513e-06
⋮	⋮	⋮

However, we opted to keep the growth factor within our simulations as unity after these tests had been performed as new high performance computing facilities became available at the ARI⁴. As the simulations would run faster on these newly available machines, we also chose to reduce the run time of larger future simulations by lowering the resolution of the simulation as this has a small effect on its long term evolution, as described in Section § 4.2.2.

4.2.4 Amending timestep computation within Morpheus

During the study, an issue was identified regarding how the the timestep computational code of Morpheus dealt with the times given in the *inflow* file (one of the input files containing information for creating nova eruptions, an example is given in Table 4.1). Prior to this issue being found, the convoluted nature of the radial profiles, such as those given in Figure 4.2, 4.3, 4.4 and Figure 4.6, outputted from the simulations was not considered. This was not identified earlier, even in the prior study as detailed in Darnley et al. (2019a), through a combination of higher spatial resolution simulations being less impacted alongside the periodic nature of the inflow changes (identical eruptions every 343 days). However from work by another student also utilising Morpheus to look at the interaction of successive eruptions, but at much higher spatial resolution than being conducted in this study, a problem was found due to missing kinetic energy (and therefore missing eruptions).

The problem arises through the interaction of the *setup* file and the *extras* file within Morpheus. The *setup* file originally read the controlled *inflow* file and the *extras* file implemented the inflow parameters through setting the correct values in the inflow array. However, there was never a check to force the timesteps of the simulation

⁴See Appendix D for more details about the machines used.

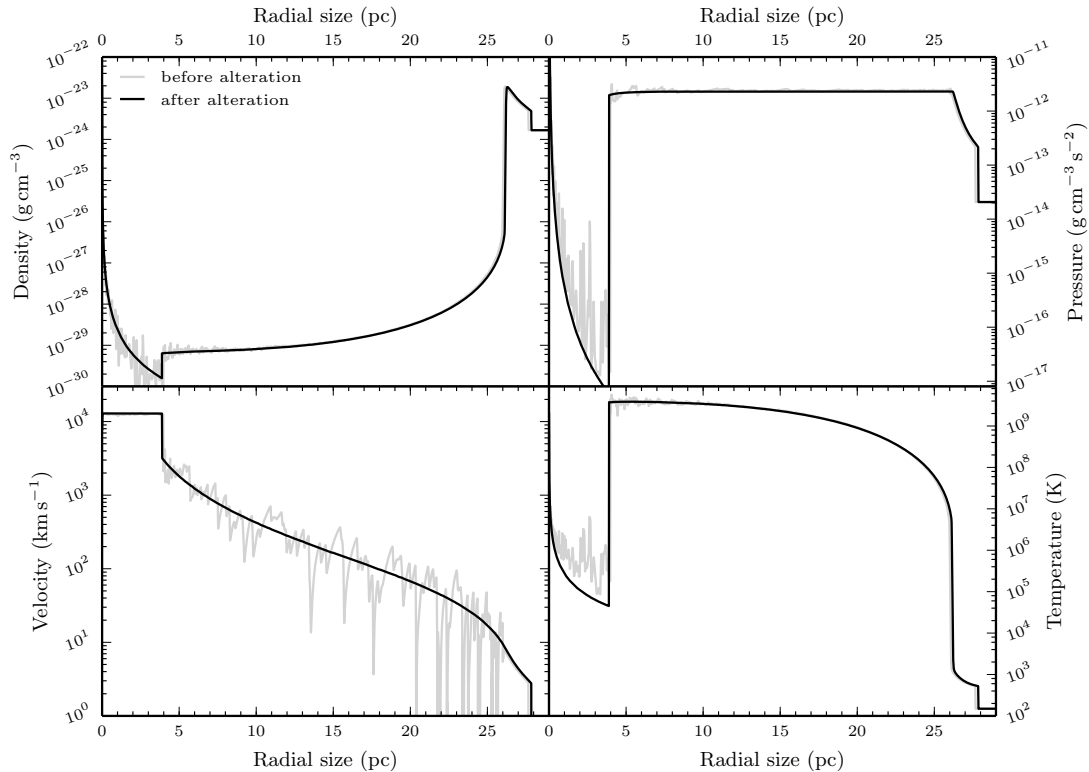


FIGURE 4.7: A comparison of the full simulations of Run 1 (see Section § 4.5.1) before altering the Morpheus code timestep computation and after.

to synchronise with the time values given in the *inflow* file, leading to changes in inflow values occurring effectively randomly, with some changes skipped entirely. The result of this was a different inflow pattern than intended and the convoluted radial profiles.

The timestep computational code was not taking into account the times given in the *inflow* file. For simulations with a low spatial resolution, the timesteps are larger, therefore each eruption (given in the *inflow* file) lasts for a longer amount of time than we would expect. Additionally, if the timesteps in the timestep computational code happened to be large, then many eruptions given in the (sometimes ignored) *inflow* file, would be ‘stepped over’ and unaccounted for.

To address this issue, the *extras* file was amended by Dr. Matt Darnley in the following way⁵. Firstly, it was made to check whether the currently computed timestep (dt) would take the time (t) past the next change in the *inflow* file. If this was true, it would truncate dt such that after the next timestep, t will be exactly equal to the time of inflow change. Secondly, it forces $dt = 1\text{ s}$ if the inflow values change from the last iteration to guarantee that the code calculates a new dt based on the new inflow values without significant changes in the simulation.

⁵See Appendix E for the part of the amended source code.

The result of changing the code to address this issue can be seen in Figure 4.7. Before altering this problem within the code, the dynamics of a full simulation (see Section § 4.5.1) were erratic. Also, the simulations with a low accretion rate of $\dot{M} = 1 \times 10^{-9} M_{\odot} \text{ yr}^{-1}$ (see Section § 4.5.4) lacked an evident shell because the timesteps were larger than the eruption lengths and so the eruptions were not occurring, analogous to a red giant wind. However, after the issue had been addressed, the radial profiles became extremely well defined, predominantly illustrated in the radial velocity profile, as well as leading to larger structures and a shell in the low accretion rate runs. This updated piece of code was then used for all of the analysis from then on.

4.3 Tests prior to main simulations

As we are predominantly concerned with the long term (and therefore large scale) structure of the shell, we want to test two different eruption characteristics and observe how the evolution of the shell is affected. Firstly, we know that the timescale of the nova eruption can vary as we see a wide range of SSS periods (see, e.g. [Henze et al., 2014a](#)). Secondly, as detailed in Section § 1.2.1 and Section § 1.2.3, it has been shown that shocks play a key role within the nova ejecta, and instead of material being ejected in one event, the outburst contains a number of components with varying masses and velocities ([Metzger et al., 2014](#); [Aydi et al., 2020a,b](#)). Therefore we want to incorporate *the time-scale of the eruption* and *a shock occurring within the outburst ejecta*.

4.3.1 Eruptions timescales

As stated previously, the code runs in the style of a top-hat function, with the nova eruption being ‘on’ for 7 days followed by an inter-eruption period of 343 days with a red giant wind blowing.

In order to determine if the length of the nova eruption itself affects the large scale structure of the nova shell, we ran high resolution (~ 4 AU/cell) simulations, each with 1000 eruptions and with varying eruption time-scales, alongside the original 7 day example: 0.07 d, 0.7 d, 70 d and 350 d. For each of these tests, we altered the time between successive eruptions such that the eruptions timescale plus the recurrence period totalled 350 days (e.g. 349.03d + 0.07d or 343d + 7d) and used the same ejecta velocity of 3000 km s^{-1} for each simulation. As we wanted each of these simulations to inject the same amount of kinetic energy, the eruption \dot{M} was

decreased sufficiently to account for the longer timescales. The long term evolution of the growing nova shell and the ejecta pile-up region is shown in left panel of Figure 4.8. As can be seen, after around 100 years, the inner and outer edge of the shell begin to follow the same evolutionary trend regardless of the length of the nova outburst, and even though the ejecta pile-up fluctuates more than the shell, they again settle into similar growth rates. This removes the need to consider eruption time-scale dependency in later simulations.

4.3.2 Intra-eruption shocks

We also wanted to test whether having a non-uniform ejection of material from the nova would affect the large scale structure of the shell. For this, we considered the composition of a classical nova whereby the eruption takes place over a certain timescale and over that time period, the speed of ejection increases (Bode & Evans, 1989; O'Brien et al., 1994; Metzger et al., 2014; Aydi et al., 2020a,b). This implies that the outburst is comprised of a slow wind followed by a faster wind, creating a shock within the ejecta (O'Brien et al., 1994; Metzger et al., 2014; Aydi et al., 2020a,b).

Therefore, to incorporate shocks within the ejecta, we ran 1000 eruptions with the 7 day timescale (length of the nova eruption) split into two separate components, representing the asymmetric nova outburst. For moderate-speed novae, the ejecta velocities range from 500 - 2000 km s⁻¹ but for fast novae, this range is 1000 - 4000 km s⁻¹ (O'Brien et al., 1994). As we are considering recurrent nova eruptions and therefore dealing with fast novae, we used the latter range of velocities for this test. We ejected half of the ejecta mass at 1000 km s⁻¹ over 3.5 days immediately followed by the half of the ejecta mass at 4123 km s⁻¹ over the next 3.5 days such that the total combined kinetic energy from both components equalled amount of kinetic energy expelled by the 7 day eruption with an ejecta velocity of 3000 km s⁻¹. As the second half of the mass is being ejected at a higher velocity than the first, we see shocks as the second ejection catches and interacts with the first ejection of material. The right panel of Figure 4.8 shows the evolution of the nova shell after 1000 eruptions with a shock during outburst in comparison to the nova shell evolution of 1000 eruptions without a shock. As can be seen, similar to changing the time-scale of the eruption in Section § 4.3.1, after around 100 years, the inner and outer edge of the shell begin to follow the same evolutionary trend. This removes the need to consider ejecta internal-shock dependency in later simulations.

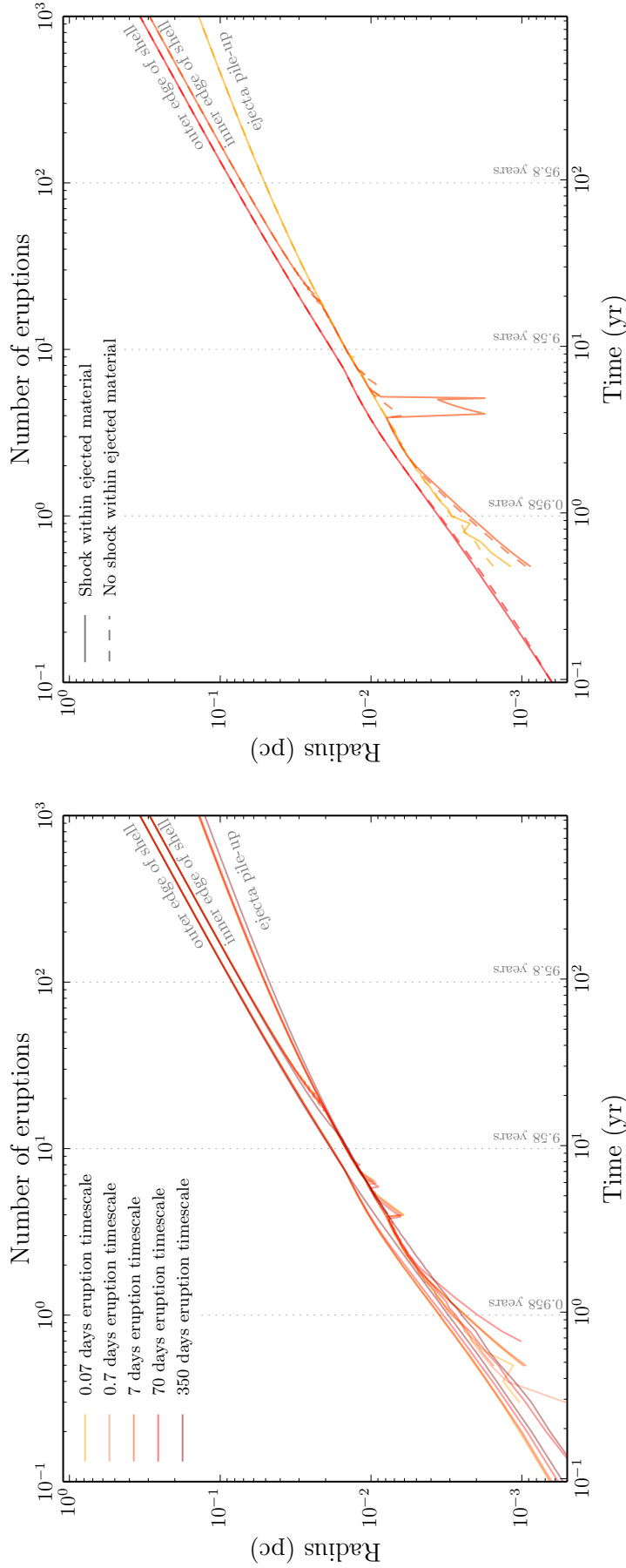


FIGURE 4.8: Left: Long term evolution of a growing nova shell, including the inner and outer edge of the shell plus the ejecta pile-up region, for nova eruptions lasting 0.07 days, 0.7 days, 7 days, 70 days and 350 days. **Right:** Long term evolution of a growing nova shell from 1000 eruptions with interacting ejecta material alongside the nova shell from 1000 eruptions without shocks.

In Section § 4.3.1 and Section § 4.3.2, we have demonstrated that the long term evolution of the ejecta from the nova is not affected by the nova outburst timescale and is not affected by internal shocks of the ejecta, and consequently, neither is the nova super-remnant. To reiterate this important conclusion, the long term structure of the nova super-remnant *is not affected* by the length of the nova outburst nor the structure of the ejecta. Instead, it depends only upon the total kinetic energy of the ejecta⁶.

4.4 Parameter space for main simulations

In this section we will outline the procedure we employed for running various simulations with varying WD temperatures, ISM densities and accretion rates. The simulations ran in Darnley et al. (2019a) to recreate the NSR surrounding M 31N 2008-12a made use of identical eruptions. Whilst a good approximation for this system during the current stage of its evolution, identical outbursts do not match the long term evolution of such a system, whereby it begins with a lower mass WD that grows, and in doing so generates ejecta with differing characteristics. Therefore, to obtain the properties of a more realistic nova system with incrementally changing nova eruptions, we were required to grow a WD (see Section § 4.4.2). We will only describe the model we used for growing the WD for a ‘reference simulation’ for illustration purposes, however this model was utilised for each of the different WD temperatures and accretion rates. As a reference simulation, we chose to grow a 1×10^7 K WD with an accretion rate of $1 \times 10^{-7} M_{\odot} \text{ yr}^{-1}$ (see Section § 4.4.1 for details), which we then placed within an environment with a hydrogen only ISM density of $1.67 \times 10^{-24} \text{ g cm}^{-3}$ (1 H atom per cubic centimeter). We refer to this ISM density throughout the thesis as $n = 1$, indicating the hydrogen number density of the ISM. We also denote $1.67 \times 10^{-23} \text{ g cm}^{-3}$ as $n = 10$ and $1.67 \times 10^{-22} \text{ g cm}^{-3}$ as $n = 100$.

4.4.1 System parameters

Yaron et al. (2005) provides a parameter space for the characteristics of a nova envelope and the outburst characteristics for an extended grid of nova models with varying WD masses, WD temperatures and accretion rates (see Table 4.2 for details). This extensive grid of models runs through all combinations of these parameters and outputs many outburst characteristics such as the mass accreted onto the WD

⁶Here, we have an adiabatic scenario so no energy is lost.

TABLE 4.2: Parameters combined to generate a parameter space for the characteristics of the nova envelope from [Yaron et al. \(2005\)](#).

White dwarf mass (M_{\odot})	0.4, 0.65, 1.00, 1.25, 1.40
White dwarf temperature (K)	1×10^7 , 3×10^7 , 5×10^7
Accretion rate ($M_{\odot}\text{yr}^{-1}$)	1×10^{-6} – 5×10^{-13}

which ignites during the TNR (m_{acc}) and the duration of the mass-loss phase (t_{ml}) i.e. the amount of time that the outburst persists for.

These models have been utilised in many studies since. For example, [Orlando et al. \(2009\)](#) used the estimates of the ejecta mass and energy of the nova explosion from [Yaron et al. \(2005\)](#) for their three dimensional modelling of the asymmetric blast wave associated with the 2006 outburst of the recurrent nova, RS Ophiuchi. The models have also been used to constrain the contribution of novae to the SNeIa rate in M 31 through computing the number distribution of novae with respect to their decline times ([Soraisam & Gilfanov, 2015](#)).

For this study, we took the values of m_{acc} , which we will call ignition mass (m_{ig}), and t_{ml} for WDs with masses 1.0, 1.25 and 1.4 M_{\odot} with the three different temperatures and an accretion rate of $1 \times 10^{-7} M_{\odot} \text{yr}^{-1}$. As the values from [Yaron et al. \(2005\)](#) belong to a very coarse grid, choosing how to interpolate between these points is an important decision. In order to interpolate and extrapolate these points for a continuous set of values for our simple model, we wanted to fit a function that evolved smoothly, behaved as a power law *and* became asymptotic as the Chandrasekhar mass was approached (see Section § 4.9.2 for an alternative approach). Therefore, we interpolated these points by fitting the following the function:

$$f(M_{\text{WD}}) = a \times M_{\text{WD}}^{-b} + c,$$

where a , b and c are constants with this function becoming asymptotic as M_{WD} approaches the Chandrasekhar limit. From this fit we were able to determine two relationships: $M_{\text{WD}} - m_{\text{ig}}$ and $M_{\text{WD}} - t_{\text{ml}}$. For the Chandrasekhar limit in this case, we chose $M_{\text{Ch}} = 1.408 M_{\odot}$ as this is when these two relationships break down. We then found a relationship between the recurrence period (P_{rec}) and WD mass:

$$P_{\text{rec}} = \frac{m_{\text{ig}}}{\dot{M}},$$

with \dot{M} being the same accretion rate used when selecting values ($1 \times 10^{-7} M_{\odot} \text{yr}^{-1}$).

The values given in [Yaron et al. \(2005\)](#) we have already interpolated between were derived to replicate the nova outburst on the surface of the WD. These values of m_{ig} and t_{ml} , and therefore P_{rec} , are valid for our simple model. But we also wish to be consistent with observed characteristics of the nova eruption as these relate directly to the ejecta that we are modelling. Therefore, we will use observationally determined relations to determine the terminal ejecta velocity of the outburst. Firstly, it can be shown with the following relations:

$$t_3 \approx 2.75 \times t_2^{0.88} \quad (4.3)$$

from [Warner \(1995\)](#) and

$$t_{\text{on}} = 10^{(0.8 \pm 0.1)} \cdot t_{2,R}^{(0.9 \pm 0.1)} \quad (4.4)$$

$$t_{\text{on}} = 10^{(5.6 \pm 0.5)} \cdot v_{\text{exp}}^{(-1.2 \pm 0.1)} \quad (4.5)$$

from [Henze et al. \(2014a\)](#) where $t_{2,R}$ is decline time in the R -band and v_{exp} is the expansion velocity of the ejected envelope, that the mass-loss phase, t_{ml} , is equivalent to the decline time t_3 (the time taken for a nova to fade from peak by 3 magnitudes) through dividing equation 4.4 by equation 4.3 such that:

$$\frac{t_{\text{on}}}{t_3} \approx \frac{10^{(0.8 \pm 0.1)} \cdot t_2^{(0.9 \pm 0.1)}}{2.75 \cdot t_2^{0.9}} = 2 \pm 1 \quad \Rightarrow \quad t_{\text{on}} \approx (2 \pm 1) t_3. \quad (4.6)$$

We know that t_{on} can be used to approximate the mass loss phase of the nova eruption (t_{ml}), therefore we will take $t_{\text{ml}} \approx t_3$, consistent with [Shara \(1981, see their appendix\)](#). We can then utilise the relations above (equations 4.3, 4.4 and 4.5) to determine a relation between ejecta velocities and t_{ml} in order to formulate a $M_{\text{WD}} - v_{\text{ej}}$ relationship. We start by rewriting equation 4.3 such that:

$$t_2 \approx 0.32 \times t_3^{1.14}, \quad (4.7)$$

and highlighting that equation 4.4 is equivalent to equation 4.5 such that:

$$10^{(0.8 \pm 0.1)} \cdot t_2^{(0.9 \pm 0.1)} = 10^{(5.6 \pm 0.5)} \cdot v_{\text{exp}}^{(-1.2 \pm 0.1)} \quad (4.8)$$

Substituting equation 4.7, with t_{ml} now replacing t_3 , into equation 4.8 (omitting uncertainties) leads to:

$$\begin{aligned} 10^{0.8} \cdot [0.32 \times t_{\text{ml}}^{1.14}]^{0.9} &= 10^{5.6} \cdot v_{\text{exp}}^{-1.2} \\ \Rightarrow 0.32 \times t_{\text{ml}}^{1.026} &= \frac{10^{5.6}}{10^{0.8}} \cdot v_{\text{exp}}^{-1.2} = 10^{4.8} \cdot v_{\text{exp}}^{-1.2} \end{aligned}$$

$$\begin{aligned} \implies v_{\text{exp}}^{-1.2} &= 10^{-5.3} \cdot t_{\text{ml}}^{1.026} \\ \therefore v_{\text{exp}} &= 10^{4.42} \cdot t_{\text{ml}}^{-0.855}. \end{aligned} \quad (4.9)$$

We then used equation 4.9 to formulate a $M_{\text{WD}} - v_{\text{ej}}$ relationship. All four of these interpolated relationships are now presented:

$$\begin{aligned} m_{\text{ig}} &= (1.23 \times 10^{-5}) \times M_{\text{WD}}^{-3.8} - (3.34 \times 10^{-6}) && \text{for } M_{\text{WD}} - m_{\text{ig}} \\ t_{\text{ml}} &= 662 \times M_{\text{WD}}^{-1.1} - 452 && \text{for } M_{\text{WD}} - t_{\text{ml}} \\ P_{\text{rec}} &= 123 \times M_{\text{WD}}^{-3.8} - 33 && \text{for } M_{\text{WD}} - P_{\text{rec}} \\ v_{\text{ej}} &= 10^{4.42} \times (662 \times M_{\text{WD}}^{-1.1} - 452)^{-0.855} && \text{for } M_{\text{WD}} - v_{\text{ej}} \end{aligned}$$

and are illustrated in Figure 4.9 alongside the three different WD temperatures for other accretion rates, $1 \times 10^{-8} M_{\odot} \text{ yr}^{-1}$ and $1 \times 10^{-9} M_{\odot} \text{ yr}^{-1}$.

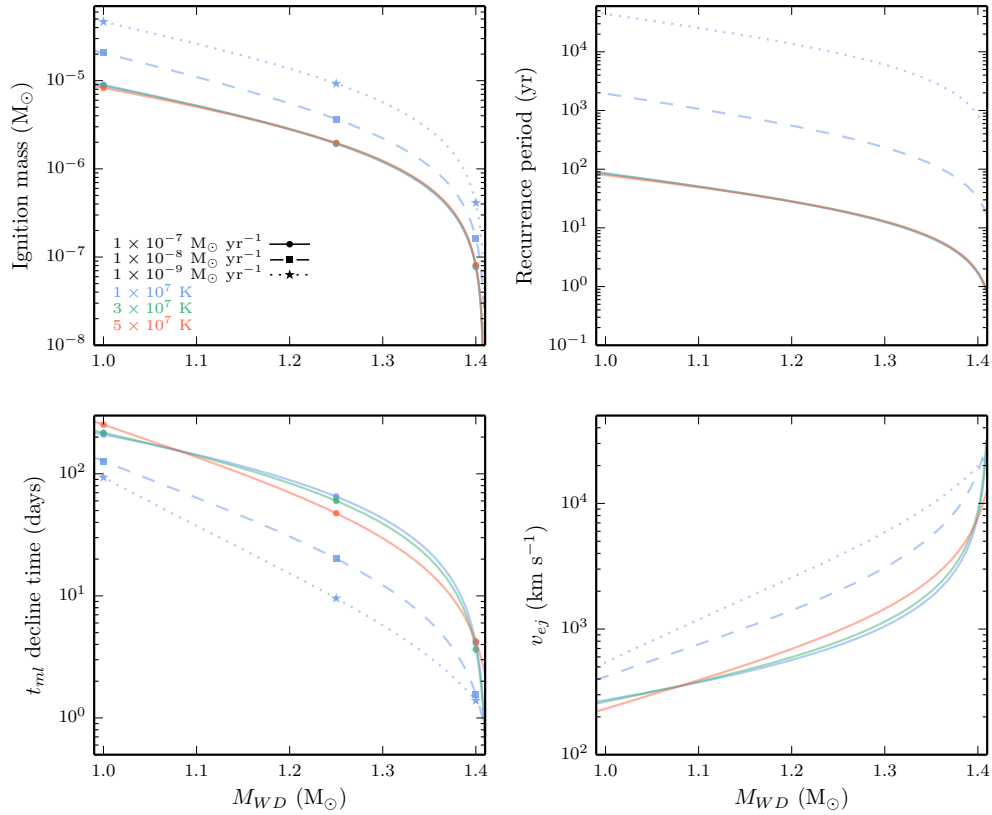


FIGURE 4.9: **Top left:** $M_{\text{WD}} - m_{\text{ig}}$. The points are the output characteristics for m_{acc} from Yaron et al. (2005) which we used for interpolation. **Top right:** $M_{\text{WD}} - P_{\text{rec}}$. **Bottom left:** $M_{\text{WD}} - t_{\text{ml}}$. Again, the points are the output characteristics for t_{ml} from Yaron et al. (2005) which we used for interpolation. **Bottom right:** $M_{\text{WD}} - v_{\text{ej}}$.

4.4.2 Growing a white dwarf

We grew a $1 M_{\odot}$ white dwarf using the interpolated relationships given in Section § 4.4.1 in order to obtain properties of each nova eruption. For this example, a $1 M_{\odot}$ WD with a temperature of 1×10^7 K experiences approximately 820,000 eruptions to grow from $1 M_{\odot}$ to just over $1.4 M_{\odot}$. This upper limit on the WD mass is chosen to be when the recurrence period of the nova eruption becomes ~ 50 days as this is the theoretical lower limit (Kato et al., 2014). This found mass then became the upper limiting mass on each of the other WD growing models.

After an eruption, a WD is grown according to how much of the material that it accreted between outbursts is retained. Based on eruption parameters of the RRN, M31N 2008-12a, Kato et al. (2015) found that the WD ejected 37% of the material it accretes. This corresponds to a mass accumulation efficiency of $\eta = 0.63$. We will adopt $\eta = 0.67$ for our study such that the WD retains two-thirds of the mass it accretes between eruptions. This small difference has no significant impact on the final results (see Section § 4.9.1). This can be summarised as the following:

$$M_{\text{WD},i+1} = M_{\text{WD},i} + (m_{\text{ig},i} \times \eta) \quad \text{while } M_{\text{WD}} < M_{\text{Ch}} \quad (4.10)$$

with $M_{\text{WD},i}$ being the pre-eruption mass of the WD, $m_{\text{ig},i}$ being the mass accreted by the WD before the eruption (ignition mass) and $M_{\text{WD},i+1}$ being the post-eruption mass of the WD. With the initial WD mass being $1 M_{\odot}$, we utilised the relationships found in Section § 4.4.1 to give the associated m_{ig} value for equation 4.10. This determined post-eruption mass was then used as the M_{WD} value in the next iteration and we continued this until we reached the limiting mass stated previously. Throughout this evolution, the mass accumulation efficiency remains constant⁷. We used the output parameters from this iterative model in our simulations.

With each iteration, we were also able to use the relationships found in Section § 4.4.1 to illustrate the evolution of a number of parameters in terms of white dwarf mass, recurrence period, the cumulative time of all eruptions and the number of eruptions. These are given in Figure 4.10, Figure 4.11, Figure 4.12 and Figure 4.13, respectively.

We will focus on Figure 4.10 as this illustrates how various system parameters evolve as the mass of the WD increases towards the M_{Ch} (Figure 4.11, Figure 4.12 and Figure 4.13 can be utilised when referring to the output from simulations described

⁷Even though there is some variation in η for various WD masses and mass accretion rates, a constant η is a reasonable approximation here as there is not a significant difference within the region of \dot{M} and M_{WD} we focus on (S. Starrfield, private communication).

TABLE 4.3: A comparison of the predicted values taken from Figure 4.11 and the observed values for each parameter for two recurrent novae. (★) The predicted recurrence periods were chosen to match the current observational value for each system. The predicted values are taken from the model with a 1×10^7 K WD growing from $1M_{\odot}$ with a mass accretion rate of $1 \times 10^{-7} M_{\odot} \text{ yr}^{-1}$. This is a reasonable mass accretion rate to use for the following systems as their accretion rates are $(6 - 14) \times 10^{-7} M_{\odot} \text{ yr}^{-1}$ for M 31N 2008-12a (Darnley et al., 2017b) and $2 \times 10^{-7} M_{\odot} \text{ yr}^{-1}$ for RS Ophiuchi (Osborne et al., 2011). Note that other than the recurrence period, the other predicted values (M_{WD} , t_3 and v_{ej}) for M 31N 2008-12a *have not* been tuned to match the system.

Parameters★	Prediction	Observation	References
M 31N 2008-12a			
P_{rec} (years)	1	0.99 ± 0.02	1
M_{WD} (M_{\odot})	1.398	$\simeq 1.38$	3
t_3 (days)	5	~ 3	2
v_{ej} (km s^{-1})	6624	~ 6200	2
RS Ophiuchi			
P_{rec} (years)	21–9	15 ± 6	4
M_{WD} (M_{\odot})	1.239 – 1.322	1.35	5
t_3 (days)	70 – 34	9.5	6
v_{ej} (km s^{-1})	690 – 1300	~ 4000	6

References. – (1) Darnley & Henze (2020), (2) Kato et al. (2015), (3) Henze et al. (2018a), (4) Darnley (2021), (5) Osborne et al. (2011), (6) Bode et al. (2006)

later in the chapter). As described earlier with interpolating the values from Yaron et al. (2005), ignition mass m_{ig} and decline time t_3 monotonically decrease because as the WD increases in mass and becomes more extreme thus burning at a higher rate, less material is needed to trigger a nova eruption and as such, the eruption is increasingly short lived. For the same reasoning, the recurrence period P_{rec} of the growing WD system also shortens and as the ejected mass m_{ej} is directly linked to the constant mass accumulation efficiency (η) in the system, this decreases as the WD mass increases. An increasing surface gravity on the growing WD results in the ejecta velocity v_{ej} increasing, consequently contributing to the evolution of the momentum, total momentum, kinetic energy and total kinetic energy. The number of eruptions begins slowly, reflecting the large periods of time between initial outbursts, however this increases drastically as the M_{Ch} is approached, due to later quick-fire eruptions. Consequently, the cumulative time increases substantially, however when reaching $\sim 1.2 M_{\odot}$, this plateaus and increases relatively little up to the limiting mass.

Lastly, we have chosen two recurrent novae (M 31N 2008-12a and RS Ophiuchi) to illustrate how the predicted values from Figures 4.10, 4.11, 4.12 and 4.13 compare with observations. We did this by taking the observed recurrence period for each

RN and found the associated M_{WD} , t_3 and v_{ej} for this P_{rec} from Figure 4.11. This comparison is given in Table 4.3. As shown, the predicted values for M 31N 2008-12a match the observed values reasonably well. The WD mass is approaching the Chandrasekhar limit as expected, the t_3 decline time is close to that observed and the ejecta velocity is consistent with observations of the bulk ejecta 0.54 days after eruption (Henze et al., 2018a), however note that the velocity of 13000 km s^{-1} was seen $\lesssim 1$ day after the 2015 eruption (Darnley et al., 2016). For RS Ophiuchi, the predicted WD mass is reasonable (with Mikołajewska & Shara 2017 also predicting a mass range of $1.2 - 1.4 M_{\odot}$), however both the decline time and ejecta velocity differ from observations, possibly resulting from the lower mass accretion rate utilised in comparison to the real system or stemming from the system's recurrence time being highly variable, impacting the observed properties given. Additionally, the observed velocity given here is the early ejecta velocity and therefore may not account for the slower velocity of the bulk ejecta given in Evans et al. (2007) as $\sim 500 - 600 \text{ km s}^{-1}$ between day 12 and day 56 (from infrared line widths), close to our predicted value in Table 4.3. The predicted decline time may be more attuned to the observed value if we take equation 4.6 with its associated errors, giving a lower limiting predicted values of $t_3 \sim 11$ days, similar to the observed 9.5 days.

4.5 Main simulations

In this section we will provide the results of the simulations we ran for a growing nova remnant with different system parameters. For ease of reference, we refer to the different simulations as Run 1, Run 2 etc. and summarise the specific parameters used for each in Table 4.4. In the same manner, we will assign the full simulation from Darnley et al. (2019a) to be Run 0 as it will be used as a comparison throughout. This simulation had 100,000 identical eruptions with each eruption ejecting $5 \times 10^{-8} M_{\odot}$ at a terminal velocity of 3000 km s^{-1} . Each outburst lasted seven days and repeated every 343 days to make up an approximate 350 day recurrence period (Darnley et al., 2019a).

4.5.1 Run 1 (reference simulation)

Our first simulation (Run 1 and the reference simulation) contains a WD with a temperature of $1 \times 10^7 \text{ K}$, an accretion rate of $1 \times 10^{-7} M_{\odot} \text{ yr}^{-1}$ ejecting material into a surrounding ISM with density $1.67 \times 10^{-24} \text{ g cm}^{-3}$ ($n = 1$). Utilising our model (equation 4.10) given in Section § 4.4.2, we estimated that it would take 6,073,159

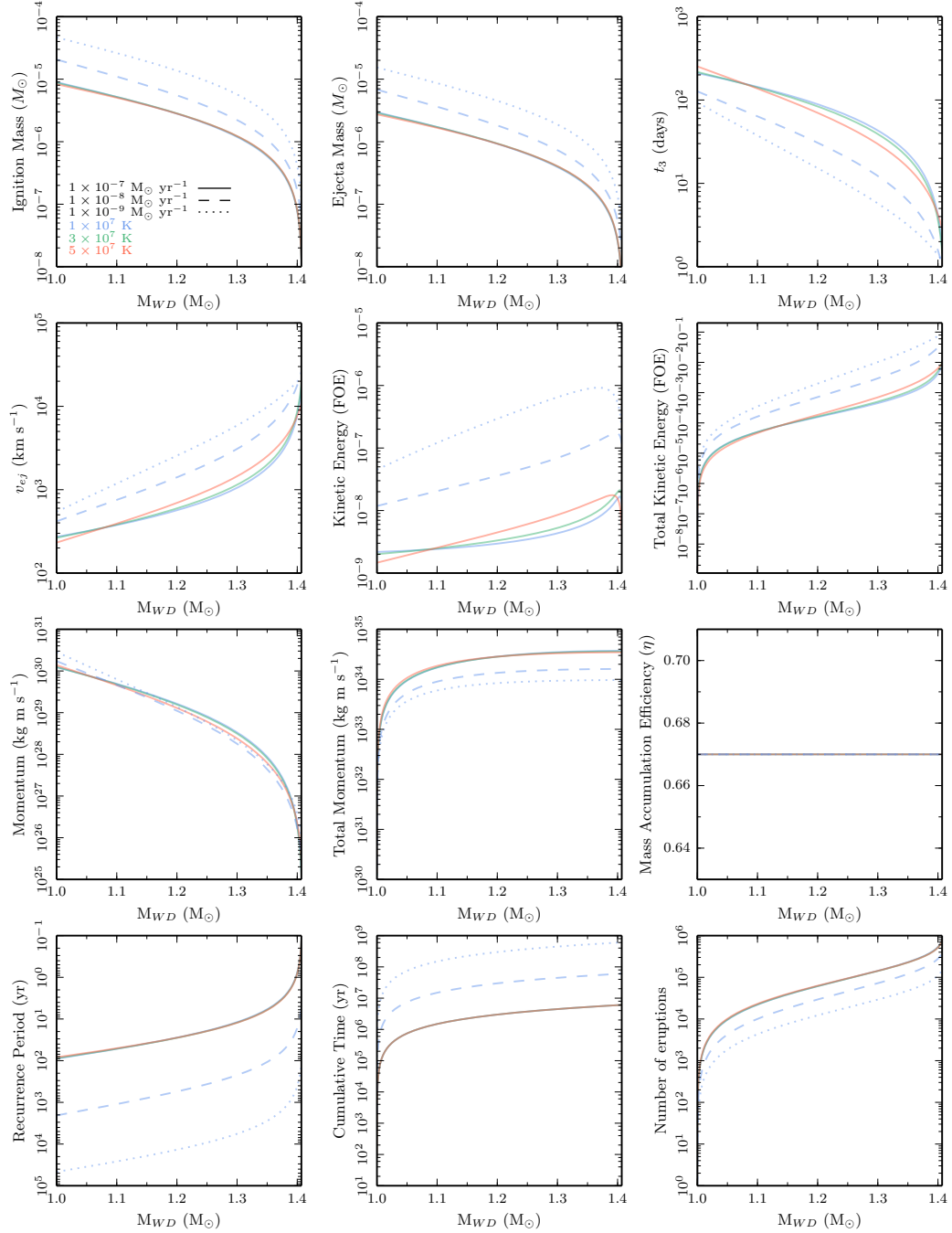


FIGURE 4.10: Evolution of system parameters with respect to the mass of the white dwarf for the three different white dwarf temperatures with three different accretion rates. These are m_{ig} : ignition mass, m_{ej} : ejected mass, t_3 : decline time, v_{ej} : the velocity of the ejecta from the surface of the white dwarf, kinetic energy, total kinetic energy, momentum, total momentum, mass accumulation efficiency parameter, P_{rec} : the recurrence period, cumulative time of all the eruptions and the number of eruptions. Kinetic energy and total kinetic energy are presented in units of 1×10^{51} ergs ("[ten to the power of] fifty-one ergs" or FOE).

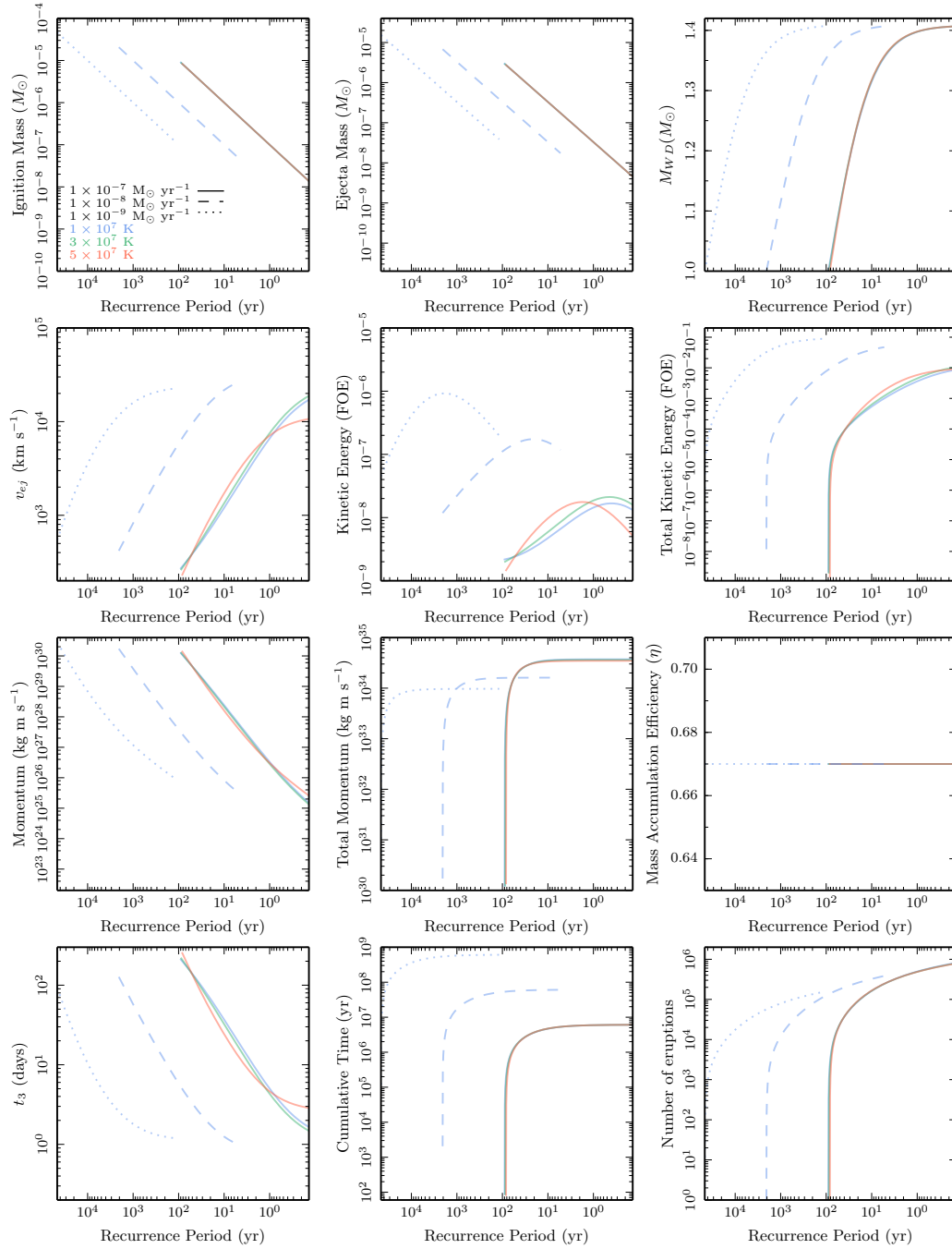


FIGURE 4.11: Same as Figure 4.10 but with respect to the recurrence period of the system.

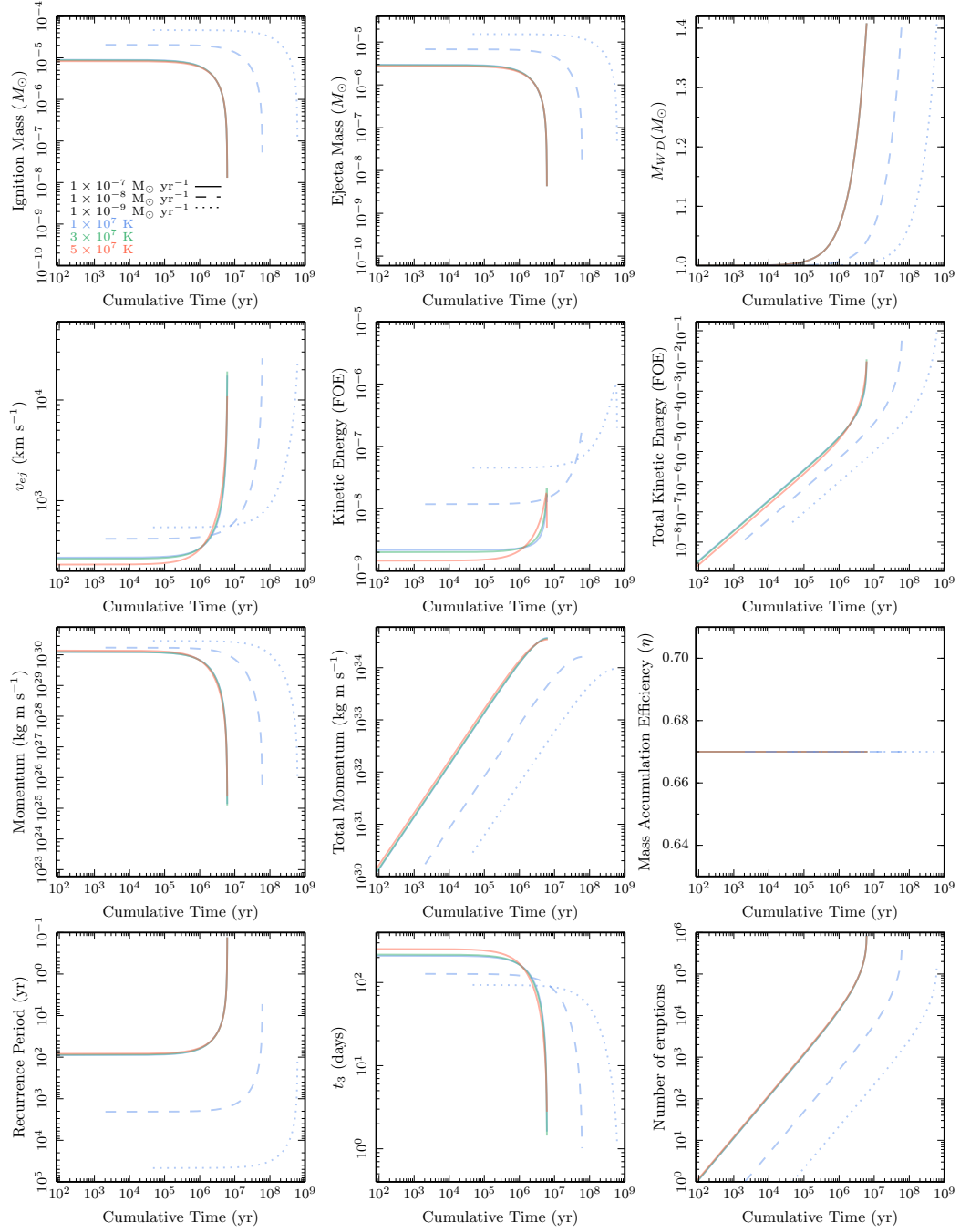


FIGURE 4.12: Same as Figure 4.10 but with respect to the total time of all the nova eruptions.

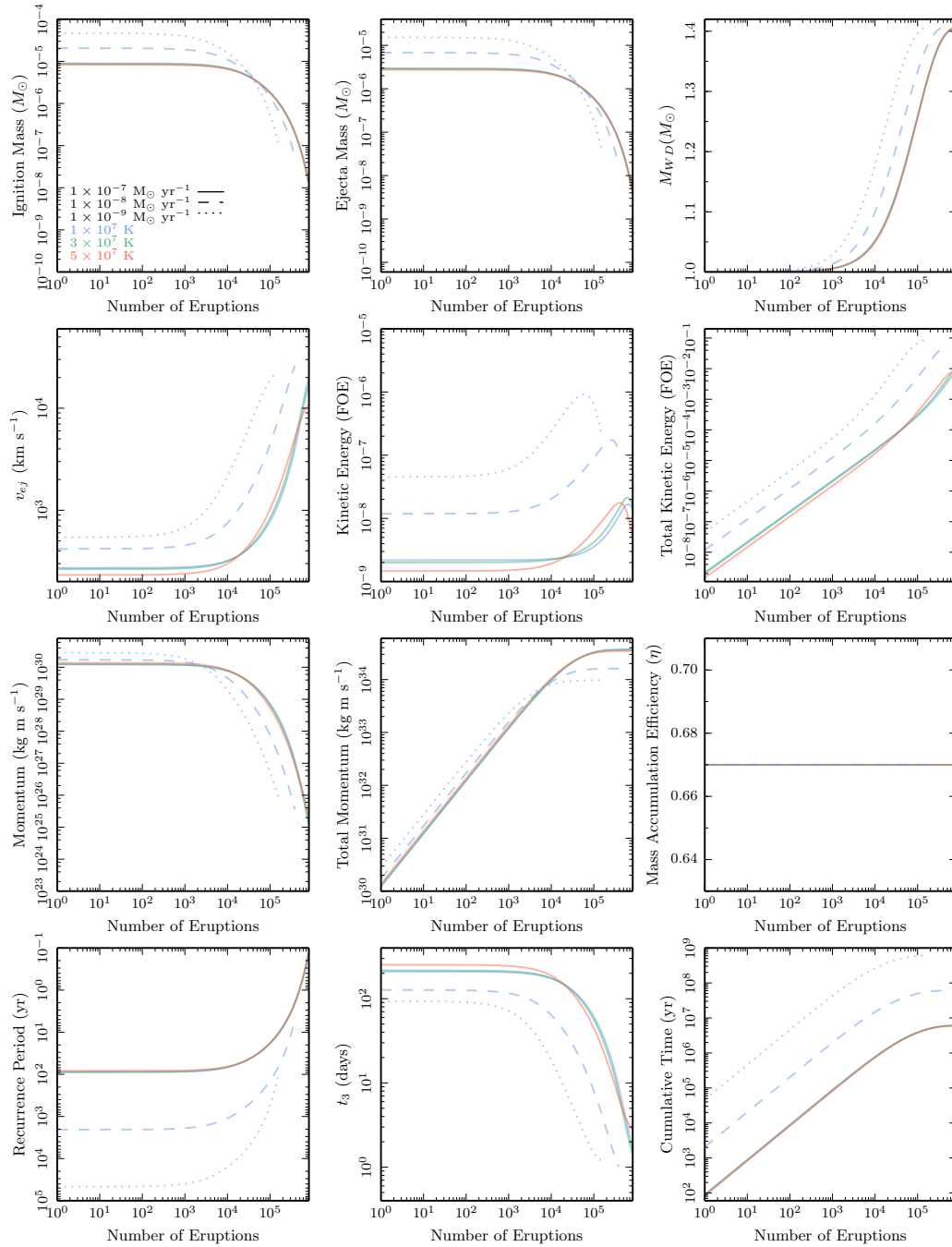


FIGURE 4.13: Same as Figure 4.10 but with respect to the number of nova eruptions.

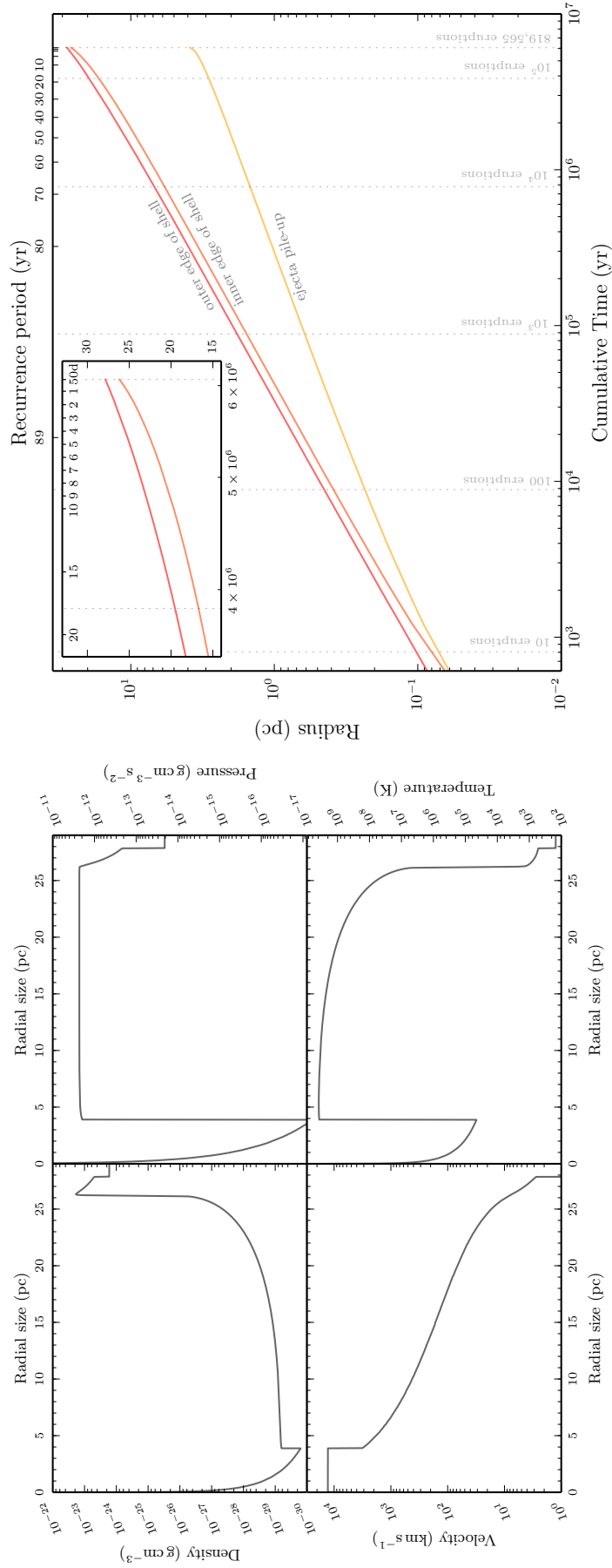


FIGURE 4.14: **Left:** Dynamics of the nova remnant with $\dot{M} = 1 \times 10^{-7} M_{\odot} \text{ yr}^{-1}$ and $n = 1$ after 819,565 eruptions with a resolution of 100 AU/cell. **Right:** Evolution of the outer edge, inner edge and ejecta pile-up region with respect to cumulative (elapsed) time and recurrence period.

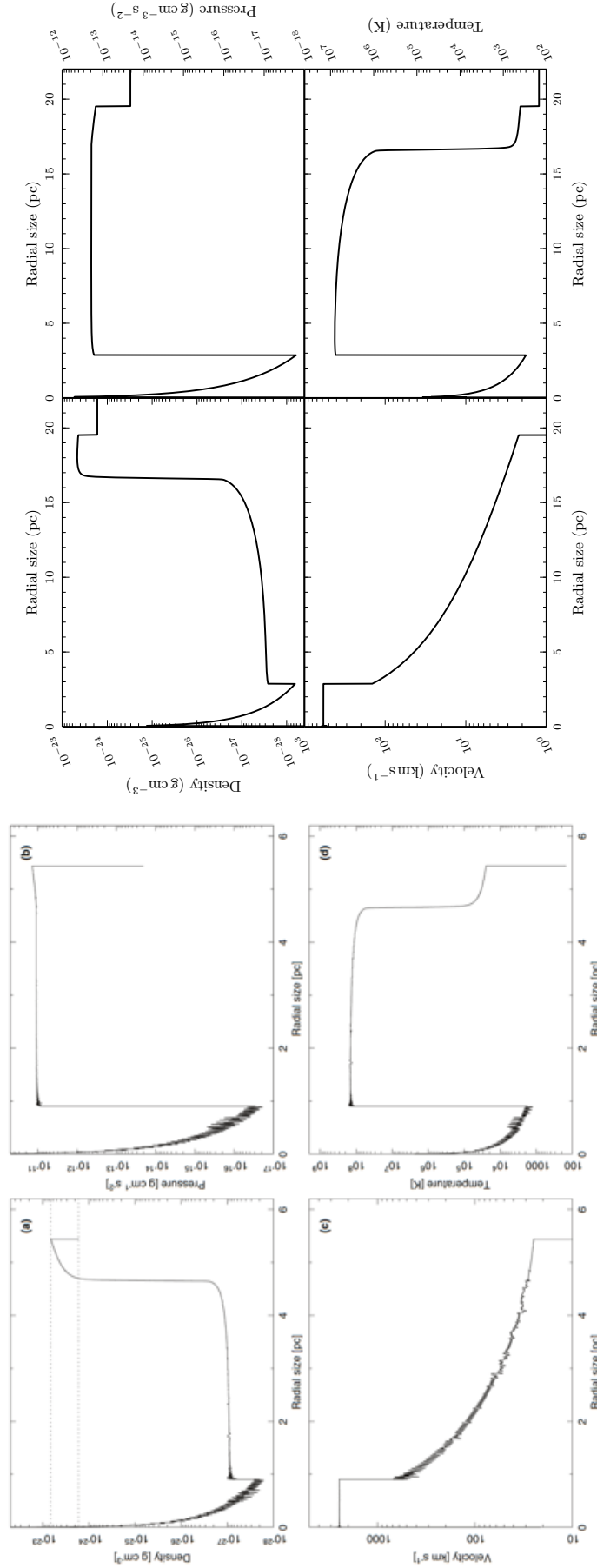


FIGURE 4.15: **Left:** The full simulations of 100,000 identical eruptions from Darnley et al. (2019a). **Right:** Dynamics of the nova remnant with $M = 1 \times 10^{-7} M_{\odot} \text{ yr}^{-1}$ and $n = 1$ after 100,000 eruptions with a resolution of 100 AU/cell.

TABLE 4.4: Parameters for each run. The final column is the number of eruptions needed for a $1 M_{\odot}$ to grow to $\sim 1.4 M_{\odot}$ with each specific set of parameters. This upper limit of the WD mass was chosen to be when the recurrence period of Run 1 was ~ 50 days, the theoretical lower limit (Kato et al., 2014). We also assign the full simulation from Darnley et al. (2019a) to be Run 0. *We note that all 100,000 eruptions for this simulation were identical, unlike all other runs.

Run # (no cooling)	Run # (cooling)	T_{WD} (K)	\dot{M} ($M_{\odot}\text{yr}^{-1}$)	ISM density ($1.67 \times 10^{-24} \text{ g cm}^{-3}$)	Number of eruptions
0	-	-	1.6×10^{-7}	1	100,000*
1	12	1×10^7	1×10^{-7}	1	819,565
2	13	1×10^7	1×10^{-7}	10	819,565
3	14	1×10^7	1×10^{-7}	100	819,565
4	15	1×10^7	1×10^{-8}	1	384,257
5	16	1×10^7	1×10^{-8}	10	384,257
6	17	1×10^7	1×10^{-8}	100	384,257
7	18	1×10^7	1×10^{-9}	1	153,451
8	19	1×10^7	1×10^{-9}	10	153,451
9	20	1×10^7	1×10^{-9}	100	153,451
10	-	3×10^7	1×10^{-7}	1	798,381
11	-	5×10^7	1×10^{-7}	1	793,802

years (over 819,565 eruptions) for the WD in this system to grow from $1 M_{\odot}$ to a mass whereby it is experiencing nova eruptions with inter-eruption times of ~ 50 days.

After finding that a lower resolution simulation with 100 AU/cell would have little effect on the long term structure of the remnant, as discussed in Section § 4.2.2, we ran this reference simulation with the full 819,565 eruptions at a resolution of 100 AU/cell. The dynamics of this full simulation are given in Figure 4.14 and in Figure 4.15 we compare the first 100,000 eruptions from Run 1 to the full 100,000 identical eruptions from Darnley et al. (2019a). Figure 4.16 compares the dynamics from the full results of the simulations with the three largest numbers of eruptions (10,000 eruptions at 10 AU/cell, 100,000 eruptions at 100 AU/cell and the full 819,565 eruptions also at 100 AU/cell). The left plot of Figure 4.14 shows the density, pressure, velocity and temperature characteristics of the nova remnant shell after growing from $1 M_{\odot}$ to just over $1.4 M_{\odot}$ and the right plot shows the radial size of the shell after the same amount of time (cumulative time) as well as with respect to the recurrence period of the system.

In the top left panel of the left plot of Figure 4.14 we see that the boundary of the inner edge and the outer edge of the shell extends to approximately 26 and 28 parsecs, respectively, giving a shell thickness of approximately 7%. This is clearly much thinner than the NSR surrounding M31 2008-12a ($\sim 22\%$ from both observations

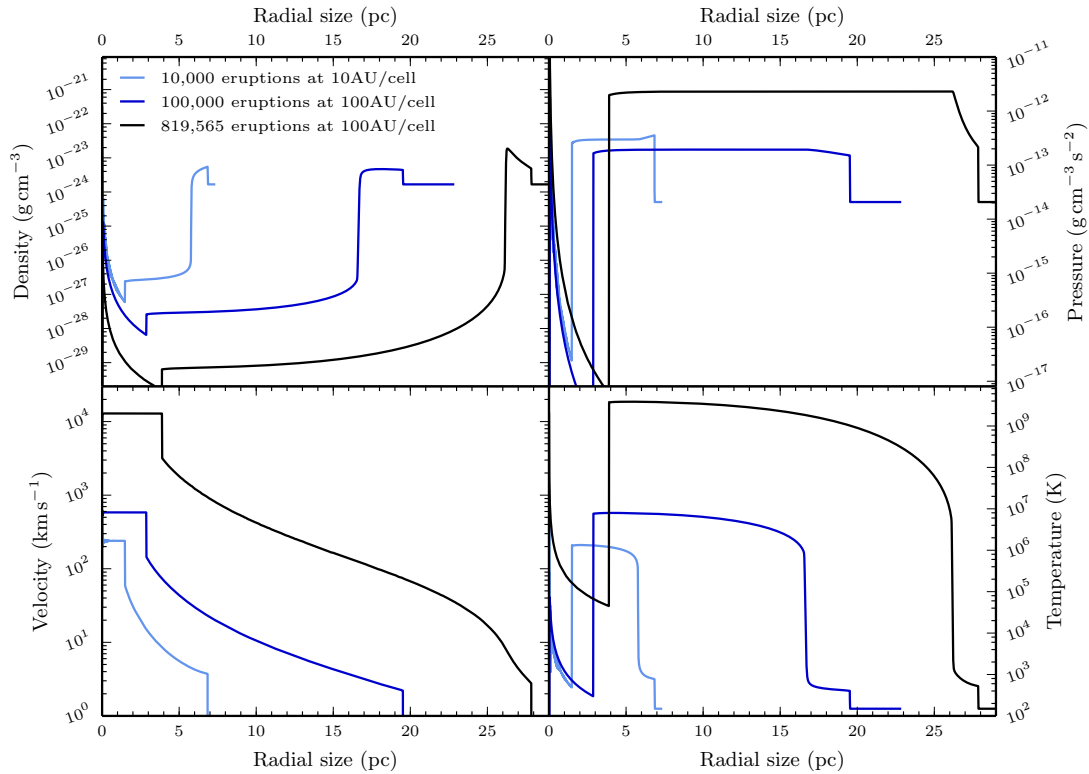


FIGURE 4.16: Dynamics of the nova remnant from three separate simulations with $\dot{M} = 1 \times 10^{-7} M_{\odot} \text{ yr}^{-1}$ and $n = 1$. One has 10,000 eruptions at a resolution of 10AU/cell, another has 100,000 eruptions at a resolution of 100 AU/cell, and the other shows the full 819,565 eruptions at a resolution of 100 AU/cell.

and simulations; Darnley et al., 2019a). However, as can be seen in the right plot of Figure 4.14 and the inset, this final shell thickness was not a constant feature of the remnant over the whole time period of evolution. This is also illustrated in Figure 4.17, which shows how the shell narrowed from having a thickness of $\sim 15\%$ ($P_{\text{rec}} = 50$ years) to $\sim 7\%$ ($P_{\text{rec}} = 1$ year) to $\sim 6\%$ ($P_{\text{rec}} = 50$ days) unlike the constant shell thickness from the identical eruption simulations from Darnley et al. (2019a). The inner and outer edge of the shell remained at a constant distance ratio for $\sim 5.2 \times 10^6$ years before compressing. This is equivalent to when the system’s recurrence period becomes shorter than approximately 5 years.

The denser composition of the NSR’s inner edge ($2 \times 10^{-23} \text{ g cm}^{-3}$) compared to the outer edge ($\sim 5 \times 10^{-24} \text{ g cm}^{-3}$) can be attributed to the differences in exposure to the newer eruptions. The propagation of the NSR shell into the surrounding ISM, and therefore the outer edge of the shell, is based upon the combined properties of the majority of previous eruptions, whereas the inner edge is influenced by the increasing rate of arriving material. Effectively, the outer edge of the shell represents the combined properties of all previous ejecta and the inner edge represents the properties of the newest material.

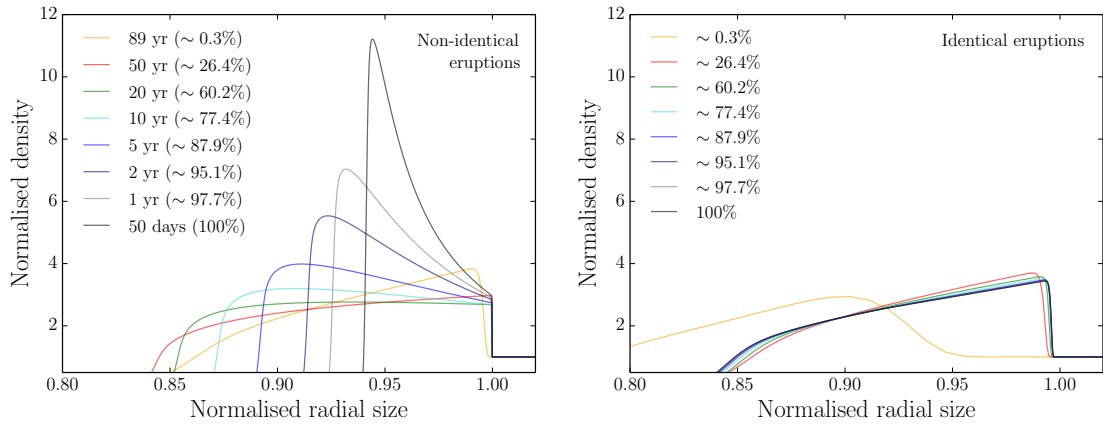


FIGURE 4.17: Comparison of the evolution of shell thickness for the non-identical eruptions simulation vs the identical eruptions simulations given in [Darnley et al. \(2019a\)](#). The points of each simulation coinciding with the particular shell sizes are given as percentages. For example, after $\sim 26.4\%$ of the non-identical eruptions simulation, the recurrence period of the system was 50 years. The radii have been normalised with the respect to the size of the nova shell at each recurrence period whereas density has been normalised with respect to the ISM density.

As evident in the bottom left panel of the left plot of Figure 4.14, the velocity of the material within the inner cavity is high ($\sim 1.5 \times 10^4 \text{ km s}^{-1}$) as it expands freely with little resistant matter. The velocity then drops substantially as the ejecta pile-up region is encountered for the first time, with temperatures increasing by up to four orders of magnitude (see bottom right panel of the left plot). The velocity and temperature within the ejecta pile-up region then declines continuously out to the NSR as the ejecta encounters both previously ejected material and reverse shocks, with the cool outer edge expanding at a relatively low $\sim 20 \text{ km s}^{-1}$.

4.5.2 Run 2 and Run 3

Run 2 and Run 3 are simulated in a similar way to Run 1 (see Section § 4.5.1) using the same system parameters and only the ISM density varying. Run 2 is prepopulated by an ISM with density $1.67 \times 10^{-23} \text{ g cm}^{-3}$ ($n = 10$) and the ISM density of Run 3 is $1.67 \times 10^{-22} \text{ g cm}^{-3}$ ($n = 100$). A comparison of the NSR shell for the three different ISM densities is given in Figure 4.18. As can be seen in the top left panel on the left plot, the size of the nova shell after the same number of eruptions diminishes as the ISM density increases, only extending to $\sim 18 \text{ pc}$ and $\sim 11 \text{ pc}$ for the $n = 10$ and $n = 100$ environments, respectively. As can be seen in the top panels of Figure 4.19, the width ratio of the shell can also be seen to decrease as the surrounding material's density increases as the same kinetic energy from the identical nova systems meet an increasingly higher resistance.

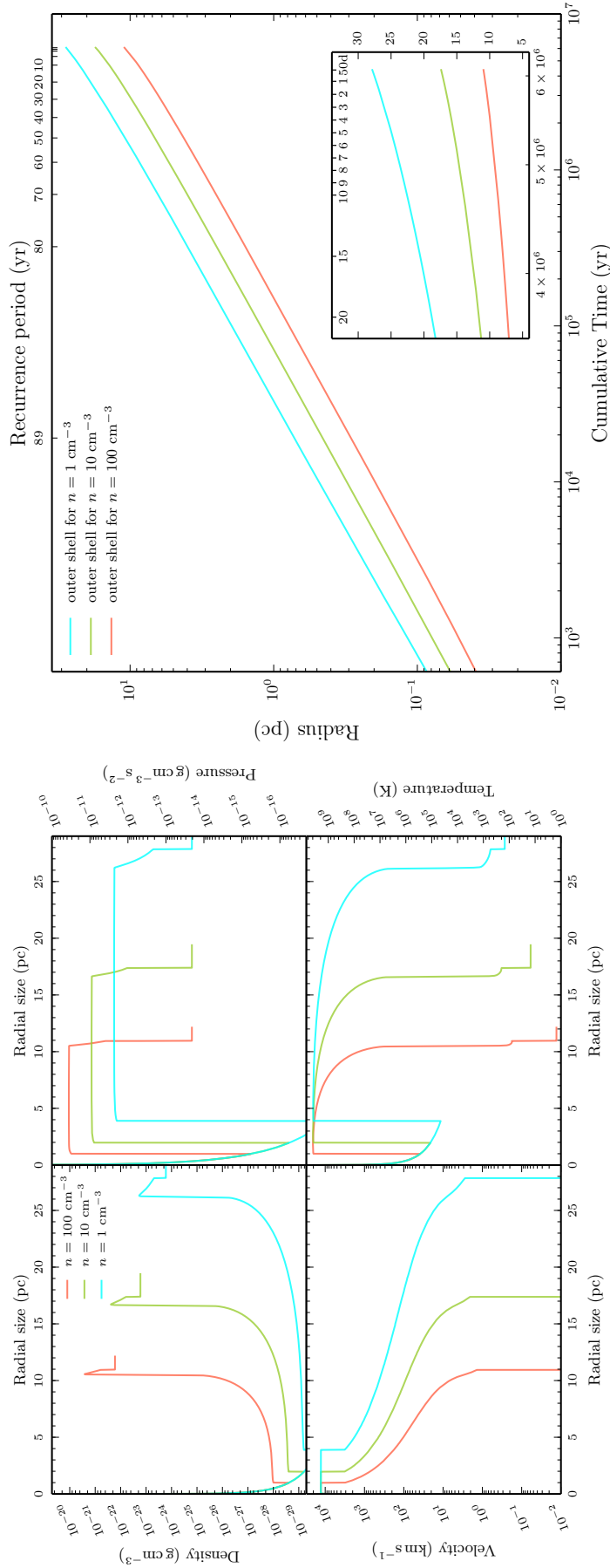


FIGURE 4.18: **Left:** Dynamics of the nova remnant with $\dot{M} = 1 \times 10^{-7} M_{\odot} \text{ yr}^{-1}$ for three different ISM densities after 819,565 eruptions with a resolution of 100 AU/cell. **Right:** Evolution of the outer edge of the shell with respect to cumulative (elapsed) time and recurrence period for the three different ISM densities.

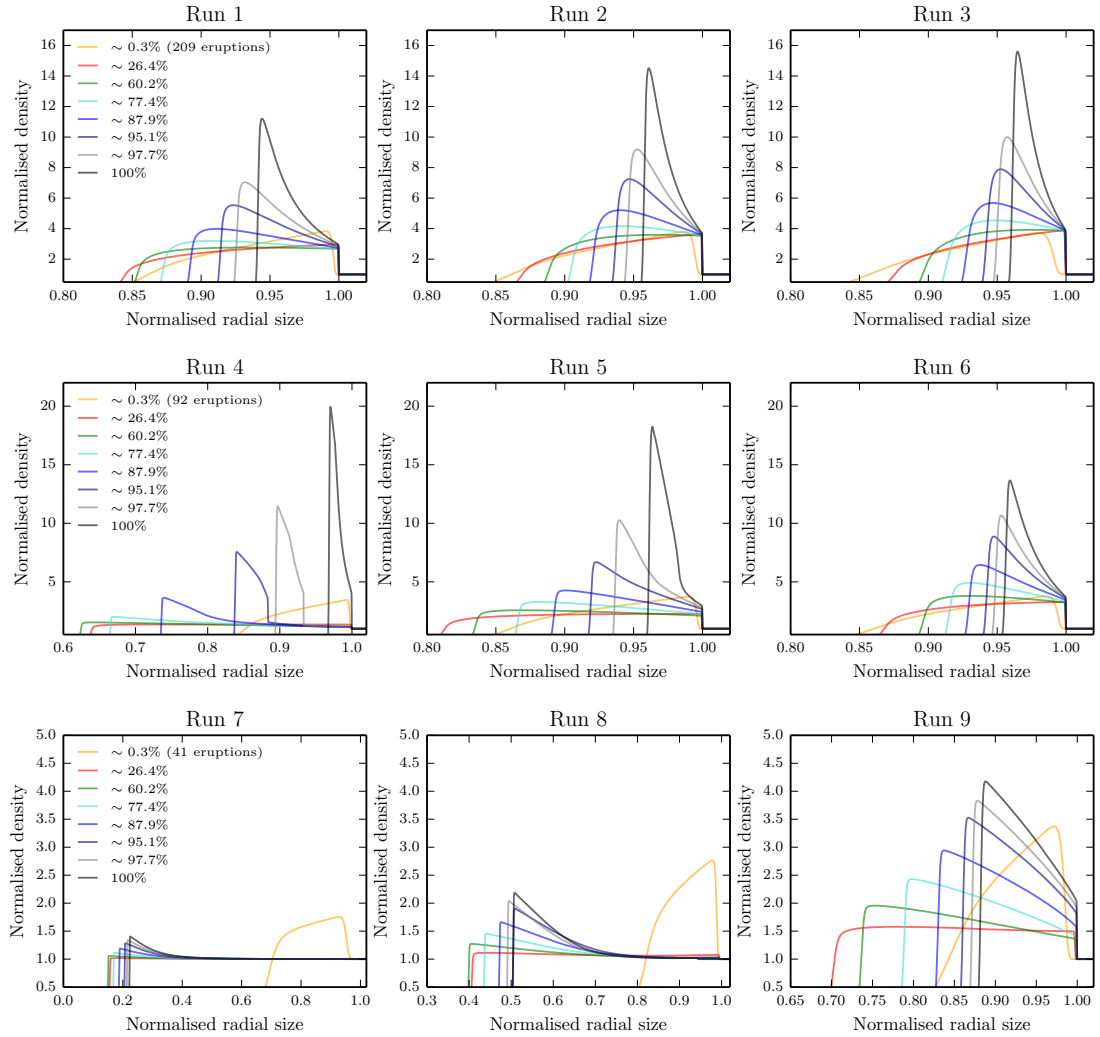


FIGURE 4.19: The evolution of the remnant shell at the same stage of each simulation for Runs 1 – 9. The top left panel showing the evolution of the $1 \times 10^{-7} M_{\odot} \text{ yr}^{-1}$ shell in the $n = 1$ environment is the same as that shown in the left panel of Figure 4.17. The points of each simulation coinciding with the particular shell sizes are given as percentages. For example, after $\sim 0.3\%$ of Run 1, 2 and 3, there have been 209 eruptions (Run 4, 5 and 6 have 92 eruptions after $\sim 0.3\%$ of the simulations and Run 7, 8 and 9 have 41 eruptions after $\sim 0.3\%$).

As expected, the density in the cavity and ejecta pile-up regions is larger for the higher density ISM by approximately the same factor as its surroundings (see the top left plot of Figure 4.18). These regions are not only denser as a result of their ISM environments, but are also more compressed for higher n , leading to increased pressures. The velocity of the material contained inside the inner cavity from each of the three runs is identical because, as in the case for Run 1, the ejecta is essentially in a state of free expansion. Also, temperatures in this same region for each $1 \times 10^{-7} M_{\odot} \text{ yr}^{-1}$ run all reach the same extreme temperature of $\sim 5 \times 10^9$ K, as nova ejecta expanding without resistance collide into earlier ejected matter in the pile-up region, before dropping away to < 100 K at the nova shell’s inner edge (i.e. the

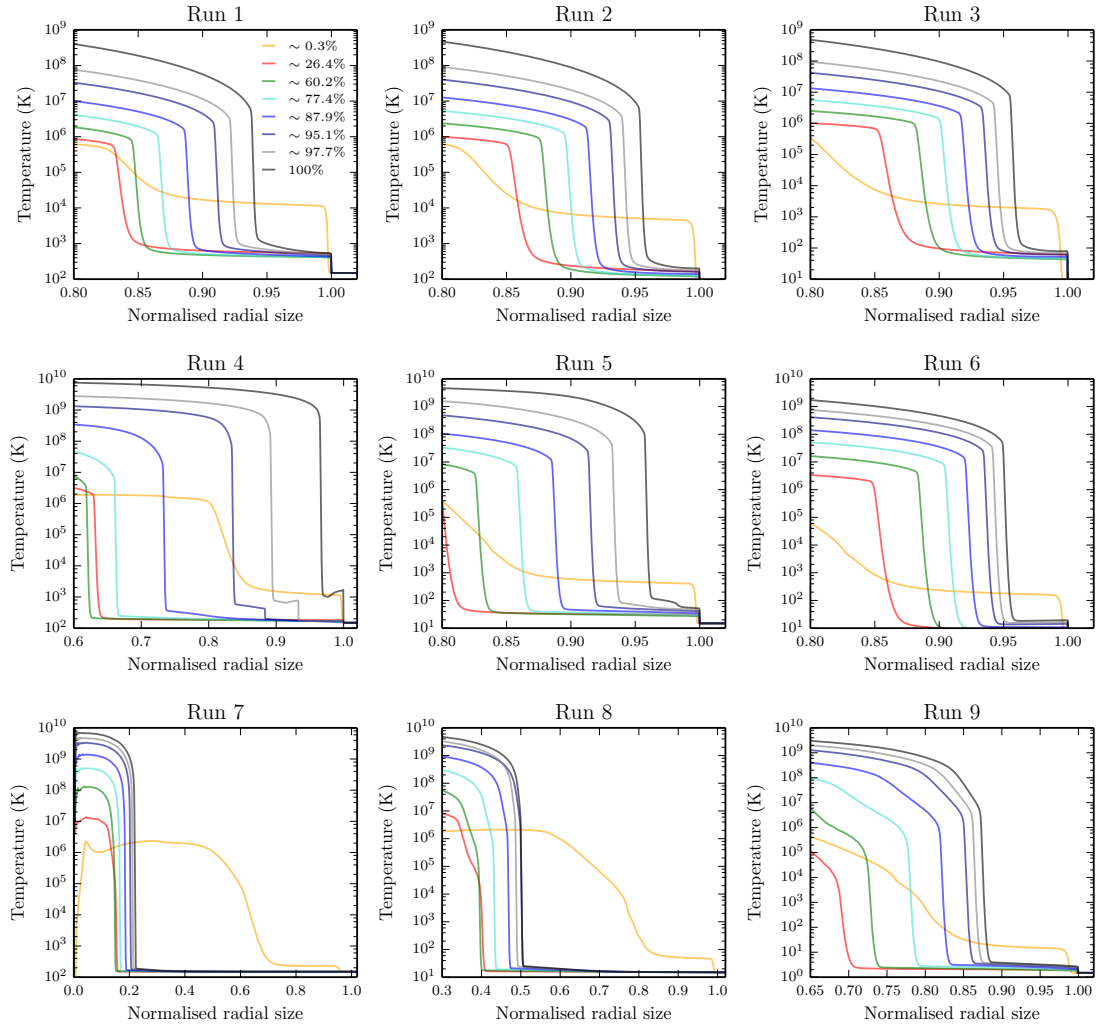


FIGURE 4.20: The temperature evolution of the remnant shell at the same stage of each simulation for Runs 1 – 9. Similar to Figure 4.19, the points of each simulation coinciding with the particular shell sizes are given as percentages.

properties in this region don't strongly depend upon n). The temperature of the shell for each run begins hot ($\sim 10^4$ K) but then cools after $\sim 25\%$ of the simulation where it then maintains the same temperature throughout the rest of its evolution (see the top panels of Figure 4.20).

The growth of each shell within all three different ISM densities follow similar power law evolution as illustrated in the right plot of Figure 4.18. However, as we can see, the gradient (and therefore the index) of the power law changes over time, reflecting the continuously changing eruptions shaping the NSR evolution. This can be seen most clearly for the radial growth curve of Run 1 in the inset of Figure 4.18. The effect of varying ISM density on the radial size evolution of the NSR is captured by a translation of the power law i.e. changing the y-intercept.

4.5.3 Run 4, Run 5 and Run 6

The next set of simulations consisted of a WD with a temperature of 1×10^7 K accreting hydrogen rich material at a rate of $\dot{M} = 1 \times 10^{-8} M_{\odot} \text{ yr}^{-1}$ within the same three ISM densities introduced previously. If the accretion rate in a true nova system was lower than that in the first three runs, then possible physical reasons behind this could be either a lower density wind coming from the donor or a different accretion mechanism present within the system. Therefore, the red giant wind mass loss rate described in Section § 4.2 was lowered, like the accretion rate, by the same factor of ten in Run 4, 5 and 6. The simple model we produced found that it would take this system 60,727,590 years (over 384,257 eruptions) for the WD to grow from $1 M_{\odot}$ to the upper limiting $\sim 1.4 M_{\odot}$. At the upper limiting WD mass that we have set, this system has a recurrence period of ~ 5.3 years.

A comparison of the NSR shell for the three different ISM densities is given in Figure 4.21. The overall structure of the remnants are similar to those grown from the higher mass accretion rate. The major difference is seen in their much larger size. The shell grown in the lowest density ISM reaches out to approximately 115 pc, a consequence of the larger amount of kinetic energy produced by this system (see, for example, Figure 4.10) from the longer evolutionary period growing the WD to M_{Ch} (~ 60 Myr compared to ~ 6 Myr in Run 1). Additionally, we know that the total kinetic energy from the red giant wind in these runs (as well as Runs 1–3 and Runs 7–9) is much lower than the total kinetic energy from the nova eruptions throughout the full evolution (see Figure 4.22). This tells us that ejecta from the nova is still the influencing factor in growing this NSR, even for systems with low accretion rates. Even the shell grown in the high density environment ($n = 100$) is larger (~ 40 pc) than the largest remnant grown from $1 \times 10^{-7} M_{\odot} \text{ yr}^{-1}$. Unlike Run 1, 2 and 3, the pressures seen through the remnants of Run 4, 5 and 6 are alike, reflecting the near identical lower limiting densities and upper limiting temperatures seen in all three cavity regions, resulting from system having long amounts of times to recover between eruptions.

The bottom right panel of Figure 4.21 shows that within the low density environment (Run 4) and the high density environment (Run 6), the remnant shell exhibits a temperature gradient, lower at the inner edge than the outer edge. We can see this feature clearly in the middle panels of Figure 4.20 for the $n = 1$ remnant, forming after approximately 97% of the simulation, however with further inspection of the shell grown in the $n = 100$ environment, the temperature gradient across this shell is marginal. The feature in the $n = 1$ shell can be attributed to the pressure gradient seen in the shell whereby there are lower pressures at the outer edge for each

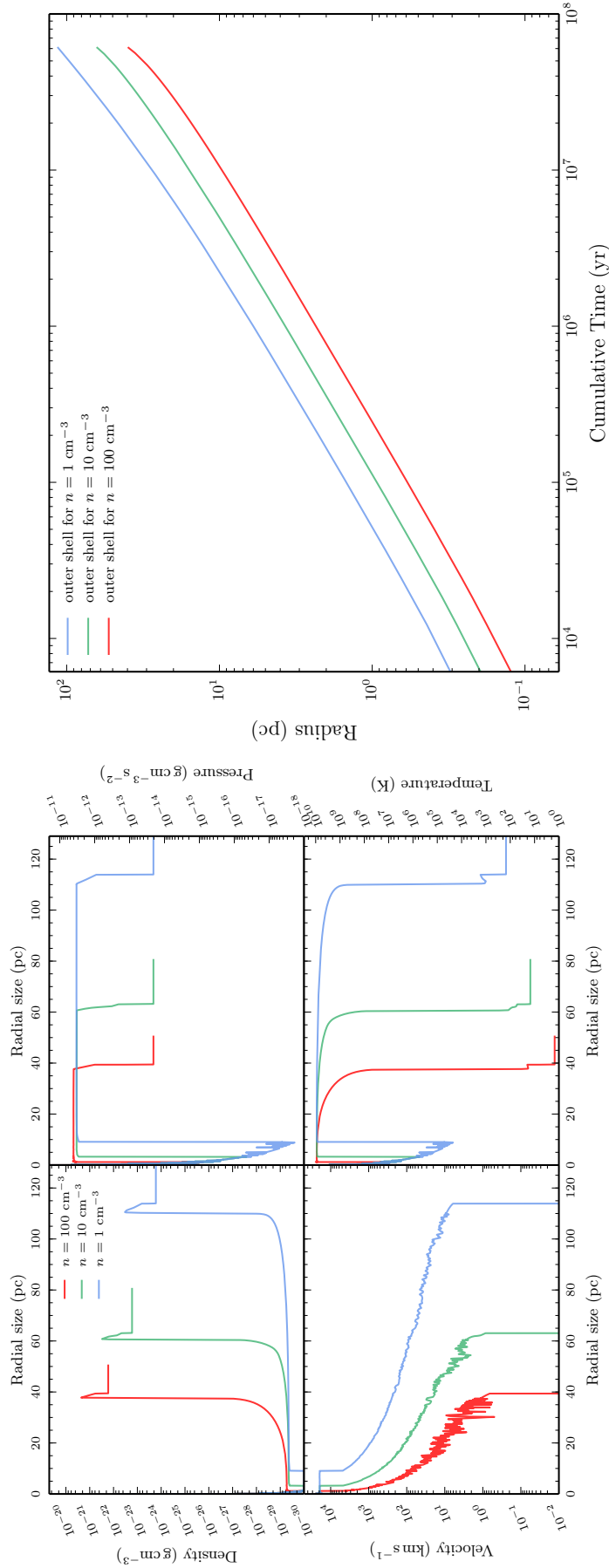


FIGURE 4.21: **Left:** Dynamics of the nova remnant $1 \times 10^{-8} M_{\odot} \text{ yr}^{-1}$ for three different ISM densities after 384,257 eruptions with a resolution of 200AU/cell. **Right:** Evolution of the outer edge of the shell with respect to cumulative (elapsed) time and recurrence period for the three different ISM densities.

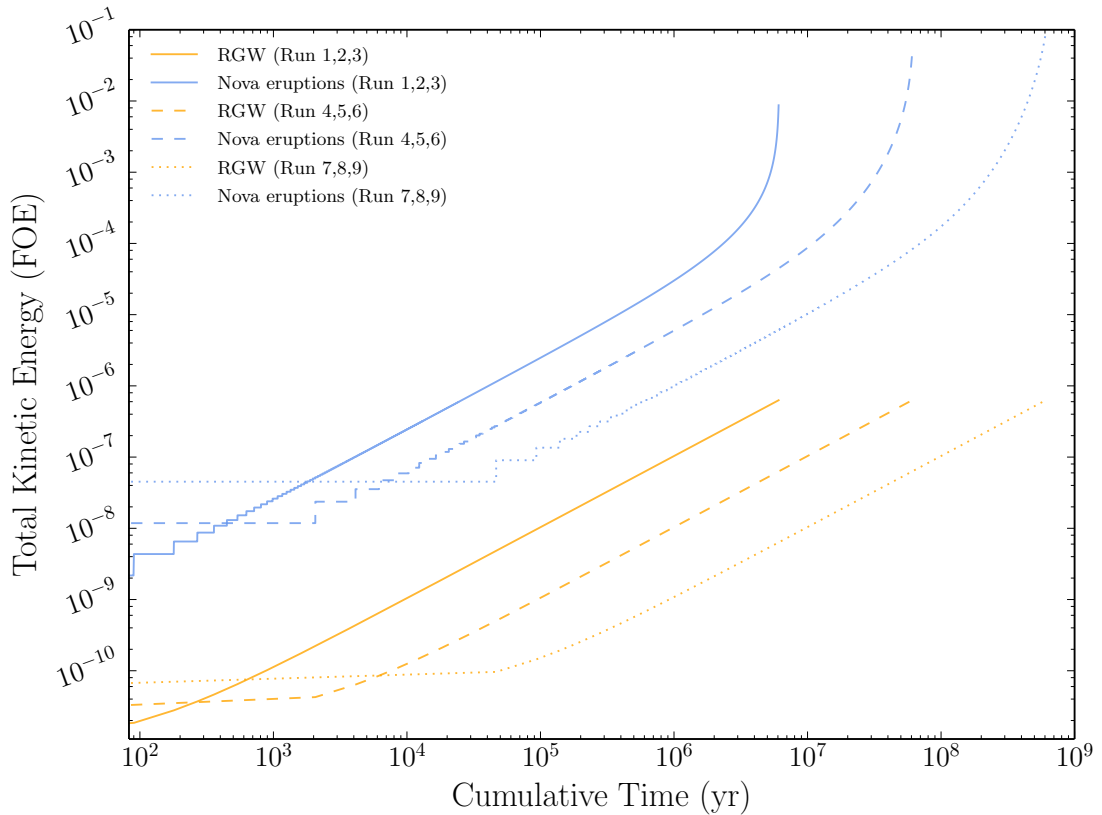


FIGURE 4.22: A comparison of the evolution of kinetic energy from nova eruptions and red giant wind for Runs 1–9.

remnant, yet for $n = 1$ and $n = 100$ this difference is not as large as $n = 10$. In the velocity panel of the full simulations in Figure 4.21, we also begin to see the results of fewer total eruptions in Runs 4–6, through fully resolving individual outbursts in the form of the disturbed profile. We can see in the right plot of Figure 4.21 that the outer edge of the shell follows a power law growth (in the same manner as the shells in Figure 4.18). As before, the index of the power law continuously changes as a result of the non-identical ejecta, with the changes in shell growth due to varying ISM densities captured with a simple translation in the y-axis (change of y-intercept).

The middle panels of Figure 4.19 show how the shell evolves for the three different ISM environments. The evolution of the shell in the higher density ($n = 100$) environment looks remarkably similar to the $1 \times 10^{-7} M_{\odot} \text{ yr}^{-1}$ NSR shell in the lower $n = 1$ ISM environment throughout. The remnant shells grown with $1 \times 10^{-8} M_{\odot} \text{ yr}^{-1}$ in the low density ISM ($n = 1$ and $n = 10$) appear to evolve in a considerably different manner, starting with a very wide ($\sim 40\%$ of the remnant’s size for $n = 1$) low density shell that compresses into a thin high density border.

4.5.4 Run 7, Run 8 and Run 9

The next set of simulations consisted of a WD with a temperature of 1×10^7 K accreting material at a rate of $\dot{M} = 1 \times 10^{-9} M_{\odot} \text{ yr}^{-1}$. This is still a feasible mass accretion rate to use as systems with even lower rates than this have been shown to produce novae in which the WD is growing in mass towards M_{Ch} (Starrfield et al., 2020). As in Run 4, 5 and 6, the red giant wind mass loss rate described in Section § 4.2 was lowered, like the accretion rate, by a factor of 100 in Run 7, 8 and 9. The simple model we use for growing a WD determined that it would take this system 607,231,855 years (but only over 153,451 eruptions) for the WD to grow from $1 M_{\odot}$ to the upper limiting $\sim 1.407 M_{\odot}$. At the upper limiting WD mass that we have set, this system has a recurrence period of ~ 117.6 years, and so incidentally would not be classed as a recurrent nova.

A comparison of the NSR shell for the three different ISM densities is given in Figure 4.23. The remnant grown in the higher density ISM takes the familiar shape we have seen in Figure 4.18 and Figure 4.21 with a very low density cavity preceding a high density shell approximately 140 pc in size. However, this same structure is not found for the $n = 1$ and $n = 10$ ISM remnants. Instead, we see a very low density cavity bordered by considerably wide shell that is indistinguishable from the surrounding ISM density, especially in the case of $n = 1$. These differing shell structures with their low temperatures (< 100 K) can be seen clearly in the bottom panels of Figure 4.19 and Figure 4.20, respectively. The inner edge of the NSR grown in the low density medium extends to approximately 200 pc as a result of the large injection of kinetic energy from the underlying system (see, for example, Figure 4.10), not dramatically larger than those in the higher density environments, yet the width of this shell is gargantuan, potentially reaching out to 900 pc. As expected, the outer shells of the remnants grown in systems with a lower accretion rate follow the same power law growth over time as previous runs. Yet there is more of a deviation between these curves at later stages of the NSR's evolution because of the much larger period of time for these systems to grow to the M_{Ch} ($\sim 6 \times 10^8$ years compared to $\sim 6 \times 10^6$ years for Run 1, 2 and 3).

The nova eruptions from this system occur infrequently for the vast majority of the evolution, starting with recurrence periods of $\sim 50,000$ years when the WD is $1 M_{\odot}$ and only dropping to ~ 100 years at the limiting WD mass (see Figure 4.12). Therefore, a combination of low energetic eruptions and long periods between each lead to a very wide, nearly non-existent shell as the ejecta individually dissipate into the surrounding ISM without any pile-up occurring. Observationally, this type of NSR would be difficult to discern from the local environment. However, we would

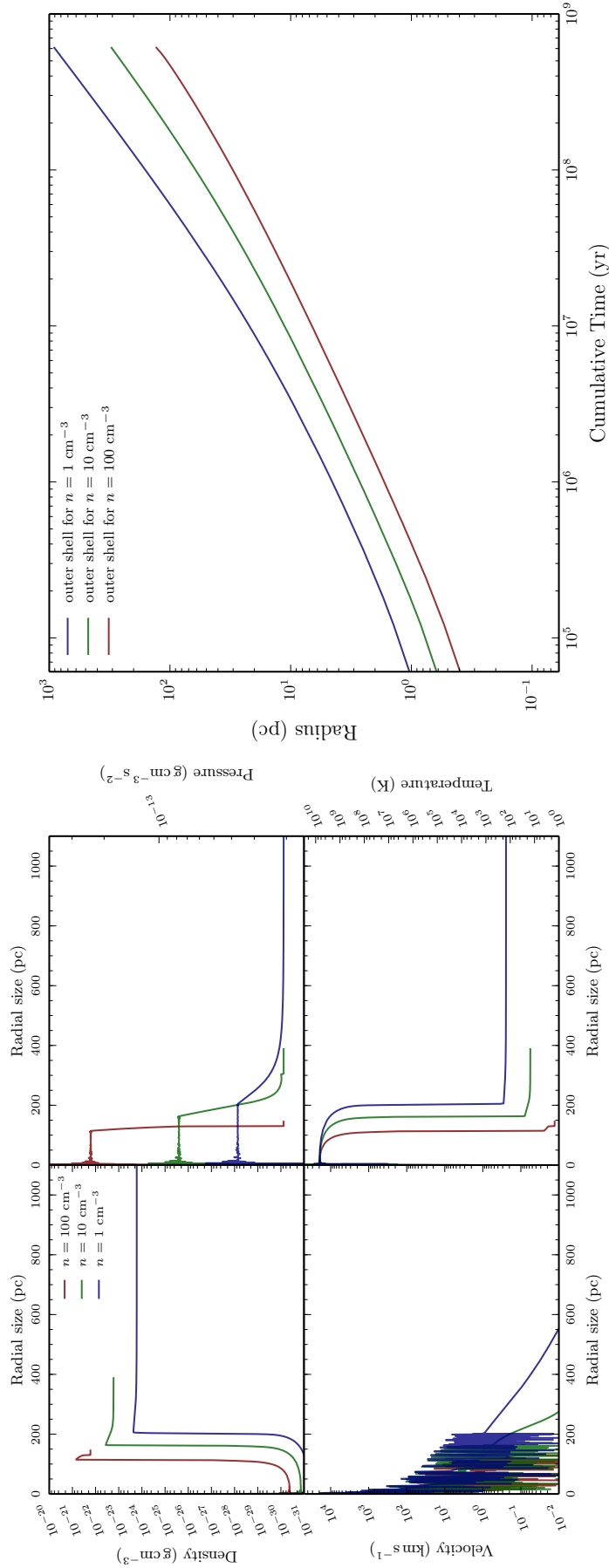


FIGURE 4.23: **Left:** Dynamics of the nova remnant $1 \times 10^{-9} M_{\odot} \text{ yr}^{-1}$ for three different ISM densities after 153,451 eruptions with a resolution of 1000 AU/cell. **Right:** Evolution of the outer edge of the shell with respect to cumulative (elapsed) time and recurrence period for the three different ISM densities.

not expect this form of shell to exist around currently known recurrent novae as the system we have simulated here does not have short inter-eruptions times, the shortest (~ 100 years) being on the border of the current definition of a recurrent nova (see Section § 1.4).

4.5.5 Run 1, Run 10 and Run 11

The underlying WD temperature does not have a significant impact on the evolution of the various parameters given in Section § 4.4.2 (see Figure 4.10 to Figure 4.13). As an example, for the system with an accretion rate of $\dot{M} = 1 \times 10^{-7} M_{\odot} \text{ yr}^{-1}$, the evolution of each parameter is very similar throughout, regardless of the WD temperature. This is also true for the total kinetic energy generated from the entirety of the nova eruptions.

This is reflected in the set of simulations with the WD temperature being varied from $1 \times 10^7 \text{ K}$ to $3 \times 10^7 \text{ K}$ to $5 \times 10^7 \text{ K}$ and setting the accretion rate as $\dot{M} = 1 \times 10^{-7} M_{\odot} \text{ yr}^{-1}$ and the ISM density as $n = 1$. A comparison of the NSR shell for the three different WD temperatures is given in Figure 4.24. Clearly, the overall structure of each NSR is very similar, with the shell only becoming moderately larger as the WD temperature increases. The outer edge of the remnant shell for the coolest WD is $\sim 28 \text{ pc}$ whereas the hottest WD leads to an outer edge of $\sim 30 \text{ pc}$ informing us that, for the highest accretion rate we have considered, the WD temperature has a small impact on the large scale structure of the NSR. The radial growth curves on the right of Figure 4.24, in the form of power laws with time dependent indices, are close to being indiscernible for the majority of the evolution, with the small deviations occurring in last $\sim 1 \text{ Myr}$.

We also see these similarities with the evolution of the shell for each WD temperature (see Figure 4.25), such that at each epoch, the density and width of the shells are a close match. Furthermore, it is apparent through looking at how the recurrence period (shown in Figure 4.26) and the total kinetic energy (shown in Figure 4.27) change as the NSR grows in each of the systems, that the temperature of the underlying WD has little impact. This is likely to be because the system has a high accretion rate ($1 \times 10^{-7} M_{\odot} \text{ yr}^{-1}$), so is dominated by accretion heating⁸. However, the influence of the WD temperature may become more substantial as the accretion rate is lowered due to the accretion heating becomes less severe.

⁸Yaron et al. (2005) accounted for accretional heating within their computations.

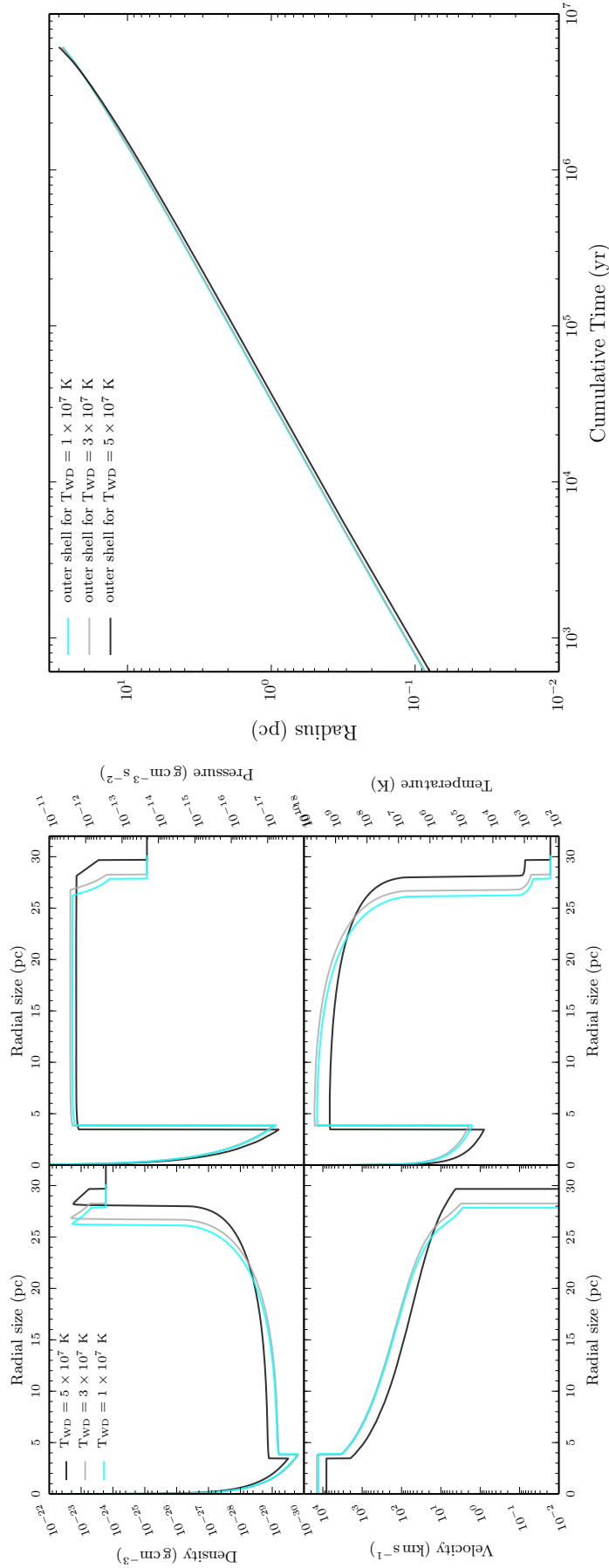


FIGURE 4.24: Left: Dynamics of the nova remnant $1 \times 10^{-7} M_{\odot} \text{ yr}^{-1}$ with $n = 1$ for three different WD temperatures with 819,565 eruptions with a resolution of 100 AU/cell. **Right:** Evolution of the outer edge of the shell with respect to cumulative (elapsed) time and recurrence period for the three different WD temperatures.

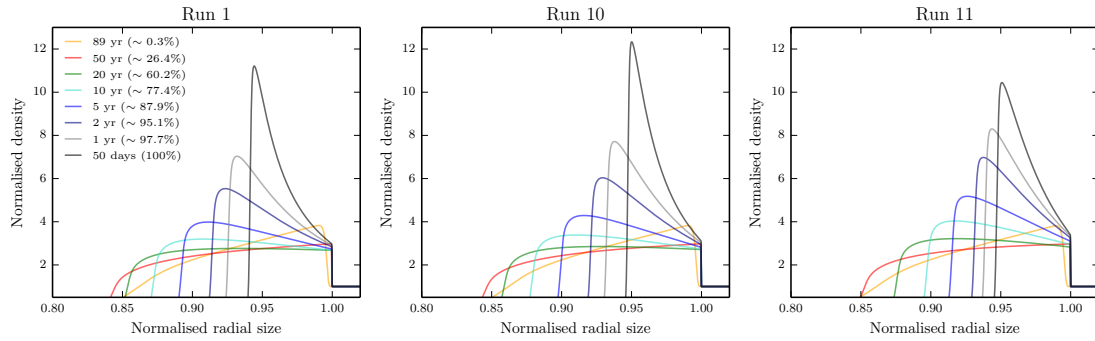


FIGURE 4.25: The evolution of the remnant shell at the same stage of each simulation for the three different WD temperatures, Run 1 (1×10^7 K), Run 10 (3×10^7 K) and Run 11 (5×10^7 K) with the surrounding ISM density of $n = 1$. Similar to Figure 4.17, the points of each simulation coinciding with the particular shell sizes are given as percentages with the recurrence period at that point.

4.6 Main simulations with radiative cooling

The ejected material from nova eruptions, like any astrophysical material, will lose energy through radiative cooling. This mechanism of radiative cooling, which would take place early on in the evolution of the NSR when outbursts have more mass but are less energetic, will affect emission signatures as well as the dynamics. Therefore, in order to simulate a more realistic NSR system, we implemented this process within the full set of previous simulations, as outlined in Table 4.4.

The cooling model utilised in Morpheus was taken from Figure 1 of Raymond et al. (1976). The cooling rate is given as a function of gas temperature of an optically thin plasma, with no dust or molecules, made up of hydrogen, helium, carbon, nitrogen, oxygen, neon, magnesium, silicon, sulphur, calcium, iron and nickel. The cooling processes that are considered for this function include permitted, forbidden, and semiforbidden line transitions, dielectronic recombination and Bremsstrahlung, radiative recombination, as well as two-photon continua (Raymond et al., 1976). From this function, it is evident that radiative cooling becomes ineffective below a temperature of 10^4 K (Vaytet et al., 2007b). Also, above 10^8 K, all of the gas becomes ionised and so will only radiate through free-free Bremsstrahlung (Vaytet et al., 2007b). For the range of temperatures between these limits, cooling is dominated by line-cooling from the metals within the gas (Vaytet et al., 2007b).

The cooling curve presented in Raymond et al. (1976) was tabulated and interpolated between to take into account the cooling rate power index for all required temperatures (Vaytet, 2009). For each cell of a simulation, the energy lost through radiative cooling is implemented through subtracting an amount of energy from the total amount of energy in that cell (Vaytet, 2009; Vaytet et al., 2007b). Additionally,

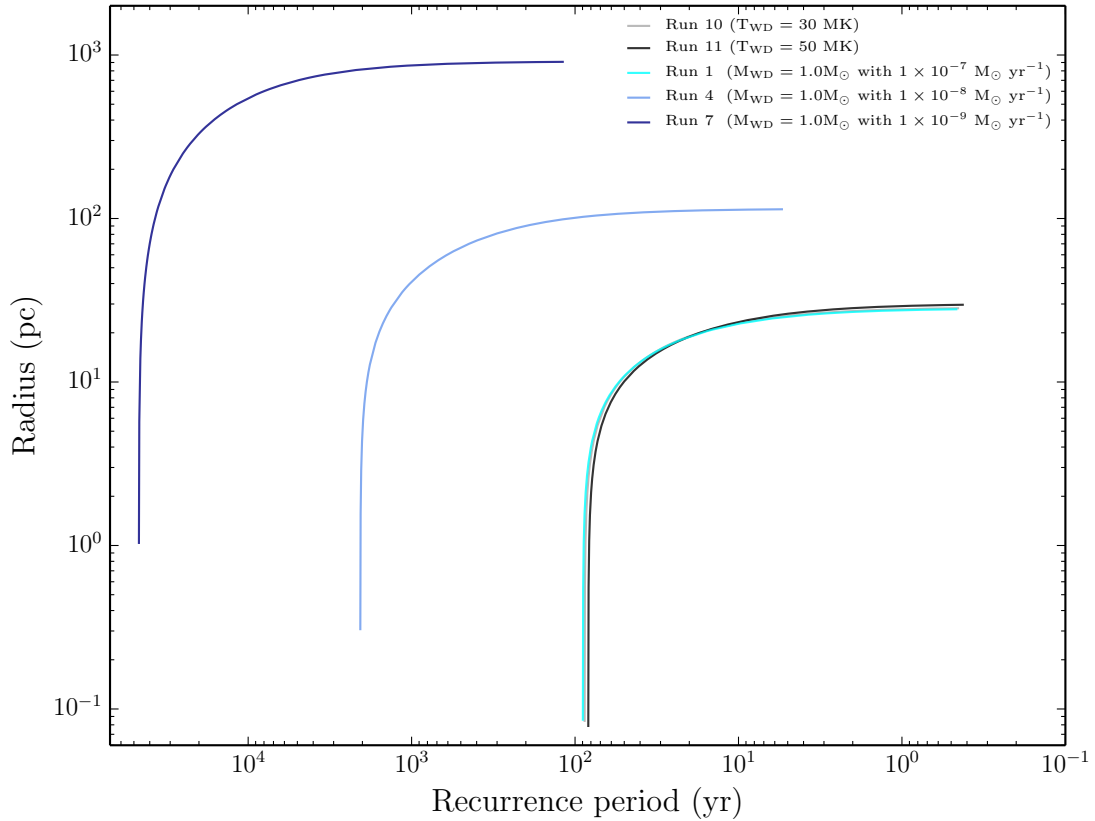


FIGURE 4.26: The radial size evolution of the remnant shell with respect to the recurrence period of the system for different WD temperatures (Run 1, 10 and 11). We have also included changes to accretion rate runs (Run 4 and Run 7) to illustrate the largely different impacts from varying each parameter.

a cooling timescale must be accounted for alongside the dynamical timescale (the amount of time for a wave to cross the width of an entire cell) when considering the minimal timestep of the simulations. The cooling timescale in this case is an approximation of the time it would take for a cell to lose all of its energy from the cooling rate in [Raymond et al. \(1976\)](#) if it remained constant ([Vaytet, 2009](#)).

4.6.1 Run 12 (reference simulation with radiative cooling)

We took the same parameters as the reference simulation (Run 1; Section § 4.5.1) to run our reference simulation with radiative cooling (Run 12). Specifically, we simulated nova eruptions from a growing WD with a temperature of 1×10^7 K accreting at a rate of $1 \times 10^{-7} M_{\odot} \text{ yr}^{-1}$ within a low density ISM ($1.67 \times 10^{-24} \text{ g cm}^{-3}$). As with Run 1, we estimated that it would take 6,073,159 years (over 819,565 eruptions) for the WD in this system to grow from $1 M_{\odot}$ to the Chandrasekhar limit. We then implemented radiative cooling in this simulation. The reference simulation including

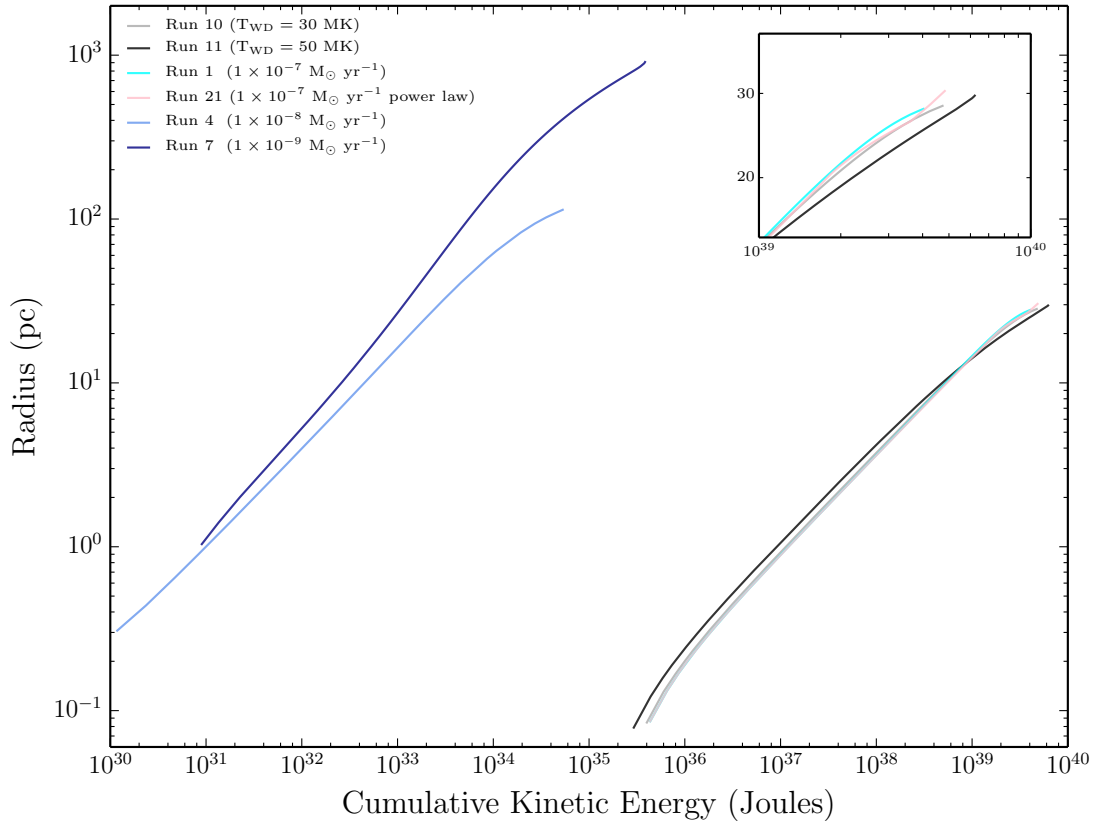


FIGURE 4.27: The radial size evolution of the remnant shell with respect to the cumulative kinetic energy of the system for different WD temperatures (Run 1, 10 and 11). Again, like Figure 4.26, we have also included changes to accretion rate runs (Run 4 and Run 7) to illustrate the largely different impacts from varying each parameter. We can also see the increase in total kinetic energy from Run 21 (the power law interpolation, see Section § 4.9.2 for more details). It is important to note that the cumulative kinetic energy for Run 4 and Run 7 is much lower than seen in Figures 4.10, 4.11, 4.12 and 4.13 as here we are taking a small subset of the kinetic energy values generated by our simple model of a growing WD, in line with the number of outputs from the simulations.

radiative cooling after 1000 eruptions is shown on the right of Figure 4.28 and the full reference simulation with radiative cooling is shown in Figure 4.29.

The major differences we see when comparing Run 1 (without cooling) and Run 12 (with cooling) in both Figure 4.28 (right side) and Figure 4.29 revolves around the radial size of the remnant and, in Figure 4.29, the remnant’s shell. This is dramatically different to the negligible effects of radiative cooling on the structure of the NSR in Run 0 (see left side of Figure 4.28; Darnley et al., 2019a).

The crucial reason for differences with cooling and without cooling in our study lies with the characteristics of the eruptions. The remnant in our study is grown with non-identical eruptions with shortening recurrence periods, unlike the remnants

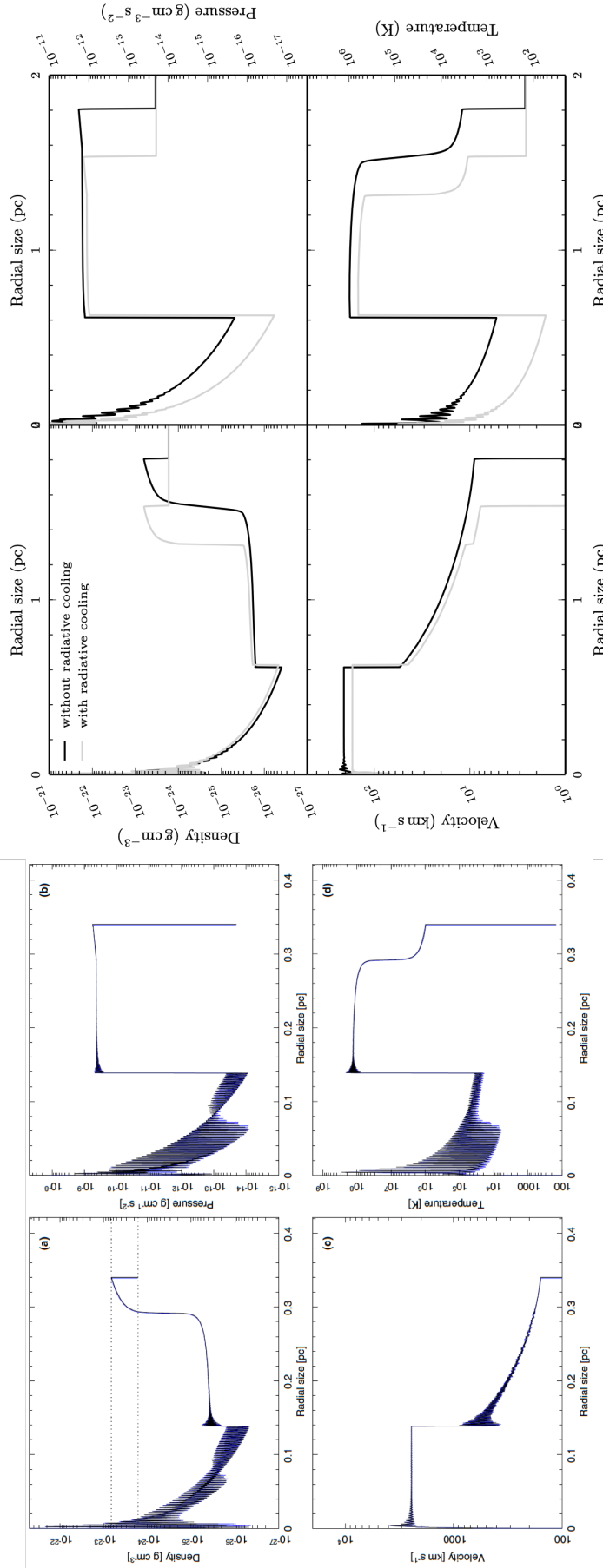


FIGURE 4.28: Comparison of effect of radiative cooling in identical and non-identical eruptions. **Left:** There is a close match between simulations of 1,000 identical eruptions without (black) and with (blue) radiative cooling (Darnley et al., 2019a). **Right:** Comparison of the dramatic effect of radiative cooling in the reference simulation after 1000 eruptions.

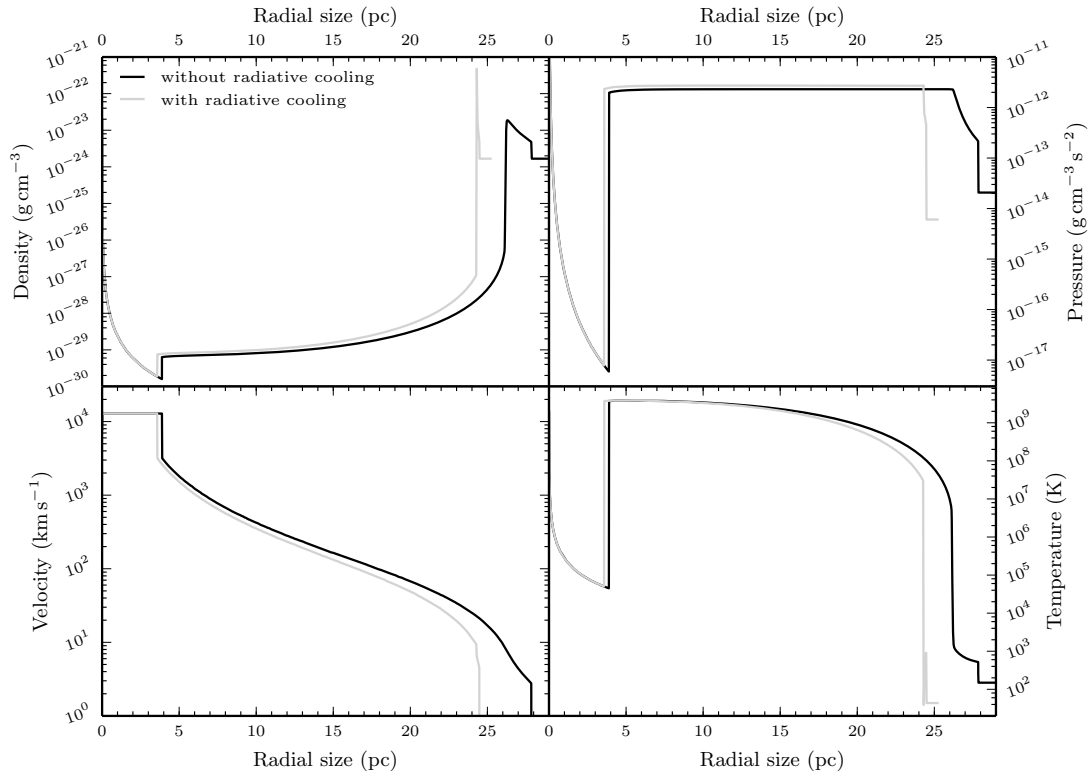


FIGURE 4.29: The dynamics of the simulated nova super-remnants from Run 1 and Run 12, comparing the dramatic effect of radiative cooling in the full reference simulation after 819,565 eruptions. Also note that the characteristics of the surrounding ISM alter with cooling incorporated as the ISM can cool on these very long timescales.

in Run 0 (Darnley et al., 2019a) that had identical eruptions with the same inter-eruption times. As such, the initial eruptions in Run 1 and Run 12 have low velocity, low mass ejecta and long periods between consecutive eruptions allowing the remnant to cool between outbursts. Also, the conditions for cooling are met during this epoch of the remnant’s evolution (see Section § 4.6). The remnant in Run 0, on the other hand, was unable to cool down between eruptions as they were so frequent and so energetic each time, leading to near-identical remnants with and without radiative cooling.

In Figure 4.29, the outer edge of the shell in our reference simulation (Run 1) extends to approximately 28 parsecs, yet the remnant with cooling only reaches a maximum size of ~ 24.5 parsecs. This decrease in radial size is attributed to energy losses within the ejected material reducing the effectiveness of sweeping up the surrounding ISM. Additionally, the shell of the remnant with cooling is much thinner ($\sim 1\%$ of the remnant’s size) as can be seen in the top right panel of Figure 4.30. This results from the material in the early remnant shell losing energy via radiative cooling and therefore lacking the necessary pressure to retain its size. This suppresses the early

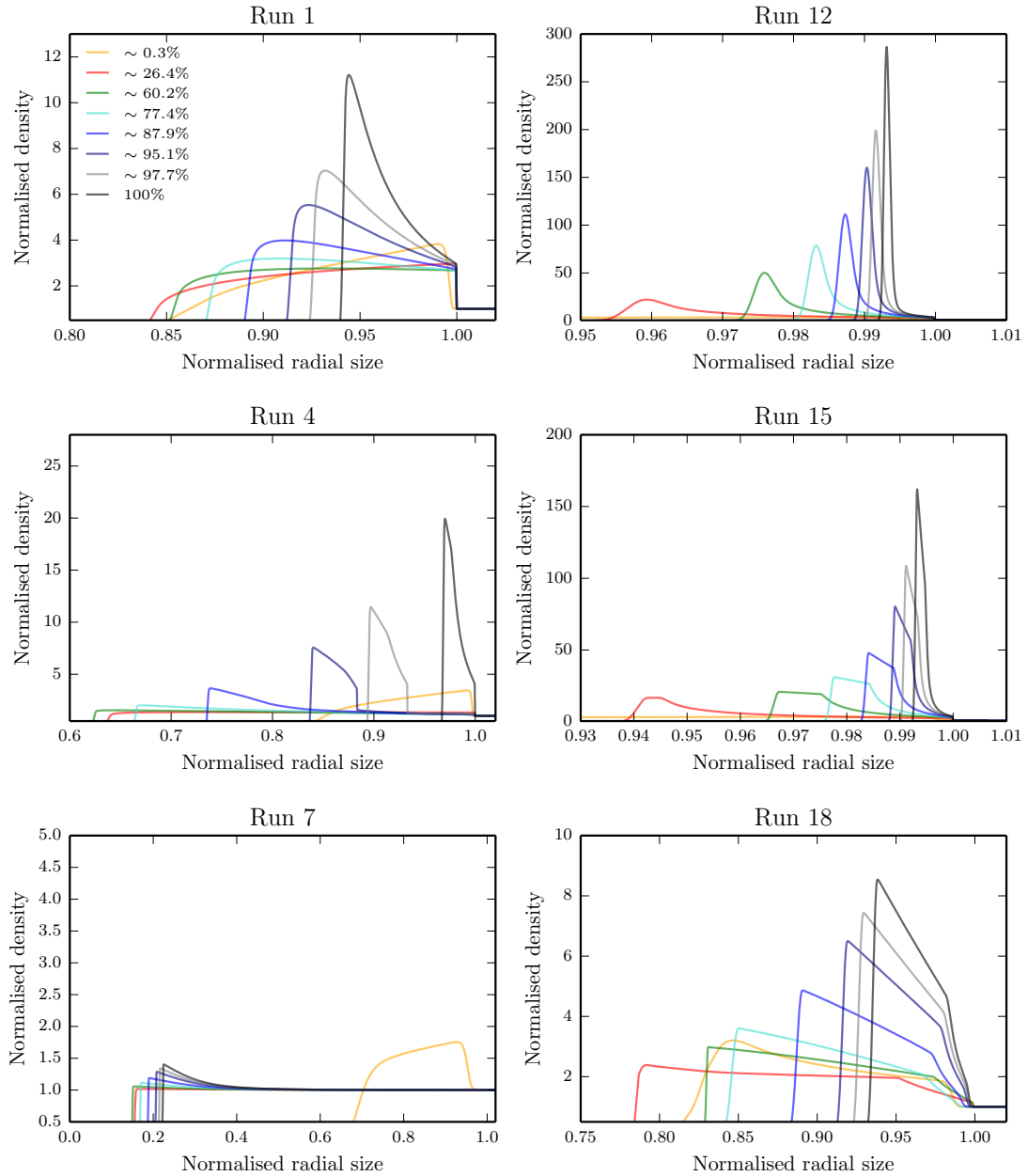


FIGURE 4.30: The evolution of the remnant shell at the same stage of each simulation for Run 1 ($1 \times 10^{-7} M_{\odot} \text{ yr}^{-1}$ and $n = 1$), Run 4 ($1 \times 10^{-8} M_{\odot} \text{ yr}^{-1}$ and $n = 1$) and Run 7 ($1 \times 10^{-9} M_{\odot} \text{ yr}^{-1}$ and $n = 1$) alongside the equivalent simulation with radiative cooling (Run 12, Run 15 and Run 18). Similar to Figure 4.19, the points of each simulation coinciding with the particular shell sizes are given as percentages.

shell formation so when the shell compression begins to take place later on in the system's evolution (as more energetic ejecta collide with the inner edge of the shell), it is starting with a thinner shell and is unable to grow further. This full simulation also exhibits a sharp contact discontinuity (see density panel of Figure 4.29) resulting from the high spatial resolution of this simulation (100 AU/cell).

The cavity and ejecta pile up boundary at ~ 4 parsecs reveals a very similar density,

pressure, velocity and temperature in Run 1 and Run 12 (see Figure 4.29). At the later stages of these simulations, the frequency and energy of the eruptions results in the scenario we see in Run 0, whereby there is not enough time for the ejecta or remnant to cool between impacts. Consequently, we see the effects of radiative cooling at the front end of the remnant, a relic of the earlier spaced out less energetic outbursts with the centre of the NSR reflecting the later frequent eruptions. Furthermore, this point can be extended to all of the simulations conducted throughout this chapter, whereby the growth of the nova super-remnant is shaped heavily by its early evolution (also see Figure 4.19).

4.6.2 Run 12, Run 13 and Run 14

In this section we will consider the reference simulation with radiative cooling (Run 12) alongside the same system in high density surroundings. We consider $1.67 \times 10^{-23} \text{ g cm}^{-3}$ ($n = 10$) and $1.67 \times 10^{-22} \text{ g cm}^{-3}$ ($n = 100$) which are Run 13 and Run 14, respectively. The full simulations are given in Figure 4.31 in addition to the outer edge radial growth curve of each NSR shell. We can see that the remnants shaped in both the higher density ISM are completely reminiscent of the $n = 1$ version with a smaller NSR and an exceptionally thin shell. Furthermore, the radial growth curves of the remnants simulated with radiative cooling show the same power law trend as the simulated shells without, and have a similar changing gradient indicative of the later, more energetic, influencing nova eruptions.

The cooled remnants extend to $\sim 24.5 \text{ pc}$, $\sim 15 \text{ pc}$ and $\sim 9 \text{ pc}$ for $n = 1$, $n = 10$ and $n = 100$, respectively. If we compare the sizes with those remnants without radiative cooling in Figure 4.18, we see that the remnants with cooling are approximately 88%, 85% and 80% of the size of their respective counterpart due to the increase in resistance from the higher density ISM. The comparison is illustrated in the top row of Figure 4.34. As mentioned earlier, for the case of $n = 1$, we can see by comparing the top panels of Figure 4.30 that the shell width is dramatically reduced when incorporating radiative cooling due to a suppression of the early shell formation.

4.6.3 Run 15, Run 16 and Run 17

We now look at a set of simulations with an accretion rate of $\dot{M} = 1 \times 10^{-8} \text{ M}_{\odot} \text{ yr}^{-1}$ including radiative cooling. The full simulations for $n = 1$ (Run 15), $n = 10$ (Run 16) and $n = 100$ (Run 17) are given in Figure 4.32 with Run 15 having a spatial resolution of 200 AU/cell and Run 16 and 17 both having a resolution of 1000 AU/cell. These remnants are smaller than the equivalent group with cooling disabled,

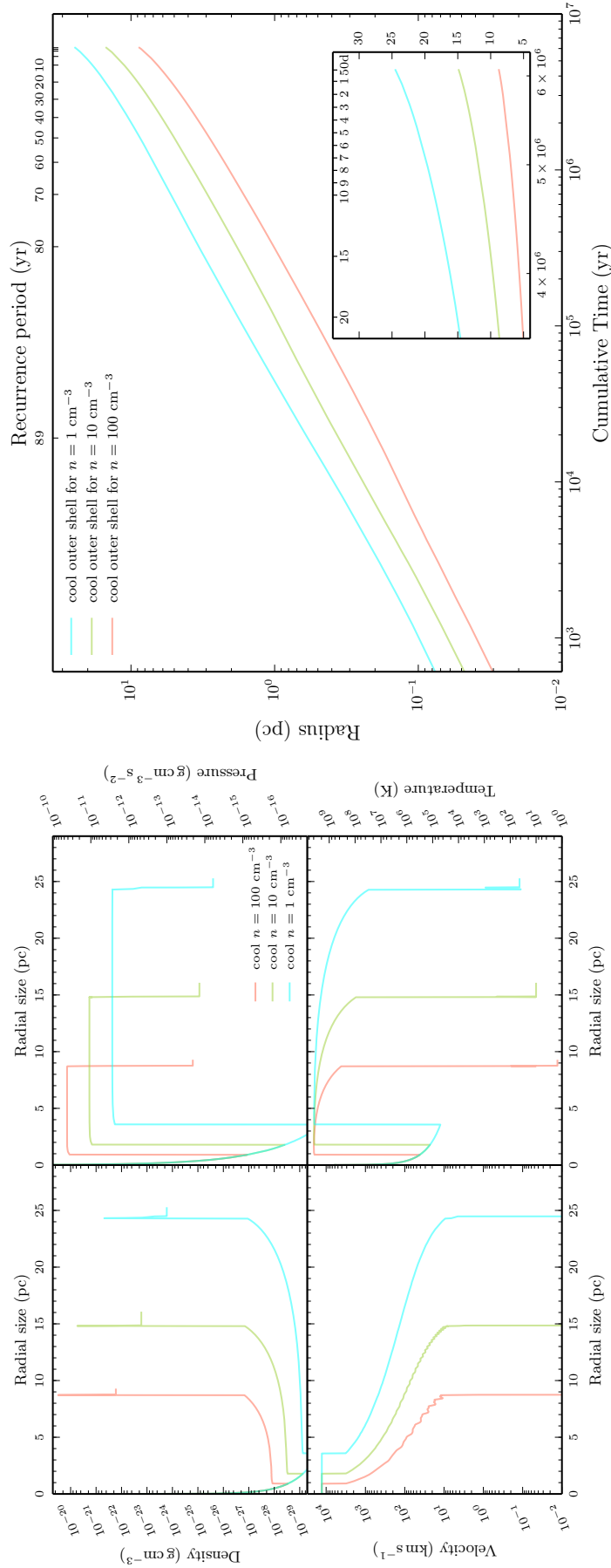


FIGURE 4.3: **Left:** Dynamics of the nova remnant with $\dot{M} = 1 \times 10^{-7} M_{\odot} \text{ yr}^{-1}$ for three different ISM densities after 819,565 eruptions with a resolution of 100 AU/cell and radiative cooling. **Right:** Evolution of the outer edge of the shell with respect to cumulative (elapsed) time and recurrence period for the three different ISM densities.

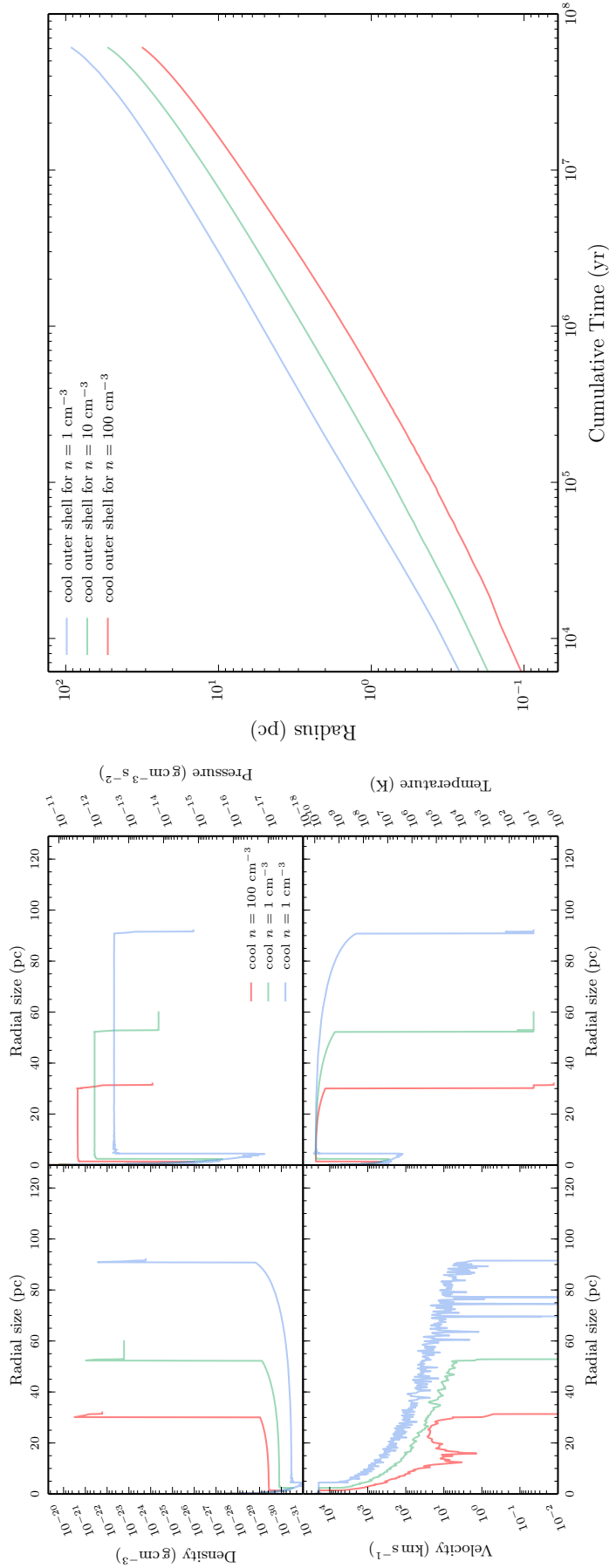


FIGURE 4.32: **Left:** Dynamics of the nova remnant with $\dot{M} = 1 \times 10^{-8} M_{\odot} \text{ yr}^{-1}$ for three different ISM densities after 384,257 eruptions with radiative cooling. Run 15 has a spatial resolution of 200 AU/cell and Run 16 and Run 17 have a spatial resolution of 1000 AU/cell. **Right:** Evolution of the outer edge of the shell with respect to cumulative (elapsed) time and recurrence period for the three different ISM densities.

namely Run 4, 5 and 6. The NSRs with cooling reach out to ~ 93 pc, ~ 48 pc and ~ 30 pc for $n = 1$, $n = 10$ and $n = 100$, respectively, approximately 80%, 74% and 75% of the size of the remnants without radiative cooling. Again, for the case of $n = 1$, we can see by comparing the middle panels of Figure 4.30 that the shell width is much smaller when incorporating radiative cooling ($\sim 0.8\%$) than without ($\sim 4\%$). Unlike previous simulations, the temperature of the ejecta pile-up boundary decreases as the density of the ISM decreases, with $n = 1$ reaching $\sim 1 \times 10^{10}$ K and dropping tenfold for a $n = 10$ ISM.

4.6.4 Run 18, Run 19 and Run 20

The next set of simulations comprise of nova eruptions from a 1×10^7 K WD with a mass accretion rate of $1 \times 10^{-9} M_{\odot} \text{ yr}^{-1}$ with radiative cooling included. Each run has a very low spatial resolution with Run 18 having a resolution of 20,000 AU/cell, Run 19 having a resolution of 25,000 AU/cell and Run 20 having a resolution of 13,366 AU/cell, and we again vary the ISM density such that Run 18, 19 and 20 have $n = 1$, $n = 10$ and $n = 100$ ISM, respectively. The results of these runs are shown in Figure 4.33. Except for the $n = 100$ run, the remnant shells in the equivalent runs without cooling (Run 7, 8 and 9; see Section § 4.5.4) are difficult to discern from the surrounding ISM hence it is difficult to pin down the exact radial size of these. Whilst also true for the cooled $n = 10$ (Run 19) remnant which looks to extend to ~ 140 pc with a shell ~ 40 pc wide, the remnants grown in the $n = 1$ (Run 18) and $n = 100$ (Run 20) look to have more defined boundaries. The NSR in the $n = 1$ environment reaches ~ 270 pc and has a shell thickness of $\sim 8\%$ and the remnant with $n = 100$ reaches ~ 85 pc with a shell thickness of $\sim 25\%$.

4.7 Diagnostics of Runs 1, 2, 3 and Runs 12, 13, 14

In Section § 4.5.2 and Section § 4.6.2, we presented the results of our reference simulation in three different environments without and with radiative cooling. As we wanted to focus on the large scale structure of the nova super-remnants, only the final epoch of each simulation was shown. This is helpful to understand the density, pressure, velocity and temperature profiles of the remnants with respect to their radial size once the upper limiting WD mass has been reached, however we will now look at the evolution of these parameters, as well as mass, over time in the following diagnostic plots.

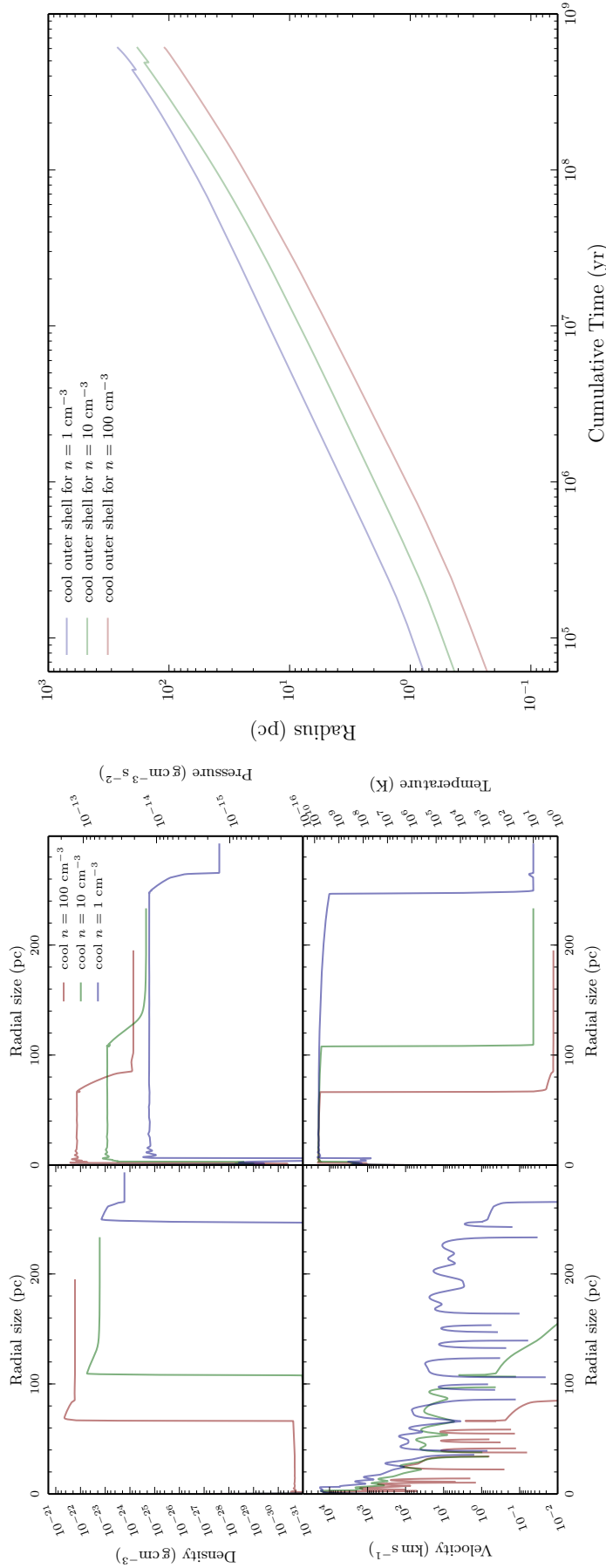


FIGURE 4.33: **Left:** Dynamics of the nova remnant with $\dot{M} = 1 \times 10^{-9} M_{\odot} \text{ yr}^{-1}$ for three different ISM densities after 153,451 eruptions with radiative cooling. Run 18 has a spatial resolution of 20,000 AU/cell, Run 19 has a spatial resolution of 25,000 AU/cell and Run 20 has a spatial resolution of 13,366 AU/cell. **Right:** Evolution of the outer edge of the shell with respect to cumulative (elapsed) time and recurrence period for the three different ISM densities.

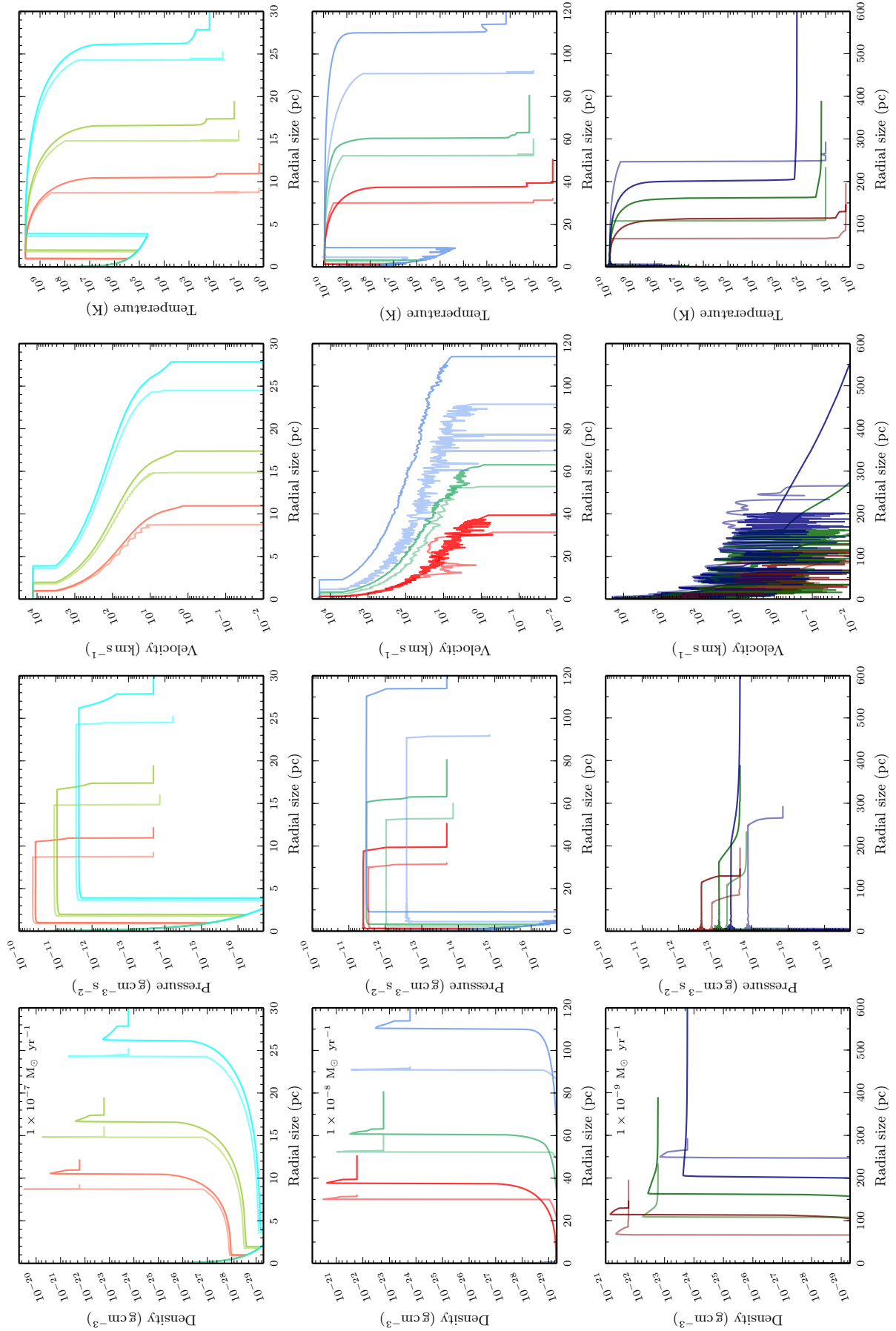


FIGURE 4.34: Comparison of Runs 1 – 9 (simulations with varying accretion rates and varying ISM densities without radiative cooling) and Runs 12 – 20 (simulations with varying accretion rates and varying ISM densities with radiative cooling).

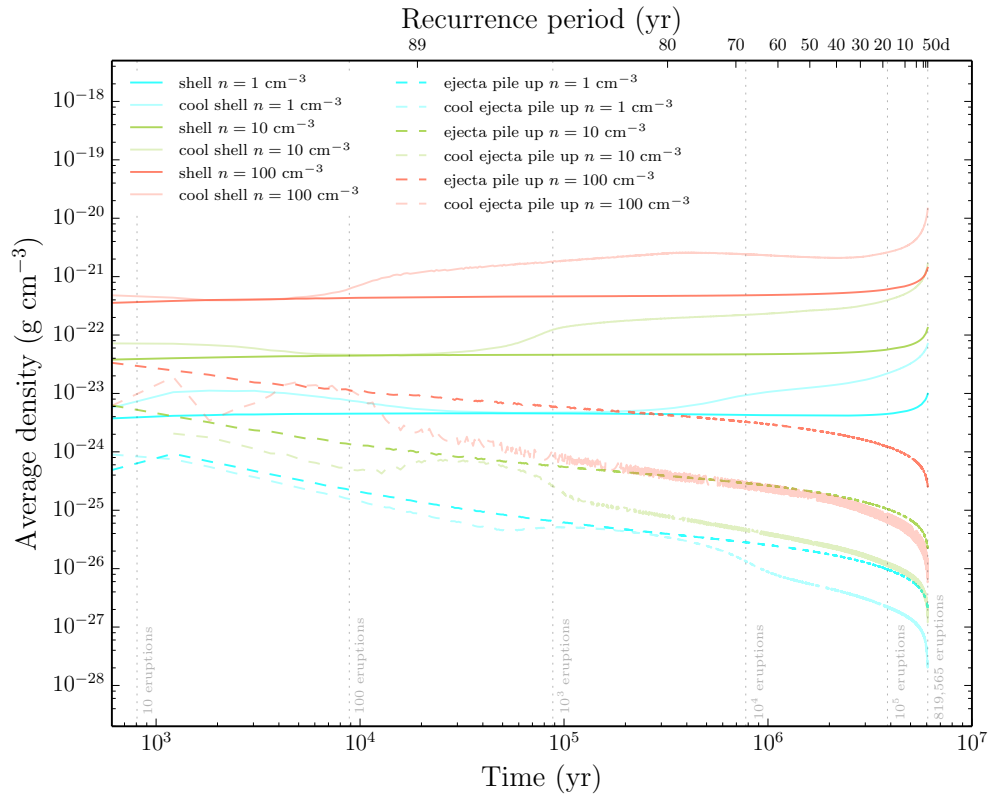


FIGURE 4.35: The evolution of average density in the remnant shell and ejecta pile-up region for the reference simulation in $n = 1$, $n = 10$ and $n = 100$ ISM without and with radiative cooling.

We will first look at the evolution of the average density in the remnant shell and the ejecta pile-up region for the reference simulations with and without cooling. This is shown in Figure 4.35. Firstly, we can see that the average density in the shell without cooling is approximately a factor of two higher than the surrounding ISM in all three environments for the first $\sim 4 \times 10^6$ years. The shells with cooling initially have similar densities but divert from the shells without cooling at different points of the evolution dependent upon the ISM density. For $n = 1$, this is after $\sim 3 \times 10^5$ years, for $n = 10$ it is $\sim 4 \times 10^4$ years and for $n = 100$, only after $\sim 9 \times 10^3$ years. In each case, this is very early on in the evolution of the remnant, demonstrating that the high density shells we see in Figure 4.31 are a relic of the first thousand eruptions, the future structure set in place. As shown, the average density within the remnant shells with cooling increases substantially compared to the shells without cooling as these shells lose energy and compress against the surrounding ISM. The defined ejecta pile-up region increases in size throughout the remnant's evolution resulting in the average density continuously decreasing.

The average pressure within the remnant shells with and without cooling is initially high as they begin as thin high density regions at high temperatures. The pressure

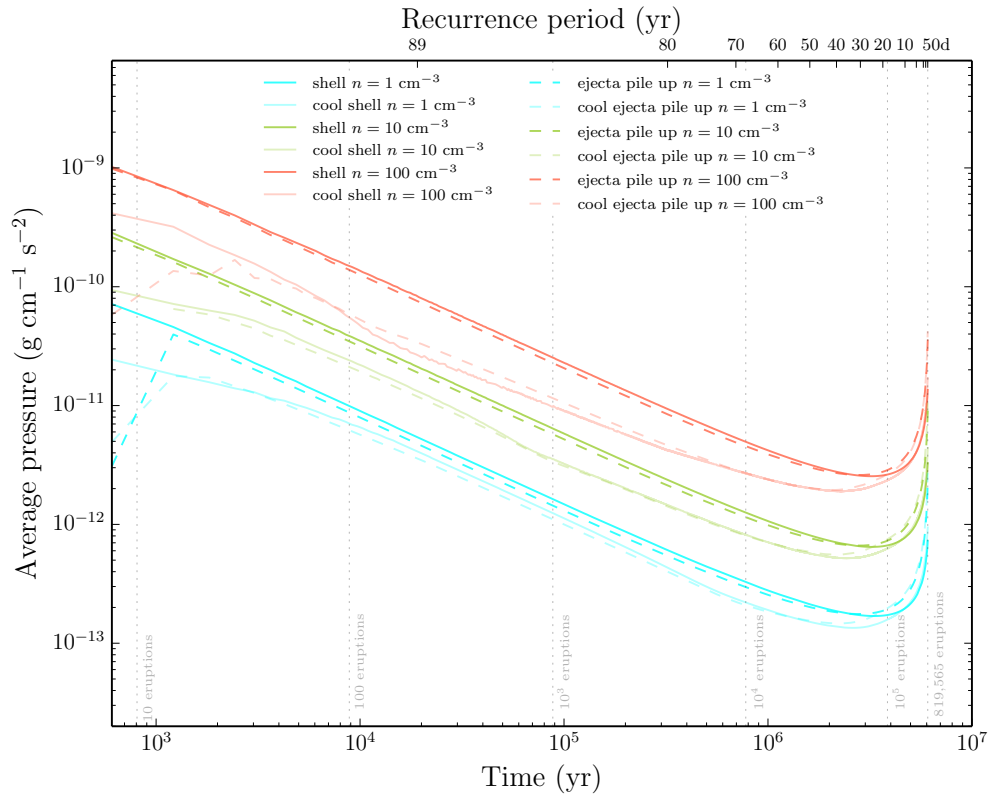


FIGURE 4.36: The evolution of average pressure in the remnant shell and ejecta pile-up region for the reference simulation in $n = 1$, $n = 10$ and $n = 100$ ISM without and with radiative cooling.

within the shells then decreases until it matches the average pressure within the ejecta pile-up region after $\sim 4 \times 10^6$ years. The outer edge of the shell then continues to experience the same pressure for the entirety of the simulations. However, the pressure at the inner edge increases, creating a pressure gradient within the shell, resulting in an increase of its average pressure as shown in Figure 4.36. With the average temperature of the ejecta pile-up region increasing monotonically throughout its evolution (see Figure 4.37), the pressure within follows the same trend once the region's size is established. The average pressure evolution illustrates how the remnant shell's compression takes place during an intermediary period. The shell forms initially without compression, is then compressed as it is subjected to pressure gradients and after $\sim 4 \times 10^6$ years, the thinner shell remains. This evolutionary compression can be clearly seen in the top panels of Figure 4.30.

As can be seen in Figure 4.37, the average temperature of the shell without radiative cooling falls during the evolution as the remnant cools adiabatically through its expansion into the surrounding ISM, whilst the average temperature of the shell within the radiative cooling simulations falls as a direct result of cooling. This is

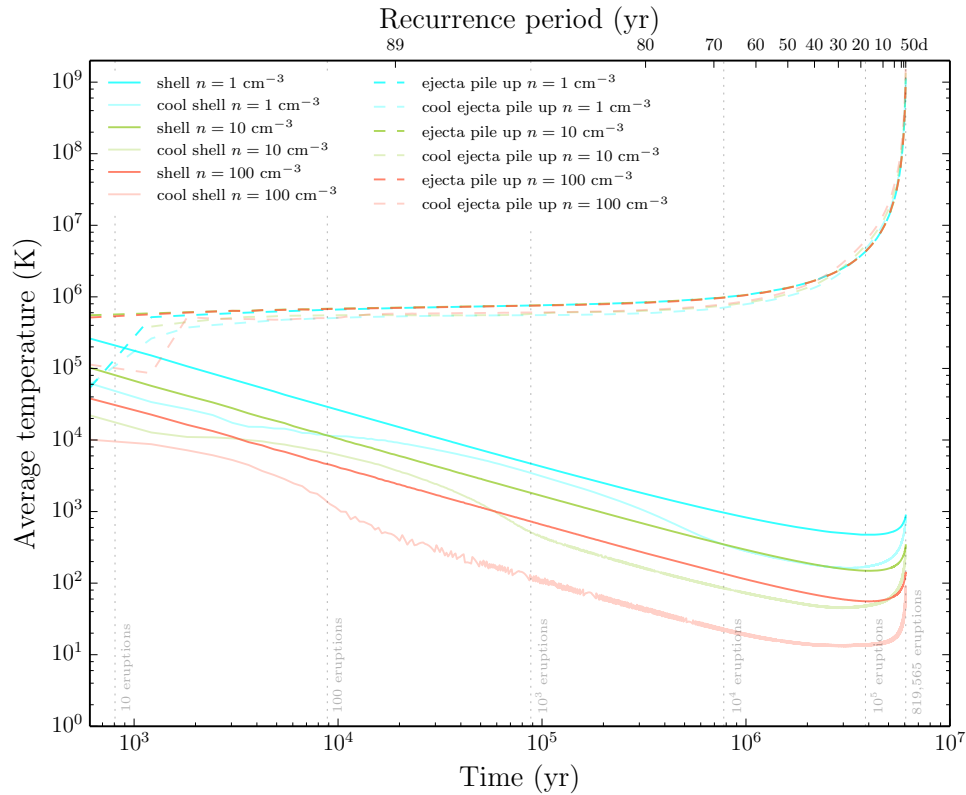


FIGURE 4.37: The evolution of average temperature in the remnant shell and ejecta pile-up region for the reference simulation in $n = 1$, $n = 10$ and $n = 100$ ISM without and with radiative cooling.

seen most dramatically in the cooled $n = 100$ simulation where the average temperature drops from an initial 10^4 K to ~ 10 K after $\sim 4 \times 10^6$ years before increasing modestly to ~ 100 K as outbursts become more frequent and begin to impact the inner edge of the shell through the ejecta pile-up region, leading to compression and re-heating. On the other hand, the ejecta pile-up region in all cases, begins with higher temperatures with the highest seen in $n = 10$ and $n = 100$ as the ejecta experiences the most resistance from the higher density ISM. After a brief period of discrepancy (~ 2000 years which is negligible within these simulations), average temperatures in all ejecta pile-up regions converge to $\sim 8 \times 10^5$ K (modestly lower for the reference simulations with radiative cooling) before dramatically increasing to 10^9 K after the full 6×10^6 years, maintaining extremely high temperatures through more frequent and more powerful shocking of the material within.

The average velocity of the remnant shell, like the average temperature and average pressure, decreases throughout the NSR's evolution before a slight increase for the final 1×10^6 years (see Figure 4.38). The velocity of the shell's outer edge is initially ~ 10 km s $^{-1}$ and remains below this velocity during the whole simulation, however

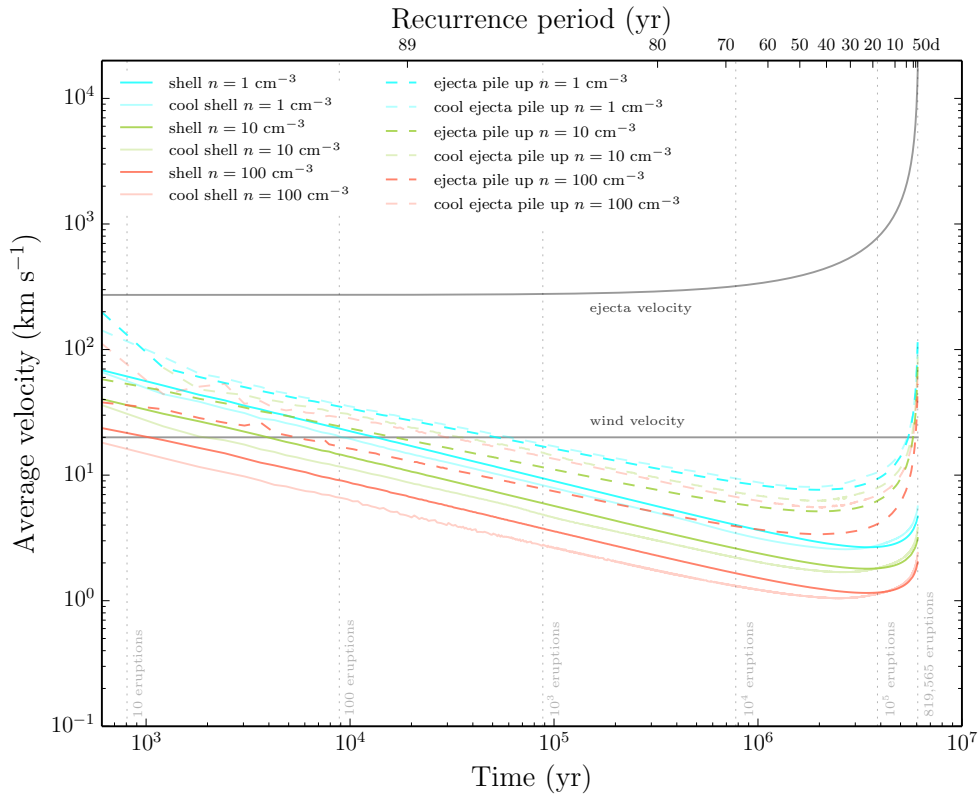


FIGURE 4.38: The evolution of average velocity in the remnant shell and ejecta pile-up region for the reference simulation in $n = 1$, $n = 10$ and $n = 100$ ISM without and with radiative cooling. The constant wind velocity used within the simulations is illustrated, as is the evolution of the nova ejecta velocity.

the velocity of the inner edge does increase due to the more frequent collisions occurring within the ejecta pile-up region, leading to a small velocity gradient within the shell and therefore an increase in its average velocity. The ejecta pile-up region follows a similar trend but with higher average velocities, a result of consistent and increasingly frequent ejecta impacting the ejecta pile-up boundary.

The mass of the remnant shells grow as a power law (see Figure 4.39). Without radiative cooling, the shell grows substantially more massive ($\sim 200 M_{\odot}$ compared to $\sim 100 M_{\odot}$ for $n = 1$, $\sim 500 M_{\odot}$ compared to $\sim 300 M_{\odot}$ for $n = 10$ and $\sim 1000 M_{\odot}$ compared to $\sim 800 M_{\odot}$ for $n = 100$), due to the system's loss of kinetic energy reducing the amount of total ISM being swept up into the shell. The mass within the ejecta pile-up regions similarly increases as a power law however after $\sim 5 \times 10^6$ years, this region begins to lose mass, possibly as more energetic later ejecta collide with this transient region and push the material towards the inner edge of the remnant shell. Also, as described earlier, the average density within this region diminishes as a result of continuously growing in size, therefore the mass in the region will similarly decrease.

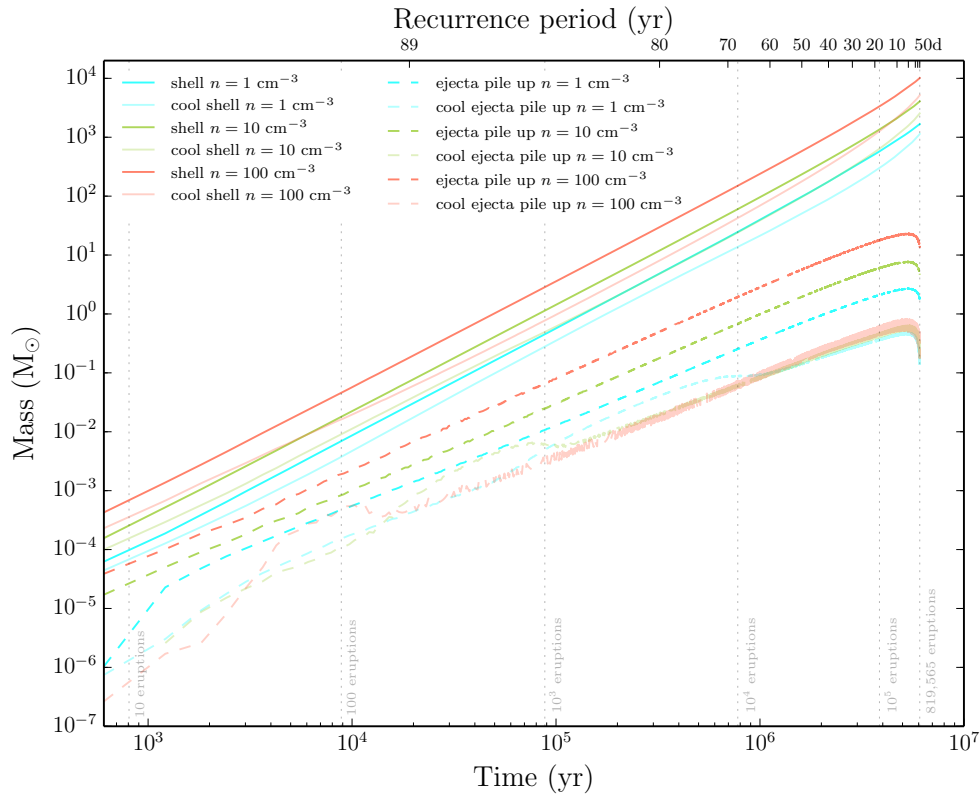


FIGURE 4.39: The evolution of the mass of the remnant shell and ejecta pile-up region for the reference simulation in $n = 1$, $n = 10$ and $n = 100$ ISM without and with radiative cooling.

4.8 Comparing simulations to M 31N 2008-12a NSR

In order to determine how well the simulations we have outlined recreate a realistic nova super-remnant, we will compare them to the observations of the shell surrounding M 31N 2008-12a. For this, we will consider the simulated remnant grown from a system with parameters that most resemble 12a along with the inclusion of radiative cooling. As indicated in Table 1.3, the mass accretion rate derived from observations for this RRN is $(6 - 14) \times 10^{-7} M_{\odot} \text{ yr}^{-1}$, therefore the closest mass accretion rate we have considered is $1 \times 10^{-7} M_{\odot} \text{ yr}^{-1}$, utilised within Run 12, 13 and 14. Additionally, we know that the recurrence period of this system is ~ 1 year so we will look at the epoch of the simulations when the recurrence period coincides with this ($\sim 97.7\%$ through the simulations). The dynamics of the remnants in the three ISM environments at this epoch ($P_{\text{rec}} = 1 \text{ yr}$) are shown in Figure 4.40.

The most immediate difference we see between observations and the simulations is the radial size of the remnant and the shell thickness. Even within the lowest density ISM surroundings we consider, the shell reaches out to only ~ 24 pc compared to the observed 67 pc (Darnley et al., 2019a). Furthermore, as outlined in Section

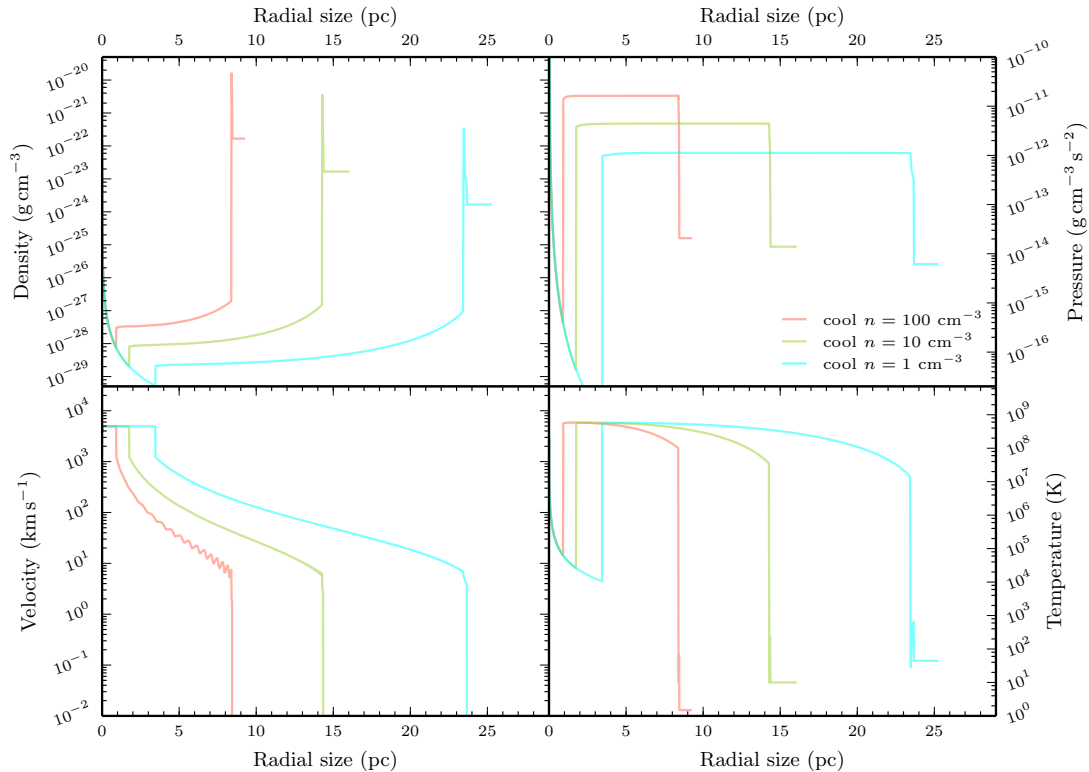


FIGURE 4.40: The dynamics of the simulated nova super-remnants from Run 12 ($n = 1$), Run 13 ($n = 10$) and Run 14 ($n = 100$) with radiative cooling at the epoch when the recurrence period is that of M 31N 2008-12a ($P_{\text{rec}} = 1$ yr).

§ 3.4, we would expect a much higher density ISM surrounding this nova system as it is located within a star forming region of M 31, which would lead to a smaller NSR, as shown in Figure 4.40. The shell thickness of the remnant within the $n = 1$ environment is $\sim 1\%$ (this can be seen clearly in the top right panel of Figure 4.30), dramatically different from a shell thickness of 22%, from observations of the inner and outer edges of the NSR (Darnley et al., 2019a).

As with the first study (Run 0) of a simulated NSR, the *structure* of the remnants in Run 12 – 14 are similarly reminiscent of the observed shell. They all have a very low density cavity at the centre with freely expanding high velocity ejecta leading up to a very hot ejecta pile-up region. This ejecta then collides with previously distributed material leading to extreme heating from shocks within this region. At the outer edge of the remnant, we then have a very thin high density shell sweeping up the surrounding ISM.

The dynamics of the simulated remnants we are considering here were created from a simple model of a growing WD in a system with an *unchanging* mass accretion

rate⁹. However, the mass accreted from the donors in true systems changes over its evolution (see Section § 4.9.4) implying that we would have remnants grown more akin to those with low mass accretion rates such as Figure 4.33 (as it is the early eruptions that set the scene), before evolving towards the remnants we see in Figure 4.40, and the superposition of all rates in between. We briefly look at a first order approximation of this type of scenario in Section § 4.9.4. As a consequence, we would see the larger remnant comparable to that seen around 12a, with the wider shell.

We can conclude that the simulations we have ran that most resemble the 12a system, in terms of mass accretion rate, density of ISM and radiative cooling (Run 12 – 14), do not replicate the nova super-remnant seen. As a result, there must be other contributing factors in the shaping of these structures that we have not fully considered. In Section § 5.8, we will look at the parameter space of ISM density and mass accretion rate needed to recreate a nova super-remnant with the radial size of that seen around M 31N 2008-12a and investigate whether the observed NSR around 12a is made up of both a photoionisation region as well as a dynamically formed remnant. We will also briefly outline other possible considerations in Section § 7.2.1.

4.9 Tests post main simulations

4.9.1 Varying Mass Accumulation Efficiency

As discussed in Section § 4.4.2, we adopted a mass accumulation efficiency of 67%. Of course, in the case of $\eta = 0$ ¹⁰, we would see much more ejecta from the system but with zero growth of the white dwarf. On the other hand, if $\eta = 1$, the system would not deposit any material into the surroundings. For the case of $\eta < 1$, the nova would eject a proportion of material into its surrounding but retain a fraction of the ejecta, resulting in a growing WD. In order to find the effect of this parameter on our simulations, using total kinetic energy as a proxy, we varied this mass accumulation efficiency parameter from 10% to 90% for the 1×10^7 K WD accreting at $1 \times 10^{-7} M_{\odot} \text{ yr}^{-1}$, with the outcome illustrated in Figure 4.41. Additionally, to illustrate the total kinetic energy produced by systems with a lower mass accretion rates, we have presented the evolution of kinetic energy for $1 \times 10^{-8} M_{\odot} \text{ yr}^{-1}$ and $1 \times 10^{-9} M_{\odot} \text{ yr}^{-1}$, both with $\eta = 0.67$.

⁹If we extended our parameter space of mass accretion rates to $1 \times 10^{-6} M_{\odot} \text{ yr}^{-1}$ to be more in line with the 12a system, we would have yet a smaller remnant.

¹⁰This was the case for Run 0 from Darnley et al. (2019a).

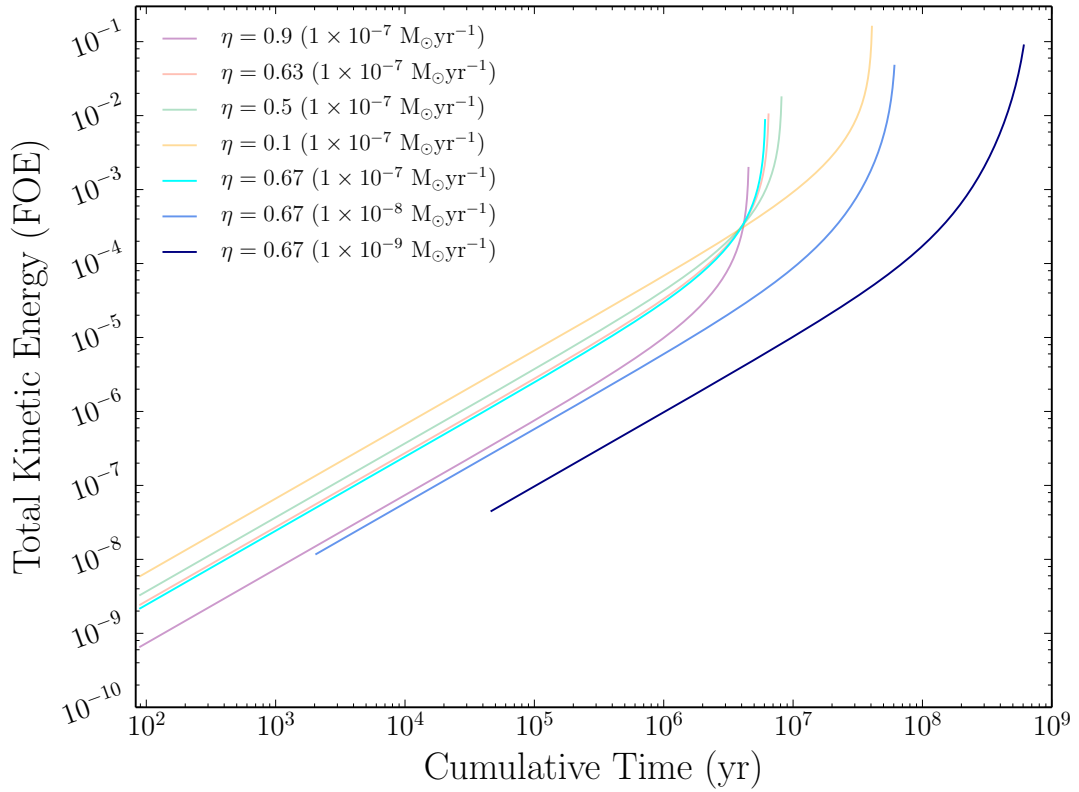


FIGURE 4.41: Comparing the total kinetic energy from recurrent nova eruptions from variation of the mass accumulation efficiency. Here we also vary the mass accretion rate for the case of $\eta = 0.67$ to illustrate its effect on the total kinetic energy.

As can be seen, the total kinetic energy is affected more at low η (yellow line) due to a (slow) continued growth of the WD dramatically lengthening the time for the WD to reach the Chandrasekhar limit and consequently producing many more eruptions and more kinetic energy. We see this same effect also from lowering the accretion rate with increased total kinetic energy compared to the $1 \times 10^{-7} M_{\odot} \text{ yr}^{-1}$ system. We can see that there is a small difference in total kinetic energy and cumulative time for $\eta = 0.63$ given in [Kato et al. \(2015\)](#) and $\eta = 0.67$ adopted for our study. Whilst not identical, this change will have very little effect on the overall shaping and evolution of the NSRs in our work.

4.9.2 Fitting a power law to find system parameters

For the main simulations given in Section § 4.5, we utilised ejecta characteristics determined from our simple model of a growing WD. This model was based on interpolating between the results of multicycle nova evolutionary simulations given in [Yaron et al. \(2005\)](#), namely ignition masses and mass loss times (see Section § 4.4.1).

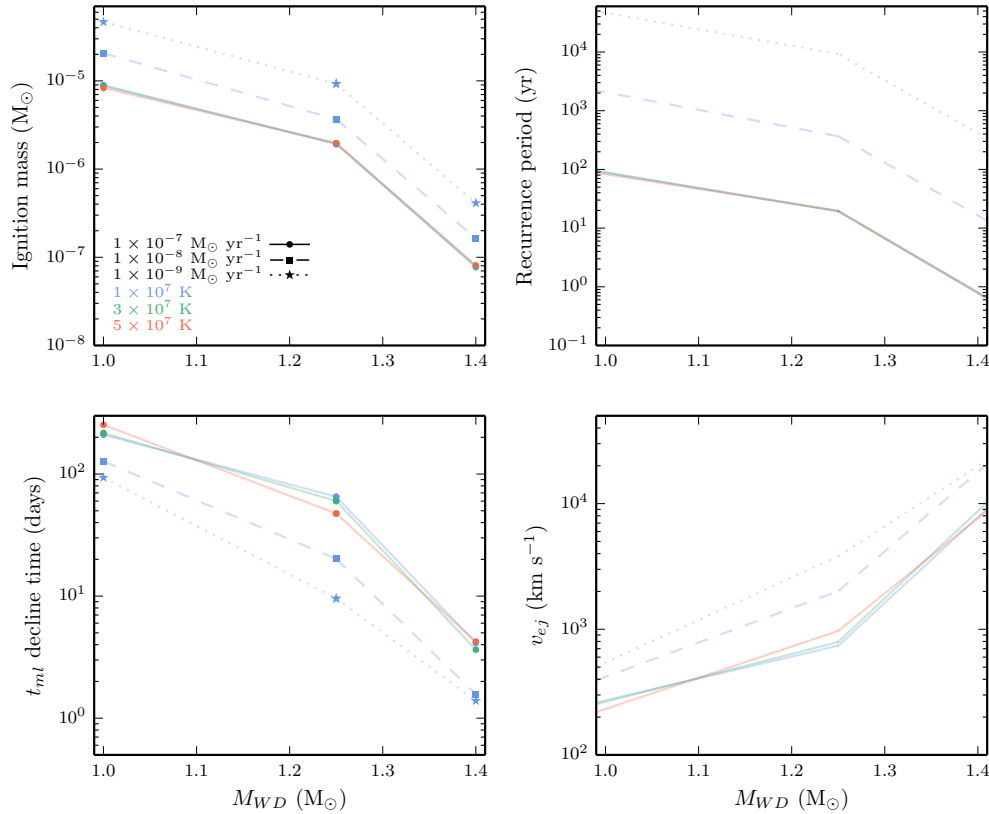


FIGURE 4.42: **Top left:** $M_{WD} - m_{ig}$. The points are the output characteristics for m_{acc} from Yaron et al. (2005) which we have interpolated between with two distinct power laws in the same manner as Soraisam & Gilfanov (2015). **Top right:** $M_{WD} - P_{rec}$. **Bottom left:** $M_{WD} - t_{ml}$. Again, the points are the output characteristics for t_{ml} from Yaron et al. (2005) which we used for interpolation. **Bottom right:** $M_{WD} - v_{ej}$.

In our work, a smooth function asymptotically approaching the Chandrasekhar limit was fitted to these values.

An alternative way of fitting a function to these values is with a ‘knee’ function, as given in Figure 1 of Soraisam & Gilfanov (2015). We replicated this alternative by fitting two distinct power laws, as illustrated in Figure 4.42. From here, we again grew a $1M_{\odot}$ WD with our simple model as outlined in Section § 4.4.2, but referring in this case to the two distinct power law fits.

As done with our smooth fit, with each iteration, we were also able to use the relationships to determine the evolution of a number of parameters in terms of white dwarf mass, recurrence period, the cumulative time of all eruptions and the number of eruptions. These are given in Figure 4.43, Figure 4.44, Figure 4.45 and Figure 4.46, respectively. As can be seen, these parameters evolve in the same way as

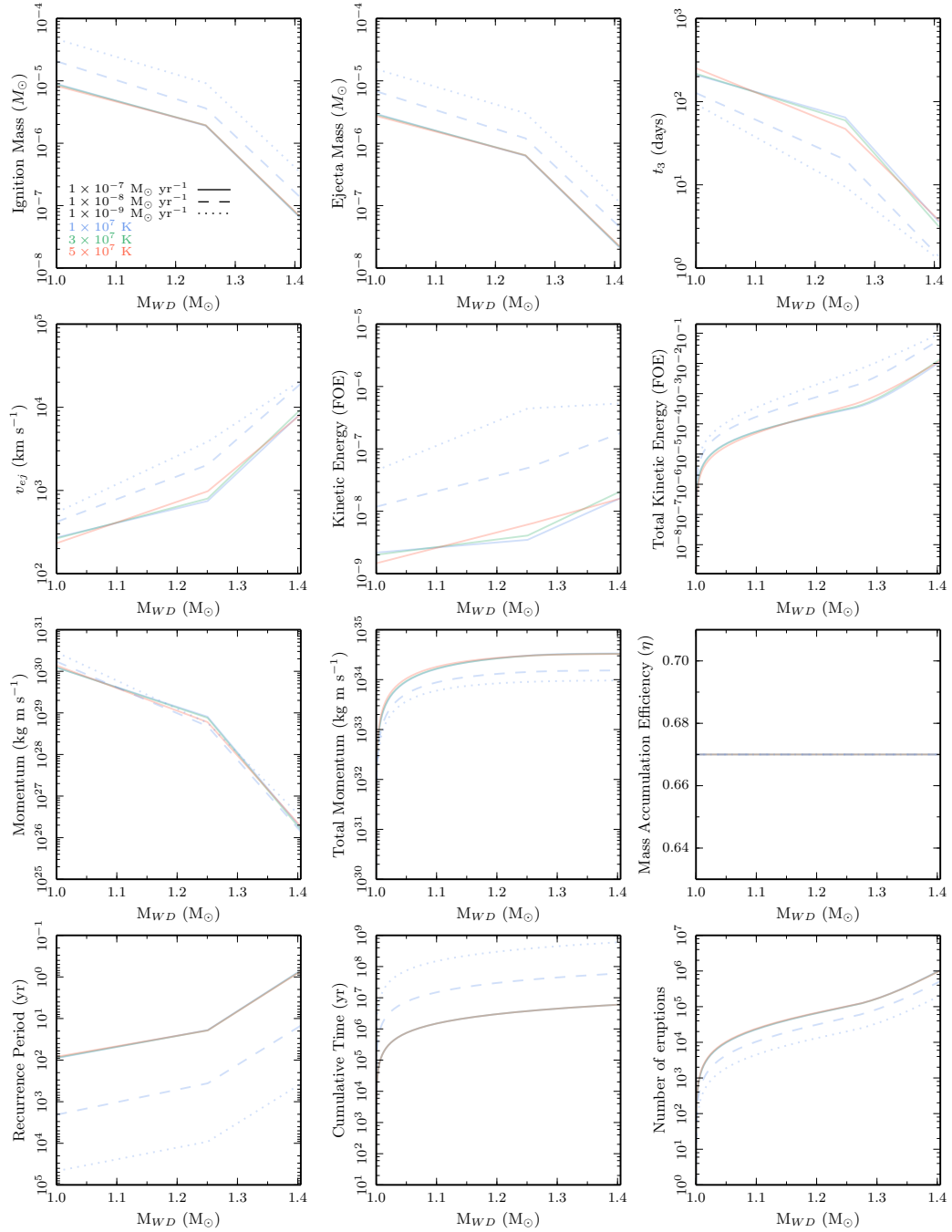


FIGURE 4.43: Evolution of system parameters with respect to the mass of the white dwarf for the three different white dwarf temperatures with three different accretion rates using the power law fit. As in Figure 4.10, these are m_{ig} : ignition mass, m_{ej} : ejected mass, t_3 : decline time, v_{ej} : the velocity of the ejecta from the surface of the white dwarf, kinetic energy, total kinetic energy, momentum, total momentum, mass accumulation efficiency parameter, P_{rec} : the recurrence period, cumulative time of all the eruptions and the number of eruptions. Kinetic energy and total kinetic energy are presented in units of 1×10^{51} ergs ("[ten to the power of] fifty-one ergs" or FOE).

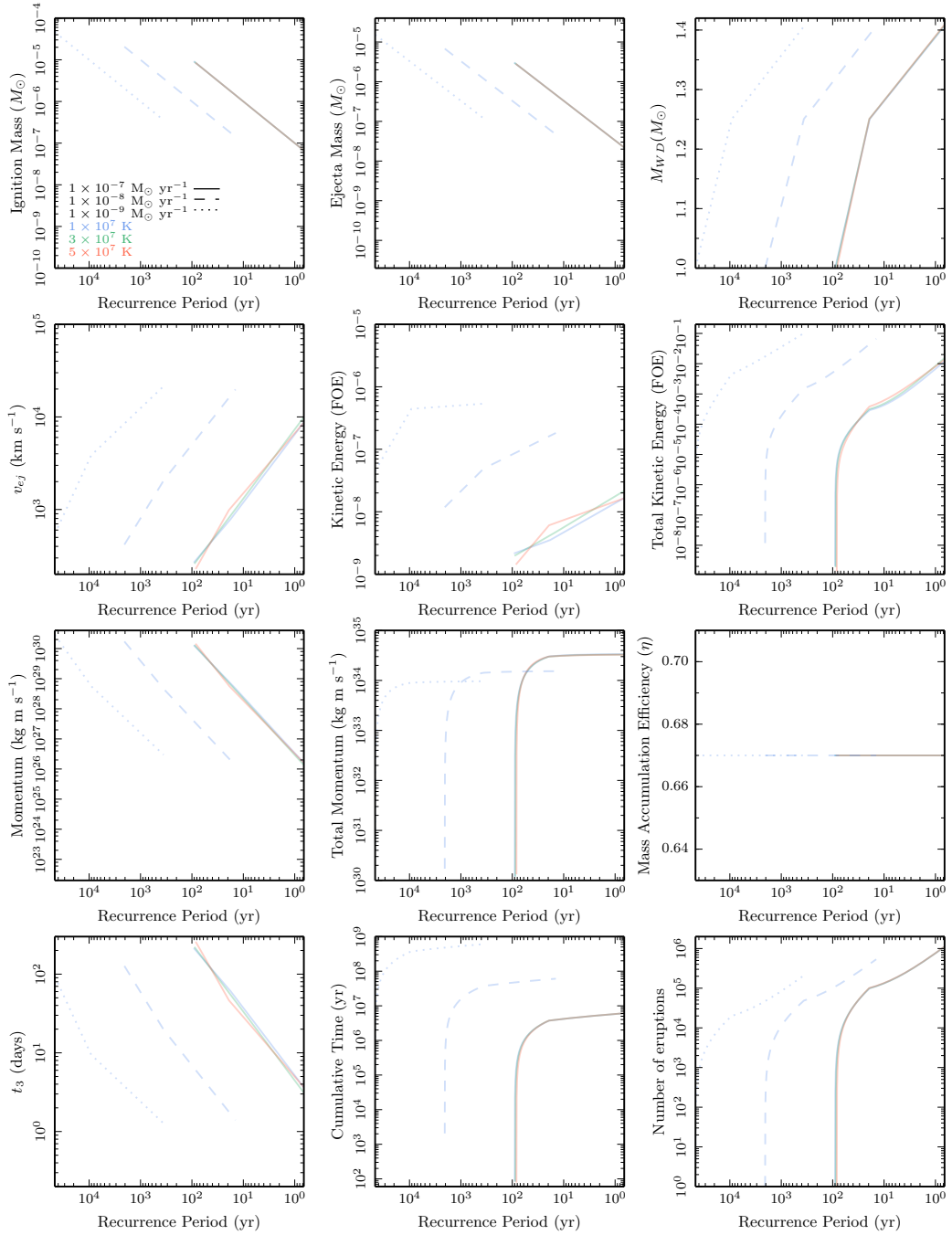


FIGURE 4.44: Same as Figure 4.43 but with respect to the recurrence period of the system.

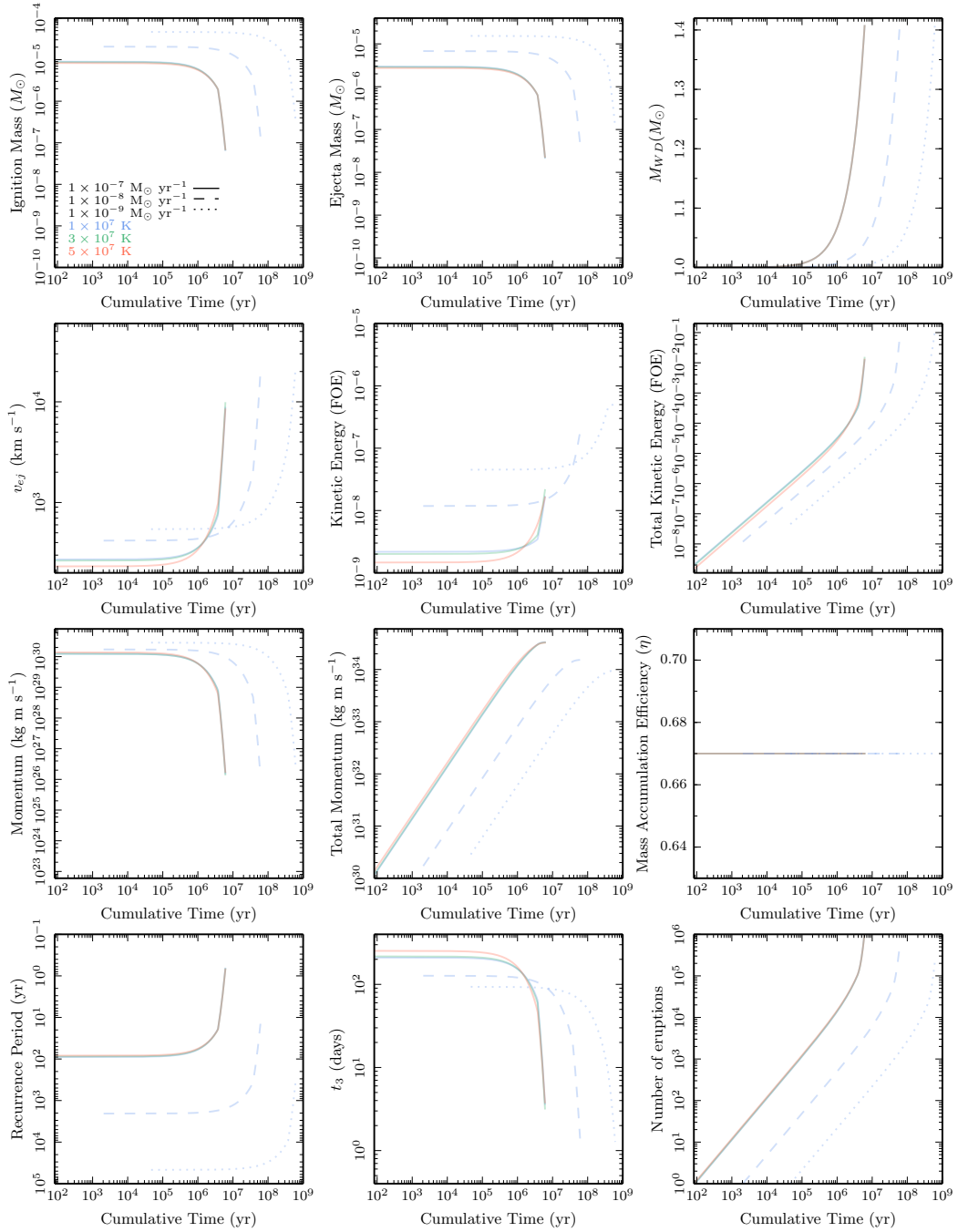


FIGURE 4.45: Same as Figure 4.43 but with respect to the total time of all the nova eruptions.

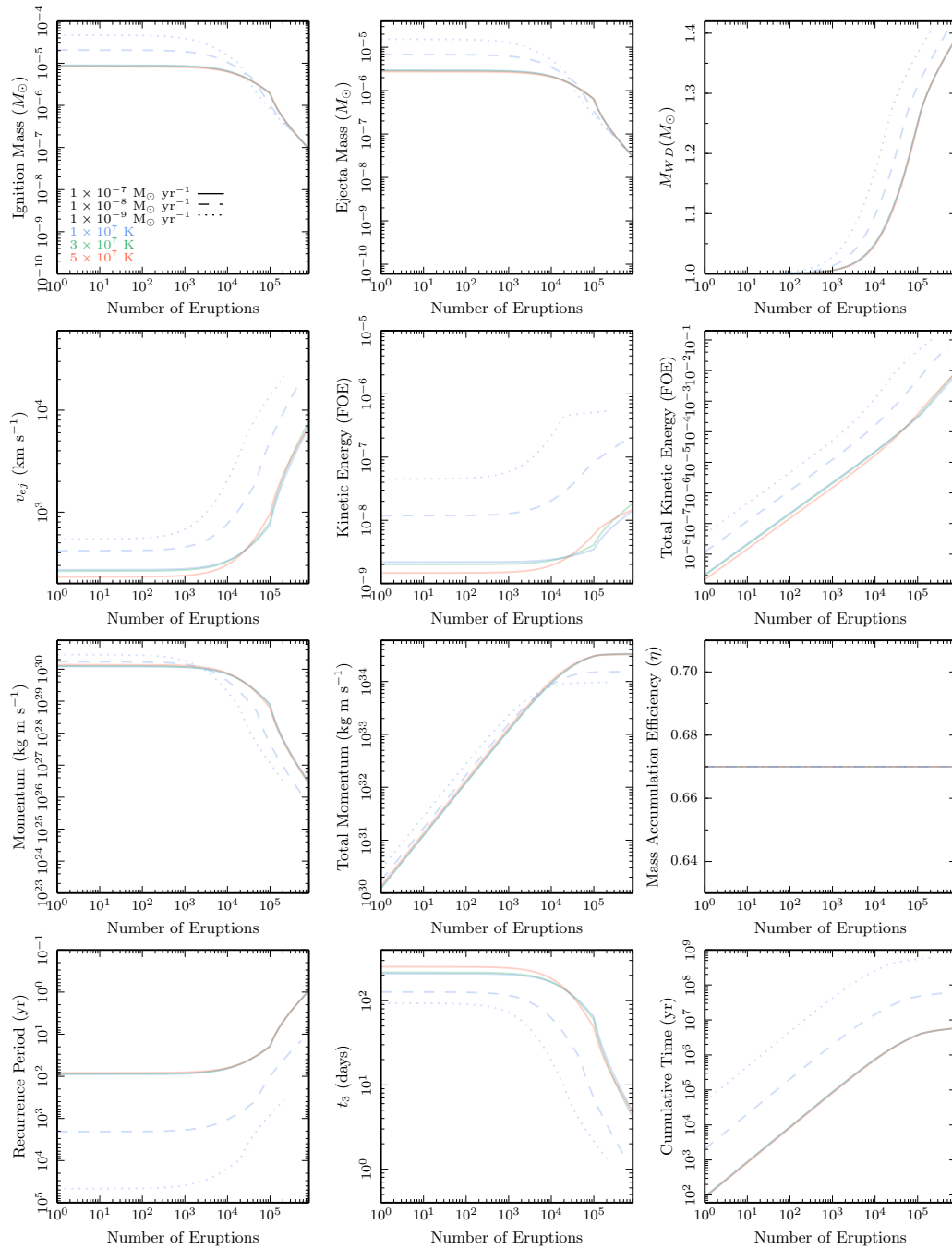


FIGURE 4.46: Same as Figure 4.43 but with respect to the number of nova eruptions.

TABLE 4.5: Parameters for each run. The ejecta characteristics for these runs were found by interpolating between the output characteristics given in Yaron et al. (2005) using power laws in the same manner as Soraisam & Gilfanov (2015).

Run # (no cooling)	Run # (cooling)	T_{WD} (K)	\dot{M} ($M_{\odot}\text{yr}^{-1}$)	ISM density ($1.67 \times 10^{-24} \text{ g cm}^{-3}$)	Number of eruptions
21	24	1×10^7	1×10^{-7}	1	1,110,182
22	-	1×10^7	1×10^{-7}	10	1,110,182
23	-	1×10^7	1×10^{-7}	100	1,110,182

those from the smooth function fitting, with the main difference being the abrupt ‘knee’ at $1.25 M_{\odot}$. The total kinetic energy at the end of the WD growth is $\sim 1.5 \times 10^{-2}$ FOE (“[ten to the power of] fifty-one ergs”) is much greater than the total kinetic energy generated from our smooth fitting function in Section § 4.4.2, this ending with $\sim 1 \times 10^{-2}$ FOE. This reflects the more extreme eruptions later on in this system’s evolution as a direct result of the higher ejecta velocities after the WD has surpassed $1.25 M_{\odot}$. This is evident in Figure 4.27 where we see the radial size of the NSR for the power law run remaining below that of Run 1 (from our interpolation of the Yaron et al. (2005) models) until later times when the total amount of kinetic energy then surpasses the reference simulation and the shell goes on to grow larger.

We ran four simulations of nova eruptions that utilise the two distinct power law fits, with one incorporating radiative cooling (see Table 4.5 for details). Run 21, 22 and 23 are the same as the reference simulations with $\dot{M} = 1 \times 10^{-7} M_{\odot} \text{ yr}^{-1}$ and a WD temperature of 1×10^7 K placed in environments of varying ISM density. The results of these full simulations are shown in Figure 4.47 in which we have plotted the results of Run 1, 2 and 3 for comparison. The shells grown from the power law fitting become larger than those grown from the smooth fitting as a result of the significant increase in kinetic energy from the more energetic nova outbursts from these systems. Yet this deviation only becomes substantial at approximately $P_{\text{rec}} = 20$ years (see the inset panel in right plot of Figure 4.47), coinciding with the recurrence period we find at $1.25 M_{\odot}$ where the break in power laws is located, as a result of the later eruptions becoming more extreme. This break seen in the outer shell radial growth curves is highly likely to be responsible for the different remnant shell structure. The smooth gradient in the shell from the inner edge to outer edge in Run 1 – 3 is replaced by an evident step in Run 21, 22 and 23. This also has a greater impact on the temperature gradient of the shell with the outer edge being hotter than the inner edge, unlike the reference simulation. The temperature of the ejecta pile up region is much lower in Run 21, 22 and 23 compared to the reference

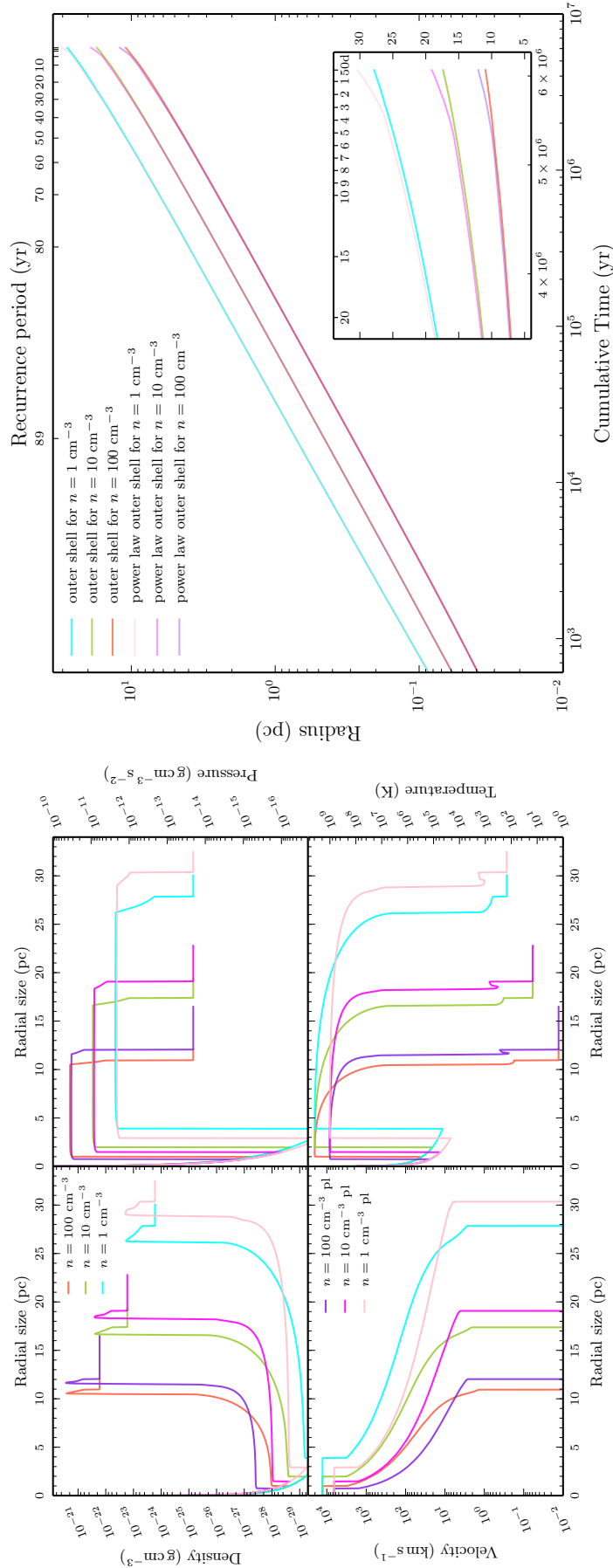


FIGURE 4.47: **Left:** Dynamics of the nova remnant with $\dot{M} = 1 \times 10^{-7} M_{\odot} \text{ yr}^{-1}$ for three different ISM densities after 819,565 eruptions with a resolution of 100 AU/cell (Run 1 – 3) compared to the dynamics of the nova remnant with $\dot{M} = 1 \times 10^{-7} M_{\odot} \text{ yr}^{-1}$ for three different ISM densities after 1,110,182 eruptions with a resolution of 100 AU/cell (Run 21 – 23; from interpolating points from Yaron et al. (2005) with two distinct power laws). **Right:** Evolution of the outer edge of the shell with respect to cumulative (elapsed) time and recurrence period for the three different ISM densities.

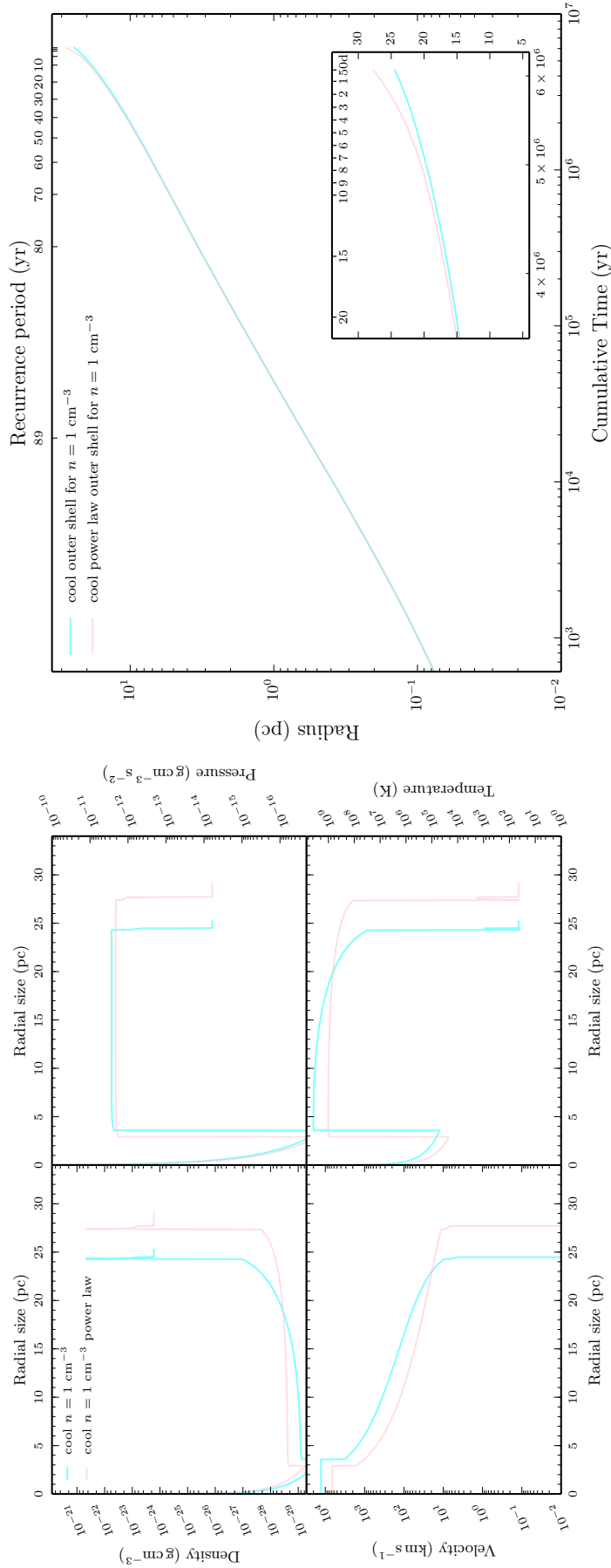


FIGURE 4.48: Left: Dynamics of the nova remnant with $\dot{M} = 1 \times 10^{-7} M_{\odot} \text{ yr}^{-1}$ for $n = 1$ after 819,565 eruptions with a resolution of 100 AU/cell and radiative cooling (Run 12) compared to the dynamics of the nova remnant with $\dot{M} = 1 \times 10^{-7} M_{\odot} \text{ yr}^{-1}$ for $n = 1$ after 1,110,182 eruptions with a resolution of 100 AU/cell and radiative cooling (Run 24; from interpolating points from Yaron et al. (2005) with a power law). **Right:** Evolution of the outer edge of the shell with respect to cumulative (elapsed) time and recurrence period.

TABLE 4.6: Parameters for each run with a WD growing from an initial mass of 0.8, 0.9 and 1.1 M_{\odot} . These runs all had a ISM density of $1.67 \times 10^{-24} \text{ g cm}^{-3}$.

Run # (no cooling)	Run # (cooling)	T_{WD} (K)	\dot{M} ($M_{\odot}\text{yr}^{-1}$)	Initial M_{WD} (M_{\odot})	Number of eruptions
25	-	1×10^7	1×10^{-7}	0.8	840,301
26	28	1×10^7	1×10^{-7}	0.9	832,564
27	-	1×10^7	1×10^{-7}	1.1	797,550

simulations as the eruptions impacting this region are less energetic on account of the much lower velocities of the ejecta travelling through the cavity (see Figure 4.47).

The full simulation we ran whilst including radiative cooling is shown in Figure 4.48 alongside the reference simulation with radiative cooling (Run 12). We again see the outer shell radial growth curves overlapping until reaching the break point of $P_{\text{rec}} \sim 20$ years, exhibited with the larger shell in the radial profiles. As with the simulations without radiative cooling, the overall structure of the shells remain very similar apart from a lower velocity of the ejecta in the cavity resulting in a lower temperature at the ejecta pile up region.

It is clear that using an alternative interpolation to the values given in Yaron et al. (2005) does have an effect on the final simulated NSR. In each case, the shell width remains the same but the size of the remnant increases by a factor of $\sim 10\%$. Whilst a non-negligible difference, we consider the more realistic smooth evolution of system parameters adopted for our study to be a truer representation for NSR simulations.

4.9.3 Varying the initial WD mass

Throughout our study so far we have considered nova eruptions generated by a WD growing from 1 M_{\odot} to 1.4 M_{\odot} . In this section, we will consider a number of different initial WD masses (0.8 M_{\odot} , 0.9 M_{\odot} and 1.1 M_{\odot}) each accreting mass at a rate of $\dot{M} = 1 \times 10^{-7} M_{\odot} \text{ yr}^{-1}$ within a low density ISM ($n = 1$). The upper limiting mass here is the upper formation limit for a CO WD (Ritossa et al., 1996). The number of eruptions naturally increases as we lower the initial WD mass, as more eruptions are needed to reach M_{Ch} (see Table 4.6).

A comparison of the NSR shell for these three different initial WD masses is given in Figure 4.49 alongside the NSR from the reference simulation (Run 25, 26 and 27 compared to Run 1). Each remnant becomes marginally larger as the initial WD mass is lowered, as more eruptions lead to more ejecta impacting the surrounding

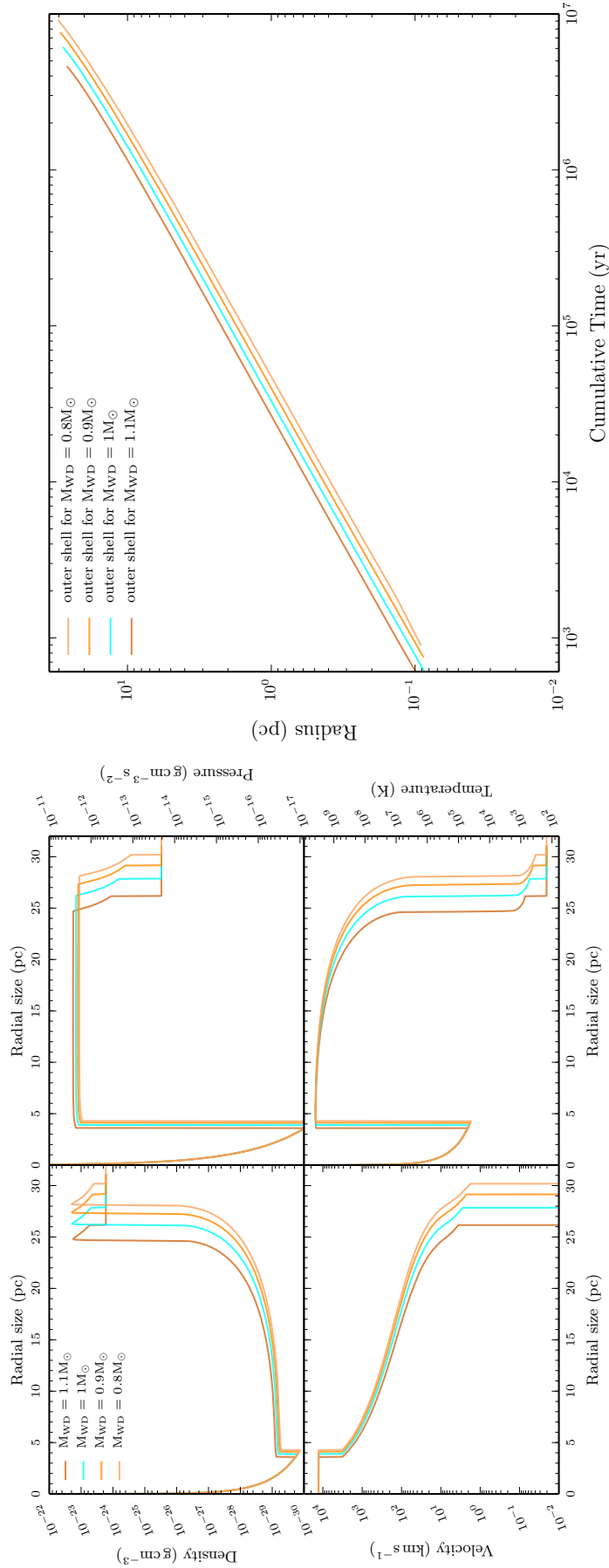


FIGURE 4.49: **Left:** Dynamics of the nova remnant with $1 \times 10^{-7} M_{\odot} \text{ yr}^{-1}$ and $n = 1$ for four different WD masses with a resolution of 100 AU/cell (Run 1 and Runs 25 – 27). **Right:** Evolution of the outer edge of the shell with respect to cumulative (elapsed) time and recurrence period for the four different WD masses.

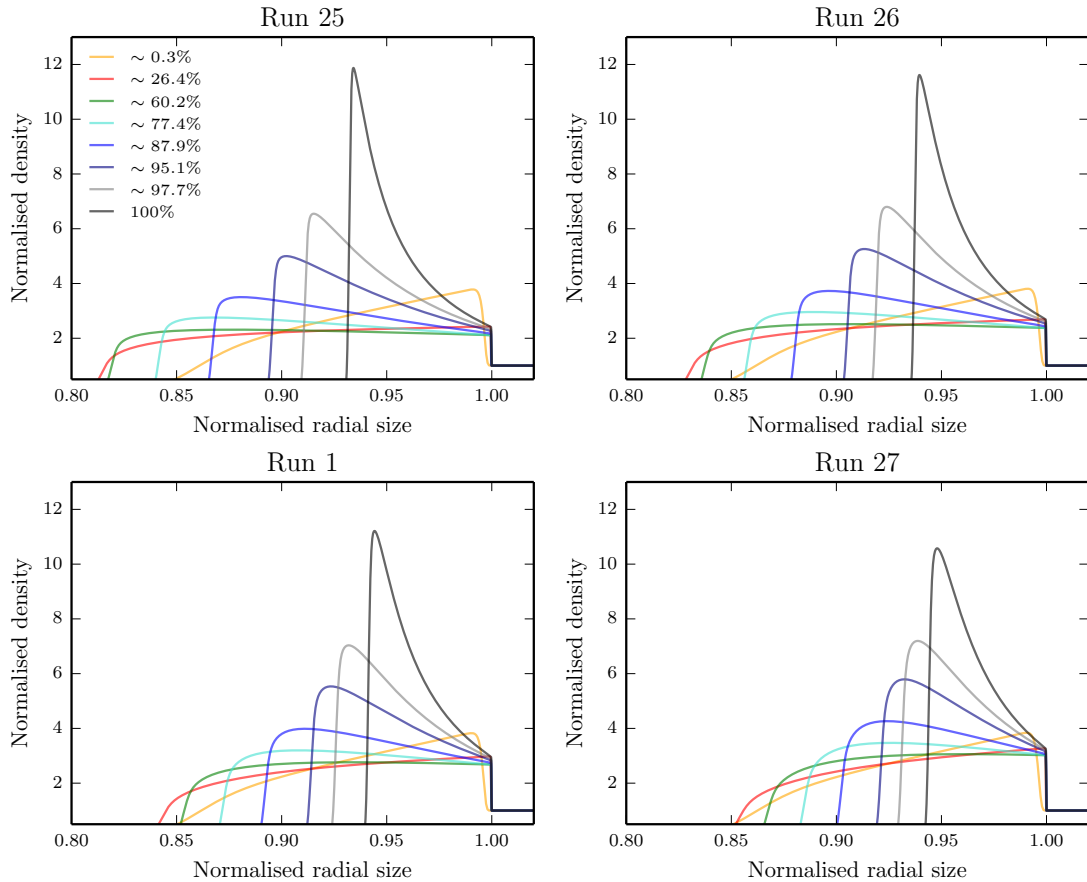


FIGURE 4.50: The evolution of the remnant shell at the same stage of each simulation for the four different initial WD masses: Run 25 ($0.8 M_{\odot}$ WD), Run 26 ($0.9 M_{\odot}$ WD), Run 1 ($1 M_{\odot}$ WD) and Run 27 ($1.1 M_{\odot}$ WD) with an ISM density of $n = 1$. Similar to Figure 4.19, the points of each simulation coinciding with the particular shell sizes are given as percentages.

ISM over a longer period of time. The structure of the shell for each remnant is remarkably similar, as can be seen in Figure 4.50, with the $0.8 M_{\odot}$ WD simulation finishing with a shell thickness of $\sim 7\%$ compared to $\sim 5\%$ for the $1.1 M_{\odot}$ WD simulation. Each remnant shell also follows a very similar transition, with similar shell widths ratios at the same epochs. This is further reinforced when looking at similar radial sizes of each NSR when the recurrence period in each system is matching (shown in Figure 4.51) as well as when the total kinetic energy from the system is at the same value (shown in Figure 4.52).

The radial growth curves of each simulation follow the same power law evolution with the $0.8 M_{\odot}$ WD taking approximately double ($\sim 9 \times 10^6$ years) the amount of time to reach the Chandrasekhar limit than the $1.1 M_{\odot}$ WD ($\sim 4.5 \times 10^6$ years). We also illustrate the outcome of a system with a WD growing from a different initial mass whilst incorporating radiative cooling in Figure 4.53. This was only tested with the $0.9 M_{\odot}$ WD and compared to the reference simulation with radiative cooling (Run

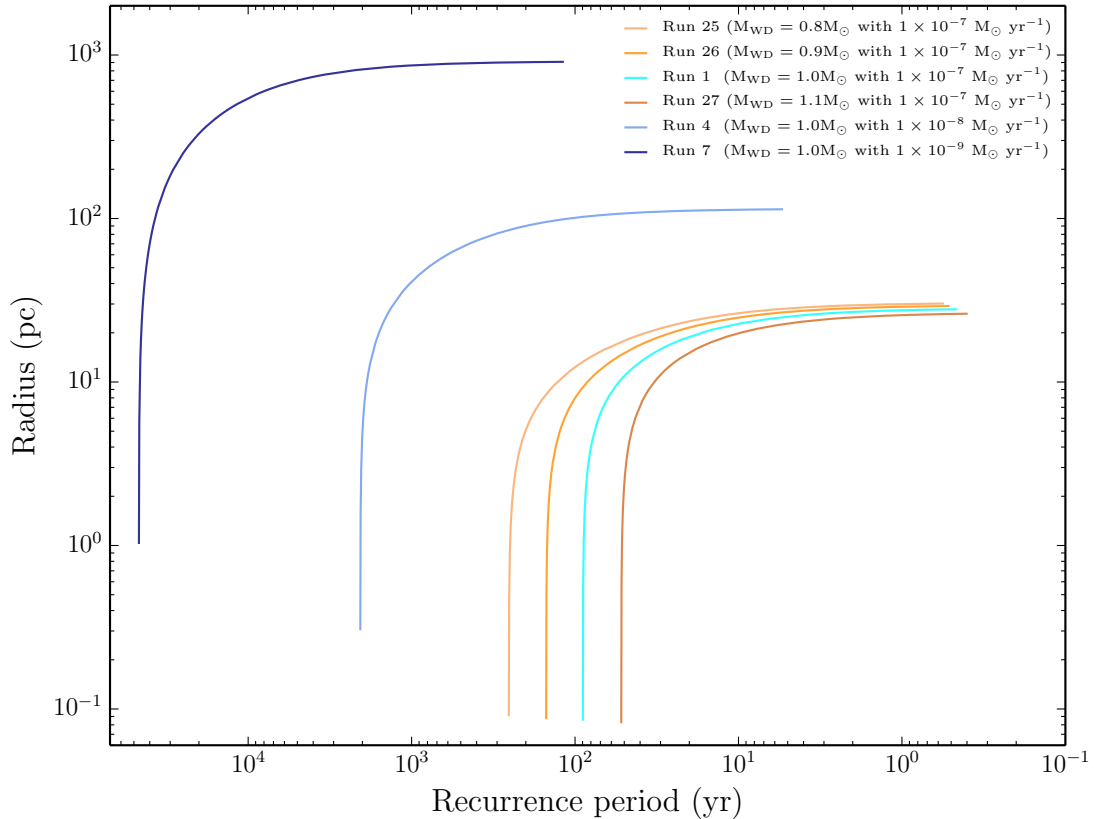


FIGURE 4.51: The radial size evolution of the remnant shell with respect to the recurrence period of the system for different initial WD masses (Run 25, 26, Run 1 and Run 27). We have also included changes to accretion rate runs (Run 4 and Run 7) to illustrate the largely different impacts from varying each parameter.

12) to highlight the same increase in radial size of the NSR from a system growing from a less massive WD. In the simulations without cooling and with cooling, we see that the initial WD mass has little impact on the final structure of the NSR, much less than the prominent influences of the mass accretion rate and surrounding ISM density.

4.9.4 Changing accretion rate within simulation

Another aspect of the nova system that we preliminarily looked at was a change of the mass accretion rate. Throughout our simulations, we have chosen a mass accretion rate and set it as a constant as the WD is grown. However, in reality, every nova eruption will irradiate the donor of the system and overflow the star's Roche surface (Kovetz et al., 1988; Hillman et al., 2020a) which drives up the accretion rate. The brighter disk resulting from the increase in mass transfer then irradiates the donor further and is sufficient enough to drive the mass transfer on its own (Ginzburg & Quataert, 2021), leading to a continuous change of accretion in the

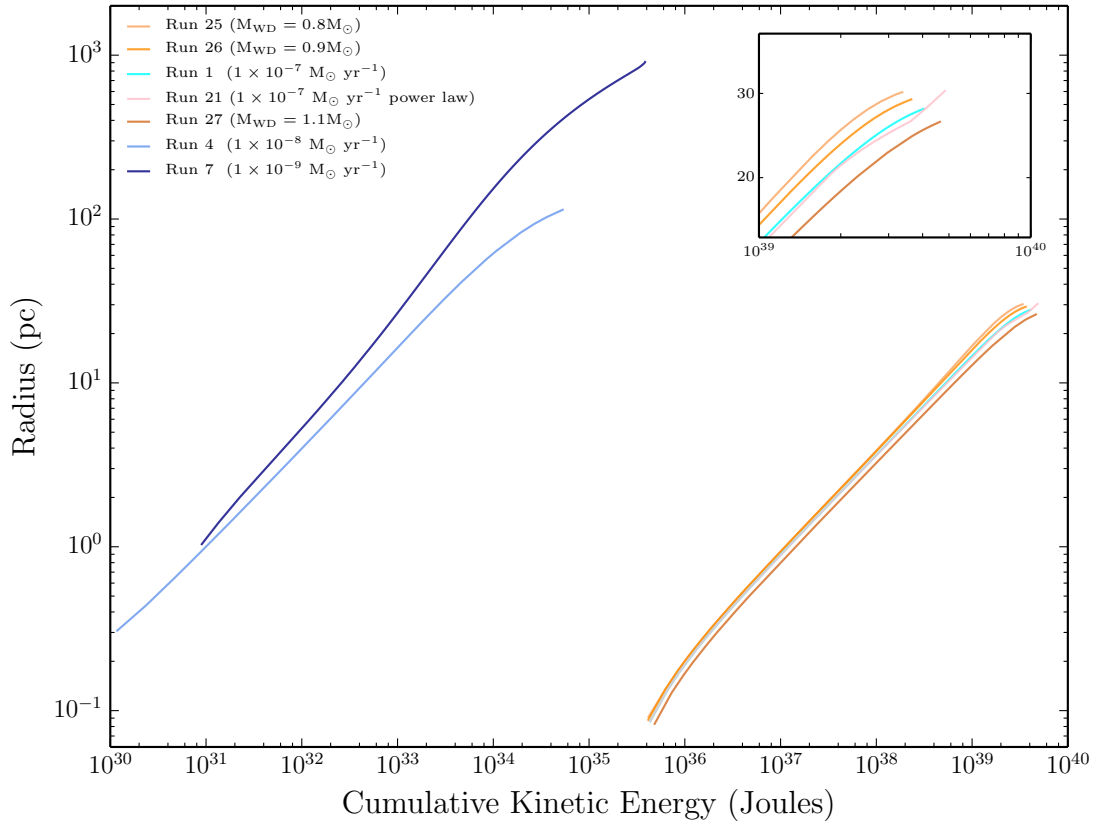


FIGURE 4.52: The radial size evolution of the remnant shell with respect to the cumulative kinetic energy of the system for initial WD masses (Run 25, 26, Run 1 and Run 27). Again, like Figure 4.51, we have also included changes to accretion rate runs (Run 4 and Run 7) to illustrate the largely different impacts from varying each parameter. We have also included the evolution of total kinetic energy from Run 21 (the power law interpolation, see Section § 4.9.2 for more details). Similar to Figure 4.27, it is important to note that the cumulative kinetic energy for Run 4 and Run 7 is much lower than seen in Figures 4.10, 4.11, 4.12 and 4.13 as here we are taking a small subset of the kinetic energy values generated by our simple model of a growing WD, in line with the number of outputs from the simulations.

system. Examples of this are seen in the Galactic recurrent novae, T Pyxidis (Knigge et al., 2000; Schaefer et al., 2010) and IM Normae (Schaefer et al., 2010).

As such, we ran a low resolution simulation (1000 AU/cell) in a low density environment ($n = 1$) starting with an accretion rate of $1 \times 10^{-8} M_{\odot} \text{ yr}^{-1}$ until the WD reached $1.25 M_{\odot}$, when the accretion rate was then increased to $1 \times 10^{-7} M_{\odot} \text{ yr}^{-1}$. Of course, this abrupt change in mass accretion rate is not physical but is simply a first order approximation. Also, the WD mass separating the different accretion rates was chosen solely because of the grid of parameters given in Yaron et al. (2005). Utilising our model of a growing WD, we estimated that this particular system would take 39,651,618 years (over 1,059,493 eruptions) for the WD to grow from $1 M_{\odot}$ to the upper limiting WD mass we set, with a recurrence period of ~ 242 days. The dynamics of the NSR formed from this set up is shown in Figure 4.54 with a comparison to

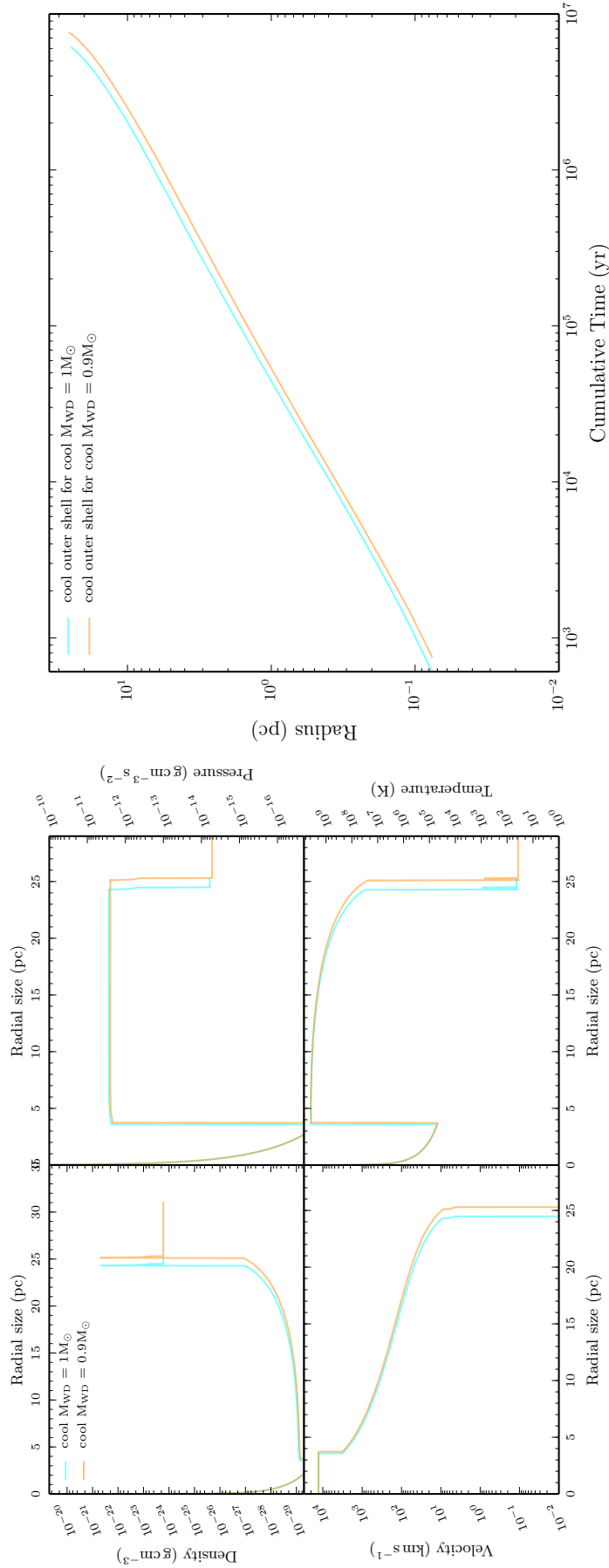


FIGURE 4.53: **Left:** Dynamics of the nova remnant with $1 \times 10^{-7} M_{\odot} \text{yr}^{-1}$ and $n = 1$ for initial WD masses of $0.9 M_{\odot}$ and $1 M_{\odot}$ with a resolution of $100 \text{AU}/\text{cell}$ (Run 12 and Run 28). **Right:** Evolution of the outer edge of the shell with respect to cumulative (elapsed) time and recurrence period.

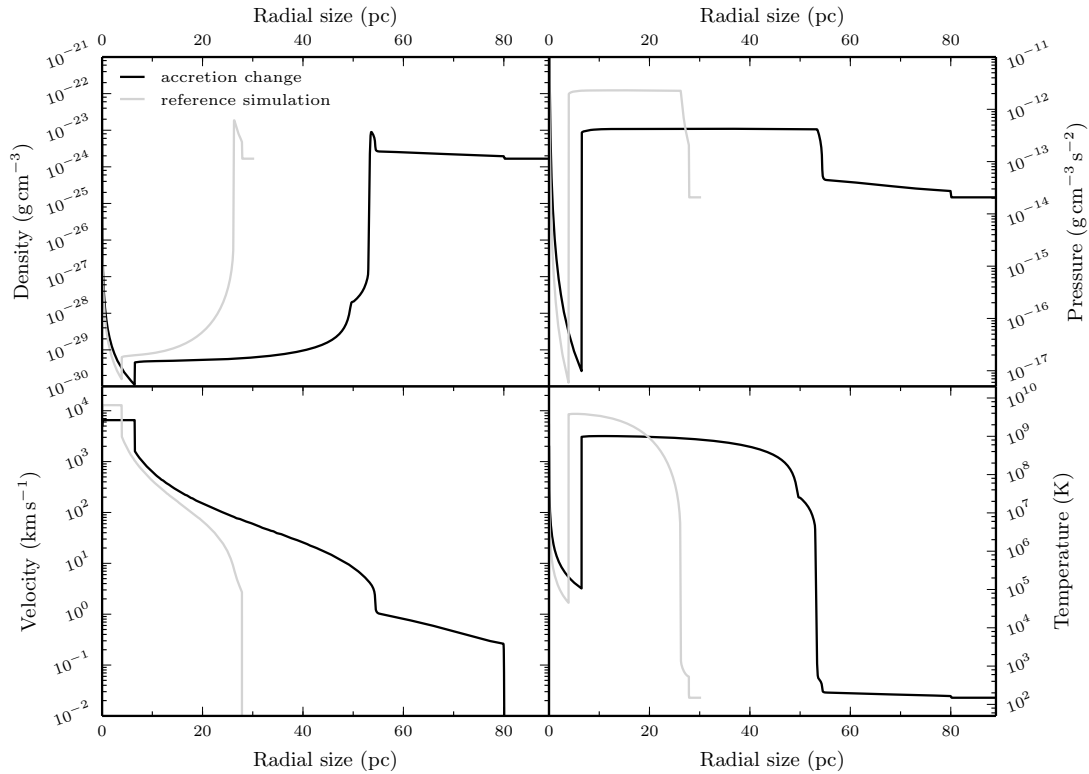


FIGURE 4.54: Dynamics of a NSR grown with a change of accretion rate during its evolution with a comparison to the reference simulation.

the NSR grown in Run 1.

We cannot see detail in this low resolution simulation however the gross structure of the remnant is clear. We see a small cavity extending from the nova system to approximately 6 pc before reaching the ejecta pile-up region. This ejecta pile up region spans tens of parsecs before reaching the inner edge of the remnant shell at ~ 50 pc. The shape of this shell looks to be a superposition of the $1 \times 10^{-7} M_{\odot} \text{ yr}^{-1}$ ($n = 1$) shell shown in Figure 4.18 and the $1 \times 10^{-8} M_{\odot} \text{ yr}^{-1}$ ($n = 1$) shown in Figure 4.21. The high density inner edge is approximately 3 pc in width with an extended lower density front ranging from 55 pc to 80 pc. The initial lower accretion rate creates a cavity in the ISM but the infrequent nature of the eruptions allow the remnant to start dissipating. However, once the accretion rate increases, and therefore the recurrence periods shorten, the more frequent ejecta collide at the inner edge of the shell. We see this in the other profiles also whereby there are high pressures in the ejecta pile-up region up to the inner edge of the shell before a pressure gradient within the extended portion of the shell. Similarly, the velocity and temperature in this wider component of the NSR shell drops substantially from those seen in the high density inner edge. Specifically, the velocity and temperature

of the inner edge reach $\sim 100 \text{ km s}^{-1}$ and $2 \times 10^7 \text{ K}$, respectively, but then drop to $\sim 0.3 \text{ km s}^{-1}$ and 200 K at the outer edge of the extended component.

If there was a smooth transition between the accretion rates instead of an abrupt change that we have simulated, we would see more of a ‘wedge-like’ structure, the higher density inner edge connected to the lower density outer edge with a smoother front. This would also be seen in the pressure, velocity and temperature profiles as a smoother gradient across the thin and wide shell component.

4.10 Summary

In this chapter, we have presented a large suite of hydrodynamical simulations of recurrent nova eruptions in order to determine how system parameters such as mass accretion rate, ISM density, WD temperature and initial WD mass affect the growth of a nova super-remnant. Here, we will summarise the key points:

1. Nova super-remnants should be found around other recurrent novae, as a high mass WD, a high mass accretion rate, and therefore a short period between outbursts, is the driving mechanism for their creation.
2. NSRs offer an opportunity to find locations of previously unknown recurrent novae, ‘extinct’ novae (donor is fully depleted) and identify sites of upcoming or previous SN Ia.
3. We have conducted full hydrodynamical simulations (with and without radiative cooling) to find the dependence of system parameters (T_{WD} , M_{WD} , \dot{M} , ISM density) on the growth of NSRs. Below are the range of parameters used:

Mass accretion rate (\dot{M}): $1 \times 10^{-7} M_{\odot} \text{ yr}^{-1}$, $1 \times 10^{-8} M_{\odot} \text{ yr}^{-1}$, $1 \times 10^{-9} M_{\odot} \text{ yr}^{-1}$

ISM density: $1.67 \times 10^{-24} \text{ g cm}^{-3}$, $1.67 \times 10^{-23} \text{ g cm}^{-3}$, $1.67 \times 10^{-22} \text{ g cm}^{-3}$

White dwarf temperature (T_{WD}): $1 \times 10^7 \text{ K}$, $3 \times 10^7 \text{ K}$, $5 \times 10^7 \text{ K}$

Initial white dwarf mass (M_{WD}): $0.8 M_{\odot}$, $0.9 M_{\odot}$, $1.0 M_{\odot}$, $1.1 M_{\odot}$

4. To replicate more realistic recurrent nova eruptions, we utilised results from [Yaron et al. \(2005\)](#) to create a simple model to grow a WD from $1M_{\odot}$ to $\sim M_{\text{Ch}}$. This simple model generated characteristics of non-identical outbursts, namely ejecta velocity, ejecta mass and recurrence period, to be used in our simulations.

5. We found that the long term structure of the NSR, with or without radiative cooling incorporated, is not affected by the length of the nova outburst nor the structure of the ejecta (internal shocks).
6. The evolving eruptions create NSRs many parsecs in radius comprising of a very low density cavity, bordered by a very hot ejecta pile-up region and surrounded by a cool high density remnant shell.
7. A higher density ISM restricts the size of the super-remnant, as does a high mass accretion rate.
8. The temperature of the underlying WD has little impact on the size of the NSR.
9. A lower initial WD mass also has little impact on the size of the NSR.
10. Incorporating radiative cooling leads to smaller NSRs with thinner high density shells.
11. The radial size of all remnants evolves as a power law with respect to time.
12. A more realistic representation of the NSR growth with radiative cooling does not replicate the structure of the NSR surrounding M 31N 2008-12a.

Chapter 5

Searching for Recurrent Nova Super-Remnants

5.1 Introduction

In this chapter, I will provide observables of NSRs derived from the simulations outlined in Chapter 4, which can be used to find more examples of these enormous shells. This includes a predictive tool used to estimate the radial sizes of potential remnants on the sky, alongside a description of the first ever targeted search for these phenomenon in the Galaxy; X-ray luminosity evolution and synthetic X-ray spectra to determine the feasibility of X-ray follow-up; and finally, synthetic sky images to aid observations and compare with the only example we currently have.

In Section § 5.2 we present the preliminary relationship found between the system parameters ρ and elapsed time, and the radial size of a NSR. We then estimate the ISM densities around the ten Galactic recurrent novae in Section § 5.3 to illustrate the utility of the preliminary radial size relationship and our attempt to find further examples of these vast shells around six Galactic recurrent novae in Section § 5.4. We then show a further refined predictive tool derived from simulations with varying the mass accretion rate of the systems in Section § 5.5. After consideration of the radial sizes of NSRs, in Section § 5.6 we calculate and examine the emission measure of the NSR from our reference simulation when the recurrence period of the system is one year. These predictions are then extended in Section § 5.7 to the whole reference simulation in order to explore the evolution of observational indicators associated with NSRs. Finally, we bring together these findings in Section

§ 5.8 in order to determine the parameters needed to recreate the 12a NSR and illustrate similarities of synthetic sky images with observations, before summarising this chapter in Section § 5.9.

5.2 Preliminary radial size equation

NSRs are best searched for extragalactically (Darnley & Henze, 2020; Darnley, 2021), due to their low surface brightness and large size, however, characteristics of known Galactic recurrent nova systems allow for a targeted approach with deeper photometric imaging. Therefore, it is essential to know the approximate area of the sky within which to look around these systems to find these elusive shells.

We have covered a broad area of parameter space with the suite of simulations outlined in Chapter 4, including varying the local ISM density, accretion rate of the system and the temperature and initial mass of the hosting WD. Consequently, we can fit functions to the evolutionary curves of these different nova shells to determine specific mathematical dependencies of the underlying parameters on the radial size of the NSR¹.

In Section § 4.5.1 and § 4.5.2, we presented the full simulations of a growing $1 M_{\odot}$ WD system accreting at a rate of $1 \times 10^{-7} M_{\odot} \text{ yr}^{-1}$ erupting within varying densities of surrounding ISM (Run 1, 2 and 3). As discussed, we see a reduction in NSR size as the density of the ISM increases, further illustrated with the associated radial growth curves in Figure 4.18. As in Section § 4.2.1, an analytic solution for a kinetic energy dominated steady-state outflow of the form $r \propto t^{0.6}$ can be fitted to the three distinct growth curves. However, in order to fit the growth curves more precisely, we utilised a curved power law of the form $r \propto t^{0.6+\beta t}$. An example of these fits are shown in Figure 5.2 (note that this illustrates the curved power law fit with a second order polynomial exponent discussed in Section § 5.5). The value of β and the proportionality constant were found by comparing the three distinct growth curves:

$$r_1(t) = 0.0019 \cdot t^{0.6+1.969 \times 10^{-9} \times t}, \quad (5.1)$$

$$r_2(t) = 0.0012 \cdot t^{0.6+1.990 \times 10^{-9} \times t}, \quad (5.2)$$

$$r_3(t) = 0.0008 \cdot t^{0.6+2.001 \times 10^{-9} \times t}. \quad (5.3)$$

¹For this, we utilised the simulations without radiative cooling as those with cooling incorporated were still running at the time of analysis.

We wanted an equation for radial size that is dependent on ISM density, ρ , and cumulative time, t , such that $r(\rho, t) = a \cdot t^{0.6+b \times t} \rho^c$ (the density term, ρ , has power law dependence as shown in Section § 4.2.1). Firstly, from equation 5.1, equation 5.2 and equation 5.3, we can simply set $b = 2 \times 10^{-9}$. Then, it is clear for each equation:

$$a \cdot \rho_1^c = 0.0019, \quad (5.4)$$

$$a \cdot \rho_2^c = 0.0012, \quad (5.5)$$

$$a \cdot \rho_3^c = 0.0008. \quad (5.6)$$

The ISM density for the growth curves are normalised with respect to the mass of a hydrogen atom therefore $\rho_1 = 1$, $\rho_2 = 10$ and $\rho_3 = 100$. Substituting these values into equation 5.4, equation 5.5 and equation 5.6 leads to:

$$\log(0.0019) = -2.721 = \log(a) + c \log(1) = \log(a), \quad (5.7)$$

$$\log(0.0012) = -2.921 = \log(a) + c \log(10) = \log(a) + c, \quad (5.8)$$

$$\log(0.0008) = -3.097 = \log(a) + c \log(100) = \log(a) + 2c. \quad (5.9)$$

We can directly take $a = 0.002$ from equation 5.7. The value of c can then be obtained by subtracting equation 5.7 from equation 5.8 (or likewise subtracting equation 5.8 from equation 5.9) to give $c = -0.2$, the same index we found with the analytic solution in Section § 4.2.1. The radius equation now takes the following form (showing the ISM density normalisation explicitly):

$$r(\rho, t) = 0.002 \cdot \left(\frac{\rho}{1.67 \times 10^{-24} \text{ g cm}^{-3}} \right)^{-0.2} \cdot t^{0.6+2 \times 10^{-9} \times t} \text{ pc}. \quad (5.10)$$

Finally, we will normalise the cumulative time, t , in this equation by a factor of 1 Myr, and take out a factor of 1.67 from the ISM density normalisation terms, which leads to:

$$r(\rho, t) = 9 \cdot \left(\frac{\rho}{10^{-24} \text{ g cm}^{-3}} \right)^{-0.2} \cdot \left(\frac{t}{1 \text{ Myr}} \right)^{0.6+2 \times 10^{-3} \times \frac{t}{1 \text{ Myr}}} \text{ pc}, \quad (5.11)$$

where r is the radius of the NSR, ρ is the estimated local ISM density and t is elapsed time from the starting mass of $1 M_{\odot}$. This elapsed time is related to the recurrence period of the system. The \dot{M} is set as a constant $10^{-7} M_{\odot} \text{ yr}^{-1}$ which is reasonable as most Galactic recurrent novae exhibit an accretion rate with the same order of magnitude as this. Finally, we can compare equation 5.11 to the analytic version

detailed in Section § 4.2.1 (equation 4.2) in the same form below (equation 5.12).

$$r(\rho, t) \approx 4411 \cdot \left(\frac{\dot{m}v^2}{\pi}\right)^{0.2} \cdot \left(\frac{\rho}{10^{-24} \text{ g cm}^{-3}}\right)^{-0.2} \cdot \left(\frac{t}{1 \text{ Myr}}\right)^{0.6} \text{ pc.} \quad (5.12)$$

5.3 Estimating the local ISM density

As detailed, in order to utilise equation 5.11, we need to know the density of the local ISM surrounding the nova system. We made use of two different methods to estimate this ISM density. The first method, suggested and guided by Prof. Steven Longmore, utilises the Besançon model of the Galaxy which provides the extinction distribution along different lines of sight (Marshall et al., 2006)². The second method utilises the 3D dust map given in Green et al. (2019)³.

5.3.1 Method 1

The Besançon model of the Galaxy (see, for e.g. Marshall et al., 2006) provides a heliocentric grid-like domain with the total K_s -band extinction to a particular distance defined as the sum of the extinction within in each grid along the line of sight. Therefore, we took the Galactic coordinates and respective distance in kiloparsecs to the nova, and found the relevant grid cell containing the system. We then took the distance and cumulative extinction to the inner radius ($d_{\text{in}, 1}$; $A_{K, \text{in}}$) and the outer radius ($d_{\text{out}, 1}$; $A_{K, \text{out}}$) to this particular grid cell to estimate the ISM density, ρ_{ISM} .

The extinction within the grid cell is simply $A_{K, \text{grid}} = A_{K, \text{out}} - A_{K, \text{in}}$ which we converted to a column density. Using the following relation between optical extinction, A_V , and hydrogen column density, N_{H} , from Güver & Özel (2009) (their equation 1):

$$N_{\text{H}} (\text{cm}^{-2}) = (2.21 \pm 0.09) \times 10^{21} A_V, \quad (5.13)$$

converting this to K band extinction using Cardelli et al. (1989):

$$\frac{A_K}{A_V} \simeq 0.114 \Rightarrow A_V \simeq 8.7 A_K,$$

and dividing by the solar hydrogen abundance $X = 0.739$ (Basu & Antia, 2004; Lodders, 2019) leads to a relation between a column density of solar material and

²<http://cdsarc.u-strasbg.fr/viz-bin/qcat?J/A+A/453/635>

³<http://argonaut.skymaps.info>

the K_s band extinction:

$$N_{\text{solar}} (\text{cm}^{-2}) = (2.61 \pm 0.11) \times 10^{22} A_K. \quad (5.14)$$

In order to find the total number of particles in the grid cell, we need to multiply the column density by the area of the grid. The volume density (ISM density) is then found by dividing the total number of particles within the grid cell by the volume of the cell. Instead, these two procedures can be combined to estimate the surrounding ISM density by dividing equation 5.14 by the length of the grid cell such that:

$$\rho_{\text{ISM}, 1} = \frac{N_{\text{solar, grid}}}{L_{\text{grid}}} = \frac{(2.61 \pm 0.11) \times 10^{22} A_{K, \text{grid}}}{d_{\text{out}, 1} - d_{\text{in}, 1}}. \quad (5.15)$$

Since we are calculating a volume-average density, it should be noted that the ISM is hierarchical and so there will be a lot of contrast in density within that volume, such that substantial fractions have significantly higher and lower values than the average (S. Longmore, private communication). This also applies to the following method in Section § 5.3.2.

5.3.2 Method 2

The three-dimensional map of dust reddening detailed in [Green et al. \(2019\)](#) is based on Gaia parallaxes and stellar photometry from Pan-STARRS 1 and 2MASS, and reaches out several kiloparsecs. As with method 1 in Section § 5.3.1, we took the distance to the nova system and used the uncertainties on this distance to create a grid cell. Using the dust map, we found an associated reddening with the upper ($d_{\text{out}, 2}; E(g-r)_{\text{out}}$) and lower ($d_{\text{in}, 2}; E(g-r)_{\text{in}}$) limits of the distance. The reddening in the grid cell is simply $E(g-r)_{\text{grid}} = E(g-r)_{\text{out}} - E(g-r)_{\text{in}}$ which we will convert to a column density.

Utilising the following relation for optical extinction and assuming that $R_V = 3.1$ (see, e.g. [Savage & Mathis, 1979](#)) such that:

$$A_V = R_V E(B-V) \quad \Rightarrow \quad A_V = 3.1 E(B-V),$$

with the conversion given for the dust map,

$$E(B-V) = 0.884 \times E(g-r),$$

leads to

$$A_V = 3.1 \times 0.884 \times E(g-r) \simeq 2.74 E(g-r). \quad (5.16)$$

The relation between optical extinction and hydrogen column density (equation 5.13) can be rewritten by substituting equation 5.16:

$$N_{\text{H}} (\text{cm}^{-2}) = (2.21 \pm 0.09) \times 10^{21} A_V = (2.21 \pm 0.09) \times 10^{21} \times 2.74 E(g-r)$$

$$\therefore N_{\text{H}} (\text{cm}^{-2}) = (6.06 \pm 0.25) \times 10^{21} E(g-r). \quad (5.17)$$

As with Section § 5.3.1, dividing equation 5.17 by the solar hydrogen abundance $X = 0.739$ (Basu & Antia, 2004; Lodders, 2019) leads to a relation between a column density of solar material and the reddening given in the 3D dust map:

$$N_{\text{solar}} (\text{cm}^{-2}) = (8.20 \pm 0.34) \times 10^{21} E(g-r). \quad (5.18)$$

Again, this solar material column density can then be divided by the length of the grid cell to estimate the local ISM density:

$$\rho_{\text{ISM}, 2} = \frac{N_{\text{solar, grid}}}{L_{\text{grid}}} = \frac{(8.20 \pm 0.34) \times 10^{21} E(g-r)_{\text{grid}}}{d_{\text{out}, 2} - d_{\text{in}, 2}}. \quad (5.19)$$

5.4 First search for Galactic nova super-remnants

Using the radial size equation described in Section 5.2, we wanted to predict the radial size of the potential NSR surrounding the ten Galactic recurrent novae. Firstly, we took a subset of four RNe: U Scorpii, V3890 Sagittarii, T Coronae Borealis, V2487 Ophiuchi, to guide our pilot study search with the Liverpool Telescope. These four systems were chosen as they were visible with the Liverpool Telescope during the semester I was applying for observing time, plus they were the smaller remnants predicted. Afterwards, whilst this study was ongoing, we chose an additional two RNe: RS Ophiuchi and CI Aquilae, this time visible during the next viewing semester with the Liverpool Telescope, to extend this study further.

The radial size equation (equation 5.11) requires knowledge of the system's recurrence period (to convert to t) as well as an estimate for the local ISM density. We used known recurrence periods for the ten RNe (see Table 5.1) to find an associated elapsed time, t , for the system. We then took the Galactic coordinates of the ten RNe and their respective distances in kiloparsecs (see Table 5.1) to estimate the ISM. For six systems, their location in the sky restricted the use of one of the methods for estimating the ISM. In those cases, we were only able to utilise either method 1 (Section § 5.3.1) or method 2 (Section § 5.3.2), however for the other four systems, we were

TABLE 5.1: Radial size predictions of the ten Galactic recurrent novae. The six RNe chosen for our pilot study to search for associated NSRs are shown with an asterisk (*). The ISM density ρ_{ISM} for each were estimated as outlined in the text. The notation (B), (D) and (A) represents the ISM density being estimated with method 1 only (Besançon model), method 2 only (3D dustmap) or an average of the two methods, respectively. Shell radius and shell thickness were derived using equation 5.11 and angular size was found from the distance to the system.

Nova	Distance (kpc)	P_{rec} (yr)	ρ_{ISM} ($1.67 \times 10^{-24} \text{ g cm}^{-3}$)	Shell radius (pc)	Angular size (arcmin)	Shell thickness (% of shell radius)
U Sco*	12 ± 2 [1]	10 ± 1 [2]	0.0199 ± 0.0008 (D)	49.1 ± 0.4	28 ± 5	$\sim 12\%$
RS Oph*	$1.4^{+0.6}_{-0.2}$ [3]	15 ± 6 [2]	0.049 ± 0.002 (A)	37.7 ± 0.2	160 ± 40	$\sim 14\%$
T Pyx	3 ± 1 [1]	24 ± 12 [2]	0.038 ± 0.002 (B)	34.4 ± 0.3	80 ± 26	$\sim 15\%$
V745 Sco	3.50 ± 0.85 [4]	26 ± 1 [2]	0.38 ± 0.02 (B)	20.3 ± 0.2	40 ± 10	$\sim 15\%$
CI Aql*	3.0 ± 0.5 [4]	27 ± 4 [2]	0.49 ± 0.02 (A)	19.0 ± 0.1	44 ± 7	$\sim 15\%$
V3890 Sgr*	$4.4^{+2.6}_{-1.3}$ [5]	29 ± 1 [2]	0.153 ± 0.005 (A)	23.1 ± 0.1	32 ± 12	$\sim 15\%$
V394 CrA	2.0 ± 1.0 [4]	40 ± 20 [6]	0.0085 ± 0.0004 (B)	36.0 ± 0.3	120 ± 60	$\sim 16\%$
T CrB*	0.8 ± 0.03 [5]	80 ± 20 [7]	1.33 ± 0.05 (D)	5.20 ± 0.04	45 ± 2	$\sim 14\%$
IM Nor	2.4 ± 0.8 [4]	80 ± 20 [8]	0.50 ± 0.02 (B)	6.3 ± 0.1	18 ± 6	$\sim 15\%$
V2487 Oph*	1.08 ± 0.28 [4]	100 ± 20 [9]	0.52 ± 0.02 (A)	2.93 ± 0.02	19 ± 5	$\sim 14\%$

References: [1] Schaefer (2010) – [2] Darnley (2021) and references therein – [3] Barry et al. (2008) – [4] given as 2.0 in Özdönmez et al. (2016) – [5] Bailer-Jones et al. (2018) – [6] given as ~ 38 in Darnley (2021) – [7] given as ~ 80 in Darnley (2021) – [8] given as ~ 82 in Darnley (2021) – [9] given as ~ 98 in Darnley (2021).

able to use both methods and take an average⁴. Table 5.1 outlines the estimated ISM density, normalised to $1.67 \times 10^{-24} \text{ g cm}^{-3}$, as well as the method used.

The ISM densities estimated around the ten Galactic RNe above indicate that three of these systems are located within coronal gas (a hot ionised medium) where we see densities of $10^{-4} - 10^{-2} \text{ particles cm}^{-3}$ and the rest are likely to be situated in warm (neutral or ionised) medium (Ferrière, 2001). This is not surprising as coronal gas makes up between 30 – 70% of the fractional volume of the Galaxy and the warm medium makes up the rest, with low fractions of matter accounting for the molecular clouds, H II regions and the cold medium (Ferrière, 2001). However, it is important to note that the grid cells we utilised to estimate these ISM densities are very large, on the order of kiloparsecs, and so we are very likely to be underestimating the densities.

Substituting these ISM density values into equation 5.11 produces a radial size of the potential NSR. A simple function fitted to the shell thickness evolution of the NSR simulations also reveals an estimate for the shell thickness. This radial size and shell thickness estimate can then be combined with the known distance to the nova to determine an upper and lower limit of the shell’s angular size on the sky (see Table 5.1). The upper and lower limits for the radial size of the six recurrent novae used to guide the observations with the Liverpool Telescope in our pilot study are shown in Figure 5.1.

However, note that these are preliminary estimates for the radial size. As a result of the developing nature of the pilot study and the need to acquire observing time, the ISM densities used to predict these shell sizes were not estimated using the methods detailed in Section § 5.3.1 and Section § 5.3.2, but with a more rudimentary use of method 1. Utilising the methods from Section § 5.3.1 and Section § 5.3.2 would likely lead to smaller NSRs as the updated ISM density estimates were higher than before, something that can be implemented in future analysis (see Section § 7.2.2.1).

5.5 Refinement of radial size equation

Up until now, we have considered the role of ISM density as well as elapsed time of the growing WD (related to the system’s recurrence period) in shaping the radial size of the NSR. We will now look at the inclusion of other system parameters utilised in our simulations. Clearly, the rate of mass accretion within the system has a major influence on the sizes of these vast remnants, as we have shown in Section

⁴The density calculated with method 2 is systematically $\sim 2 \times$ the density found with method 1.

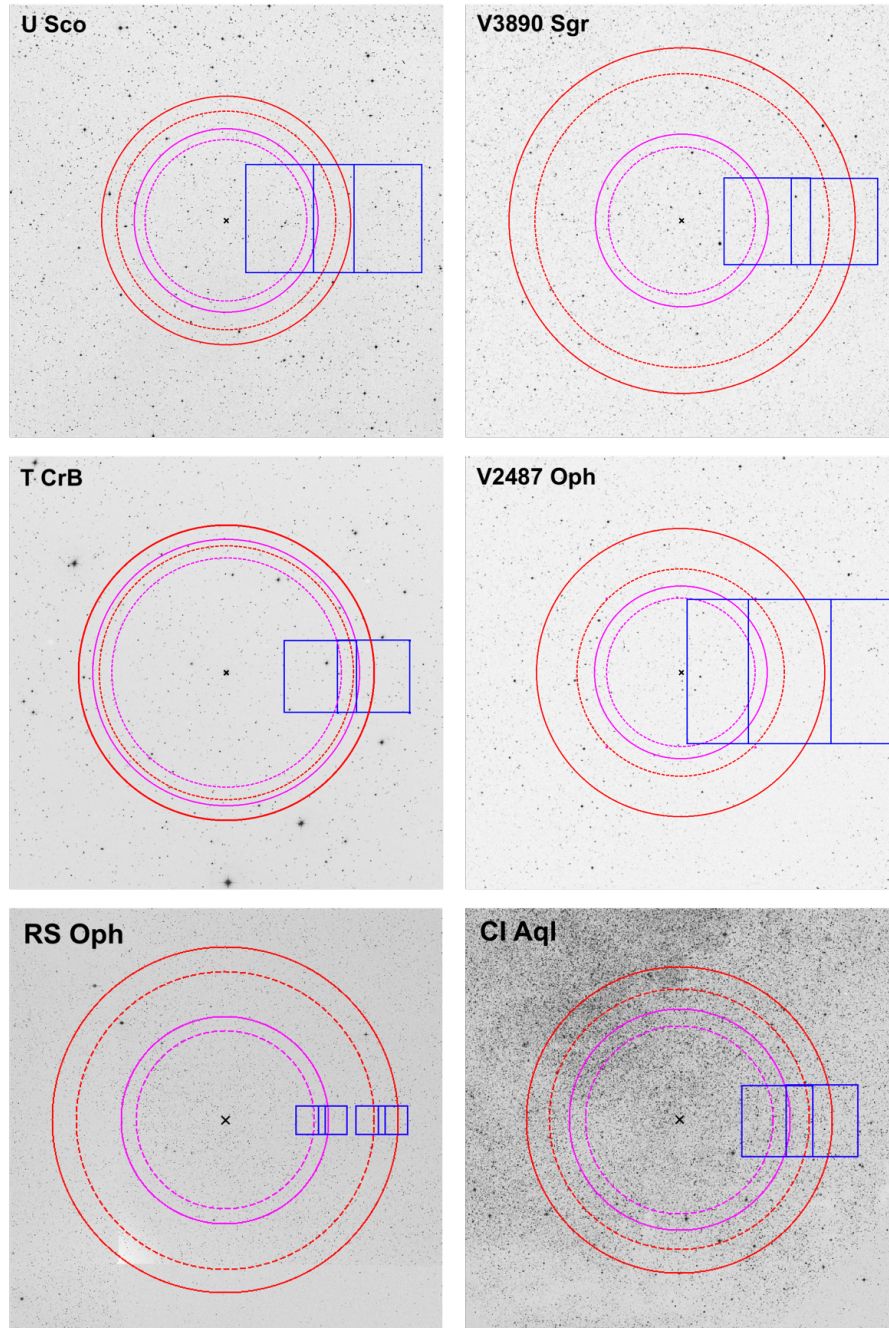


FIGURE 5.1: Colour inverted DDS field images of the sky centred on the six Galactic recurrent novae chosen for our pilot study to search for associated NSRs from predictions: U Scorpii (U Sco), V3890 Sagittarii (V3890 Sgr), T Coronae Borealis (T CrB), V2487 Ophiuchi (V2487 Oph), RS Ophiuchi (RS Oph) and CI Aquilae (CI Aql). The location of the nova is marked with a black cross. The *upper limit* on the outer and inner edge of the shell is indicated by the red and magenta *solid* lines and the *lower limit* on the outer and inner edge of the shell is indicated by the red and magenta *dashed* lines. The blue boxes indicate the fields to be observed with the LT FOV. Images sizes: U Sco ($30' \times 30'$), V3890 Sgr ($50' \times 50'$), T CrB ($60' \times 60'$), V2487 Oph ($30' \times 30'$), RS Oph ($2.5^\circ \times 2.5^\circ$) and CI Aql ($60' \times 60'$). Note that the angular sizes of these predictions are from a preliminary estimate of the ISM density, not from the ISM densities found from method 1 (Section § 5.3.1) and method 2 (Section § 5.3.2) in Table 5.1.

§ 4.5.2, § 4.5.3 and § 4.5.4 (and see Figure 4.34). However, the initial mass and the temperature of the WD does not significantly alter the NSR size as we have shown in Section § 4.5.5 for WD temperature and Section § 4.9.3 for initial WD mass. Therefore, in a similar fashion to Section § 5.2, we will now construct a more refined radial size equation to incorporate the mass accretion rate of a system alongside the ISM density and recurrence period dependence.

Unlike the previous fits to the power law growth curves of Run 1, 2 and 3 which considered a linear exponent of time in Section § 5.2, we will now adopt a second order polynomial in the exponent to reflect the considerable change in radial size as the system reaches the later stages of its evolution. The curved power law fits we now consider have the form $r \propto t^{0.6+\beta t^2}$ and are shown in Figure 5.2. Here, we have omitted the linear t term as the function fitting is dominated by the t^0 and t^2 terms. As done previously, the value of β , as well as the proportionality constant, were found by comparing the fits of the three distinct growth curves:

$$r_4(t) = 0.0020 \cdot t^{0.6+2.59 \times 10^{-16} \times t^2}, \quad (5.20)$$

$$r_5(t) = 0.0013 \cdot t^{0.6+2.65 \times 10^{-16} \times t^2}, \quad (5.21)$$

$$r_6(t) = 0.0008 \cdot t^{0.6+2.67 \times 10^{-16} \times t^2}. \quad (5.22)$$

We again want an equation for radial size that is dependent on ISM density, ρ , and cumulative time, t , such that $r(\rho, t) = a \cdot t^{0.6+b \times t^2} \rho^c$. Using the same method we employed in Section § 5.2, we find the constants of this equation to give:

$$r(\rho, t) = 9 \cdot \left(\frac{\rho}{10^{-24} \text{ g cm}^{-3}} \right)^{-0.2} \cdot \left(\frac{t}{1 \text{ Myr}} \right)^{0.6+2.6 \times 10^{-4} \times \left(\frac{t}{1 \text{ Myr}} \right)^2} \text{ pc}, \quad (5.23)$$

where r is the radius of the NSR, ρ is the estimated local ISM density and t is elapsed time from the starting mass of $1 M_\odot$. This elapsed time is related to the recurrence period of the system.

Previously, the mass accretion rate, \dot{M} , was set as a constant $10^{-7} M_\odot \text{ yr}^{-1}$, however we will now incorporate this parameter into our radial size equation. We do this by fitting curved power laws with a second order polynomial exponent to the radial growth curves of Run 4, Run 5 and Run 6, those simulations with a lower mass accretion rate ($1 \times 10^{-8} M_\odot \text{ yr}^{-1}$) as can be seen in Figure 5.3. We now take the function, $r_4(t)$, (equation 5.20) fitted to the radial growth curve of Run 1 ($n = 1$ and $1 \times 10^{-7} M_\odot \text{ yr}^{-1}$) alongside the function fitted to the radial growth curve of Run 4

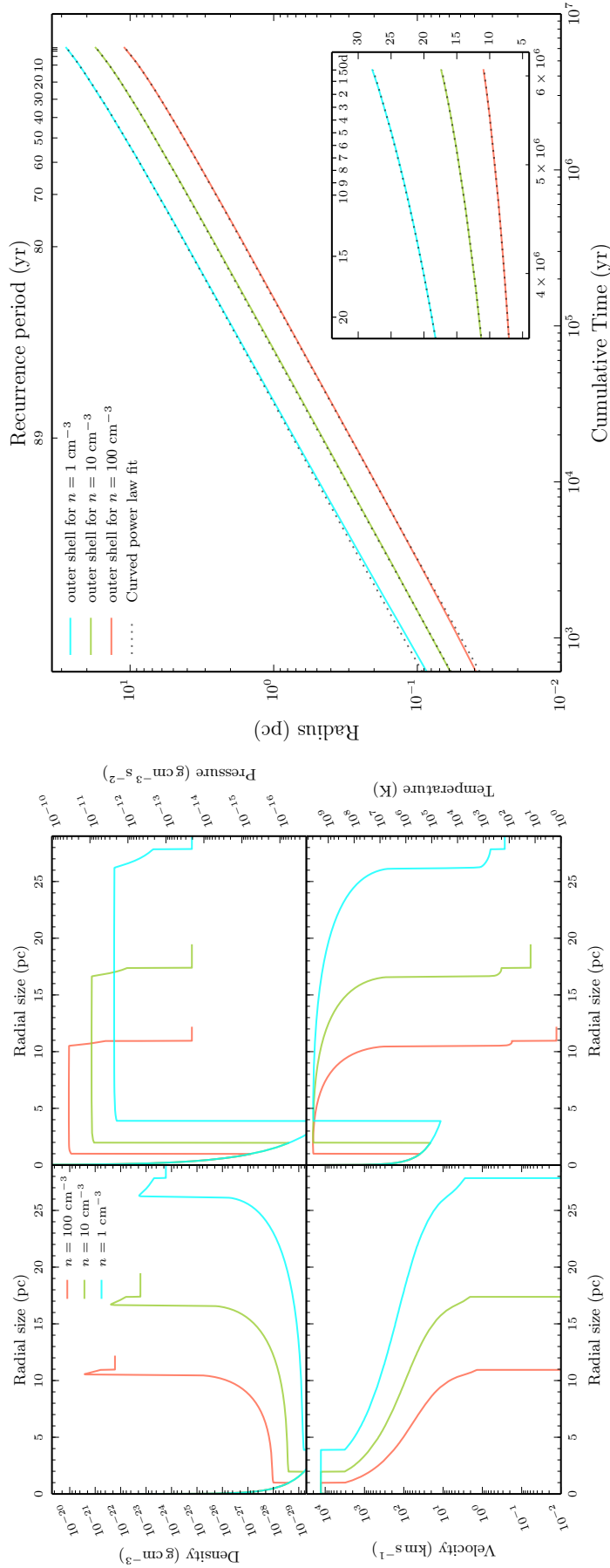


FIGURE 5.2: Left: Dynamics of the nova remnant with $\dot{M} = 1 \times 10^{-7} M_{\odot} \text{ yr}^{-1}$ for three different ISM densities after 819,565 eruptions with a resolution of 100 AU/cell. **Right:** Evolution of the outer edge of the shell with respect to cumulative (elapsed) time and recurrence period for the three different ISM densities. A curved power law with a second order polynomial exponent is fitted to the three curves.

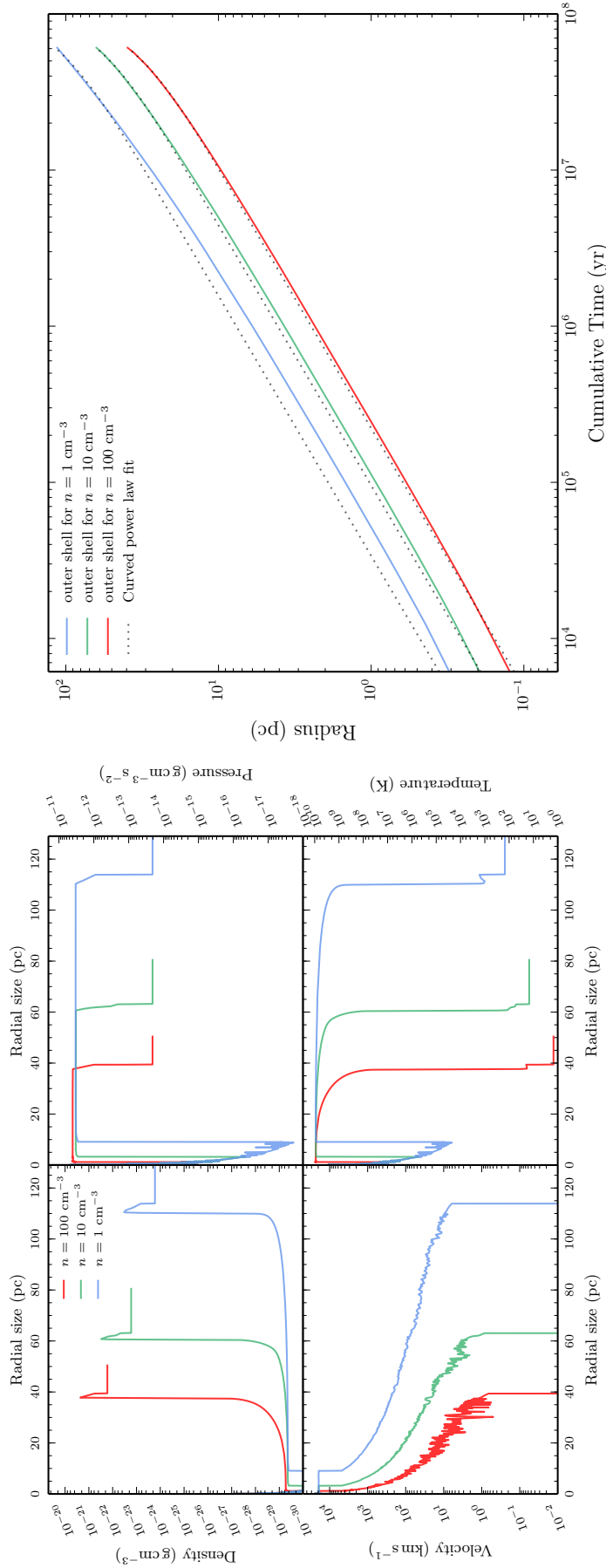


FIGURE 5-3: Left: Dynamics of the nova remnant with $\dot{M} = 1 \times 10^{-8} M_{\odot} \text{ yr}^{-1}$ for three different ISM densities after 384,257 eruptions with a resolution of 200 AU/cell. **Right:** Evolution of the outer edge of the shell with respect to cumulative (elapsed) time for the three different ISM densities. A curved power law with a second order polynomial exponent is fitted to the three curves. At first glance the fits look very poor up until 10^7 years, however this is only $\sim 16\%$ of the total simulation. We have plotted the radial growth curves on a logarithmic scale here simply to illustrate the contrast at short timescales but this is not indicative of what happens at longer timescales where the fitting is much better.

($n = 1$ and $1 \times 10^{-8} \text{ M}_\odot \text{ yr}^{-1}$) which we will call $r_7(t)$:

$$r_7(t) = 0.0020 \cdot t^{0.6+4.1 \times 10^{-18} \times t^2}, \quad (5.24)$$

to determine a dependence of the mass accretion rate within our refined radial size equation. Through comparing equation 5.20 and equation 5.24, we can see that the multiplicative factor for the t^2 term is affected by the change of mass accretion rate. Therefore, we can let:

$$a \cdot \dot{M}_1^\alpha = 2.6 \times 10^{-16}, \quad (5.25)$$

$$a \cdot \dot{M}_2^\alpha = 4.1 \times 10^{-18}. \quad (5.26)$$

If we let the higher accretion rate of $1 \times 10^{-7} \text{ M}_\odot \text{ yr}^{-1}$ be $\dot{M} = 1$, then it follows that the lower accretion rate ($1 \times 10^{-8} \text{ M}_\odot \text{ yr}^{-1}$) can be represented as $\dot{M} = 0.1$. Substituting these values into equation 5.25 and equation 5.26 leads to:

$$\log(2.6 \times 10^{-16}) = -15.59 = \log(a) + \alpha \log(1) = \log(a), \quad (5.27)$$

$$\log(4.1 \times 10^{-18}) = -17.39 = \log(a) + \alpha \log(0.1) = \log(a) - \alpha. \quad (5.28)$$

From equation 5.27 we can directly see that $a = 2.6 \times 10^{-16}$. Substituting this value of a into equation 5.28 leads to $\alpha = 1.8$. The new radius equation takes the following form (showing the ISM density and mass accretion rate normalisation explicitly):

$$r(\rho, \dot{M}, t) = 0.002 \cdot \left(\frac{\rho}{1.67 \times 10^{-24} \text{ g cm}^{-3}} \right)^{-0.2} \times \left(\frac{t}{1 \text{ Myr}} \right)^{0.6+2.6 \times 10^{-16} \times \left(\frac{\dot{M}}{1 \times 10^{-7} \text{ M}_\odot \text{ yr}^{-1}} \right)^{1.8} \left(\frac{t}{1 \text{ Myr}} \right)^2} \text{ pc.} \quad (5.29)$$

Finally, we will normalise the cumulative time, t , in this equation by a factor of 1 Myr, and take out a factor of 1.67 from the ISM density normalisation terms. This leads to our final NSR radial size equation:

$$r(\rho, \dot{M}, t) = 9 \cdot \left(\frac{\rho}{10^{-24} \text{ g cm}^{-3}} \right)^{-0.2} \cdot \left(\frac{t}{1 \text{ Myr}} \right)^{0.6+2.6 \times 10^{-4} \times \left(\frac{\dot{M}}{10^{-7} \text{ M}_\odot \text{ yr}^{-1}} \right)^{1.8} \left(\frac{t}{1 \text{ Myr}} \right)^2} \text{ pc}$$

where r is the radius of the NSR, ρ is the estimated local ISM density, \dot{M} is the mass accretion rate of the system and t is elapsed time from the starting mass of 1 M_\odot . This elapsed time is related to the recurrence period of the systems. As detailed in Section 4.5.3, the outbursts from systems with lower accretion rates are less frequent than those with higher accretion rates. The related recurrence period

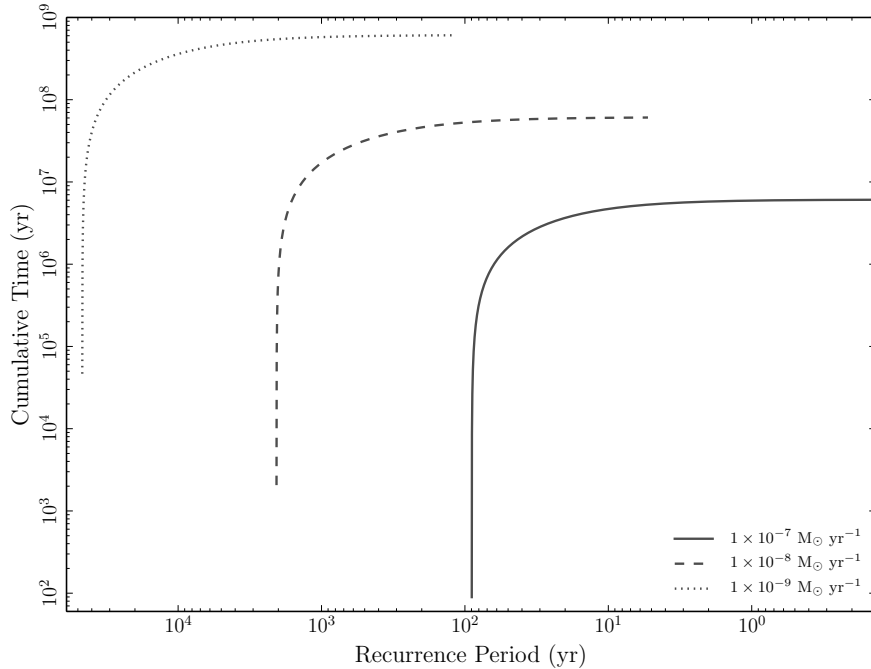


FIGURE 5.4: The recurrence period vs cumulative time for different accretion rates.

to elapsed time is therefore different for different accretion rates and can be looked up accordingly (see, for example, Figure 5.4).

5.6 Predictions of NSR emission at $P_{\text{rec}} = 1$ year epoch

As well as understanding the radial sizes of these shells, it is important to know the location and form of emission produced for any follow-up campaigns. The simplest way to predict the emission over the simulated nova shells is making the assumption of an environment completely made up of hydrogen. We can then calculate the fraction of this hydrogen that is ionised to find the contribution of different parts of the shell towards the total emission and from this, compute synthetic X-ray spectra.

In this section, we will use the epoch of our reference simulation (Run 1 from Chapter 4) that coincides with a recurrence period of 1 year (after 5.9×10^6 years when the WD has grown from $1M_{\odot}$ to $\sim 1.4M_{\odot}$) as this gives us an insight into the structure of the remnant from simulations that can be directly compared to the nova super-remnant surrounding 12a. We will then extend this analysis by predicting the evolution of NSR emission throughout the full reference simulation in Section § 5.7.

5.6.1 Fraction of ionisation within NSR

We will begin with the Saha equation, which can be used to calculate the ionisation state of a gas in equilibrium at a temperature T :

$$\frac{N_{j+1}}{N_j} = \frac{2Z_{j+1}}{n_e Z_j} \left(\frac{2\pi m_e kT}{h^2} \right)^{3/2} e^{-\chi_j/kT}. \quad (5.30)$$

Here, N_j is the number of atoms in state j , n_e is the electron number density, m_e is electron mass, k is the Boltzmann constant, h is Planck's constant, χ_j is the ionisation energy for an electron in state j and Z_j is the partition function:

$$Z_j = \sum_{n=1}^{\infty} g_n e^{-\frac{(E_n - E_j)}{kT}},$$

with g_j being the statistical weight of state n (the number of states with the same energy E_n) and E_m being the energy of another state. As we are only interested in hydrogen, we can use the relationship $g_s = 2s^2$ between statistical weight g_s and state j (where $j = 1$ is the ground state) in the following calculation.

If we assume that most of the neutral hydrogen is in the ground state then $Z_{\text{I}} \approx g_1 = 2$ (with g_1 being the statistical weight of the ground state). For the case of ionised hydrogen, the ionised state is a proton, therefore $Z_{\text{II}} = 1$, and the ionisation energy to remove an electron from the hydrogen nucleus is $\chi = 13.6$ eV so the Saha equation 5.30 becomes:

$$\frac{N_{\text{II}}}{N_{\text{I}}} = \frac{2Z_{\text{II}}}{n_e Z_{\text{I}}} \left(\frac{2\pi m_e kT}{h^2} \right)^{3/2} e^{-\chi_{\text{I}}/kT} = \frac{1}{n_e} \left(\frac{2\pi m_e kT}{h^2} \right)^{3/2} e^{-13.6\text{eV}/kT}. \quad (5.31)$$

We know that there is one electron for every H II ion therefore, taking n_H to be the number of atoms or ions per unit volume and accounting for conservation of charge, we can express the electron number density, n_e , in the following way:

$$\begin{aligned} n_e &= \frac{N_{\text{II}}}{N_{\text{I}} + N_{\text{II}}} n_H \\ \Rightarrow \frac{1}{n_e} &= \frac{N_{\text{I}} + N_{\text{II}}}{N_{\text{II}}} \frac{1}{n_H}. \end{aligned} \quad (5.32)$$

Substituting this alternative expression for n_e (equation 5.32) into the Saha equation (equation 5.31) and noting that $N \equiv N_{\text{I}} + N_{\text{II}}$ gives:

$$\begin{aligned} \frac{N_{\text{II}}}{N_{\text{I}}} &= \frac{N_{\text{I}} + N_{\text{II}}}{N_{\text{II}}} \frac{1}{n_{\text{H}}} \left(\frac{2\pi m_e kT}{h^2} \right)^{3/2} e^{-13.6\text{eV}/kT} \\ \Rightarrow \frac{N_{\text{II}}^2}{N_{\text{I}}(N_{\text{I}} + N_{\text{II}})} &= \frac{N_{\text{II}}^2}{(N - N_{\text{II}})N} = \frac{1}{n_{\text{H}}} \left(\frac{2\pi m_e kT}{h^2} \right)^{3/2} e^{-13.6\text{eV}/kT} \\ \Rightarrow \frac{N_{\text{II}}^2}{(1 - N_{\text{II}}/N)N^2} &= \frac{1}{n_{\text{H}}} \left(\frac{2\pi m_e kT}{h^2} \right)^{3/2} e^{-13.6\text{eV}/kT}. \end{aligned} \quad (5.33)$$

Finally, introducing the ionisation fraction as $f = N_{\text{II}}/N$ into equation 5.33 leads to:

$$\frac{f^2}{1-f} = \frac{1}{n_{\text{H}}} \left(\frac{2\pi m_e kT}{h^2} \right)^{3/2} e^{-13.6\text{eV}/kT}, \quad (5.34)$$

a quadratic equation for finding the ionisation fraction from the number density n_{H} and temperature T .

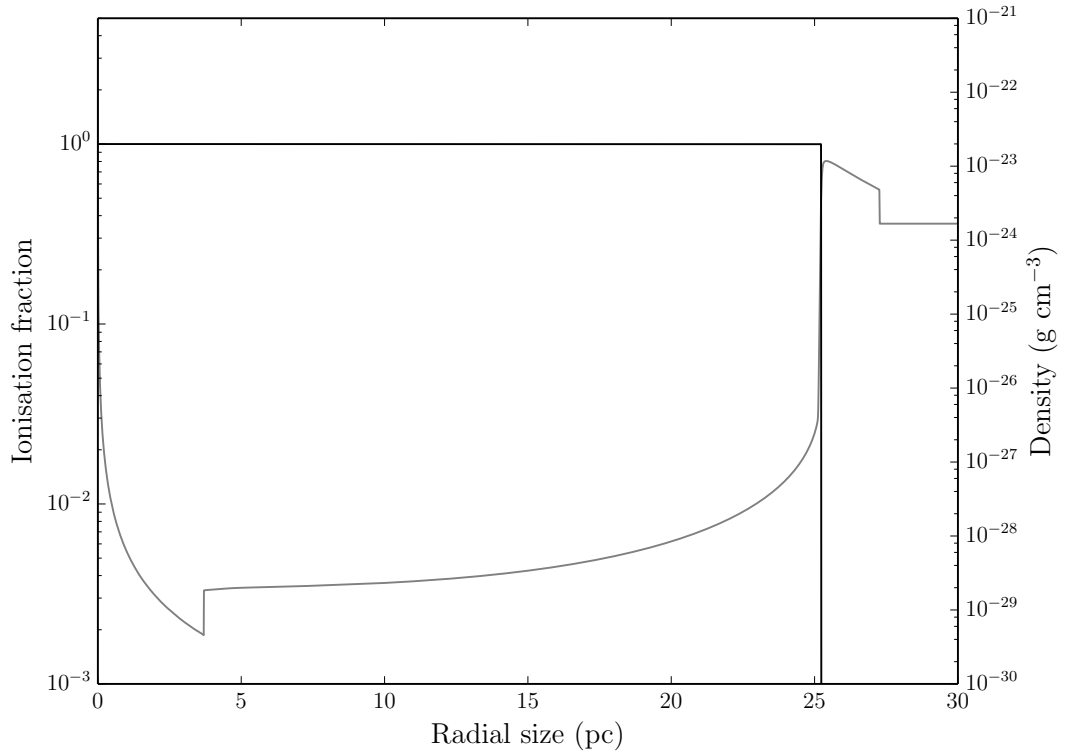


FIGURE 5.5: The solid line is the ionisation fraction of the reference simulation NSR at the epoch when the $P_{\text{rec}} = 1$ year and the faint line is the density distribution of the reference simulation NSR at the same point.

Now we can take the density and temperature from each cell of our reference simulation and, assuming we have only hydrogen, calculate the fraction of ionised hydrogen throughout the created NSR. Applying equation 5.34 to the reference simulations at 5.9 Myr leads to the profile given in Figure 5.5.

As can be seen in this figure, every cell within the remnant up to the inner edge of the shell is completely ionised ($f = 1$) before the ionisation drops off dramatically to negligible values within the shell. This fully ionised state within the cavity (up to ~ 4 pc in Figure 5.5) can be attributed to hydrogen (albeit low density) experiencing collisional excitation from the shocks within the wind, and therefore has no time to recombine (see Section § 5.6.3). Beyond this, within the ejecta pile up region (between ~ 4 –25 pc in Figure 5.5), the gas is continuously impacted by new eruptions and forward shocks resulting in collisional excitation and consequently an ionisation fraction $f = 1$. These shocks are also present at the inner edge of the shell (~ 25 pc in Figure 5.5) as the pile up region collides into the swept up shell. However, further into the shell regime towards the outer edge (~ 27 pc in Figure 5.5), the hydrogen atoms are more dynamically shielded from incoming shocks and so do not experience a high level of ionisation.

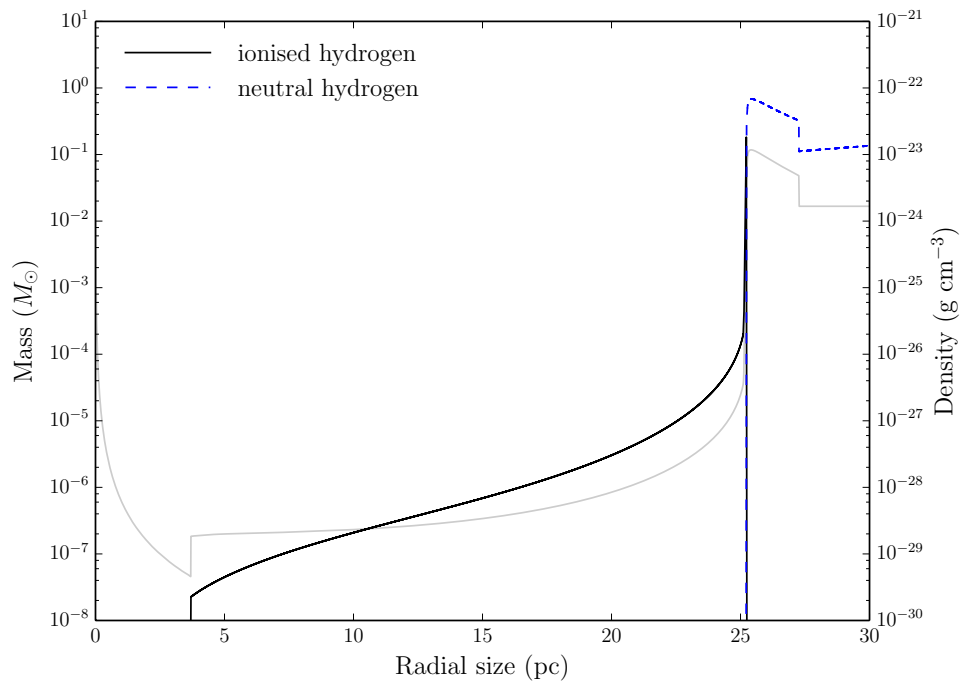


FIGURE 5.6: The solid line is the mass per shell of ionised hydrogen and the blue dashed line is the mass per shell of neutral hydrogen of the reference simulation NSR at the epoch when the $P_{\text{rec}} = 1$ year. The faint solid line is the density distribution of the reference simulation NSR at the same point.

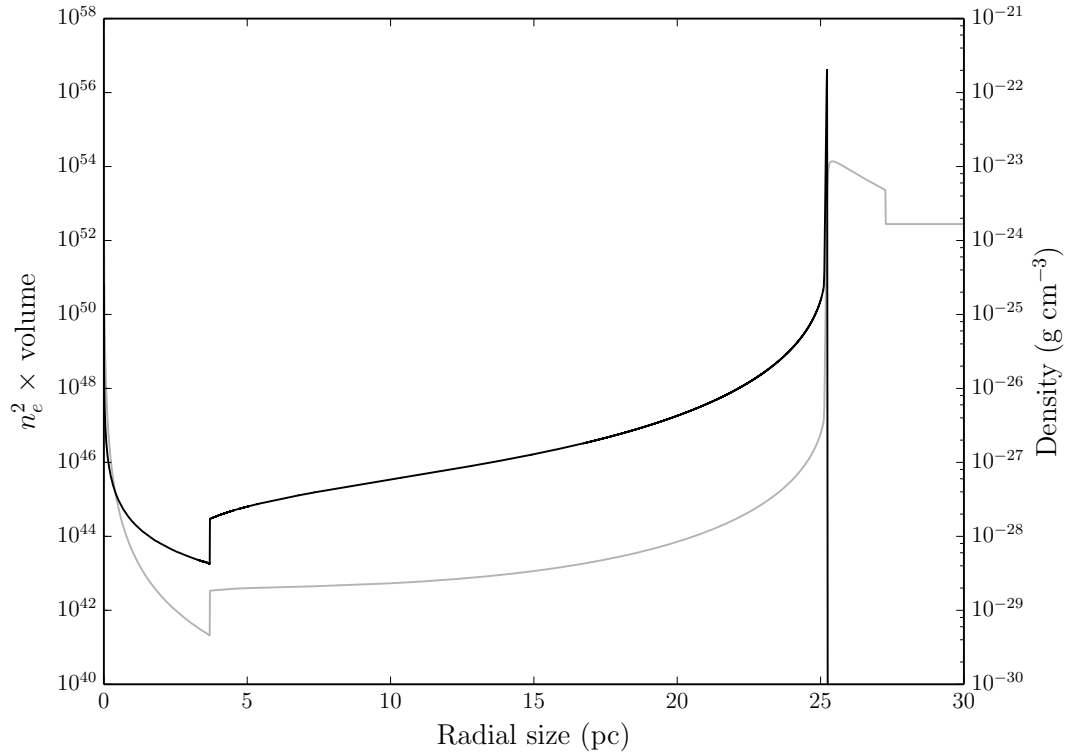


FIGURE 5.7: Emission measure ($n_e^2 \times \text{volume}$) from the NSR of the reference simulation at the epoch when $P_{\text{rec}} = 1$ year along with the density distribution of the simulated NSR.

As we know the ionisation fraction throughout the whole NSR, we can also determine the radial profile of the ionised and neutral hydrogen within the remnant by spherically integrating the whole shell. This is shown in Figure 5.6. As expected, there is negligible amounts of neutral hydrogen within the remnant in line with the full ionised radial profile of Figure 5.5 up to the inner edge of the shell. We then see a significant amount of neutral gas within the remnant shell, mimicking the structure of the density profile.

The ionised hydrogen profile, on the other hand, is only insignificant within the cavity region of the remnant. Past this empty zone, the mass of ionised hydrogen increases in accordance with the increase in density as a consequence of the constant ionisation fraction. We then see a very sharp increase in the ionised mass at the inner edge of the remnant shell (~ 25 pc) where the dramatic increase in density coincides with the near unity ionisation fraction before it drops away.

5.6.2 Emission measure and X-ray emission within NSR

After determining the ionisation fraction throughout the NSR, we can define the emission measure, E_i , in each grid cell i as:

$$E_i = \int_{V_i} n_e n_p dV_i, \quad (5.35)$$

where V_i is the volume of grid cell i , n_e is the electron density and n_p is the proton density. The electron density can be represented in terms of ionisation fraction, f , of the cell, density, ρ , within the cell and the mass of a proton, m_p , as:

$$n_e = f \times \frac{\rho}{m_p}, \quad (5.36)$$

and because the number of protons is equal to the number of electrons in a medium of fully ionised hydrogen ($n_e = n_p$), the emission measure in equation 5.35 becomes:

$$E_i = \int_{V_i} n_e^2 dV_i. \quad (5.37)$$

Using the density data from the epoch of our reference simulation that coincides with a recurrence period of 1 year along with the calculated ionisation fraction data, we found the emission measure for each cell as shown in Figure 5.7. In the same manner as Vaytet (2009), Vaytet et al. (2011) and Darnley et al. (2019a), we weighted the contributions of each cell by emission measure before binning the cells into 95 logarithmically divided temperature bins ranging from 149 K to $\sim 3.9 \times 10^9$ K (shown in Figure 5.8). These 95 binned emission measures were then inserted into XSPEC⁵ as a 95-component plasma and along with the temperature of each bin, an emissivity ε was produced. For this we used the APEC model which computes an emission spectrum from a collisionally-ionised diffuse gas⁶. The APEC model computes the emission lines for the metals helium, carbon, nitrogen, oxygen, neon, magnesium, aluminium, silicon, sulphur, argon, calcium, iron and nickel using their solar abundances (helium fixed at cosmic) and the VAPEC model computes emission lines based on inputted metal abundances. Therefore we set all metals to be zero to represent a gas made up purely of hydrogen. The synthetic X-ray spectra, ranging from 0.3 - 10 keV, for both models are shown in Figure 5.10. We then introduced absorption into the APEC and VAPEC model, under the assumption that our simulated remnant was at the distance of M 31. For the extra parameters needed in this

⁵XSPEC is an X-ray spectral fitting package with the “ability to generate simulated spectra given a theoretical model and detector response” (Arnaud, 1996). For further details, see <https://heasarc.gsfc.nasa.gov/xanadu/xspec/>.

⁶<https://heasarc.gsfc.nasa.gov/xanadu/xspec/manual/node135.html#vapec>

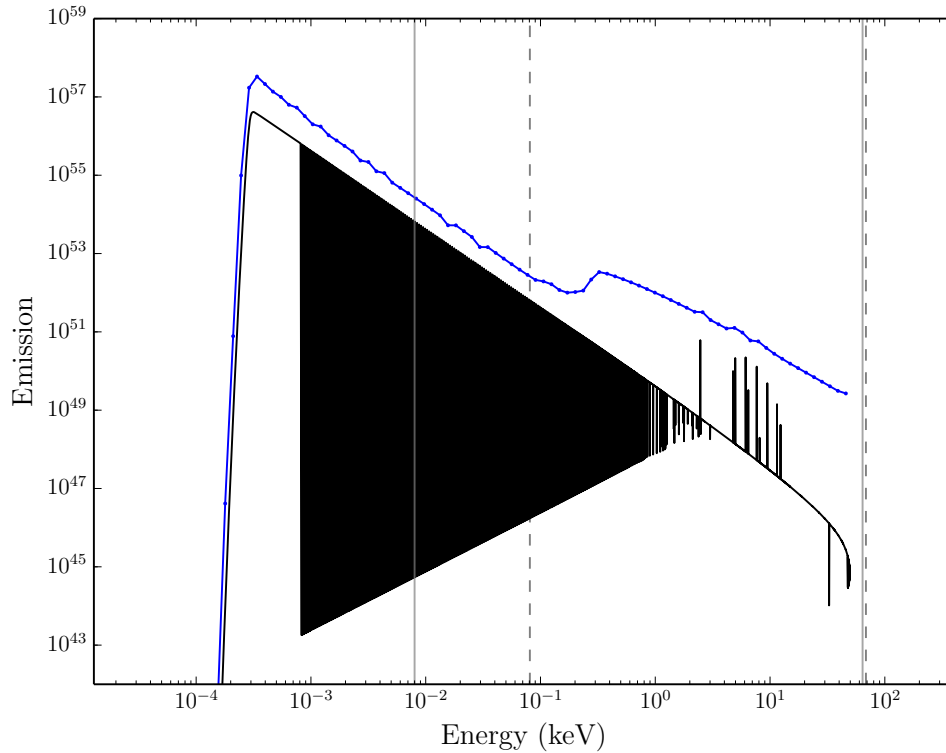


FIGURE 5.8: The black line shows the emission measure of the reference simulation at the epoch when $P_{\text{rec}} = 1$ year, ordered by temperature. The blue line shows the sum of emission measure in the 95 logarithmically placed temperature bins. The two grey lines show the upper (64 keV) and lower (0.008 keV) temperature limit of the APEC model. The two black dashed lines show the upper (68.4 keV) and lower (0.0808 keV) temperature limit of the VAPEC model.

model, we chose a column density of $N_H = 0.07 \times 10^{22} \text{ cm}^{-2}$ (Henze et al., 2018a) and a distance to M 31 of 778 kpc. The X-ray luminosity for each cell was also calculated using the APEC model with the inclusion of absorption, shown in Figure 5.9.

At the centre of the remnant, there is a high X-ray luminosity from the underlying system from the nova eruptions, however this is then followed by negligible emission from the cavity, as this region is too sparse to create any resistance, and therefore create shocks. Beyond this cavity, the ejecta begins to impact the higher density ejecta pile-up region (~ 4 pc), leading to a significant increase in the X-ray luminosity ($6 \times 10^{21} \text{ erg s}^{-1}$). As more and more ejecta contribute towards shock-heating the pile-up region further from the centre, we see a continuous increase in X-ray emission up to the inner edge of the NSR shell at ~ 25 pc, where $L_{\text{X-ray}} = 1 \times 10^{28} \text{ erg s}^{-1}$.

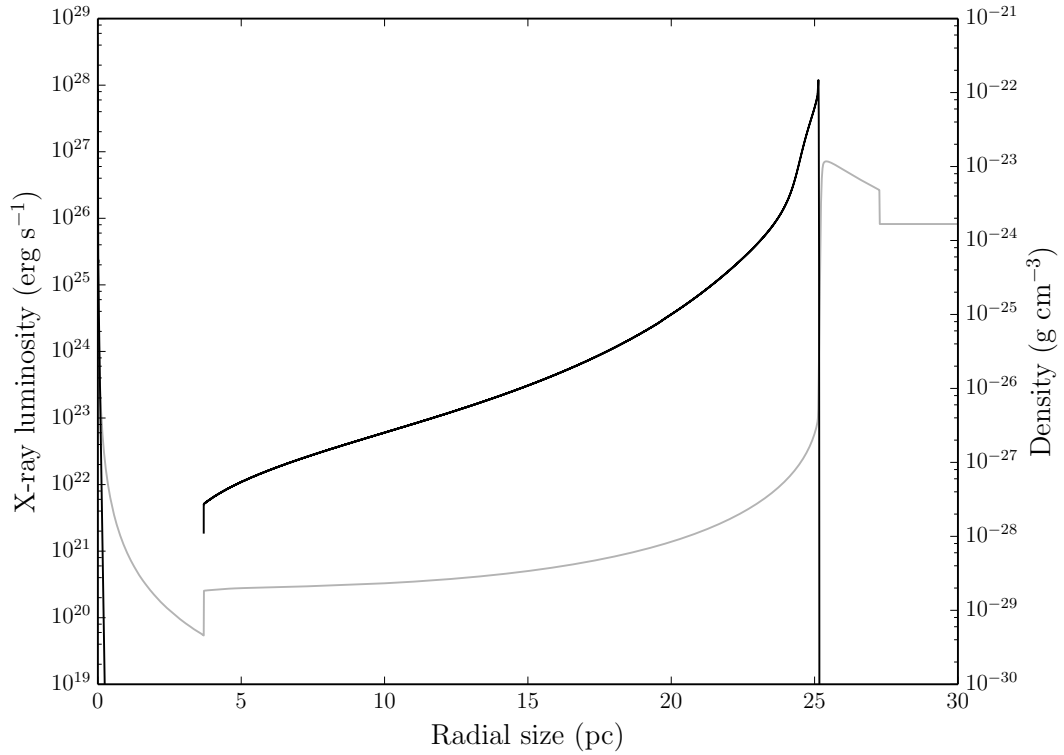


FIGURE 5.9: The black line shows the synthetic X-ray luminosity (from the APEC model with absorption) of the reference simulation at the epoch when $P_{\text{rec}} = 1$ year, along with the density distribution of the simulated NSR.

5.6.3 Recombination time within NSR

Another useful parameter to consider is the recombination time. This will inform us of the length of time the material within the remnant remains ionised and consequently the likelihood of emission from particular regions. We define the recombination time as:

$$\tau_{\text{recomb}} = \frac{1}{n_e \times \beta}, \quad (5.38)$$

where n_e is electron density and $\beta \approx 2 \times 10^{-16} \times T_{\text{ISM}}^{-0.75} \text{ m}^3 \text{ s}^{-1}$.

We firstly considered the scenario with a remnant made up of pure hydrogen. Using equation 5.36 to find the electron density from our calculated ionisation fraction (in Section § 5.6.1), along with the temperature of each cell from our reference simulation used for T , we found the radial profile of recombination time for pure hydrogen. This is illustrated in Figure 5.11 with the blue line. As we can see, the recombination times throughout the whole remnant are enormous. Owing to the extremely low densities and continuous ejecta expanding within the cavity region (up to ~ 4 pc), it would take around the age of the Universe for the hydrogen atoms to recombine

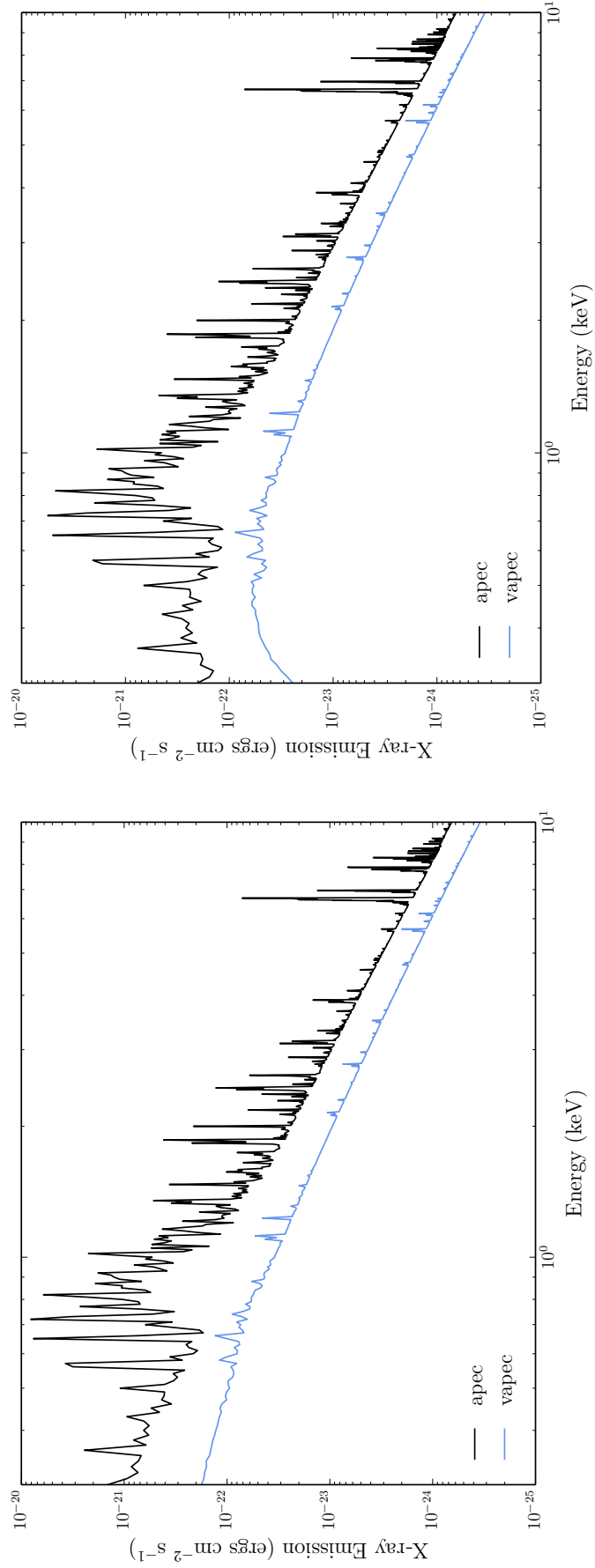


FIGURE 5.10: **Left:** Synthetic X-ray spectra of the NSR from our reference simulation at epoch when $P_{\text{rec}} = 1$ year generated with the APEC and VAPEC models ranging from 0.3 - 10 keV, with a resolution of 10 eV. **Right:** Same as the left panel with absorption included.

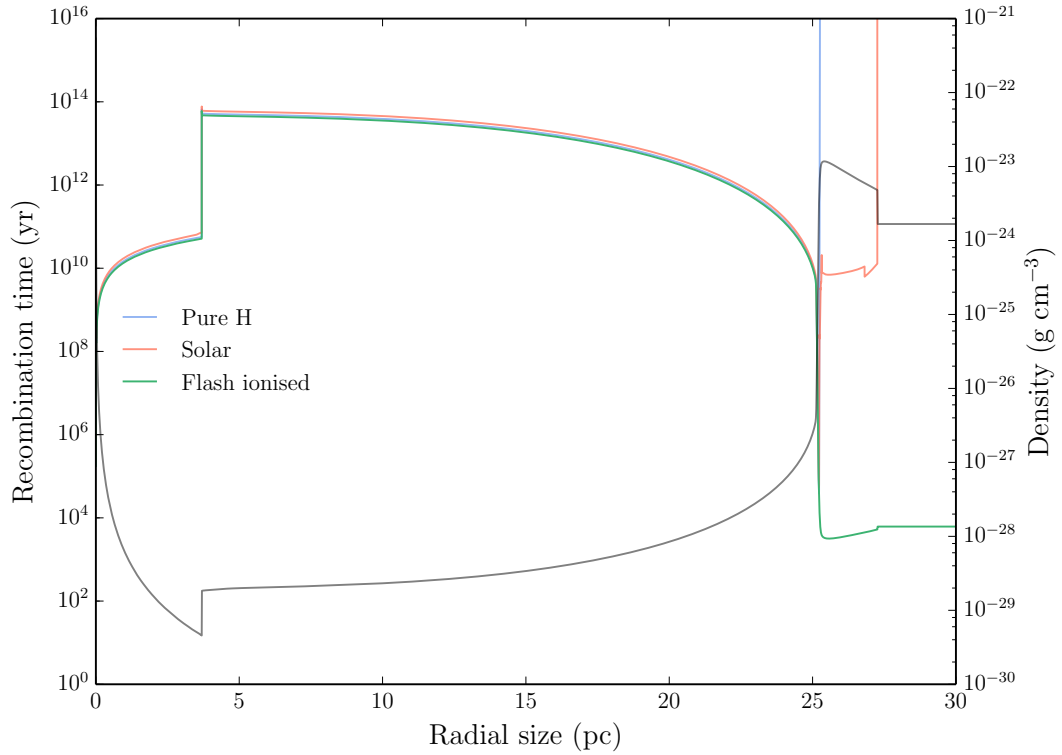


FIGURE 5.11: The blue, red and green lines are the recombination times at each point of the reference simulation NSR at the epoch when the $P_{\text{rec}} = 1$ year if the medium was comprised of pure hydrogen, solar or was completely ionised. The black line is the density distribution of the reference simulation NSR at the same point.

here. Within the ejecta pile-up region, between $\sim 4 - 25$ pc, the continual shocking from colliding ejecta results in recombination times on the order of $10^{10} - 10^{14}$ years. At the inner edge of the remnant's shell, where the density of hydrogen dramatically increases, we see recombination times dropping to a few tens of thousands of years. Beyond this inner edge, the ionisation fraction drops to effectively zero such that the material is completely neutral in the NSR shell and surroundings. Consequently, the recombination time becomes infinite as recombination cannot physically happen in this regime.

The analysis was then extended by Dr Matt Darnley to incorporate solar abundances of elements within the NSR material to determine the effect of metals on recombination time. For this, the ISM abundances from [Wilms et al. \(2000\)](#) were utilised to construct a more comprehensive Saha equation in order to determine the ionisation fraction of hydrogen, helium, carbon, nitrogen, oxygen, neon, sodium, magnesium, aluminium, silicon, phosphorus, sulphur, chlorine, argon, calcium, titanium, chromium, manganese, iron, cobalt and nickel within the remnant. The electron

density found in each cell throughout the reference simulation was then used to find the recombination time as shown in Figure 5.11 (the red line). Although very similar to the case of pure hydrogen within the cavity and ejecta pile-up region, there is a definite increase in recombination time on the order of a fraction of $10^{10} - 10^{14}$ years, a vast amount of time. This is a consequence of the large increase in the number of free electrons within an extremely sparse region. Similar to the case of pure hydrogen, the recombination time for the material at the inner edge of the remnant shell drops to only a few 10^4 years. However, unlike the pure hydrogen case where the shell is completely neutral, here we see the effects of metals being ionised within this region as the recombination times are not infinite, even though still incredibly high. It is only beyond the outer edge of the NSR shell where there is completely neutral atoms with the inability for recombination to occur.

The two scenarios we have considered so far inform us of the dynamical recombination time. Therefore, the final scenario we consider is a remnant made up of solar material (using the ISM abundances from Wilms et al. (2000) as previously) that has been completely flash ionised throughout. As all electrons have been removed from their associated nuclei, we can determine the electron density within each cell of our reference simulation to be used in equation 5.38. The radial profile of the recombination times for a flash ionised NSR is given in Figure 5.11 as the green line. In a similar manner to the pure hydrogen and solar scenarios considered before, the material within the cavity and ejecta pile-up regions have incredibly long recombination timescales.

More importantly, we do see a significant difference within the remnant's shell. As before, the timescales drop dramatically at the inner edge yet here we see recombination times of a few thousand years right across the shell. As a result of incredibly long timescales for recombination within the inner regions of the NSR and recombination times on par with the travel time needed for nova ejecta to cross the remnant ($\sim 10^4$ years for ejecta travelling at $\sim 2000 \text{ km s}^{-1}$), this structure will continue to exhibit emission induced by frequent nova outbursts.

5.7 Evolution of NSR emission

In the previous section, we explored the emission measure and X-ray spectra from the reference simulation NSR at the epoch coinciding with a recurrence period of one year. This is helpful for predicting observables for a particular snapshot of the structure's evolution and building up a picture of the emission. Now in this section,

we will investigate the evolution of these various observables to guide searches for NSR emission around other younger systems.

5.7.1 Evolution of the ionisation fraction and emission measure

We applied the same procedures used in Section § 5.6.1 and Section § 5.6.2 to find the average ionisation fraction and total emission measure within particular regions (the cavity, the ejecta pile-up region, the shell and the remnant as a whole) at every output of the reference simulation to determine the evolution of the quantities as the remnant grows.

The total emission measure from the different regions of the simulation were found by simply summing the emission from each cell of the region. In order to find the average ionisation fraction of these regions, we found the mass of each cell within a region and used the ionisation fraction to find the ionised mass of that cell. We then summed all of the ionised mass from each cell in the region and divided this by the total mass (ionised and neutral) of the region to give an average ionisation fraction, \bar{f} , as shown:

$$\bar{f} = \frac{\sum_i (f_i m_i)}{\sum_i m_i},$$

where f_i and m_i are the ionisation fraction and mass of the cell i , respectively. The evolution of the average ionisation fraction and the total emission for each of the regions is shown in Figure 5.12. Furthermore, in Figure 5.13, we can see evolution of the ionisation fraction and emission measure for the cavity, ejecta pile-up region and shell alongside the evolution of the average density and average temperature within these regions.

As illustrated in Figure 5.13, the average temperature of the ejecta pile-up region is, except possibly the first output of the simulation, always $\sim 1 \times 10^6$ K and begins to increase towards $\sim 1 \times 10^8$ K at the later stages of the system's evolution. The density of this region decreases by over a factor of 100 as it grows but the extremely high temperatures keeps the fraction of ionised material always above $\sim 40\%$. As a result, the emission from this part of the remnant is always high. The fraction of ionised material within the cavity is always above $\sim 10\%$, and so even with density decreasing over time, the emission from this region remains a contributing factor in a fluctuating manner until the later stages of the system's evolution.

If we now focus on the fraction of ionisation within the shell in Figure 5.13, we see the effects of recombination as a result of the extremely high densities. For the first

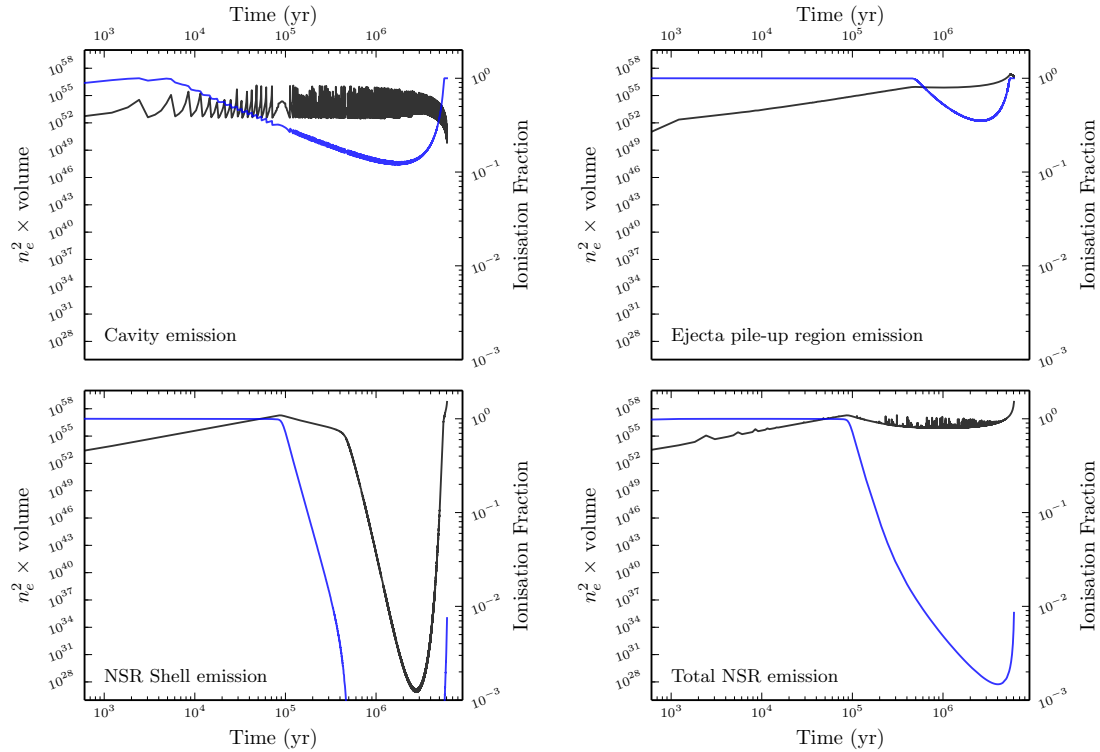


FIGURE 5.12: Evolution of ionisation fraction (blue line) and emission measure (black line) within the cavity, the ejecta pile-up region, the NSR shell and the total NSR for the reference simulation. The apparent ‘bump’ in the emission measure from the cavity at $\sim 10^5$ years is an artefact of sampling whereby we are seeing a superposition of eruptions.

10^5 years, all of the material making up the remnant shell is ionised, and therefore we see large amounts of emission. After this, the amount of ionisation within the shell decreases to negligible proportions for the vast majority of the system’s lifetime (from $\sim 10^5$ years to $\sim 6 \times 10^6$ years) which, combined with an almost constant average density during this period, leads to a drop in emission measure by around 30 orders of magnitude. However, as with the other regions, late-time frequent highly energetic outbursts begin to heat the shell, increasing the ionisation fraction within to $\sim 1\%$. Although a low proportion of ionisation, the very high densities ($\sim 1 \times 10^{-23} \text{ g cm}^{-3}$) in this region yield incredibly large amounts of emission.

Bringing these various regions together, we can describe the evolution of the emission from the whole NSR (see bottom right panel of Figure 5.12). It is initially dominated by emission from the shell when this high density region begins to sweep up the local ISM. After $\sim 1 \times 10^5$ years, the average temperature within the shell has lowered enough for the material to recombine, resulting in a decreasing fraction of ionised gas and dramatic reduction in emission from this region. As a result, the total emission from the structure becomes dominated by material in the ejecta

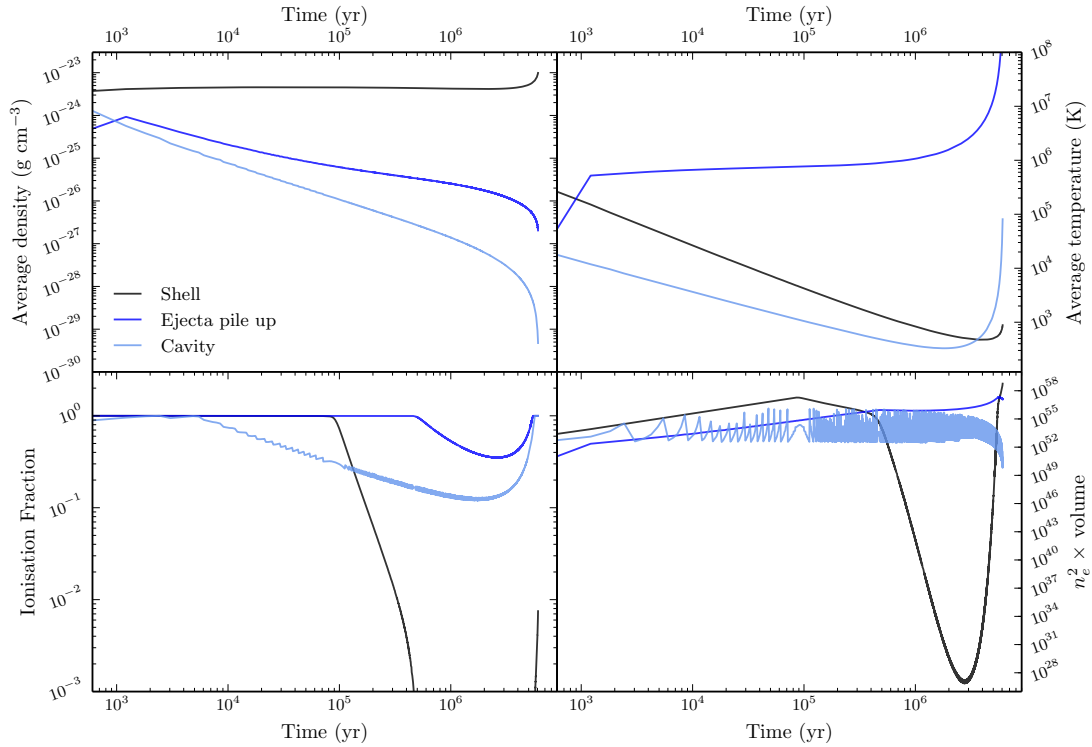


FIGURE 5.13: Evolution of the average density, average temperature, ionisation fraction and emission measure within the cavity, the ejecta pile-up region and the NSR shell for the reference simulation. As in Figure 5.12, the apparent ‘bump’ in the emission measure from the cavity at $\sim 10^5$ years is an artefact of sampling whereby we are seeing a superposition of eruptions.

pile-up region between $\sim 4 \times 10^5$ years and $\sim 6 \times 10^6$ years, with significant contribution from the fluctuating cavity emission throughout. Once the later stages have been reached (approximately the last 100,000 years), with frequent highly energetic ejecta emanating from the central source, the rate of ionisation within the very high density shell (particularly at the inner edge) once again leads to a major increase in emission from this part of the structure. However, unlike at early times when the emission was dominated by the whole shell, the emission at these later times emanates exclusively from the inner edge of the remnant shell.

The evolution of total ionised mass within each of these defined regions is shown in Figure 5.14. Firstly, we can see that the ionised mass within the cavity region remains at an almost constant few $\times 10^{-5} M_{\odot}$ for approximately 6 Myr before decreasing for the remaining 100,000 years. This is due to the frequent nova eruptions at this late evolutionary period excavating and lowering the total mass in this already sparse region further still (see the density evolution of the cavity in the top left panel of Figure 5.13). As with the evolution of the emission measure from the ejecta pile-up region, we see a continuous increase in ionised mass here, reaching $\sim 5 M_{\odot}$ after around 5 Myrs before declining during the last 100,000 years. Lastly,

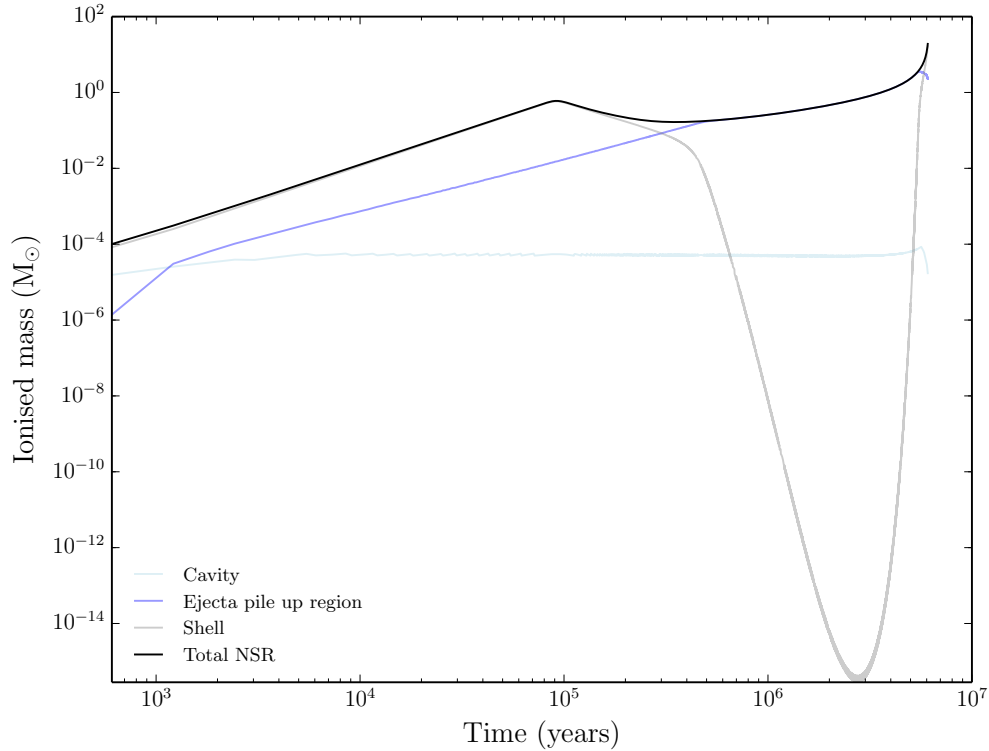


FIGURE 5.14: Evolution of ionised mass within the cavity, ejecta pile-up region, the NSR and the total NSR structure for the reference simulation.

almost $1 M_{\odot}$ of material within the remnant's shell is ionised by 10^5 years, however for the next $\sim 6 \times 10^6$ years, this decreases to as low as $10^{-16} M_{\odot}$, due to almost total recombination within the shell. This can be seen in Figure 5.15 whereby the recombination time within the whole shell after 10^5 years is always below 10^5 years, driving down the levels of ionisation within. As the underlying system reaches the limiting WD mass, the total amount of ionised mass within the shell (and effectively the NSR structure as a whole), becomes a few tens of solar masses, as large amounts of gas in the shell are heated by late-time energetic eruptions. This is once again reflected in the moderate rise of the recombination time at the inner edge of the shell in Figure 5.15.

5.7.2 Evolution of X-ray luminosity

In order to determine the evolution of X-ray luminosity, we employed the same rebinning method of the emission measure as previously described in Section § 5.6.2 for various outputs of our reference simulation coinciding with 10^n eruptions. These were after 10 eruptions, 100 eruptions, 1,000 eruptions, 10,000 eruptions, 100,000 eruptions and 819,565 eruptions. We have also shown the emission measure as a

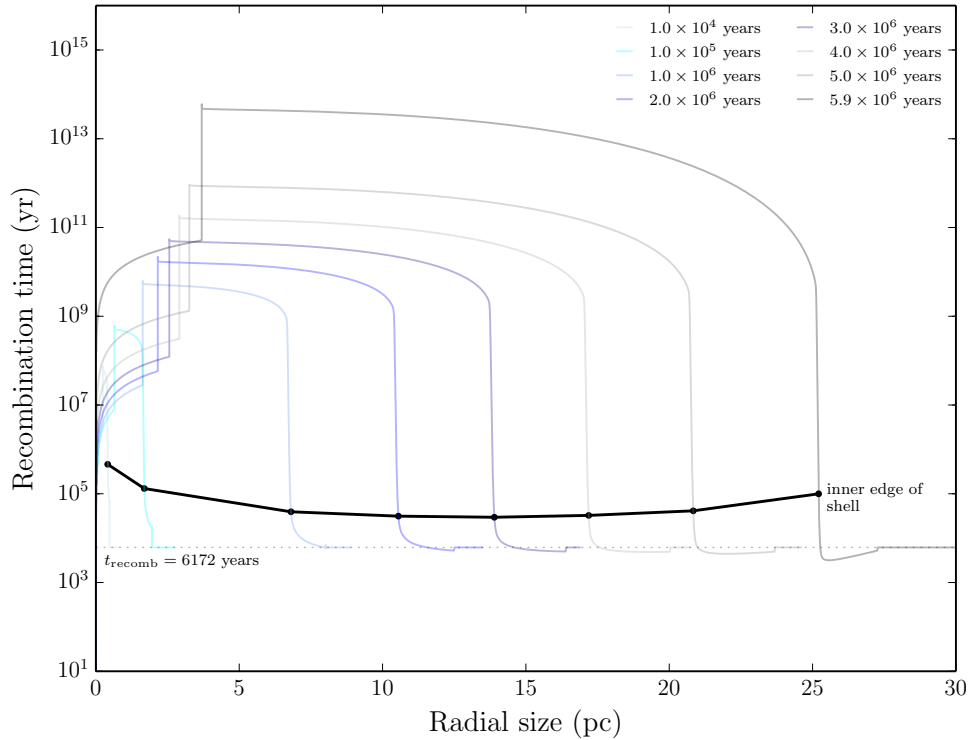


FIGURE 5.15: Evolution of recombination time for the reference simulation at various epochs after being completely flash ionised. The recombination time for the surrounding ISM is represented with the dashed line. The thick black line indicates the location of the inner edge of the NSR shell at each epoch.

function of temperature for the epoch of the reference simulation coinciding with a recurrence period of one year (after 495,997 eruptions). This is shown in Figure 5.16.

We see that the remnant simulated in Run 0 starts off at high temperatures, emitting mostly in the X-ray regime at ~ 1 keV (blue line in the left panel of Figure 5.16) due to the eruptions right from the beginning of the simulation being frequent and highly energetic. But, as the remnant grows and cools down, we see the peak in the emission measure moves towards lower energies, ending in the optical/NIR region ($\sim 2 \times 10^{-3}$ keV) after the full 100,000 eruptions. A logarithmic extrapolation of the emission measure revealed that the current peak will be in the infrared regime, around $12 - 13 \mu\text{m}$, and so could be a potential target for follow-up observations with the *JWST* (Darnley et al., 2019a).

The remnant in our study (Run 1), on the other hand, begins by mostly emitting at low energies (optical/NIR) due to the long periods of time between the low energetic outbursts allowing the remnant to cool. The remnant as a whole then does not warm up throughout its evolution as it expands and cools, indicated through the peak in

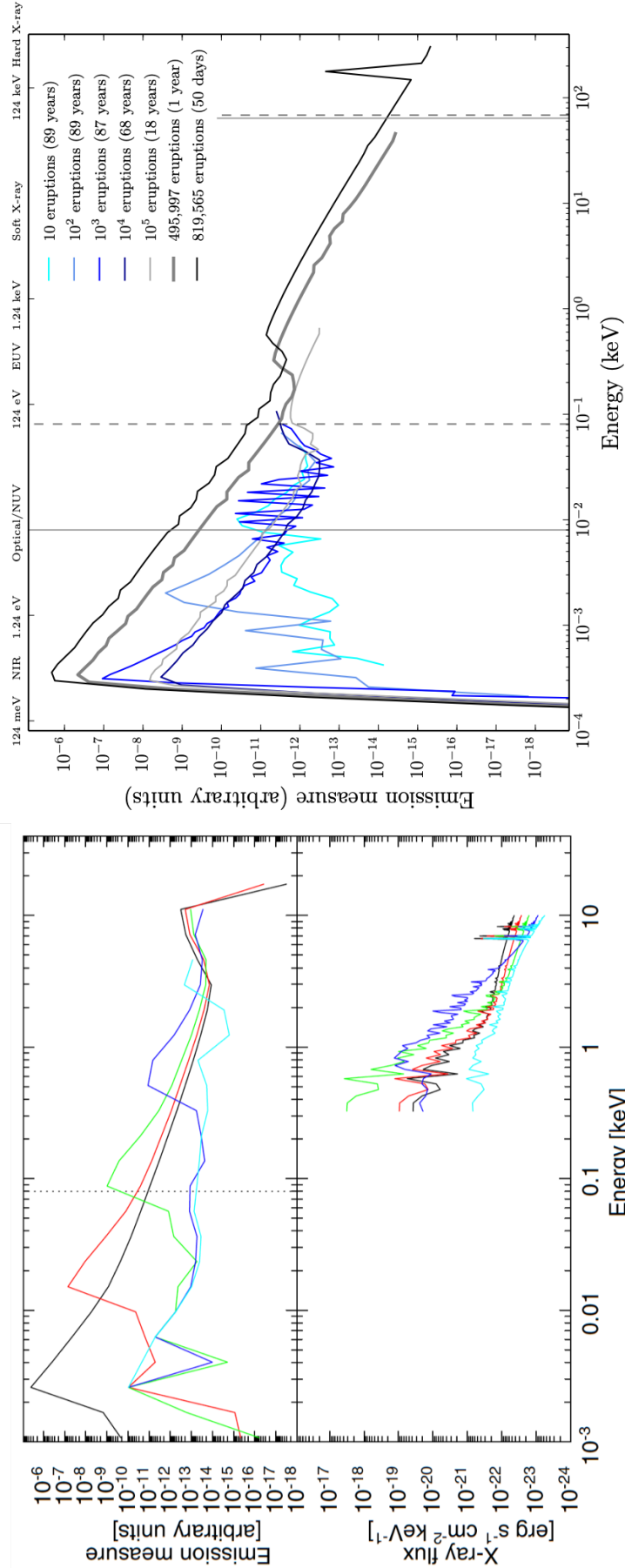


FIGURE 5.16: Comparing the evolution of emission measure of the identical eruption simulations presented in Darnley et al. (2019a) with the reference simulation detailed in Section 4.5.1. **Left:** The contribution to the NSR emission as a function of photon energy after 10 (cyan), 100 (blue), 1,000 (green), 10,000 (red) and 100,000 (black) identical eruptions is shown in the upper panel. The vertical line is the XSPEC lower limit cut-off. Synthetic X-ray spectra for the reference simulation after 10, 100, 1,000, 10,000, 100,000, 495,997 (coinciding with a recurrence period of 1 year) and 819,565 eruptions. As in Figure 5.8, the two grey lines show the upper (64 keV) and lower (0.008 keV) temperature limit of the APEC model and the two black dashed lines show the upper (68.4 keV) and lower (0.0808 keV) temperature limit of the VAPEC model.

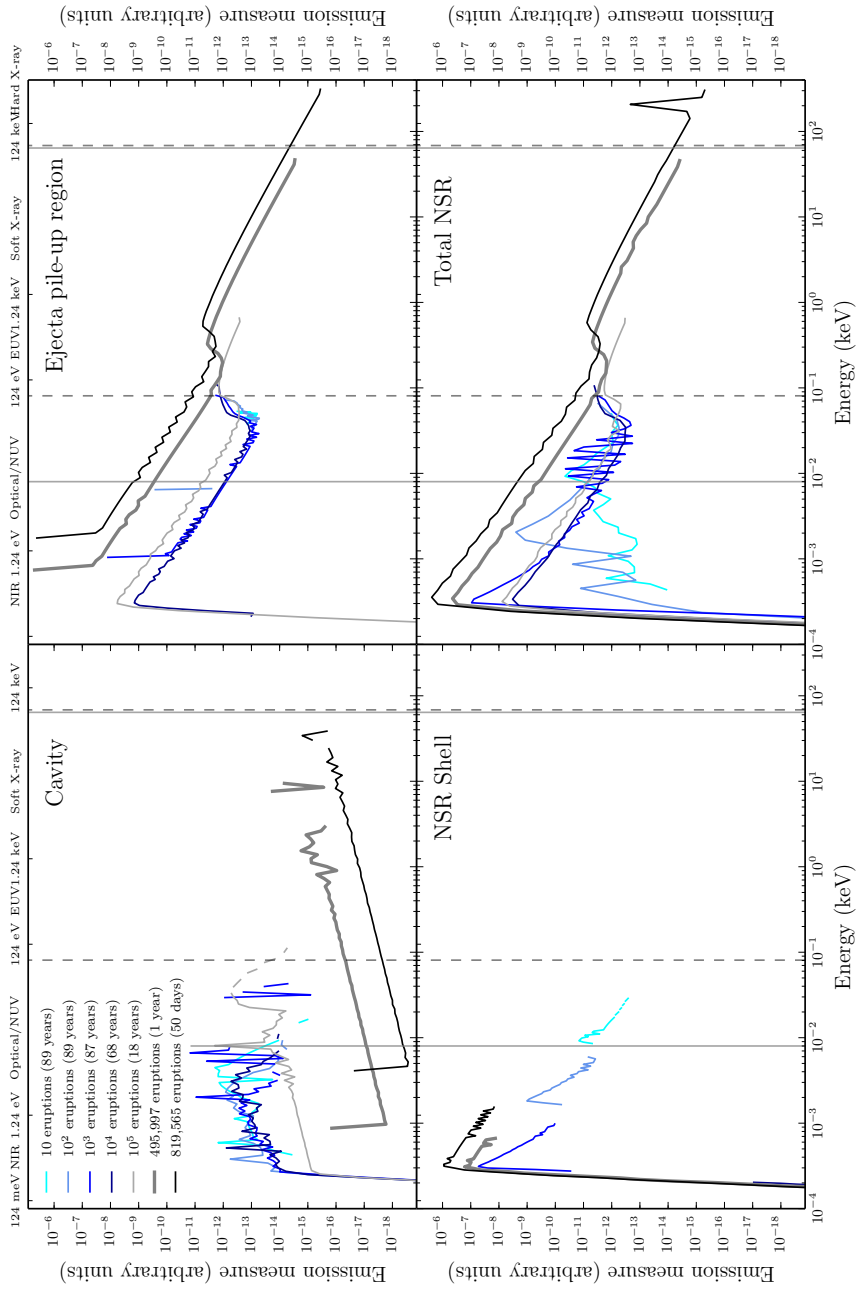


FIGURE 5.17: Emission measure ordered by temperature for the different components (cavity, ejecta pile-up region, NSR shell and whole NSR) of the reference simulation after 10, 100, 1,000, 100,000, 495,997 (coinciding with a recurrence period of 1 year) and 819,565 eruptions. As in Figure 5.16, the two grey lines show the upper (64 keV) and lower (0.008 keV) temperature limit of the APEC model and the two black dashed lines show the upper (68.4 keV) and lower (0.0808 keV) temperature limit of the VAPEC model.

the emission measure remaining at low energies for the full $\sim 820,000$ eruptions (see right panel of Figure 5.16).

By separating the emission measure evolution into component parts of the nova super-remnant structure, namely the cavity, ejecta pile-up and NSR shell, we can see the contributions from each of these regions (see Figure 5.17). The emission from the cavity remains relatively low compared to other NSR regions throughout the full evolution (see top left panel of Figure 5.17). For the first 100,000 eruptions, the cavity exclusively emits in the optical/NIR regime. However, when the recurrence period of the system reaches one year, we see the emission contribution, albeit small, branches across to higher energies. This is possibly attributed to the frequently ejected material colliding with the inner edge of the ejecta pile-up region.

Emission levels from the ejecta pile-up region are considerably higher than from the cavity and, as we would expect, have more contribution towards X-ray emission at later times as a result of collisions from incoming ejecta continuously shock-heating the pile-up material (see top right panel of Figure 5.17). In fact, after the full $\sim 820,000$ eruptions, a portion of the ejecta pile-up region is emitting beyond 120 keV. In contrast, the shell of the nova super-remnant emits mostly in the optical at early times and after only 1000 eruptions, the majority of emission lies in the near-infrared regime. The shell then continues to emit between $\sim 0.1 - 2$ eV for the full evolutionary period as it remains the coolest part of the structure, shielded from the highly energetic material colliding with the pile-up.

Finally, we can predict the evolution of the total X-ray luminosity from the reference simulation, as illustrated in Figure 5.18. However, this evolution initially looks erratic as we have captured many eruptions within our analysis. In order to see the evolutionary trends more clearly, we have calculated and plotted a moving average over every 500 outputs. This is illustrated in Figure 5.19 with comparison to the X-ray luminosity evolution from the NSR created from identical eruptions (Run 0). As we can see in the left plot of Figure 5.19, for a NSR grown with identical eruptions, the X-ray luminosity peaks at $\sim 6 \times 10^{31}$ erg s $^{-1}$ after approximately 1000 years (equivalent to 1000 eruptions for Run 0). This luminosity then fades to $\sim 9 \times 10^{29}$ erg s $^{-1}$ after 100,000 years (100,000 eruptions) and with a power-law extrapolation to the latest time, representing present day in Darnley et al. (2019a), the total X-ray luminosity drops to $\sim 3 \times 10^{29}$ erg s $^{-1}$. As detailed in Darnley et al. (2019a), the X-ray luminosities predicted for the entire evolution of the NSR all lie below the 3σ upper limiting luminosity of $\sim 9 \times 10^{34}$ erg s $^{-1}$ constrained by archival X-ray observations (see horizontal dotted line in the left plot of Figure 5.19).

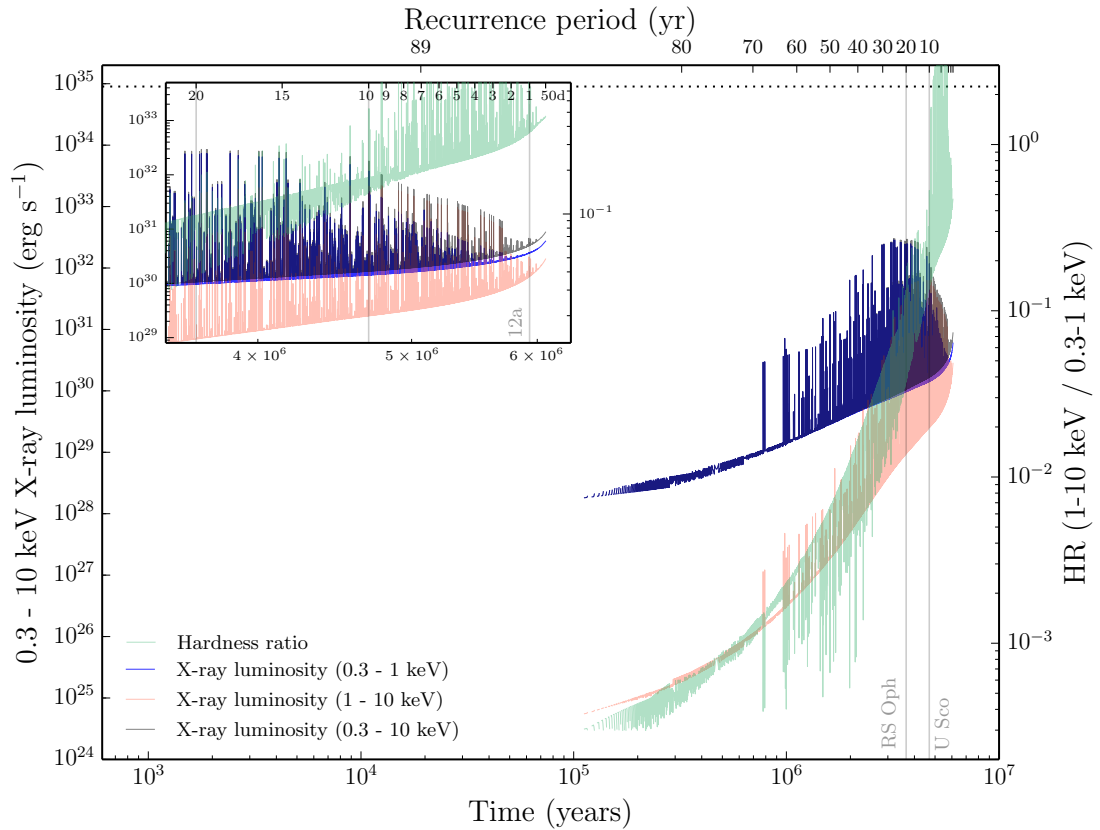


FIGURE 5.18: The evolution of the synthetic X-ray luminosity of the reference simulation from XSPEC with respect to elapsed time (bottom abscissa) and recurrence period (top abscissa). Soft X-rays are red, hard X-rays are blue, the total X-ray luminosity is black and the hardness ratio (hard/soft) is green. The recurrence periods of three recurrent novae (M 31N 2008-12a, U Scorpii and RS Ophuichi) are indicated with vertical grey lines and the dashed line indicates the 3σ upper limit from XMM-Newton observations. The inset is a zoomed in section of the X-ray luminosity from 3.5×10^6 years to the end of the evolution. Note that the hard X-rays (blue line) follow the evolution of the total X-ray luminosity (black line) very closely.

The X-ray luminosity from a NSR grown with non-identical eruptions (Run 1) conducted in this work exhibits a different evolutionary trend to that in Run 0 (see right plot of Figure 5.19). We see a continuously rising luminosity throughout, owing to the increasingly frequent ejecta shock-heating the ejecta pile-up region (also see the top right panel of Figure 5.17). Starting at $\sim 1 \times 10^{28}$ erg s^{-1} after $\sim 3 \times 10^5$ years, the early NSR X-ray luminosity is dominated by soft X-rays with energies between 0.3–1 keV as we have less energetic ejecta sweeping into the forming remnant. The ratio of hard to soft X-rays, or the hardness ratio, is very low during this period.

The influence of the more energetic outbursts begins to become evident over the next few million years as the hard X-ray emission from shock-heating, with energies between 1–10 keV, reaches $\sim 8 \times 10^{29}$ erg s^{-1} after $\sim 4 \times 10^6$ years (see inset of the right plot in Figure 5.19). This is a much larger contribution to the total X-ray

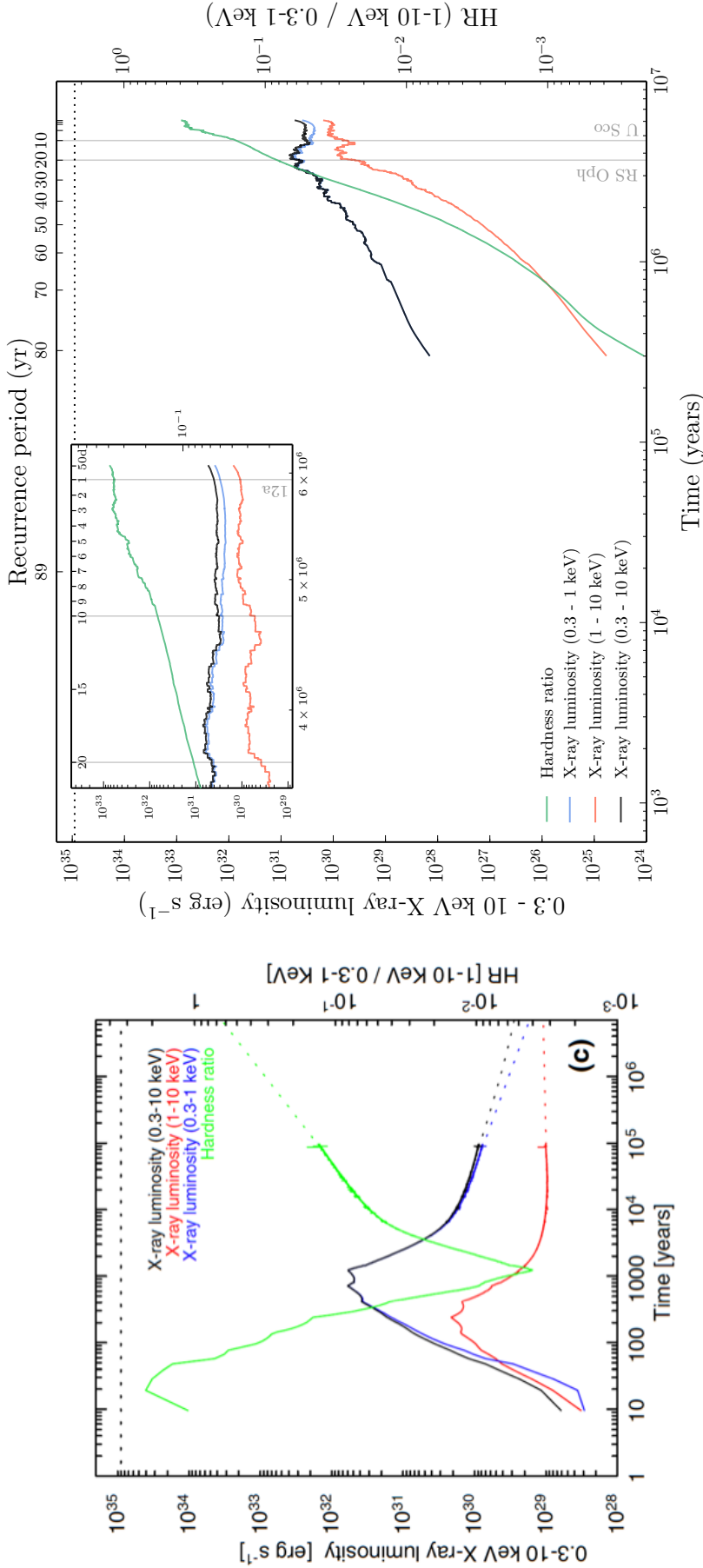


FIGURE 5.19: Evolution of the synthetic X-ray luminosity. **Left:** The evolution of the synthetic X-ray (0.3 - 10 keV) luminosity of the identical eruptions simulation from Darnley et al. (2019a). The soft X-rays (0.3 - 1 keV; blue), hard X-rays (1 - 10 keV; red) and the total X-ray luminosity (0.3 - 10 keV; black) are shown alongside the hardness ratio (hard/soft; green). The horizontal dashed line indicates the 3σ upper limit from XMM-Newton observations (see Darnley et al., 2019a, for more details). **Right:** Evolution of the synthetic X-ray luminosity of the reference simulation from xSPEC with respect to elapsed time (bottom abscissa) and recurrence period (top abscissa). A moving average (every 500 outputs) has been plotted to illustrate the evolution more clearly. Similar to the left panel, soft X-rays are red, hard X-rays are blue, the total X-ray luminosity is black and the hardness ratio (hard/soft) is green. The recurrence periods of three recurrent novae (M 31N 2008-12a, U Scorpii and RS Ophiuchi) are indicated with vertical grey lines and the dashed line again indicates the 3σ upper limit from XMM-Newton observations. As in Figure 5.18, the inset is a zoomed in section of the X-ray luminosity from 3.5×10^6 years to the end of the evolution.

luminosity of $\sim 6 \times 10^{30} \text{ erg s}^{-1}$ at this epoch, with the hardness ratio rising to a more substantial 10%. The total X-ray luminosity of the NSR then stays relatively constant for the rest of the evolution, ending with a luminosity of $\sim 7 \times 10^{30} \text{ erg s}^{-1}$, but with the hard X-ray emission becoming increasingly significant, ending with a ratio of 0.4 between hard and soft X-rays by $\sim 6 \text{ Myr}$.

For the epoch when the recurrence period of the reference simulation is one year, the total X-ray luminosity from the NSR is $\sim 6 \times 10^{30} \text{ erg s}^{-1}$ (see inset of the right plot in Figure 5.19). This is $20\times$ greater than the luminosity predicted from extrapolating the identical eruptions simulation in previous work. Additionally, the ratio of hard to soft X-rays in this work at a one year recurrence period is ~ 0.35 , much less than seen in the extrapolated value of ~ 0.6 from the identical eruptions of Run 0 (see the green dashed line on the left plot of Figure 5.19).

We have also indicated on this plot the two most rapidly recurring novae in the Galaxy, U Scorpii and RS Ophiuchi, as a means of predicting the total X-ray luminosity from the potential NSR surrounding these systems. With a recurrence period of 10 years, the remnant around U Scorpii would have a total X-ray luminosity of $\sim 3 \times 10^{30} \text{ erg s}^{-1}$ and for the NSR associated with RS Ophiuchi ($P_{\text{rec}} \sim 20 \text{ years}$), the luminosity would be $\sim 4 \times 10^{30} \text{ erg s}^{-1}$, however note that this is a moving average evolution. This same method can be extended to other systems to determine an estimate of the NSR X-ray luminosity to inform observational campaigns.

5.8 Replicating the M 31N 2008-12a NSR

We stated in Section § 4.8 that the simulations in this work with parameters that most resemble the M31N 2008-12a system do not replicate the observed NSR. Here, we will now bring together the various components of this chapter to determine the parameters we would require using our NSR radial size equation to form a dynamical nova super-remnant with the same radial size as that seen around M 31N 2008-12a; investigate the contribution of photoionisation towards growing a large remnant and finally compare synthetic sky images created from output of our simulations with *HST* observations of the 12a NSR to find any similarities.

5.8.1 Parameter space of NSR radial size equation

We outlined a NSR radial size equation in Section § 5.5 that relates the radial size of a nova super-remnant to the recurrence period (in terms of the time taken for

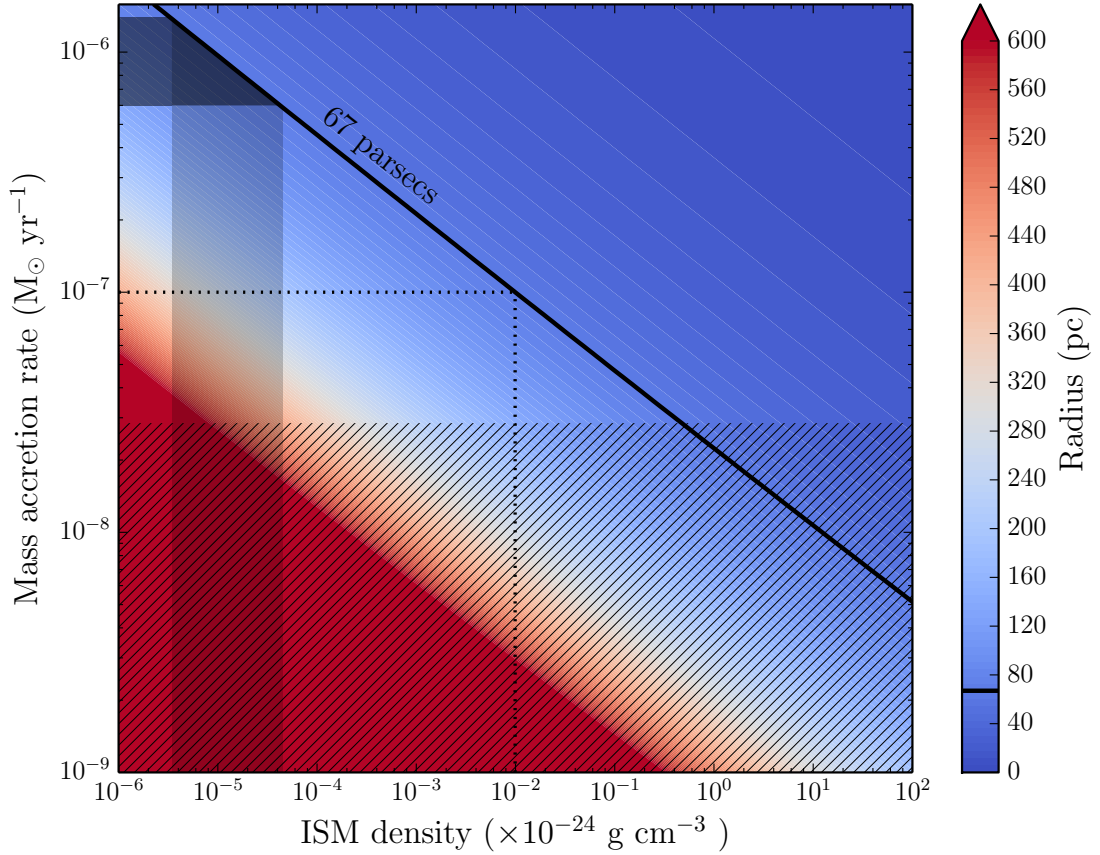


FIGURE 5.20: Parameter space of ISM density and mass accretion rate. The colour scale indicates the radial sizes of a nova super-remnant predicted from the NSR radial size equation derived in Section § 5.5 after an elapsed time of $\sim 5.9 \times 10^6$ years (time taken for the reference simulation to reach an epoch whereby $P_{\text{rec}} = 1$ year). The solid black line indicates a NSR with the radial size of that observed surrounding M 31N 2008-12a (67 parsecs). The dotted line shows the ISM density needed to grow a NSR to the size of 67 parsecs with a mass accretion rate of $1 \times 10^{-7} M_{\odot} \text{ yr}^{-1}$ within our model is $\sim 1 \times 10^{-26} \text{ g cm}^{-3}$. The shaded region shows the range of ISM densities needed to grow a NSR to the size of 67 parsecs by extrapolating our NSR radial size equation with the currently known range of mass accretion rates for 12a (see Table 1.3). The hatch-shaded region is the parameter space that would not generate a system with a recurrence period of one year within our models.

a $1 M_{\odot}$ to grow to M_{Ch}), the local ISM density and the mass accretion rate of the system. As a result, we can take the time for our reference simulation to reach a point of exhibiting a recurrence period of one year like M 31N 2008-12a ($\sim 5.9 \times 10^6$ years) and find all combinations of mass accretion rate and ISM density that would create a remnant with a radius of 67 parsecs from our NSR radial size equation. This parameter space for 67 parsecs is illustrated in Figure 5.20 as a solid black line, with the bluer colours being smaller remnants and redder colours representing larger remnants.

Clearly, in order to create a NSR from an accretion rate of $1 \times 10^{-7} M_{\odot} \text{ yr}^{-1}$ with the same radial size as seen around M 31N 2008-12a, we need to look at lower densities

than we have considered for our suite of simulations. Specifically, from our models, M 31N 2008-12a would need to reside in an environment with an ISM density of $\sim 1 \times 10^{-26} \text{ g cm}^{-3}$ to grow a remnant with a radial size of 67 parsecs (see the dashed line in Figure 5.20).

Furthermore, the lower limiting mass accretion rate of $6 \times 10^{-7} \text{ M}_{\odot} \text{ yr}^{-1}$ for M 31N 2008-12a would require a very low ISM density of $\sim 4.5 \times 10^{-29} \text{ g cm}^{-3}$ to create a 67 parsec NSR, with the upper limiting accretion rate of $1.4 \times 10^{-6} \text{ M}_{\odot} \text{ yr}^{-1}$ needing an even lower density environment of $\sim 3.5 \times 10^{-30} \text{ g cm}^{-3}$ (see the shaded regions in Figure 5.20). We have also indicated (with hatched shading) the part of the parameter space where the mass accretion rate is less than $2.85 \times 10^{-8} \text{ M}_{\odot} \text{ yr}^{-1}$ as we predict this to be the lower limit to generate a 12a-like system with our models i.e. a system that reaches a recurrence period of one year.

5.8.2 Photoionisation regions of NSR at $P_{\text{rec}} = 1$ year epoch

So far, we have considered the growth of the dynamical remnant. However, a proportion of this remnant will also be exposed to photoionisation directly from the nova eruptions, the accretion disk luminosity as well as the X-rays from shock emission. Here, we will briefly look at the contributions of these three effects to identify any significant impact they have on the radial size and structure of a NSR.

Firstly, we know that the mass of the WD in our reference simulation is 1.398 M_{\odot} at the epoch when $P_{\text{rec}} = 1$ year. We also assume in our models that $M_{\text{Ch}} = 1.408 \text{ M}_{\odot}$. Substituting these two values in the WD mass–radius relation:

$$\frac{R}{R_{\odot}} = 0.012 \cdot \sqrt{\left(\frac{M}{M_{\text{Ch}}}\right)^{-2/3} - \left(\frac{M}{M_{\text{Ch}}}\right)^{2/3}},$$

allows us to find the radius of the M 31N 2008-12a WD, consistent with our models, to be $R = 1.17 \times 10^{-3} R_{\odot}$. If we now combine this WD radius with the effective temperature of the 12a WD ($T_{\text{eff}} \sim 120 \text{ eV}$; see Darnley et al., 2016) in the Stefan-Boltzmann law as follows:

$$\frac{L}{L_{\odot}} \approx \left(\frac{R}{R_{\odot}}\right)^2 \cdot \left(\frac{T}{T_{\odot}}\right)^4 = (1.1696 \times 10^{-3})^2 \cdot \left(\frac{1.392 \times 10^6}{5778}\right)^4,$$

we find a luminosity of the 12a WD in our models to be $L \sim 4600 L_{\odot}$. Additionally, we could find the Eddington luminosity of a 1.398 M_{\odot} WD to determine the limiting

luminosity of such as system. The Eddington luminosity is defined as:

$$L_{\text{Edd}} = 3.1 \times 10^4 \left(\frac{M}{M_{\odot}} \right) L_{\odot} \Rightarrow L_{\text{Edd}} = 3.1 \times 10^4 (1.398) L_{\odot},$$

which gives us a luminosity of $L_{\text{Edd}} \sim 43,000 L_{\odot}$. If we consider that the bolometric luminosity of the system is represented by L_{Edd} , the observed luminosity is $4600 L_{\odot}$ and that most of the emission is absorbed by the surroundings, we then know that the ionising luminosity is represented by the difference ($L_{\text{Edd}} - L_{\text{obs}}$). The lower limiting number of nova outbursts we can have before part of the shell begins to recombine is 3172 (one a year for 3172 years; see the lowest recombination time below the dashed line for 5.9×10^6 years in Figure 5.15) and each nova eruption lasts for approximately two weeks. Therefore, assuming a spectrum of 15 eV photons, we can calculate the total ionising luminosity of the nova eruptions over the 3172 years as follows:

$$S_{\star, \text{nova}} = \frac{38700 L_{\odot}}{15 \text{ eV}} \times 86,400 \text{ s} \times 14 \text{ d} \times 3172 \text{ yr} = 2.4 \times 10^{58} \text{ photons.}$$

Next, we will look at the ionising luminosity of the accretion disk within the 12a system. Taking $M_{\text{WD}} = 1.398 M_{\odot}$, $R_{\text{WD}} = 1.17 \times 10^{-3} R_{\odot}$ and the mass accretion rate of the system to be $\dot{m} = 1 \times 10^{-7} M_{\odot} \text{ yr}^{-1}$, we can find the accretion disk luminosity as follows:

$$L_{\text{disk}} = \frac{G M_{\text{WD}} \dot{m}}{R_{\text{WD}}} \Rightarrow L_{\text{disk}} = 5240 L_{\odot}.$$

Unlike the outbursts that only occur for a proportion of time every year, this emission is continuous. Therefore, assuming a spectrum of 15 eV photons (likely to result in a huge over-estimate for the number of photons as $T_{\text{eff}} \sim 120 \text{ eV}$ for 12a, as detailed in Section § 1.4.4), we estimate that the total ionising luminosity from the disk over 3172 years is:

$$S_{\star, \text{disk}} = \frac{5240 L_{\odot}}{15 \text{ eV}} \times 86,400 \text{ s} \times 365.25 \text{ d} \times 3172 \text{ yr} = 8.4 \times 10^{58} \text{ photons,}$$

clearly demonstrating that the disk luminosity in this scenario dominates the total ionising emission from the system. However, note that this is likely to be an over-estimate for ionising flux and that the disk luminosity, and hence the ionising flux, depends upon the viewing angle.

Finally, we will estimate the number of ionising photons emitted from shocks taking place within the remnant. For this, we can simply take the number of photons calculated within the XSPEC APEC model (as described in Section § 5.6.2), between the model limits of 0.1 – 50 keV for the epoch when $P_{\text{rec}} = 1 \text{ yr}$. This method reveals the

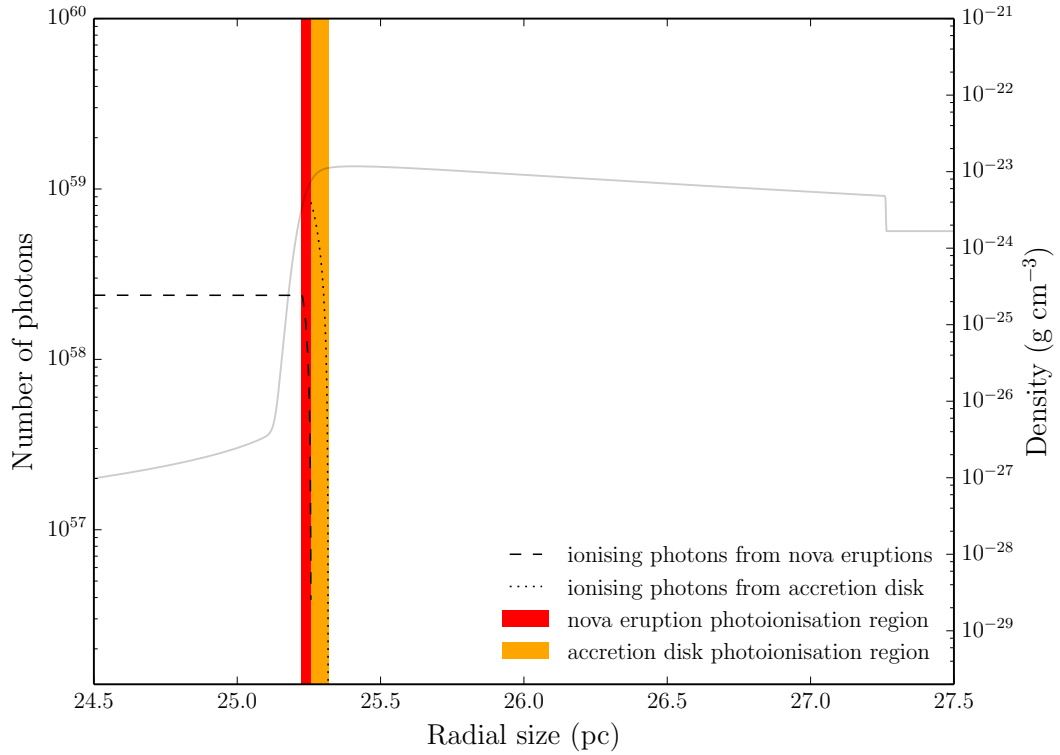


FIGURE 5.21: The photoionisation regions predicted for the reference simulation (between 24.5–27.5 parsecs) at the epoch when the recurrence period is one year, as a comparison to the NSR around M 31N 2008-12a. The faint black line is the density profile of the reference simulation. The red band and the orange band represent the photoionisation regions created from ionising photons from the nova outbursts and accretion disk emission, respectively.

flux to be $f_{\text{shocks}} = 2.5169 \times 10^{-10} \text{ photons s}^{-1} \text{ cm}^{-2}$. As this model takes the distance to the source to be that of M 31, we find that the luminosity from the shocks is:

$$L_{\text{shocks}} = 4\pi d^2 f_{\text{shocks}} = 4\pi(2.4 \times 10^{24})^2 \times (2.5169 \times 10^{-10}) = 1.8 \times 10^{40} \text{ photons s}^{-1},$$

and so the total ionising luminosity from the shock emission over 3172 years is:

$$S_{\star, \text{shocks}} = 1.8 \times 10^{40} \text{ photons s}^{-1} \times 86,400 \text{ s} \times 365.25 \text{ d} \times 3172 \text{ yr} = 1.8 \times 10^{51} \text{ photons}.$$

Now that we have the ionising luminosities for three components of the underlying nova system, we will estimate the regions of photoionisation for each. In order to do this, we will take the NSR from the reference simulation at $P_{\text{rec}} = 1 \text{ yr}$ and assume that the remnant is fully recombined, such that it is made up of neutral hydrogen. We have then defined the inner edge of the calculated photoionisation region to be the point at which 0.01% of the ionising photons (travelling from the origin) have each been absorbed by a neutral hydrogen atom and the outer edge is defined to be

the point at which all ionising photons have been absorbed.

The photoionisation region created by the nova eruptions is illustrated in Figure 5.21 as a red band that is ~ 0.03 parsecs across, with the total number of ionising photons remaining shown as a dashed line. We also show the density distribution of the high density shell between 24.5 and 27.5 parsecs to demonstrate the location and extent of the region with respect to the nova super-remnant. For the region ionised by the accretion disk emission, we define the inner edge to be the outer edge of the nova eruption's photoionisation region (as this is where the photons will travel to before reaching neutral hydrogen) and the outer edge is defined to be the point at which all of the ionising photons from the disk have been absorbed. This second region is shown as the orange band in Figure 5.21 and is approximately 0.06 parsecs across. The third region is formed by X-ray emission from shocks. However, as the number of ionising photons from this component is at least 10^6 times smaller than the nova and disk luminosities, the width of this region is negligible and therefore not included in Figure 5.21.

As we can see in Figure 5.21, the radius of the photoionisation region created by the various components of the underlying nova system remains very small in comparison to the size of the dynamical remnant (~ 0.1 parsec across). Therefore, this is not the reason for the discrepancy between the much larger radial size of the observed NSR and the remnants we have simulated. As a result, other characteristics of the system must be incorporated to accurately replicate the observed nova super-remnant.

One characteristic we can briefly consider here is the dependence of the ionisation region radial size on the ISM density, as employed by Dr Matt Darnley. As a crude approximation, we assume that the over-density with regards to the ISM for the photoionised remnant, assuming that this is much larger than the dynamic remnant and only including the remnant shell (as the pile-up region is completely ionised) is $\times 2$ the surrounding ISM, however this is likely to be a significant overestimate. We show in Figure 5.22, the dynamical remnant radial size with respect to ISM density (deemed the outer radius), determined from our NSR radial equation at the epoch when the reference simulation has a recurrence period of one year and assuming that the mass accretion rate is $1 \times 10^{-7} M_{\odot} \text{ yr}^{-1}$. We then show the inner radius of the NSR by assuming that the thickness of the remnant shell is 7% of the total NSR at this epoch (from Figure 4.17).

In order to predict the size of the photoionisation region from the nova outbursts with respect to the density of the ISM, we carry out a Strömgren analysis in a similar way as shown in Chapter 3. However, as the time period of emission is longer

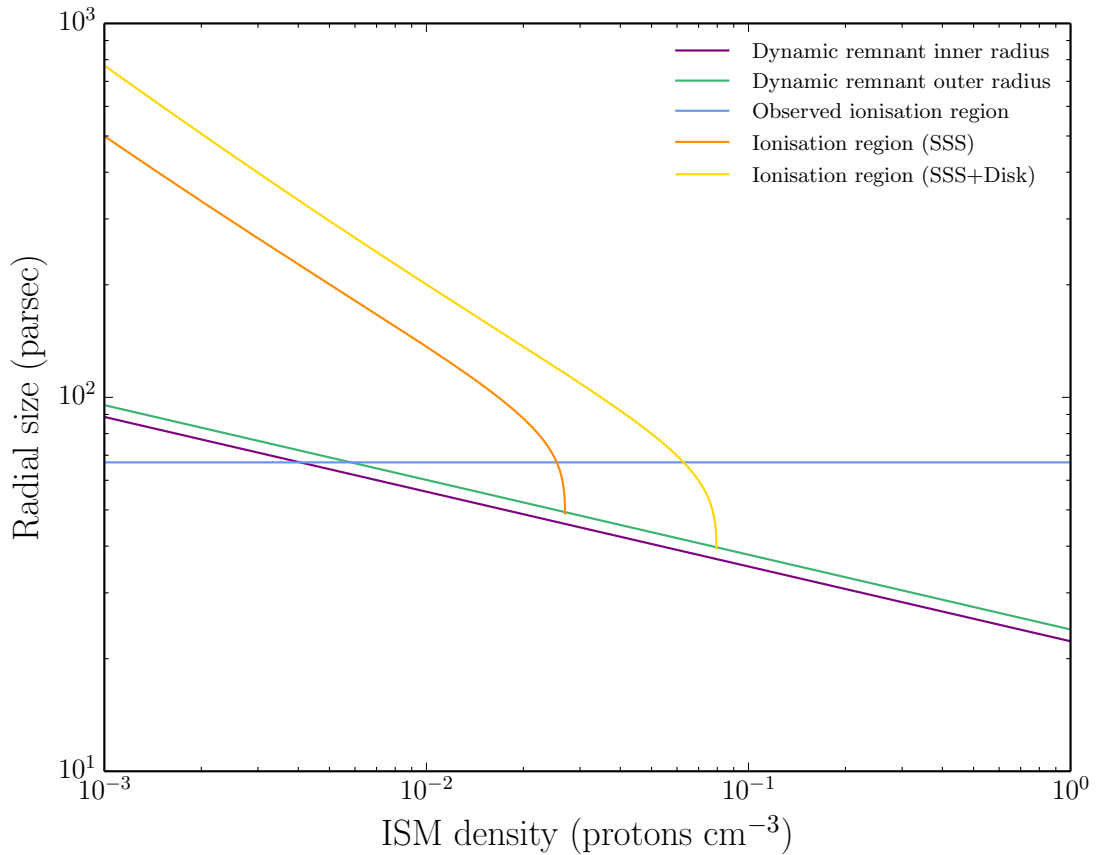


FIGURE 5.22: The radial sizes of photoionisation regions predicted for the reference simulation at the epoch when the recurrence period is one year as a function of ISM density. The blue line represents the radial size of NSR around M 31N 2008-12a (67 pc). The purple and green line represents the inner and outer radius of a dynamically grown remnant from our NSR radial size equation, respectively. The orange line indicates the radial size of an ionisation region grown through nova eruptions only and the orange line represents the radial size of an ionisation region grown through both nova eruptions and disk luminosity.

than the recombination time here, instead of a Strömgen sphere, we will have a Strömgen shell. Consequently, the ionisation region can be found by the following:

$$R_s = \left[\left(\frac{3 S_\star}{4\pi n^2 \beta} \right) - r_{\text{in}}^3 \right]^{\frac{1}{3}}, \quad (5.39)$$

where R_s is the outer edge of the sphere, S_\star is the ionising luminosity from the source, n is the number of protons per m^3 , $\beta = 6.84 \times 10^{-18} \text{ m}^3 \text{ s}^{-1}$ and r_{in} is the inner edge of the non-ionised material, which we know is the inner edge of the dynamical remnant. As earlier, we will now take the ionising luminosity from the nova eruptions (or the SSS emission) as $L_{\text{Edd}} - L_{\text{obs}} \approx 38700 L_\odot$ such that $S_{\star, \text{SSS}} = 2.36 \times 10^{47} \text{ photons s}^{-1}$. Substituting this into the equation 5.39 along with varying values for n (ISM density) provides us with the width of the ionisation

region (see the orange line in Figure 5.22). We also calculated a similar ionisation region but with the inclusion of the disk luminosity ($5240 L_{\odot}$) from earlier, alongside the SSS emission (see the yellow line in Figure 5.22). Now by simply adding the widths of these ionisation regions to the inner edge of the dynamical remnant, we can find the radial size of the NSR with the incorporation of ionisation.

As we established in Figure 5.21, the ionising emission from the nova system cannot ionise the shell. In Figure 5.22, we can see this through the absence of an ionisation region at $n = 1$, with the dynamical remnant only extending to ~ 25 pc. For the model of only incorporating SSS emission, we see that a remnant could grow to the observed NSR of 67 pc if placed within ISM with a density of $n = 0.025$, and would have a dynamical remnant of ~ 48 pc. If we also include ionising emission from the accretion disk alongside the SSS emission, a NSR with a radial size of 67 pc could grow within an ISM with a density of $n = 0.06$, and would have a dynamical remnant of ~ 40 pc. These two ISM densities are comparable to those calculated in Section § 5.4 for the ten Galactic RNe (see Table 5.1); consistent with those found for U Sco, RS Oph, T Pyx and V394 CrA.

Ultimately, from these estimates, we can see that a large enough photoionisation region to replicate the NSR seen around M 31N 2008-12a could be grown in environments with densities much lower than we have considered, yet values that are still feasible. Furthermore, this calculation implies that NSRs would only be visible in low density ISM regimes.

5.8.3 Synthetic sky images of NSR at $P_{\text{rec}} = 1$ year epoch

Even though the simulations in this work do not completely resemble the NSR associated with M 31N 2008-12a with respect to radial size, there are similarities seen in the structure as a whole. To illustrate this, we have taken the radial profiles of the density, emission measure, ionised gas density and X-ray luminosity of the reference simulation remnant (Run 1) at the epoch when $P_{\text{rec}} = 1$ year and created synthetic sky images.

The one-dimensional radial profile for each of the four parameters was taken by Dr Matt Darnley, normalised to the maximum value and integrated over the volume of a sphere. This sphere was then collapsed into a two-dimensional image to replicate the nova super-remnant on the sky. In Figure 5.23, we show these synthetic sky images for each parameter alongside the *Hubble Space Telescope* observation of the M 31N 2008-12a nova super-remnant from Darnley et al. (2019a), with the colour

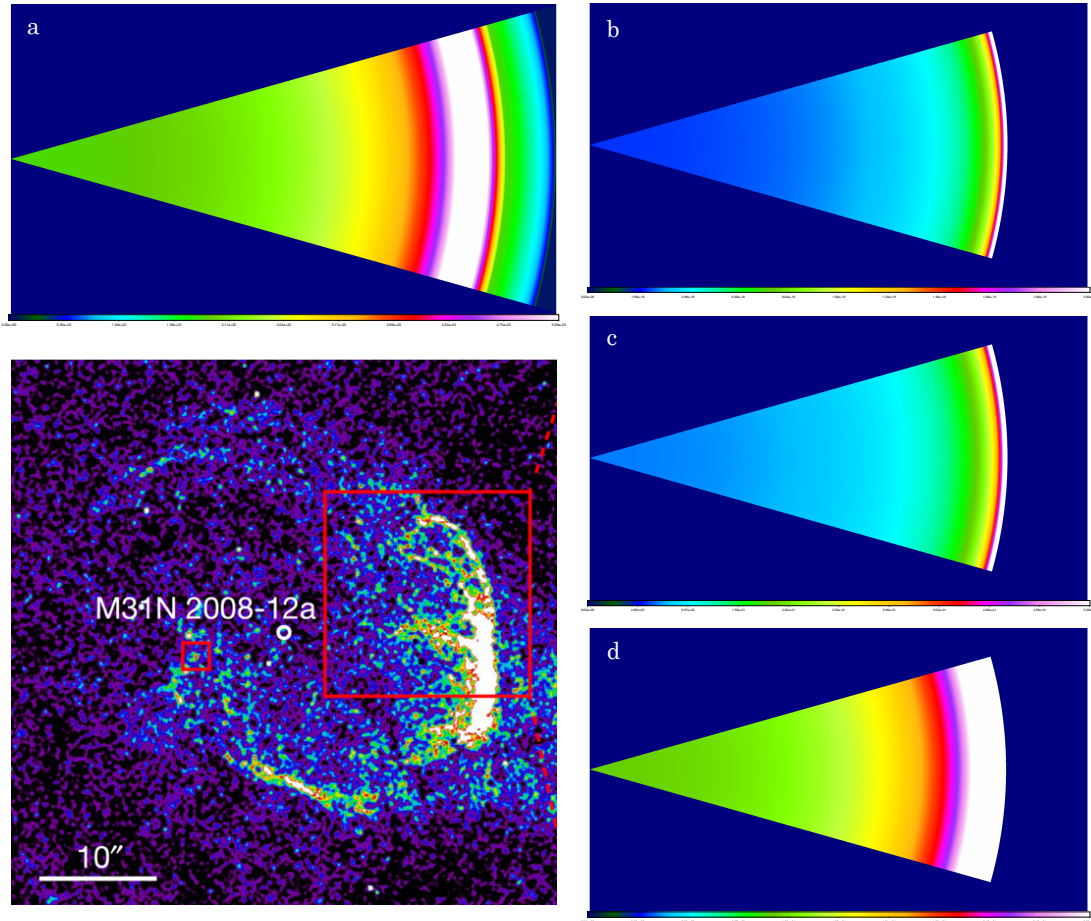


FIGURE 5.23: Synthetic sky images from simulations compared to the nova super-remnant around M 31N 2008-12a. From the reference simulation NSR (Run 1); **panel a** is the synthetic sky image of the density profile, **panel b** is the synthetic sky image of the emission measure profile, **panel c** is the synthetic sky image of the ionised gas density profile and **panel d** is the synthetic sky image of the X-ray luminosity profile. **Bottom left:** *Hubble Space Telescope* image of the NSR surrounding M 31N 2008-12a (taken from [Darnley et al., 2019a](#)).

scheme of the synthetic images being chosen to replicate that in the *HST* image (see bottom right image of Figure 5.23).

Firstly, in panel (a) of Figure 5.23, we see the high density NSR shell as the thick white band bordered by lower density material (purple and red bands). At the front end of the NSR shell (right of the white band), the drop in density is more dramatic before reaching the surrounding ISM (green and blue bands). The density within the inner edge of the NSR shell drops away more steadily, representing the ejecta pile-up region, containing the low density cavity near the origin (green region).

The synthetic sky images of the emission measure and ionised gas density given in panels (b) and (c) of Figure 5.23 are very similar to each other, owing to their dependence (emission measure is simply the square of the ionised gas density), with

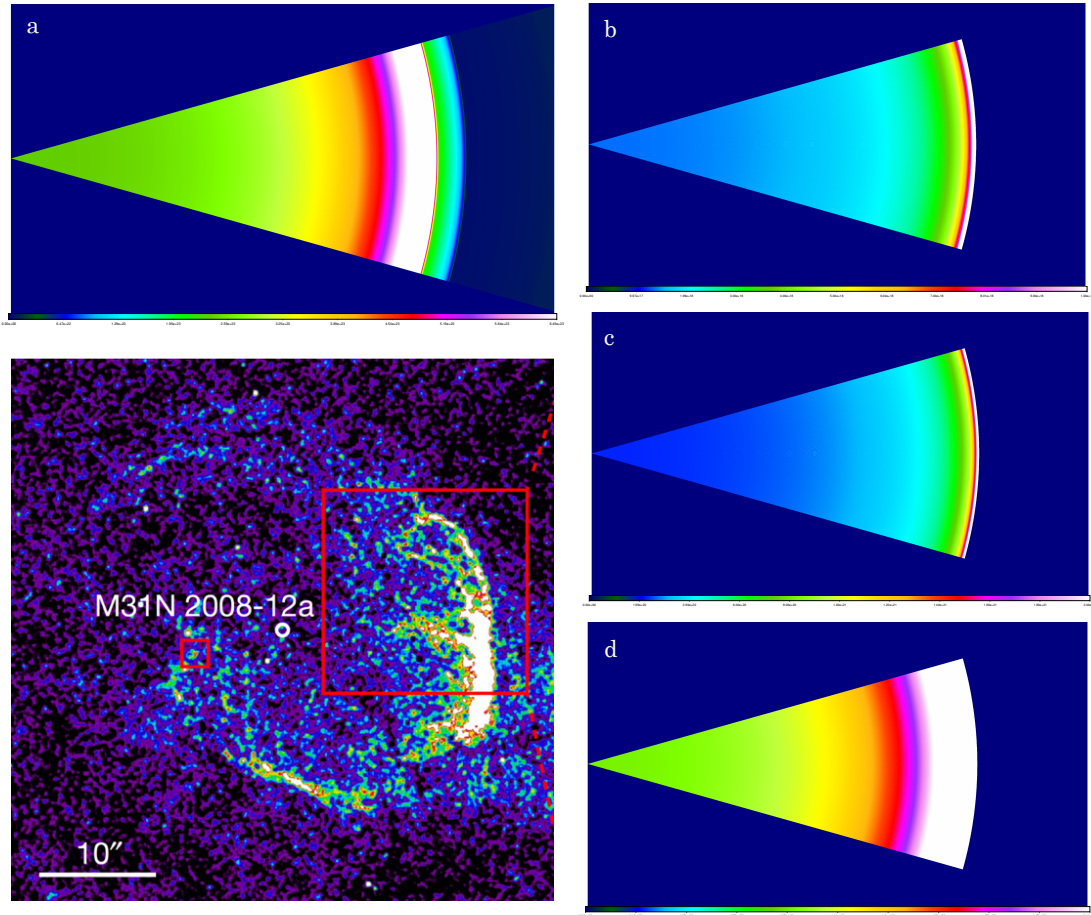


FIGURE 5.24: Synthetic sky images from simulations with radiative cooling compared to the nova super-remnant around M 31N 2008-12a. From the reference simulation NSR with radiative cooling (Run 12); **panel a** is the synthetic sky image of the density profile, **panel b** is the synthetic sky image of the emission measure profile, **panel c** is the synthetic sky image of the ionised gas density profile and **panel d** is the synthetic sky image of the X-ray luminosity profile. **Bottom left:** *Hubble Space Telescope* image of the NSR surrounding M 31N 2008-12a (taken from [Darnley et al., 2019a](#)).

the difference only seen in the widths of the bands⁷. By inspection, the structure of the simulated NSR in panel (b) and (c) does resemble the structure of the observed remnant. Specifically, for both emission measure and ionised gas density, we can see a negligible measure near the origin of the NSR (dark blue) and a very low measure at the transitional ejecta pile-up region (light blue), mimicking the *HST* observations. Then, at the inner edge of the shell, we see a vastly significant increase in the emission measure (red and white bands) as the ejecta that traversed the pile-up region collides with the extremely high density remnant shell. As expected, this high emission measure translates directly to significant X-ray emission from the

⁷The box sizes of these panels are all the same to illustrate the location of the emission measure, ionised gas density and X-ray luminosity with respect to the density profile of the NSR.

inner edge of the shell, but also from the ejecta pile-up immediately before the shell, as can be seen with the much wider white band in panel (d) of Figure 5.23.

We have also created synthetic sky images of the NSR from the reference simulation with radiative cooling, as shown in Figure 5.24, with the domain sizes of each image being the same as those in Figure 5.23. As expected, panel (a) of Figure 5.24 shows a similar structure as the NSR without cooling, with a very high density white band representing the NSR shell. The main difference between the sky image with and without radiative cooling is the smaller radial size of the remnant, as discussed in Chapter 4. The emission measure and ionised gas density in panels (b) and (c) of Figure 5.24 also resemble those sky images for the remnant without cooling, with a very low measure from the origin (dark blue) to the inner edge of the shell (yellow and red) and a very high ionised gas density in the shell (white band). Furthermore, the X-ray luminosity provided in panel (d) of Figure 5.24 is very similar to that in Figure 5.23, the only difference seen in the relative width of the band where we see significant X-ray emission (i.e. a thicker white band).

5.9 Summary

In this chapter, we have utilised the suite of simulations presented in Chapter 4 in order to determine the observational signatures associated with NSRs, including their sizes and emission characteristics. Here, we will summarise the key points:

1. A radial size equation, dependent on local ISM densities and recurrence period, was derived from curved power law fits to the radial growth curves of the simulations from Chapter 4.
2. We provide two methods utilised to estimate local ISM densities for this radial size equation.
3. A preliminary version of this relation was used to predict the sizes of the potential NSRs surrounding the ten Galactic recurrent novae. These predictions guided a number of successful telescope proposals to carry out a pilot study involving six of these systems in an attempt to find their vast NSRs. This will be discussed more in Section § 7.3.
4. A refined version of this relation was then constructed to incorporate the mass accretion rate of the system. The NSR radial size equation is as follows:

$$r(\rho, \dot{M}, t) = 9 \cdot \left(\frac{\rho}{10^{-24} \text{ g cm}^{-3}} \right)^{-0.2} \cdot \left(\frac{t}{1 \text{ Myr}} \right)^{0.6 + 2.6 \times 10^{-4} \times \left(\frac{\dot{M}}{10^{-7} M_{\odot} \text{ yr}^{-1}} \right)^{1.8}} \left(\frac{t}{1 \text{ Myr}} \right)^2 \text{ pc}$$

where r is the radius of the NSR, ρ is the estimated local ISM density, \dot{M} is the mass accretion rate of the system and t is elapsed time from the starting mass of $1 M_{\odot}$. This elapsed time is related to the recurrence period of the systems. The related recurrence period to elapsed time is therefore different for different accretion rates and can be looked up accordingly.

5. The fraction of ionised material, the emission measure, the recombination times and synthetic X-ray spectra were predicted for the reference simulation NSR at the epoch when the recurrence period coincided with that of M 31N 2008-12a (one year).
6. We then predicted the evolution of emission measure from different components of the NSR, evolution of the recombination time throughout the remnant and the evolution of X-ray luminosity for the full reference simulation.
7. The predicted evolution of X-ray luminosity can be used to estimate the total X-ray luminosity of a potential NSR with respect to the underlying system's recurrence period.
8. Utilising the NSR radial size equation, we found combinations of mass accretion rate and ISM density that would create a NSR with the same radial size as that seen around M 31N 2008-12a.
9. Photoionisation regions from various components of the underlying system, namely nova eruptions, the accretion disk luminosity and shocks, were calculated to pair with simulations of the dynamical growth of the NSR.
10. Synthetic sky images of the density, emission measure, ionised gas density and X-ray luminosity from the simulations were created to compare with *HST* observations of the NSR around M 31N 2008-12a.

Chapter 6

Post-Nova Evolution of Nova Super-Remnants

A nova super-remnant is grown as a result of recurrent nova eruptions, varying in size and structure depending upon the underlying system. Clearly though, this evolutionary process must cease at some point. The WD will either reach the Chandrasekhar limit and explode as a SNIa or it will, in a less dramatic finale, become extinct as the secondary runs out of material to donate. In this chapter, we will explore these two scenarios with simulations to understand their effects on the firmly established NSR structure and the observational signatures we can search for.

6.1 Donor material depletion

The companion star within a nova system donates material that is accreted onto the growing WD. However, what would happen if the donor was no longer able to donate matter as it had been depleted? We have modelled this scenario as understanding this post-eruption phase is crucial if we are to find systems with once active novae ([Darnley, 2021](#)).

To demonstrate this eventuality, we have taken the final epoch of the reference simulation with radiative cooling (Run 12), terminated the nova eruptions to signify a fully depleted donor and then allowed the already formed remnant to evolve. Even though not physical as the donor has been depleted, we have continued to blow a red giant wind within the simulation for computational purposes. This will not have an impact on the structure of the evolving remnant.

Up until now, we have stated that our simulations are based upon a WD with a certain initial mass growing to the Chandrasekhar limit. But if this mass was reached at the end of the reference simulation, why would we have a depleted donor scenario and not a SNIa? As our upper limiting WD mass was defined to be when the recurrence period reaches the theoretical lower limit (~ 50 days, see Section § 4.4.2), we wish to use Run 12 for illustrative purposes. In other words, we could have set the donor depletion to happen at an earlier epoch (with a less massive WD), however as we have defined our end point arbitrarily, there is no indication for a more realistic WD mass to choose.

6.1.1 Dynamical evolution of remnant after donor depletion

A snapshot of the simulation is given in Figure 6.1 approximately 2.2 Myr after the depletion of the donor, with the final epoch of Run 12 (~ 6 Myr) plotted to demonstrate the evolution. As expected, the NSR continues to expand into the surroundings due to the remaining kinetic energy of the late-time ejecta influencing the growing shell, reaching out to 40 pc by the latest epoch. This would suggest that the expansion of the NSR has accelerated at some point between 6 Myr and 8.2 Myr. From the outer shell growth curve in the right panel of Figure 6.1, we can see that this acceleration has indeed occurred, only not for the full 2.2 Myr. Instead, the shell continued to expand at an accelerating rate for next 1 Myr, likely due to the influence of the most energetic ejecta (from the last nova outbursts), before the growth slows down.

A similar trend is evident in the evolution of the shells average velocity before and after donor depletion (see Figure 6.2). As detailed in Section § 4.7, the outer edge of the remnant shell in Run 12 remains below 10 km s^{-1} during the full simulation, however the increasing velocity of the inner edge as a result of more frequent collisions into the ejecta pile-up region, drives up the average velocity of the shell for the last 1 Myr. Then, as with the remnant's expansion, the velocity of the shell continues to increase to a peak of $\sim 8 \text{ km s}^{-1}$ after 800,000 years, before decreasing for the next ~ 1.4 Myr.

As for the whole structure, we see in the bottom left panel of Figure 6.1 that the velocity of the remnant between $\sim 2\text{--}30$ pc becomes extremely low at the shown epoch, owing to the complete disappearance of the ejecta pile-up region. There is material between $\sim 35\text{--}40$ pc moving at a faster relative velocity of $\sim 3\text{--}8 \text{ km s}^{-1}$ however this is simply the residuals of the fast moving ejecta pile-up region slowing as expansion takes place. A considerable fall in the pressure of pile-up region is seen

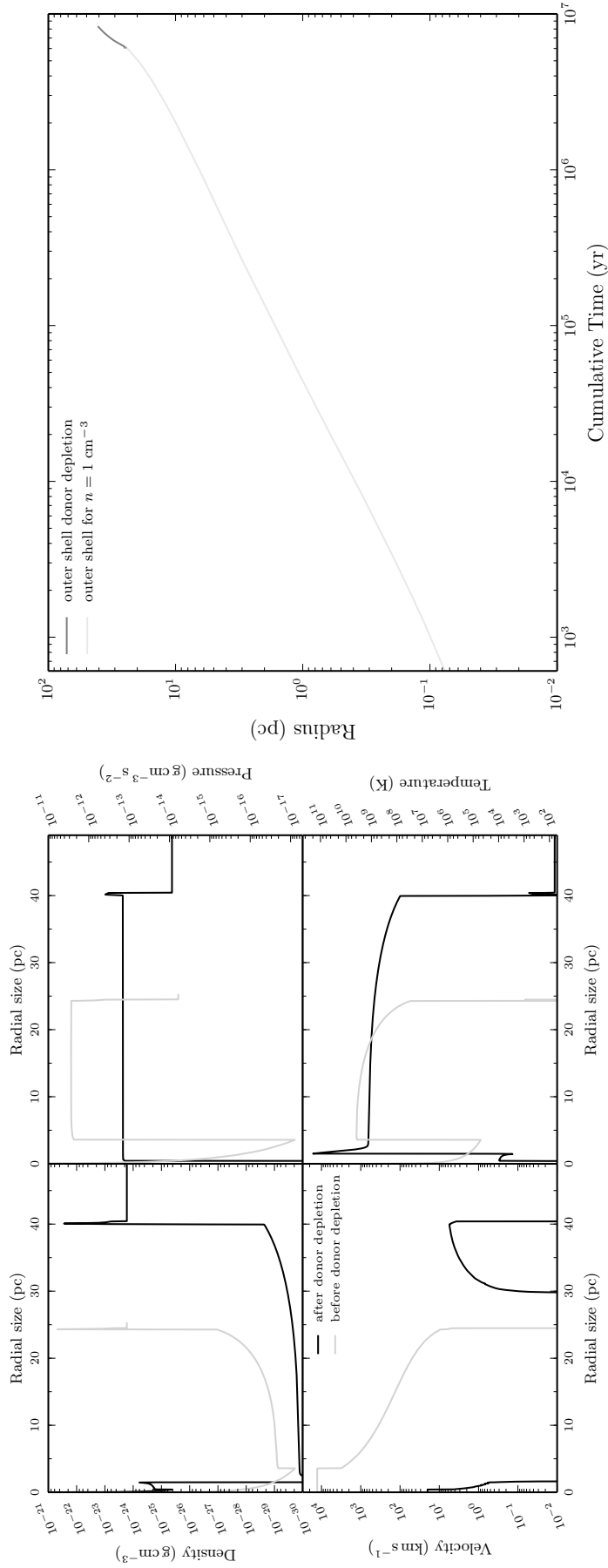


FIGURE 6.1: Left: A comparison of the dynamics of the NSR from the reference simulation with radiative cooling (Run 12) after ~ 6 Myr alongside the dynamics of the NSR ~ 2.2 Myr after the donor has depleted all of its material. **Right:** Evolution of the outer edge of the shell with respect to cumulative (elapsed) time and recurrence period for the reference simulation with radiative cooling, and the continuation for the post-nova scenario of a depleted donor.

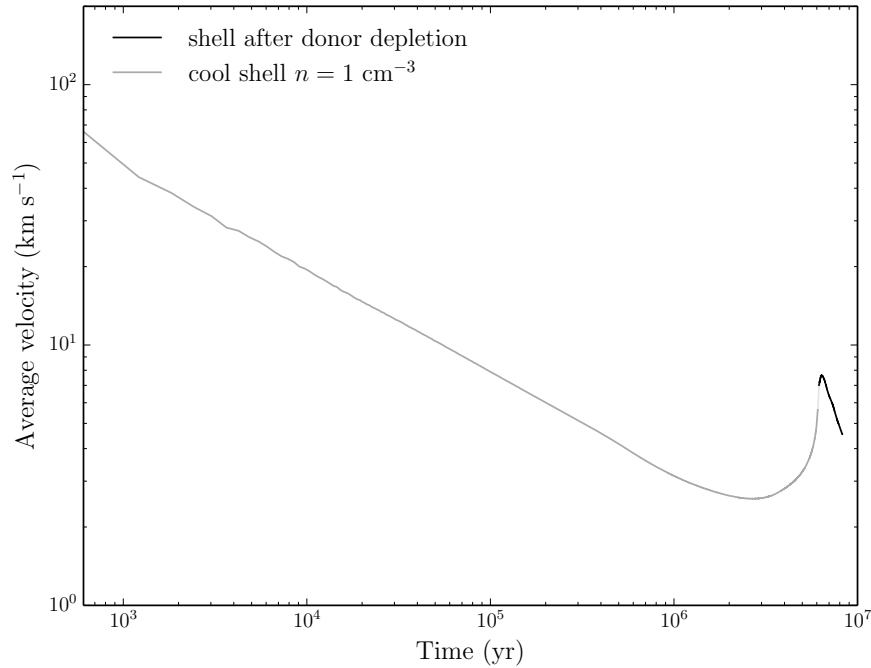


FIGURE 6.2: The evolution of the shell’s average velocity from the reference simulation with radiative cooling (Run 12) and the continuation for the post-nova scenario of a depleted donor.

as it grows in size without a fresh supply of material from incoming nova eruptions (see top right panel of Figure 6.1). The pressure in the remnant shell also drops at this epoch, however still retains pressures approximately double those seen in the ejecta pile-up as a result of the very high density shell. Moreover, as the outbursts from the nova system have ceased at this stage of the remnant’s evolution, the pile-up region (making up the considerable radial size) begins to cool down allowing recombination (see bottom right panel of Figure 6.1).

The spike we see close to the origin in the density, velocity and temperature panels of Figure 6.1 can be attributed to the artificial wind simulated from the central system. Due to collisions within the ejecta pile-up region, some material from this region will pass into the preceding cavity where the artificial red giant wind shocks the remains of the last eruptions. Consequently, we would not expect to see this component in a real nova super-remnant structure where the donor would no longer be radiating a wind.

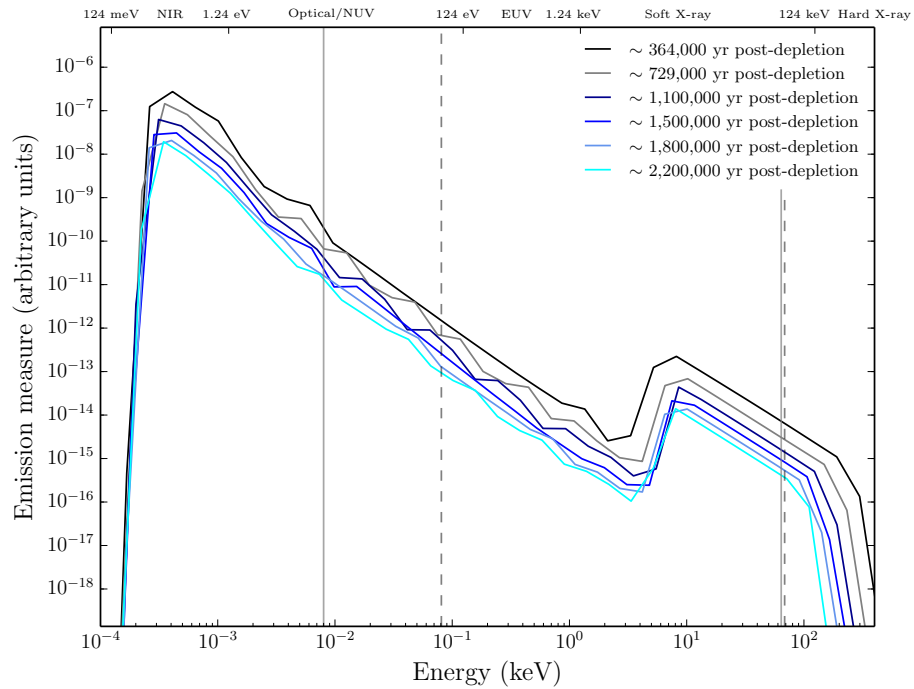


FIGURE 6.3: Emission measure ordered by temperature for the reference simulation with radiative cooling (Run 12) at various epochs following the depletion of the donor. The two grey lines show the upper (64 keV) and lower (0.008 keV) temperature limit of the APEC model and the two black dashed lines show the upper (68.4 keV) and lower (0.0808 keV) temperature limit of the VAPEC model.

6.1.2 X-ray luminosity of remnant after donor depletion

The evolution of emission measure, shown in Figure 6.3, can be used to inform us about the evolution of X-ray emission from the nova super-remnant after the depletion of the donor. After the nova eruptions have ceased, and the final ejecta has travelled through the ejecta pile-up, the total X-ray emission from the NSR will begin to decrease as the majority of X-rays previously emanated from the shocks within this region. This is evident in Figure 6.3 with both the decreasing emission measure across the full energy range and the high energy tails that progressively move to lower energies.

In Figure 6.4, we provide the X-ray luminosity radial profile of the reference simulation with radiative cooling approximately 3000 years following the depletion of the donor¹. The X-ray luminosity of the cavity and most of the ejecta pile-up region, up to ~ 20 pc, falls below 1×10^{24} erg s⁻¹, comparable with the luminosity of the reference simulation without radiative cooling (see Figure 5.9). The luminosity

¹This time was chosen in order to compare levels of X-ray emission following the donor depletion scenario with those levels from the impact of SNIa ejecta with the remnant, presented in Section § 6.2.2.

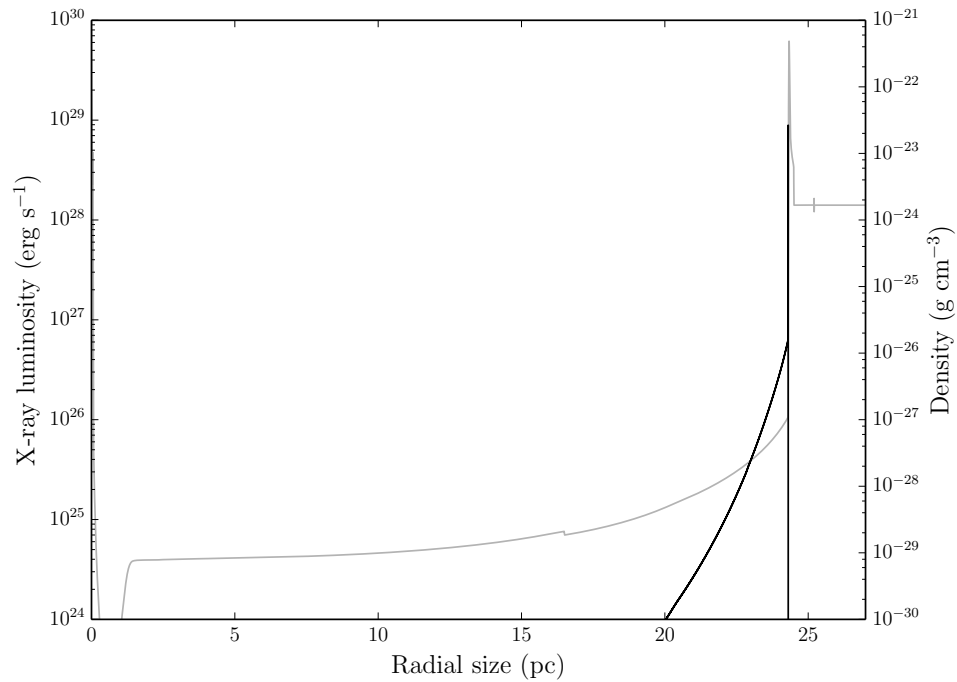


FIGURE 6.4: The X-ray luminosity radial profile of the reference simulation NSR with radiative cooling (Run 12) ~ 3000 years after the donor has been depleted. The time period coincides with the amount of time before ejecta from a SNIa (presented in Section § 6.2.2) impacts the remnant shell, for comparative purposes. The faint line is the density profile of the NSR at the same epoch.

then rises sharply at the inner edge of the dense remnant shell as the residual outbursts from the now-extinct nova reach and ionise the material there. Even though the X-ray emission from this region is approximately 10^5 times greater than any other region of the NSR, an X-ray luminosity of $1 \times 10^{29} \text{ erg s}^{-1}$ remains very low with respect to detectability at the distance of M 31 (see, for example, Figure 5.19). Furthermore, as no more energy is being supplied by the underlying system, we would not expect for this non-detectability status to change for the rest of the donor depletion scenario, in accordance with the evolution of emission measure given in Figure 6.3.

6.2 SNIa explosion within the NSR

As described in Section § 1.4.1 and Section § 4.1, the accreting WD in a RN system can grow to the Chandrasekhar limit and detonate as a SNIa. If this stellar explosion takes place within the created NSR, we will have firm evidence of the underlying progenitor system (Darnley, 2021). In this section, we will simulate how

the ejecta from a SNIa interacts with the pre-existing NSR, how its structure is then affected and the likelihood of detecting emission from this interaction.

As we did for the donor depletion scenario in Section § 6.1, to model a SNIa exploding at the centre of a formed NSR, we will use the final epoch of our reference simulation with radiative cooling (Run 12) as a starting point for the simulation. To recreate the explosion, we wish to know the mass ejected as well as the velocity of the ejecta to feed into the simulation. Taking the Chandrasekhar mass to be $1.4 M_{\odot} = 2.77 \times 10^{30}$ kg and the total kinetic energy from a SNIa to be $1 \text{ FOE} = 1 \times 10^{51}$ erg (see, for example, [Prentice et al., 2018](#)), the velocity of the ejecta is calculated to be ~ 8500 km s⁻¹. As we would be running this simulation at a resolution of 100 AU/cell and the time taken for the ejecta to cross a cell at ~ 8500 km s⁻¹ is ~ 20 days, we set the length of the SNIa explosion to be 1 day ($\ll 20$ days). Therefore, we blew a wind for one day with a velocity of $v = 8500$ km s⁻¹ and mass loss rate of $\dot{M} \sim 511 M_{\odot} \text{ yr}^{-1}$ to model a single mass ejection, acting as a supernova explosion.

6.2.1 Dynamical evolution of remnant after SNIa

The results of a SNIa exploding at the centre of a formed remnant is shown in Figure 6.5 at various epochs following the event. As the cavity region for the reference NSR with radiative cooling extends to approximately 3.5 pc (see orange dotted line in Figure 6.5) and is completely devoid of any material (including hydrogen), the freely expanding bulk ejecta travelling at ~ 8500 km s⁻¹ would have nothing to interact with and so would traverse this radial distance in ~ 400 years. Once this boundary is reached, the high density SNIa ejecta collides with the inner edge of the ejecta pile-up region and sweeps up material, leaving a much lower density ($< 1 \times 10^{-32}$ g cm⁻³) cavity in its wake. This high density spike from the SN ejecta then continues to push through the pile-up region for the next ~ 2500 years (see light grey line in the top left panel of Figure 6.5), falling in density as it does so. Additionally, it drives the formation of a forward shock, consisting of a trough behind a crest that is continuously increasing in density.

After ~ 2800 years, the high density spike (and crest feature in front) moving through the relatively low density pile-up region meets the inner edge of the NSR shell. This inner edge is 10^4 times more dense than the SN ejecta spike and so the spike effectively hits a wall and ‘squeezes’ the forward shock in-between, before ‘bouncing off’ and creating a reverse shock through the ejecta pile-up region. Due to the simulation having low resolution and lacking the incorporation of relativistic physics, this reverse shock is superluminal. However, as all material within the remnant has

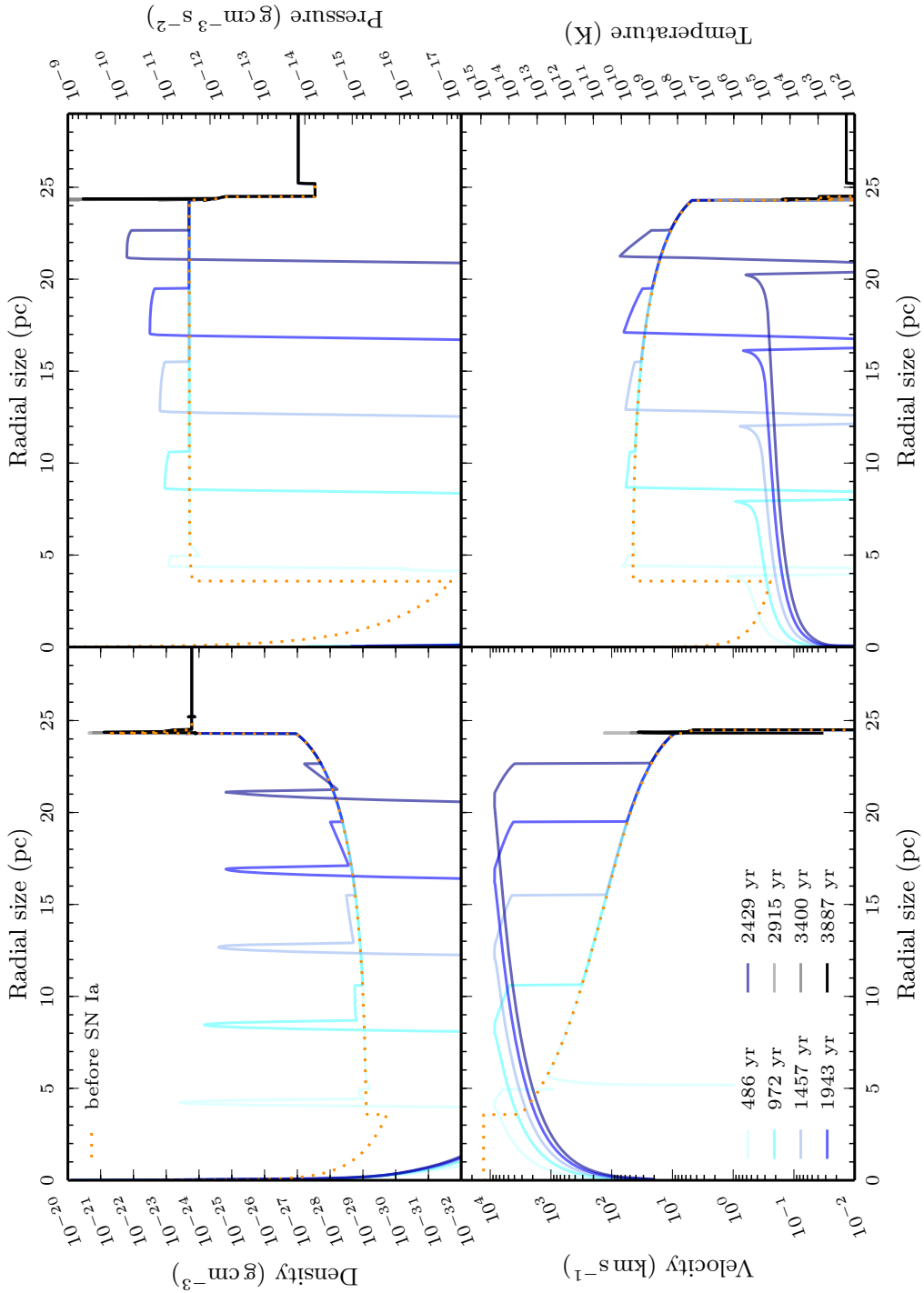


FIGURE 6.5: A comparison of the dynamics of the NSR from the reference simulation with radiative cooling (Run 12) alongside the dynamics of the NSR after a SNIa takes place at the centre of the remnant at various epochs following the explosion.

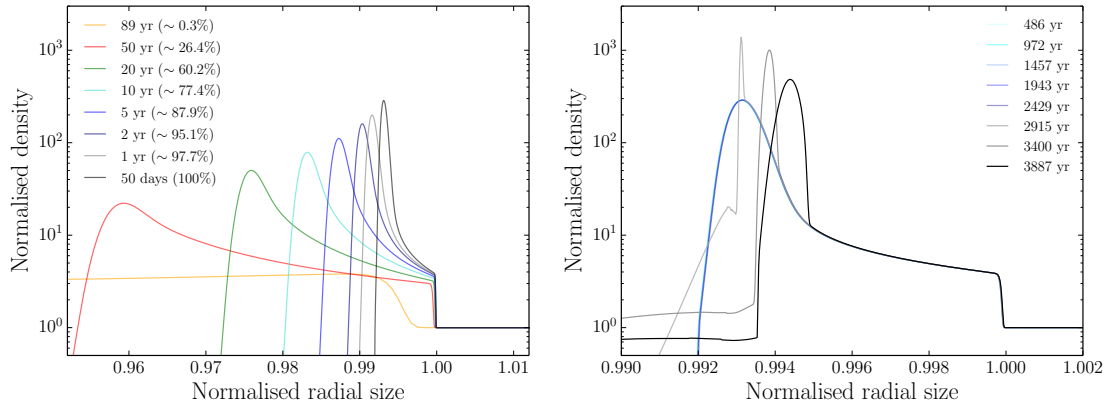


FIGURE 6.6: **Left:** The evolution of the NSR shell within the reference simulation with radiative cooling (Run 12) as previously given in Figure 4.30. **Right:** The evolution of the NSR shell from the reference simulation with radiative cooling (Run 12) at various epochs following the SNIa supernova and the consequent impact of the ejecta.

been ionised from the SNIa ejecta up to the inner edge of the shell at this point, a shock wave with velocities greater than the speed of light is considered not important here and so can be ignored (S. Kobayashi, private communication).

Focussing on the remnant shell during the post-supernova phase of the simulation reveals the impact of the explosion in more detail (see Figure 6.6). For the first ~ 2400 years following the SNIa, the remnant shell experiences very little change from how it was structured at the epoch of $P_{\text{rec}} = 50$ days (see black line in left panel of Figure 6.6 compared to the epochs of 486–2429 years in the right panel of Figure 6.6), as the SN ejecta has not yet reached this region of the fully formed NSR.

However, the epochs shown beyond this ~ 2400 years do exhibit a much different form, as the forward shock from the SN ejecta plowing through the pile-up region finally crashes into remnant shell after ~ 2800 years. Beyond this epoch, we see the influence of the SNIa ejecta impact through a compression of the shell from approximately 0.8% of the remnant’s radial size at 2429 years to $\sim 0.6\%$ by 3400 years, leading to a $\times 5$ increase in density at the inner edge. But how does the SN ejecta impacting the NSR affect observability?

6.2.2 X-ray luminosity evolution of remnant after SNIa

We have shown in Section § 6.2.1 how the material ejected from a SNIa influences the structure of the whole NSR. Now we will predict observables of this interaction in the form of X-ray emission. In Figure 6.7, we present the evolution of X-ray emission from the whole nova super-remnant for the first ~ 3900 years following the SNIa.

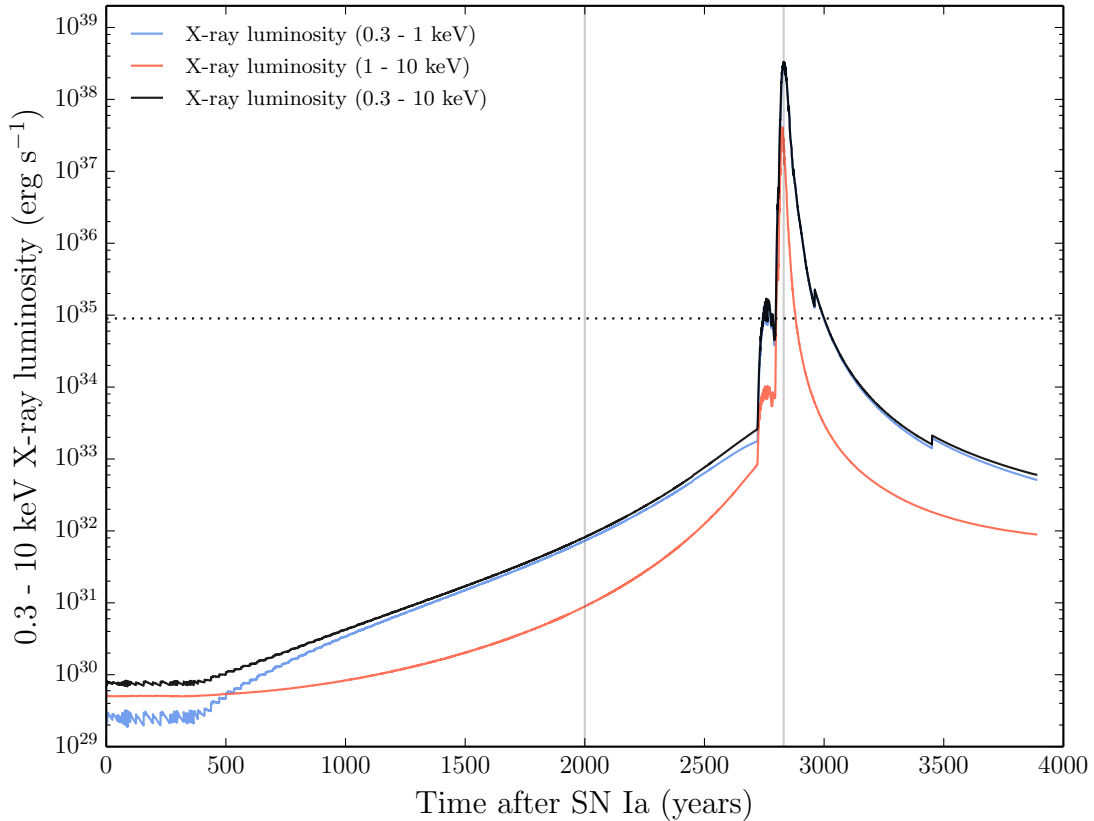


FIGURE 6.7: Evolution of the X-ray luminosity of the reference simulation NSR with radiative cooling (Run 12) after experiencing a SNIa. As in Figure 5.19, soft X-rays are red, hard X-rays are blue, the total X-ray luminosity is black and the dashed line indicates the 3σ upper limit from XMM-Newton observations of the NSR surrounding M 31N 2008-12a for reference. The vertical lines indicate the epochs designated as the rise (2000 yr) and the ejecta impact with the NSR shell (~ 2800 yr).

As in Figure 5.19, we have provided the evolution of the soft (0.3–1 keV), hard (1–10 keV) and total (0.3–10 keV) X-ray luminosity. Here, we will simply focus on the total X-ray luminosity. The luminosity of the remnant at the time of the SNIa, located at 0 years in Figure 6.7, is 8×10^{29} erg s $^{-1}$ and remains relatively stable for the first 400 years². As discussed earlier, the ejecta from the SNIa will take approximately 400 years to freely expand across the very low density cavity before reaching the ejecta pile-up region. It is this collision between the ballistic SN ejecta and the inner edge of the pile-up region that triggers the initial increase in X-ray luminosity.

The next ~ 2300 years sees the luminosity continuously increase as more and more material within the pile-up region is swept up into the progressing forward shock, rising from 8×10^{29} erg s $^{-1}$ at ~ 400 years to 2×10^{33} erg s $^{-1}$ after ~ 2700 years. For this rising phase, we have predicted the X-ray luminosity for the whole remnant

²Though similar to the total X-ray luminosity of the remnant at the end of its evolution in Figure 5.19, note that here we are using the reference simulation *with* radiative cooling as the starting point for this simulation, whereas Figure 5.19 focusses on the reference simulation without cooling.

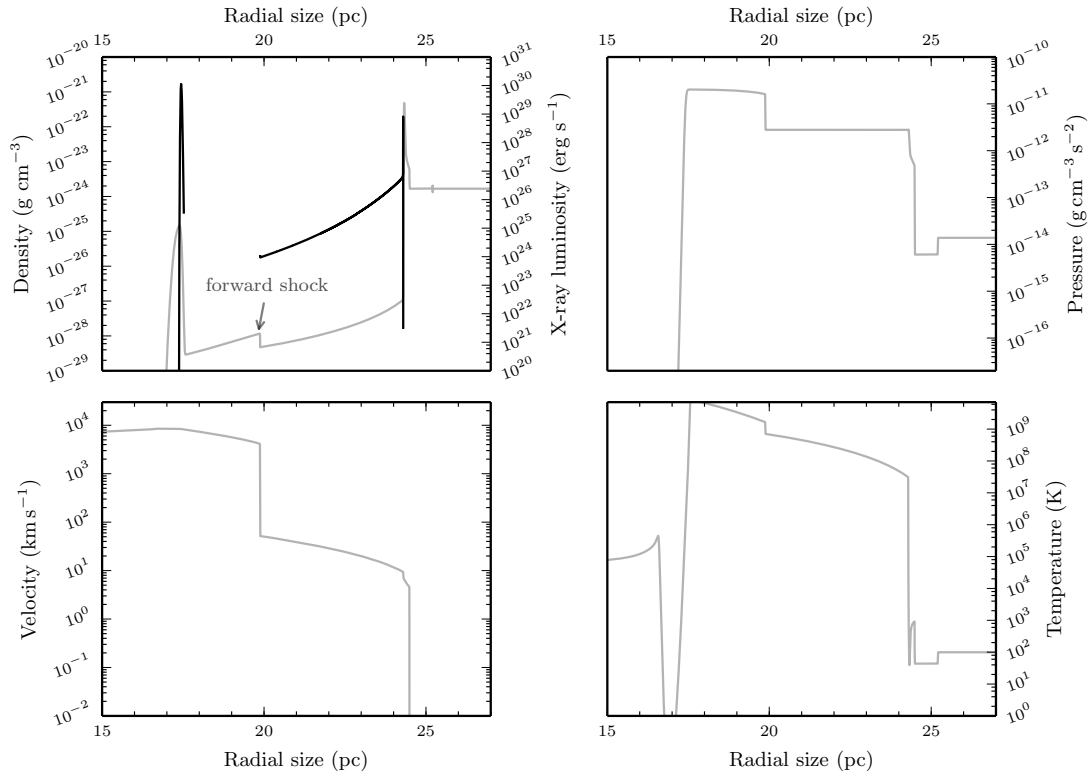


FIGURE 6.8: The X-ray luminosity radial profile of the reference simulation NSR with radiative cooling (Run 12) 2000 years after the SN alongside the dynamics of the nova remnant at the same epoch. We have focussed on the remnant from 15 parsecs to the remnant shell to view the X-ray luminosity in more detail. The faint line in the top left panel is the density radial profile for Run 12 within this region.

at 2000 years (chosen arbitrarily) in order to see how the total X-ray luminosity of $8 \times 10^{31} \text{ erg s}^{-1}$ at this stage is configured across the radial size of the NSR, shown in Figure 6.8. There are two major regions of X-ray emission. As seen previously in Section § 6.1.2, we have a large amount of X-ray emission ($1 \times 10^{29} \text{ erg s}^{-1}$) from the inner edge of the formed remnant shell as later nova ejecta interact and ionise this region. The more luminous region during this epoch, however, traces the front of the SN ejecta spike travelling through the pile-up region at approximately 17.5 parsecs. Here, the X-ray emission is $1 \times 10^{30} \text{ erg s}^{-1}$, and so will dominate the total X-ray luminosity of the NSR at this epoch of 2000 years and likely to be dominate during this whole rising phase.

Following this steady rise, we see the first significant jump in X-ray emission up to $2 \times 10^{35} \text{ erg s}^{-1}$ as the front of the forward shock collides with the high density NSR shell (see Figure 6.5). This, however, pales in comparison to the total X-ray luminosity of the remnant seen when the bulk SNIa ejecta, responsible for creating the forward shock, collides with the inner edge of the shell. At this stage, approximately 2800 years after the supernova at the centre of the nova super-remnant (indicated

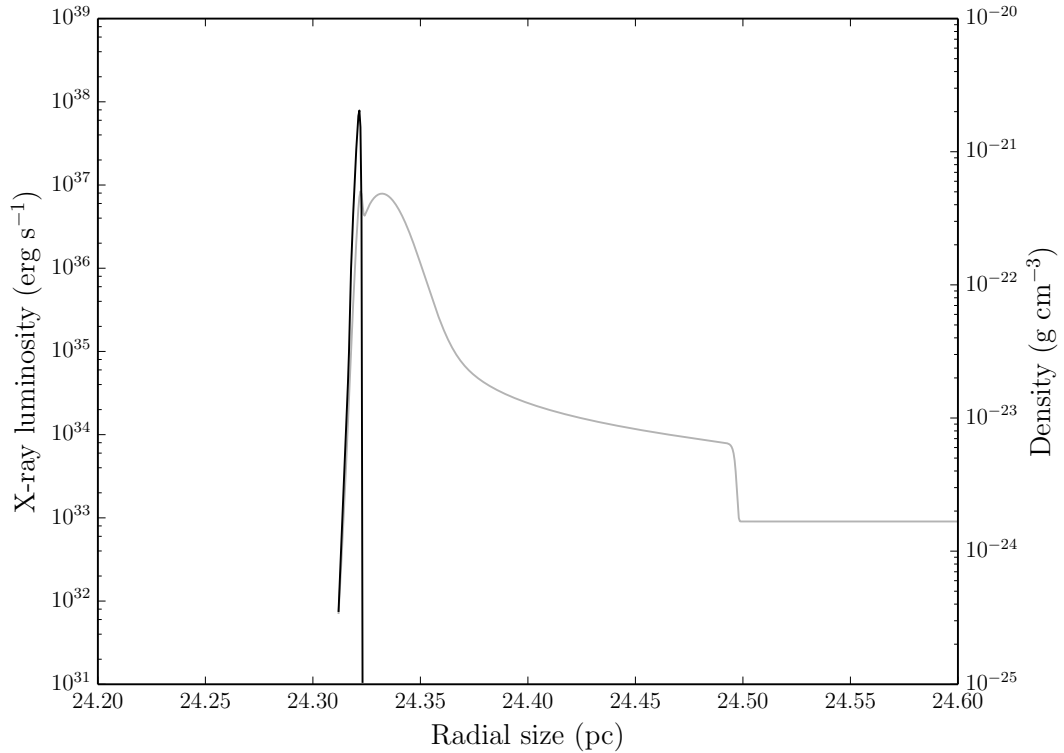


FIGURE 6.9: The X-ray luminosity radial profile of the reference simulation NSR with radiative cooling (Run 12) ~ 2800 years after the supernova has taken place. This is the amount of time taken for the SNIa ejecta to reach and impact the inner edge of the remnant shell. We have focussed exclusively on the remnant shell here and the faint line is the density radial profile of the remnant shell for Run 12.

with a vertical line in Figure 6.7), and over the course of only a century, the X-ray emission from the remnant hits a peak of $3 \times 10^{38} \text{ erg s}^{-1}$, over a billion times the luminosity of the fully formed remnant at the point of the SNIa explosion.

The radial profile of the total X-ray luminosity for this impact epoch is shown in Figure 6.9. We have focussed solely on the remnant shell as the X-ray emission from other regions of the remnant after 2800 years is completely negligible in comparison to the vast amount of X-rays emanating from the SN ejecta–NSR shell collision. An incredibly bright X-ray spike is seen as the bulk SN ejecta finally crashes into the high density remnant shell, peaking at $1 \times 10^{38} \text{ erg s}^{-1}$ and accounts for the majority of total X-ray luminosity of the structure at this stage. A synthetic X-ray spectrum at the point of peak luminosity from the impact of the SNIa ejecta with the shell is shown in Figure 6.10, the emission shifting upwards by a factor of $\sim 10^8$ from the spectra provided for the reference simulation without radiative cooling (see Figure 5.10). A number of the line fluxes at the lower energy range reach $\sim 6 \times 10^{-13} \text{ erg cm}^{-2} \text{ s}^{-1}$ and so would be detectable with current X-ray missions

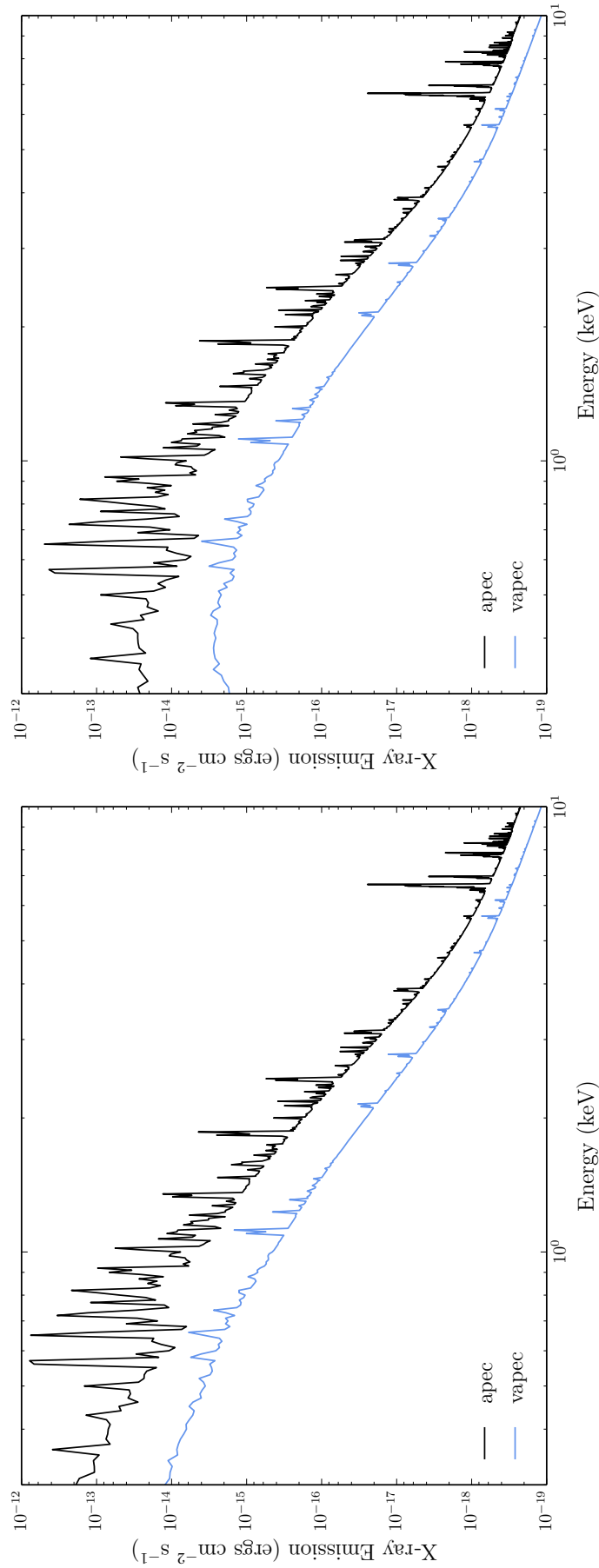


FIGURE 6.10: **Left:** Synthetic X-ray spectra of the NSR from our reference simulation at epoch when the SNIa ejecta impact the inner edge of the NSR shell, generated with the APEC and VAPEC models ranging from 0.3 - 10 keV, with a resolution of 10 eV. **Right:** Same as the left panel with absorption included.

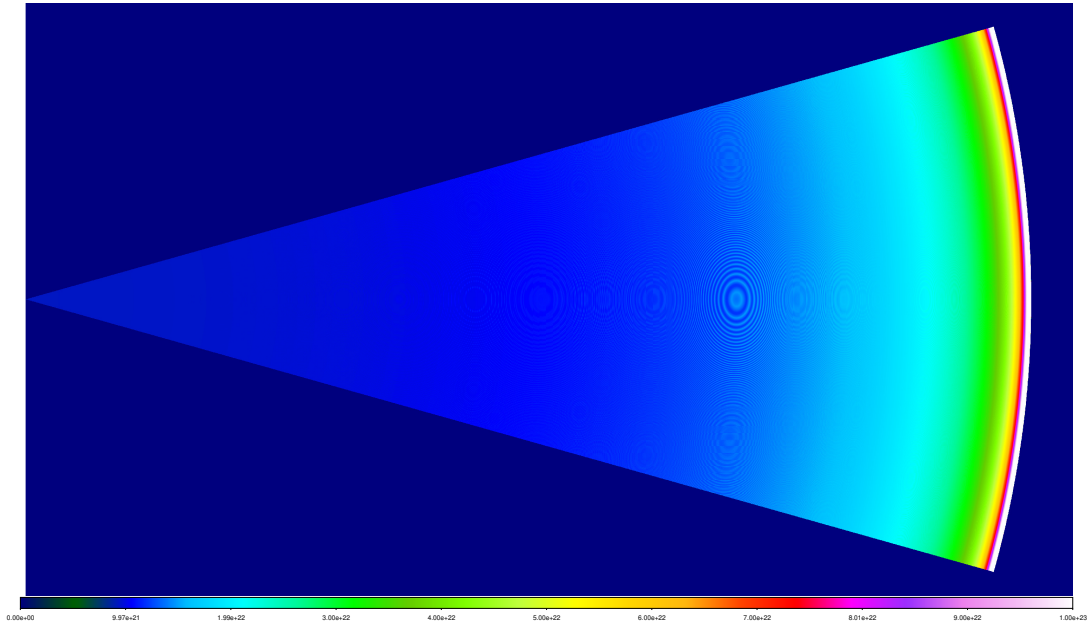


FIGURE 6.11: Synthetic sky image of the X-ray luminosity radial profile of the reference simulation NSR with radiative cooling (Run 12) ~ 2800 years after the supernova has taken place. This is the amount of time taken for the SNIa ejecta to reach and impact the inner edge of the remnant shell.

such as *Swift*³⁴ if the remnant was located in M31. Intriguingly, if we take the peak X-ray luminosity as $1 \times 10^{38} \text{ erg s}^{-1}$ and place the NSR at the distance of a Galactic RNe such as RS Ophuichi (1.4 kpc), we estimate an X-ray flux of $\sim 4.26 \times 10^{-7} \text{ erg cm}^{-2} \text{ s}^{-1}$, at the upper end of the XRT's sensitivity limit on *Swift* (the upper end of the brightness that *Swift* can observe). Finally, by converting the spike in X-ray luminosity at the collision site of the SN ejecta and the inner edge of the remnant shell, as shown in Figure 6.11, we can get an insight into how this emission would appear on the sky in the X-ray regime.

6.3 Summary

In this chapter, we have explored the two scenarios of a post-nova system. One of these looks at the evolution of the NSR after the companion star has depleted all donatable material. The other focusses on the much more eventful situation, whereby the WD in the system reaches the Chandrasekhar limit and detonates as a SNIa at the centre of the NSR. Here, we will summarise the key points:

³<https://sites.astro.caltech.edu/palomar/observer/200inchResources/swiftpspecs.html>

⁴https://swift.gsfc.nasa.gov/about_swift/xrt_desc.html.

1. The nova super-remnant surrounding an extinct recurrent nova (a system in which the companion depletes all donatable material), will continue to grow from residuals of the final outbursts.
2. The X-ray emission from this post-depletion remnant will continue to be concentrated at the inner edge of the shell, but then will precede to fall away due to the absence of nova eruptions.
3. The bulk ejecta from a type Ia supernova explosion at the centre of a nova super-remnant firstly collides with and sweeps up the pile-up region, before crashing into the remnant shell around 3000 years later.
4. The X-ray luminosity of this collision easily surpasses the detection limit of the *Swift* satellite, whether the NSR was located in the Galaxy or at the distance of M 31, providing a key observational signature for detecting this interaction, and thus providing unequivocal evidence for the single-degenerate progenitor responsible for the SNIa.

Chapter 7

Summary, Future Work and Recent Developments

7.1 Summary

My thesis is made up of three distinct projects. One of these is a thorough observational campaign of an individual nova system in NGC 6822, outlined in Chapter 2. The second project, presented in Chapter 3, is a contribution towards a larger study of the nova super-remnant surrounding the rapidly recurring nova, M 31N 2008-12a. The last project follows on from the second, using a large series of hydrodynamical simulations to recreate nova super-remnants (during the nova's evolution and beyond) and explore the growth, structure and observability within a particular parameter space, presented in Chapter 4, Chapter 5 and Chapter 6. I will now provide a brief summary of each chapter.

7.1.1 AT2017fvz - an extragalactic classical nova

The nova, AT 2017fvz was discovered on 2 August 2017 in the Local Group irregular dwarf galaxy NGC 6822. We utilised LT, ATLAS, KAIT, ASAS-SN and *Swift* to determine photometric evolution, the LT for spectroscopic characterisation and *Swift* for X-ray observational follow-up.

From the photometry, we found that AT 2017fvz is a 'very fast' fading nova (falling 2 magnitudes from peak in only 8 days) and shows evidence of a plateau in the optical light curve between 25 – 45 days post-peak, indicating the presence of a surviving or re-formed accretion disk. Spectroscopy revealed that the nova belongs to the

Fe II spectroscopic class and exhibited relatively high ejecta velocities of 2430 km s^{-1} approximately 8 days after outburst. X-rays were not detected 38 – 388 days post-eruption, indicating that the SSS phase occurred before this observation period, was hidden by the ejecta or that the X-rays were too faint to detect. During a search for a progenitor system, a source near to the location of the nova was found in archival *HST* images, however further analysis deemed this to be an unassociated O-star.

In conclusion, owing to the low luminosity ($M_V = -7.45 \pm 0.07$) and rapid decline ($t_{2(V)} = 8.1 \pm 0.2 \text{ d}$), AT 2017fvz may belong to the ‘faint and fast’ class of novae. In addition to these characteristics, the light curve plateau and potentially short SSS phase, may point towards AT 2017fvz being a recurrent nova.

7.1.2 Photoionisation analysis of M31N 2008-12a NSR

The rapidly recurring nova, M 31N 2008-12a, is surrounded by a vast remnant, over 100 parsecs across. Whilst spatially coincident with 12a, this structure was potentially created from another astrophysical mechanism. In other work, outside of this thesis, the remnant was determined to not be (i) a supernova remnant due to a lack of significant X-ray emission and absence of particular oxygen emission lines in the spectra, nor (ii) a superbubble through an absence of a detectable OB star.

In this work, we carried out Strömgren sphere analysis using the known parameters of the 12a system alongside varying densities of the surrounding ISM. With constraints on the ISM density from observations, we concluded that the remnant surrounding 12a cannot have been grown through photoionisation alone (therefore is not a Strömgren sphere), and that many past nova eruptions would be required to grow the nova super-remnant dynamically to its current size.

7.1.3 Simulations of NSRs

The nova super-remnant associated with M 31N 2008-12a is the only example we have. However, as its existence is a predominantly the result of frequently recurring nova outbursts, then other recurrent nova systems with massive WDs and high mass accretion rates could also be surrounded by a vast remnant such as this.

To explore the dependence of a number of nova system parameters (mass accretion rate, initial WD mass, WD temperature) as well as ISM density on the NSR growth and structure, we conducted a large number of hydrodynamical simulations,

with and without radiative cooling. Furthermore, these NSRs were simulated using eruptions with shortening inter-eruption times, increasing ejecta velocities and decreasing mass ejecta, to replicate a more realistic nova system as it approaches the Chandrasekhar limit.

Each simulation produced a nova super-remnant with a low density cavity region enclosed with a hot ejecta pile-up region and flanked by a cold high density remnant shell, which grew with a power law dependence. We found that the higher density the ISM environment, the smaller the final remnant. Similarly, a higher mass accretion rate within the underlying system leads to a smaller NSR. On the other hand, the temperature and initial mass of the WD was found to have a smaller influence on the NSR evolution. The incorporation of radiative cooling, further mimicking a true system, led to smaller remnants that were enclosed with thinner high density shells.

Crucially, we found that the simulation that mostly resembled the characteristics of the 12a system, with radiative cooling, did not replicate the nova super-remnant seen with observations.

7.1.4 Searching for NSRs

The purpose of simulating nova super-remnants, each with varying underlying system parameters, revolved around their use in making predictions of the potential sizes and emission characteristics of these vast shells. These predicted observables could then be used to guide searches to identify more Galactic (and extragalactic) examples.

From simulations, we were able to find a relation between the radial size of a potential remnant and the evolutionary time, including dependencies on both the density of the local ISM and the accretion rate within the nova system. A preliminary version of this relationship was utilised to predict the radial sizes of possible NSRs associated with the ten Galactic recurrent novae. The first ever search for these structures was then initiated with the Liverpool Telescope looking around six of the ten Galactic RNe, namely U Sco, V3890 Sgr, T CrB, V2487 Oph, RS Oph and CI Aql.

Many characteristics of the nova super-remnant from the reference simulation, at the epoch when $P_{\text{rec}} = 1$ year, were found to generate possible observables. These included the ionisation fraction of the whole remnant and the emission measure, leading to predictions of the recombination times across the radial size of the NSR

and finally the production of synthetic X-ray spectra. We then furthered these predictions through applying the analysis to the full evolution of the reference simulation. This evolutionary plot could possibly be used to inform us of the total X-ray luminosity of a potential NSR from the system's recurrence period.

A parameter space (comprised of mass accretion rate and ISM density) populated with contour solutions of the NSR radial size equation revealed combinations of these two parameters that would result in a remnant with the radial size of that observed around M 31N 2008-12a. Predicted photoionisation regions created by the nova eruptions, emission from the accretion disk and shocks showed a lack of influence over the size and structure of the remnant, however the structure of the observed NSR was replicated with synthetic sky images.

7.1.5 Post-nova evolution of NSRs

RN systems will eventually reach a point whereby outbursts cease to occur, stemming from the companion no longer supplying material for the WD to accrete, or the WD itself hitting the Chandrasekhar mass and being ripped apart in a SNIa event. Each eventuality will have a very different impact on the already formed remnant.

The remnant in the depleted donor scenario will simply continue to expand into the surroundings, with the shell sweeping up material and leaving an extremely low density cavity, until it no longer has sufficient kinetic energy to grow any further. The SNIa scenario, on the other hand, has an enormous part to play in the evolution of the nova super-remnant. Ejecta from the SN ploughs its way through the whole NSR structure, including the pile-up region, until it collides with the high density remnant shell and emits a huge amount of X-rays. At this stage, a few thousand years after the SNIa, we would be able to observe a bright X-ray band at the inner edge of the shell, within the range of X-ray satellites such as *Swift*.

7.2 Future Work

Ultimately, as shown in Chapter 4 and Chapter 5, it is clear that the total kinetic energy from H-flashes alone in the first simulations of 12a cannot grow a NSR to the observed size. Other factors must play a role, such as highly energetic He-flashes placed throughout the evolution as well as the interaction between nova ejecta and components of the nova system (accretion disk and donor star). Predictions I have made from a growing WD model about the size of NSRs around Galactic RNe will be

valid. However, including more RN features in the models will help the simulations better mimic the shells, clearly improving targeted searches. As done previously, from these more realistic shells, I would then be able to calculate emission characteristics of different parts of the NSR to aid in multi-wavelength observations.

7.2.1 Simulations

Running hydrodynamical simulations of identical H-flashes produced from a non-growing WD, as in [Darnley et al. \(2019a\)](#), was used as a proof of concept. However, a true RN WD does grow in mass. This was addressed in [Chapter 4](#), with simulations of increasingly frequent non-identical H-flashes from a growing WD, with less mass ejected at higher velocities. Unquestionably though, as precision of the predicted shell size and emission are vital for a targeted search, a more realistic representation of a RN, and therefore NSR, is absolutely required. What key additional factors could be addressed in future work?

7.2.1.1 Helium flashes

Incorporating He-flashes would have a dramatic effect. This would begin with a high amount of mass being ejected for the first ~ 100 He flashes until the degeneracy of the He layer is reduced by the increase in WD temperature, leading to milder eruptions with no mass loss at all ([Hillman et al., 2016](#)). Crucially, as discussed in [Chapter 4](#), the high mass ejecta from these early eruptions would heavily influence the shaping of the final nova super-remnant.

7.2.1.2 Donor and disk interaction

Evidently, the WD's accretion disk is disrupted by nova eruptions as well as ejecta interaction with the donor's outer layers, all leading to further mass loss from the system ([Figueira et al., 2018](#)). Further, high mass loss from the system correlates with increased ejecta mass but only if there is significant disk disruption, whereas the increasing ejecta velocity plays a role in increased mass loss regardless of disk-interaction ([Figueira et al., 2018](#)). Integrating these feedback features into our simulations will change the growing structure of the NSR towards a more physical model.

7.2.1.3 Varying the mass accretion rate

Throughout the large suite of simulations, we altered the mass accretion rate of the system between individual runs, however this remained constant within the simulation. As a true nova system would experience a dynamic mass accretion rate, we did consider for the first time a change of accretion rate within the same simulation in Section § 4.9.4. However, this was only a first order approximation, abruptly jumping from one rate to a higher rate in an unphysical way, therefore in future studies we could alter this in a smoother way. Furthermore, the ejecta characteristics determined from this smoothly changing accretion rate, such as the velocity and mass loss, could also be generated with a Maxwellian distribution, instead of the single bulk ejecta for each eruptions we currently use.

7.2.1.4 ISM density gradient

From the sole example of this phenomenon described extensively throughout this thesis, we see that the sweeping up of local ISM in M 31N 2008-12a's NSR is inhomogeneous, with the remnant being more elliptical than spherical. This is possibly a manifestation of the underlying system however we could test the shaping influence of the surrounding ISM by implementing a density gradient within our simulations.

7.2.2 Observables

It has already been successfully demonstrated that these shell-nebulosities can be observed with high spatial resolution extragalactically, using *HST* narrow band F675N ($H\alpha + [N II]$) imaging (see bottom right panel of Fig 1.9, Darnley et al. 2019a). However, before our pilot studies presented in Section § 5.4 (which are still ongoing during the writing of this thesis), a Galactic or extragalactic search for these structures had never been carried out.

7.2.2.1 Galactic search continuation

Guided by radius and luminosity predictions from more precise simulations (and more accurate ISM density estimates), I could observe the surroundings of the ten Galactic RNe, including the six previously observed (see Section § 5.4). At the time of writing, we have acquired observations of the surroundings of T Coronae Borealis (see Section § 7.3), CI Aquilae and RS Ophiuchi. We have recently begun to reduce the data but have not yet had sufficient time to analyse the images.

After remnants are observed with deep $H\alpha$ imaging from ground based facilities such as the Liverpool Telescope (Darnley et al., 2015a, 2019a), novel observations of the finer structures of the NSR with space based telescopes would prove to be extremely fruitful. *HST* high-spatial resolution narrow-band imaging would constrain the density profiles of the NSR, for comparison with models, as well as shock fronts (Darnley et al., 2019a). Furthermore, as shown in Figure 5.1, the predicted Galactic RNe NSRs are much larger than the field of the view of the Liverpool Telescope, therefore utilising facilities with large field of views for future searches would be beneficial.

7.2.2.2 Extragalactic search

I could also investigate extragalactic hosts such as M 31, M 33 and the LMC. Utilising archival narrow-band imaging, I would search the surrounding vicinities of known novae in these galaxies before scouring the observations for NSRs with previously unknown associated novae. As done Galactically, this would encourage further *HST* proposals to pin down density profiles of the shells, therefore constraining the number of RN systems with an associated NSR and quantifying their contribution to the SNeIa rate of that host.

7.2.2.3 Predicting X-ray observations using XSPEC

No significant X-ray emission was found coming from M 31N 2008-12a's NSR (Darnley et al., 2019a), however the distance to M 31 likely plays a significant role. On the other hand, in nearer Galactic examples, we would expect X-ray emission from the colliding shells, similar to that seen in the Galactic RN RS Ophiuchi (Bode et al., 2007), within the ejecta pile-up region, as well as the inner edge of the shell, as temperatures here can reach over $\sim 10^9$ K alongside non-negligible densities (for example, see Figure 4.14). Furthermore, we illustrated in Section § 5.7.2 that systems with higher mass WDs will exhibit X-ray luminosities of $\sim 10^{31}$ erg s⁻¹ (see Figure 5.19). Hence the *Neil Gehrels Swift Observatory* is potentially an excellent facility to look for this X-ray emission for the first time, with the larger collecting areas of the *Chandra X-ray Observatory* and *XMM-Newton* also well placed for this novel search.

Additionally, the X-ray spectral fitting package XSPEC, utilised in Section 5.6.2, has an ability to generate simulated X-ray spectra based upon different missions. Therefore, the output from our more precise simulations could be fed into this mode to aid the search for NSR X-ray emission with the above mentioned facilities.

7.2.2.4 Infrared emission from NSRs

As mentioned in Section § 5.7.2, Darnley et al. (2019a) illustrated through extrapolating simulated emission peaks to the age of 12a's NSR, that these structures will predominantly emit in the mid infrared region around 12-13 μm . This was reinforced in this thesis from simulations of a growing WD with non-identical eruptions which shows how the peak emission from the evolving NSR remains with this infrared regime (see right panel of Figure 5.16). These emission observables would be able to control our search efforts supporting the use of the upcoming *JWST* in observing NSRs when it is launched.

7.3 Observations around T Coronae Borealis

In Chapter 5, we outlined a pilot study to search for evidence of NSR's around six Galactic RNe and the successful acquisition of observing time with the Liverpool Telescope. This campaign is still underway at the time of writing this thesis, however we do have our first observations of the two overlapping fields surrounding T Coronae Borealis specified in Figure 5.1, which we provide in Figure 7.1 (note that neither image contains T Coronae Borealis).

7.4 A possible super-remnant surrounding RS Ophuichi?

My whole thesis (except for the observational campaign of the nova AT2017fvz in Chapter 2, which is a stand-alone piece of nova research) has revolved around the nova super-remnant phenomenon. I first begun by introducing the vast structure, dubbed a nova super-remnant, uniquely surrounding the most rapidly recurring nova, M 31N 2008-12a.

Next, I ran a large series of hydrodynamical simulations in order to determine how growth and structure of these nebulosities is affected by the characteristics of the underlying nova system. This modelling led to a semi-analytical predictive tool used to find more examples of these remnants to illustrate that the M 31N 2008-12a NSR is not unique, and is the first of it's kind to be found.

Intriguingly, through determining the general size of these structures, we made a discovery of a potential nova super-remnant around the Galactic recurrent nova, RS Ophuichi, separate from the pilot study with the Liverpool Telescope. Instead, our estimate of the size of the NSR surrounding RS Ophuichi led to a cavity being

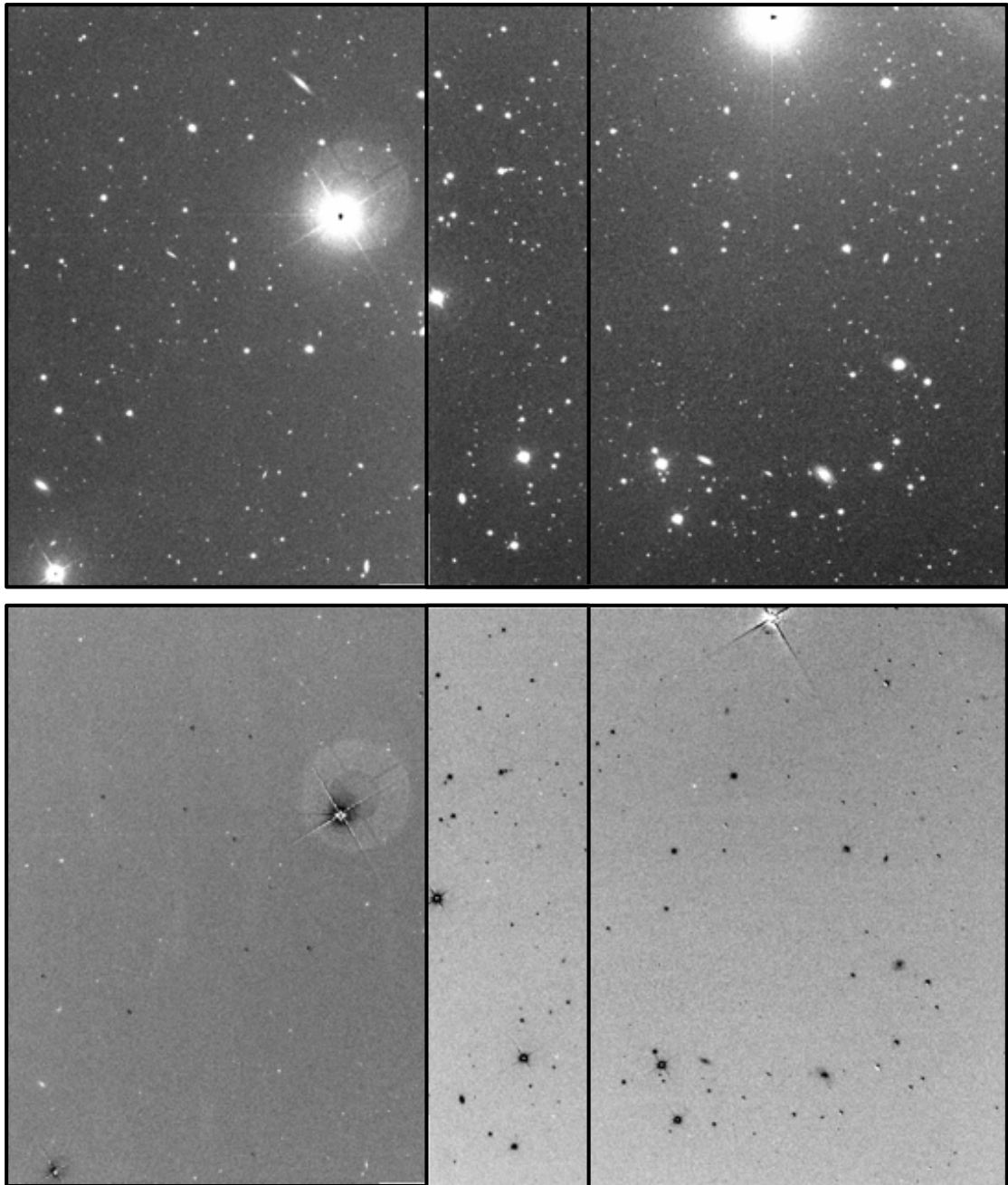


FIGURE 7.1: **Top:** Two overlapping Liverpool Telescope $H\alpha$ fields of the surroundings of the Galactic recurrent nova, T Coronae Borealis, used in an attempt to find evidence of an associated NSR. These two fields were illustrated in Figure 5.1 (note that neither image contains T CrB). Each image is made up of 5×720 s stacked $H\alpha$ images. **Bottom:** Continuum-subtracted $H\alpha$ images of the same two overlapping fields.

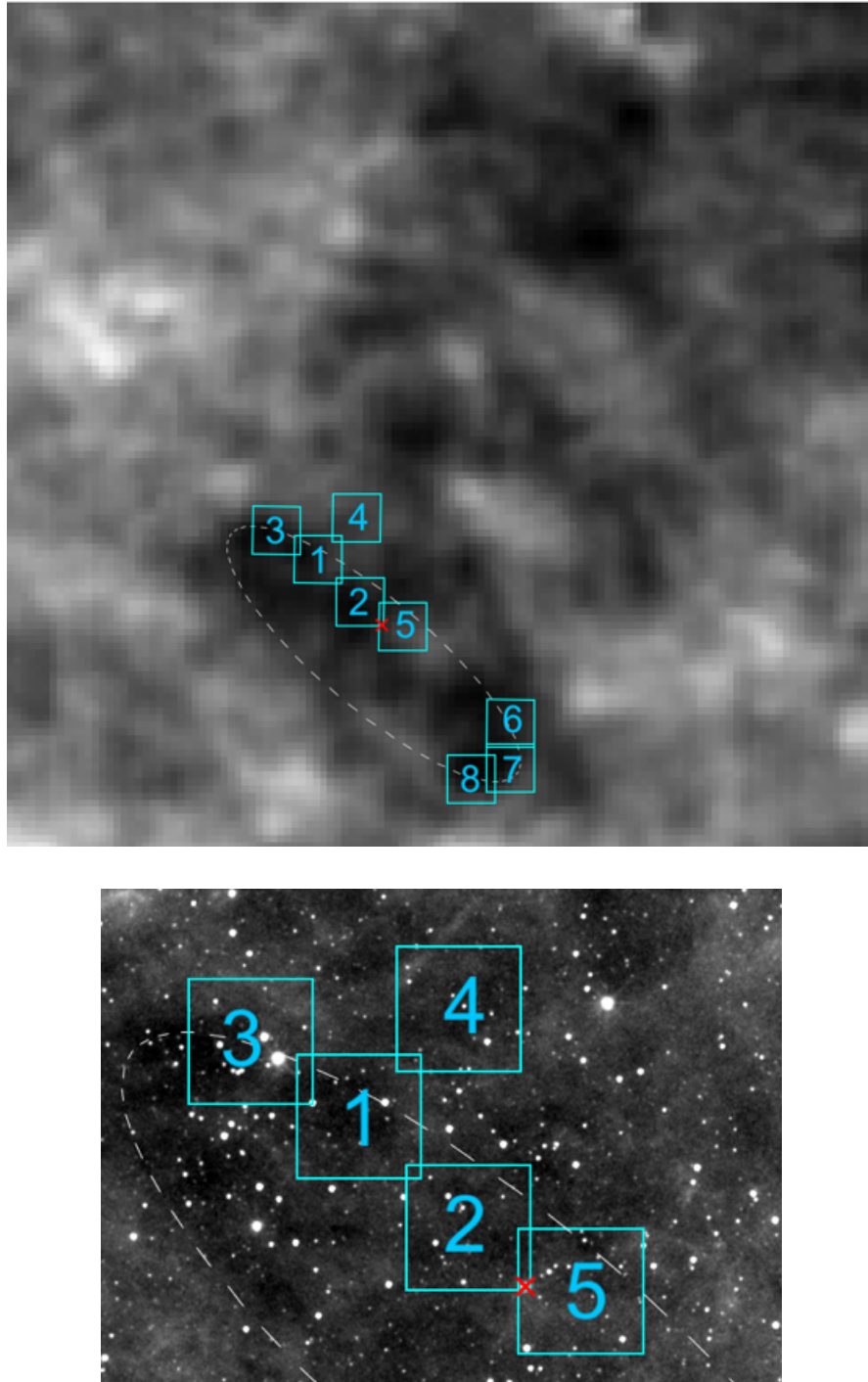


FIGURE 7.2: The possible nova super-remnant around the recurrent nova, RS Ophuichi. Each image includes the location of the nova (red cross) and the possible cavity of the nova super-remnant outlined (by eye) with a white dashed ellipse to guide the reader. The LT fields (1) to (8) to be observed are indicated with cyan boxes in the left image and a subset (1) to (5) are indicated with cyan boxes in the right image. We have chosen to place the fields (1), (2), (3) and (5) along the edge of the possible NSR overlapping the cavity and the surrounding sky, with (2) and (5) containing the position of RS Ophuichi. The opposite end of the cavity is then traced by (6), (7) and (8) in the same way, in the case of higher levels of emission from potential jets from the underlying system. Field (4) is placed such that it overlaps field (1) yet only covers the surrounding sky, away from the cavity, for comparison purposes. **Top:** $3^\circ \times 3^\circ$ IRIS field from IRAS (100 microns) of RS Ophuichi surroundings. **Bottom:** $55' \times 40'$ WISE field (12 microns) of RS Ophuichi surroundings

identified in archival infrared IRIS and WISE images that may possibly be another nova super-remnant (see Figure 7.2). By eye, the structure has semi-major and -minor axes of approximately $\sim 40'$ and $\sim 12'$, with an inclination of 140° (outlined in Figure 7.2).

Similar to the pilot study described in Section § 5.4, the possible nova super-remnant surrounding RS Ophuichi covers a larger portion of the sky than can be observed with the Liverpool Telescope. Therefore we selected a number of fields that trace the boundary of the potential remnant to investigate with the Liverpool Telescope and have shown these on the images in Figure 7.2, from which this phenomenon was first identified. As before, we proposed to obtain deep $H\alpha$ images of regions surrounding RS Ophuichi, tracing the evident cavity to detect the associated NSR.

If confirmed as another example of a nova super-remnant, this time associated with RS Ophuichi, we will have crucial evidence to show that the NSR surrounding M 31N 2008-12a is not unique. This will validate the modelling being carried out for understanding the key parameters involved in shaping NSR and will allow us to refine our models further, to search for more in future observations. Although remnants from single eruptions have been recovered around a number of Galactic novae, no Galactic (or indeed other) NSRs have ever been observed. Establishing that the vast cavity surrounding RS Ophuichi is another nova super-remnant will confirm the NSR–RN association.

7.5 The Big Picture

Through the retention of material during outburst, white dwarfs in recurrent nova systems can grow to the Chandrasekhar limit and explode as SNIa. The theoretical study of the NSR surrounding M 31N 2008-12a, alongside the thorough investigation of evolving NSRs in this work, have shown that the ejecta from increasingly frequent eruptions from the WD approaching M_{Ch} will sweep up and remove nearly all of the local material. As a result, when the WD detonates as a SNIa, there will be no hydrogen evident in the spectra as it is all over tens of parsecs away from the event in the form of a NSR shell.

The recovery of even one more NSR (either from the current Liverpool Telescope observing campaigns or the promising cavity surrounding RS Ophuichi) will prove that the 12a system is not unique and so confirm the NSR-RN association, and thus strengthen the connection between novae and SNeIa. Moreover, the recovery of a

whole collection of these vast shells would suggest prevalence, and allow a systematic study into how the characteristics of the underlying nova system affects their growth as well as constraining the number of RN with NSRs. With novae being the brightest of all the SNIa progenitors, population studies can be carried out of these phenomena to extragalactic hosts to correlate environmental effects such as star formation and metallicity with SNIa sub-classes. Ultimately, a solid understanding of RN, through the study of NSRs, will improve our knowledge of SNeIa origins and further their reputation in cosmological research.

Appendix A

Hydrodynamics Derivations

A.1 Fluid flow equations

In Section § 1.5.1, we discussed solving the fluid flow equations numerically. Here we will outline the origin of these equations and derive them using [Shore \(1992\)](#), [Anderson \(2009\)](#) and [Vaytet \(2009\)](#) for guidance.

Firstly, we start by stating that an ideal fluid, one that is incompressible and has zero viscosity, is governed by the continuity equation, the momentum equation and the energy equation, each one representing a fundamental physical principle. The continuity equation encompasses the idea that mass is conserved, the momentum equation follows from Newton's second law ($F = ma$) and the energy equation represents the principle that energy is conserved.

A.1.1 Continuity Equation

In order to derive these three fundamental equations, we will consider a control volume V enclosed by a surface S . If the gas contained within the surface has a density ρ , then the mass of the gas within the surface is simply $\int \rho dV$. As we wish for mass to be conserved, the rate of change of the mass contained within this surface must also be equivalent to the rate of change of the mass flowing across the surface. If the gas is flowing with a velocity \mathbf{u} across the surface, then the mass of the gas flowing across the boundary layers of the surface per unit time is represented by $\int \rho \mathbf{u} \cdot d\mathbf{S}$. Here, $d\mathbf{S}$ represents the unit vector normal to the surface S . As we have inflow and outflow of the system, the rate of change of mass can then be written as:

$$\frac{\partial}{\partial t} \int \rho dV = - \int \rho \mathbf{u} \cdot d\mathbf{S},$$

and applying the divergence theorem to this expression yields:

$$\frac{\partial}{\partial t} \int \rho dV = - \int \nabla \cdot (\rho \mathbf{u}) dV.$$

If we consider that the volume is divided through by the control volume we get:

$$\frac{\partial \rho}{\partial t} + \nabla \cdot (\rho \mathbf{u}) = 0.$$

Expanding this expression as follows:

$$\begin{aligned} \frac{\partial \rho}{\partial t} + \rho \nabla \cdot \mathbf{u} + \mathbf{u} \cdot \nabla \rho &= 0 \\ \Rightarrow \frac{\partial \rho}{\partial t} + \mathbf{u} \cdot \nabla \rho &= -\rho \nabla \cdot \mathbf{u} \end{aligned}$$

leads to the **continuity equation** that describes the conversation of mass:

$$\boxed{\left(\frac{\partial}{\partial t} + \mathbf{u} \cdot \nabla \right) \rho = -\rho \nabla \cdot \mathbf{u}.} \quad (\text{A.1})$$

A.1.2 Euler Equation

Next, we will derive the equation that represents conservation of momentum in fluid dynamics. We start with Newton's second law of motion:

$$\mathbf{F} = m\mathbf{a},$$

and apply this to a fluid element to give:

$$\mathbf{F} = \rho \frac{D\mathbf{u}}{Dt}, \quad (\text{A.2})$$

where \mathbf{F} represents the net forces on the fluid and the Lagrangian time derivative (or substantial derivative) is defined as:

$$\frac{D}{Dt} = \frac{\partial}{\partial t} + (\mathbf{u} \cdot \nabla). \quad (\text{A.3})$$

The quantity defined above (A.3) is the time rate of change following a moving fluid element (Anderson, 2009). The local derivative, $\partial/\partial t$, is the time rate of change at a fixed point and the convective derivative, $\mathbf{u} \cdot \nabla$, is the time rate of change brought about by movement of the fluid element from one place to another in the flow field (Anderson, 2009).

As the total net forces on the fluid element, \mathbf{F} , can be split into two sources (body forces and surface forces), we can write equation A.2 as:

$$\int \rho \frac{D\mathbf{u}}{Dt} dV = - \int p \, d\mathbf{S} + \int \mathbf{s} \, dV,$$

where p is the pressure and stress acting on the surface (surface forces) and the \mathbf{s} term contains external (body) forces such as gravitational, electric and magnetic forces (Anderson, 2009). From Green's Lemma, we know that $\int p \, d\mathbf{S} = \int \nabla p \, dV$, therefore:

$$\int \rho \frac{D\mathbf{u}}{Dt} dV = - \int \nabla p \, dV + \int \mathbf{s} \, dV.$$

If we consider that the volume is divided through by the control volume we get:

$$\rho \frac{D\mathbf{u}}{Dt} = -\nabla p + \mathbf{s},$$

and finally writing the Lagrangian time derivative explicitly leads to the **Euler equation** that describes the conservation of momentum:

$$\boxed{\rho \left(\frac{\partial}{\partial t} + \mathbf{u} \cdot \nabla \right) \mathbf{u} + \nabla p = \mathbf{s}.} \quad (\text{A.4})$$

A.1.3 Energy Equation

Finally, we will derive the energy equation which describes the conservation of energy in fluid dynamics. We will begin by considering that in an ideal gas, the dissipation of energy is ignored. As such, we have adiabatic motion of the fluid and so the entropy, S , of any particle within the fluid is constant. In other words, the rate of change of entropy of a particular fluid element is zero. Using the Lagrangian time derivative (equation A.3) to illustrate this, we have:

$$\frac{\partial S}{\partial t} + \mathbf{u} \cdot \nabla S = 0. \quad (\text{A.5})$$

The first law of thermodynamics:

$$\Delta U = Q - W,$$

where ΔU is the change in internal energy of a system, Q is the heat added to the system and W is the work done by the system on its surroundings can be represented in differential form:

$$dU = \delta Q - \delta W. \quad (\text{A.6})$$

According to the second law of thermodynamics, an element of heat transferred, δQ , is the product of the temperature of the system T (as well as the source and destination of the heat) and the system's entropy, S , such that $\delta Q = T dS$. Additionally, the work done, δW , on the system can be represented by $p dv$ where $v = 1/\rho$ is the specific volume and p is the external pressure. We can now rewrite equation A.6 as:

$$T dS = dU + p dv = dU - \frac{p}{\rho^2} d\rho,$$

or, represented with the Lagrangian time derivative, as:

$$T \frac{DS}{Dt} = \frac{DU}{Dt} - \frac{p}{\rho^2} \frac{D\rho}{Dt}.$$

Expanding this equation explicitly;

$$T \left(\frac{\partial S}{\partial t} + \mathbf{u} \cdot \nabla S \right) = \frac{\partial U}{\partial t} + \mathbf{u} \cdot \nabla U - \frac{p}{\rho^2} \left(\frac{\partial \rho}{\partial t} + \mathbf{u} \cdot \nabla \rho \right),$$

allows us to simplify this statement by noting that the term in parentheses on the left hand side of the equation is zero (from equation A.5) and the term in parentheses on the right hand side of the equation is $-\rho \nabla \cdot \mathbf{u}$, from the continuity equation (equation A.1). We now have

$$\begin{aligned} 0 &= \left(\frac{\partial}{\partial t} + \mathbf{u} \cdot \nabla \right) U - \frac{p}{\rho^2} \left(-\rho \nabla \cdot \mathbf{u} \right) \\ &\Rightarrow \left(\frac{\partial}{\partial t} + \mathbf{u} \cdot \nabla \right) U = -\frac{p}{\rho} \nabla \cdot \mathbf{u} \end{aligned}$$

leading to the **energy equation** that describes the conservation of energy:

$$\boxed{\rho \left(\frac{\partial}{\partial t} + \mathbf{u} \cdot \nabla \right) U = -p \nabla \cdot \mathbf{u}.} \quad (\text{A.7})$$

A.1.4 Equation of state

Alongside the equations describing the fluid flow of a system, we also need to know the state of the matter involved. The **equation of state** for an ideal gas is:

$$\boxed{\epsilon = \frac{p}{\rho(\gamma - 1)}} \quad (\text{A.8})$$

where p is pressure, ρ is density and γ is the ratio of the specific heats. For a monatomic gas, this ratio is $\gamma = 5/3$.

A.1.5 Shocks

If a local flow velocity within the fluid flow is travelling greater than the local sound speed (c_s) of the fluid:

$$c_s = \left(\frac{\gamma p}{\rho} \right)^{1/2},$$

then this local region imparts a discontinuous change of properties to its surroundings, known as a shock. The speed of this local shock wave, u , can be represented in terms of the local sound speed, c_s , and the dimensionless quantity known as the Mach number, \mathcal{M} , as follows:

$$\mathcal{M} = \frac{u}{c_s}.$$

A.2 Solving the fluid flow equations with Morpheus

As mentioned in Section § 1.5.1, the equations of fluid flow (A.1, A.4 and A.7) are solved numerically using a finite difference method. This method involves approximating the derivatives in the differential fluid flow equations using a Taylor series expansion, to obtain a system of linear equations. These difference scheme equations are then solved at points nearby to the discretised points of the divided grid.

The asphere code (Vaytet et al., 2007b) within the Morpheus program divides one-dimensional space up into a grid of cells (an Eulerian description) and treats the interface between any two of these cells as a discontinuity between two separate fluid states. Flux solutions at these cell boundaries are determined by solving the Riemann problem (an individual one-dimensional discontinuity in a fluid) using the Godunov (1959) scheme to second order and a finite difference scheme developed by Falle (1991). Unlike the first order Godunov (1959) approach, which treats the properties of a cell as constant throughout the cell, a second-order Godunov scheme was employed in asphere (Vaytet, 2009) as it improves the value of the interface quantity. It does this by considering the fluid variables as having gradients across cell boundaries (see Figure A.1) and in doing so, results in higher spatial and temporal resolution (Vaytet, 2009).

Finally, the Morpheus program been used extensively before for studies such as that conducted in this thesis. A single mass ejection, in the form of a wind, was simulated

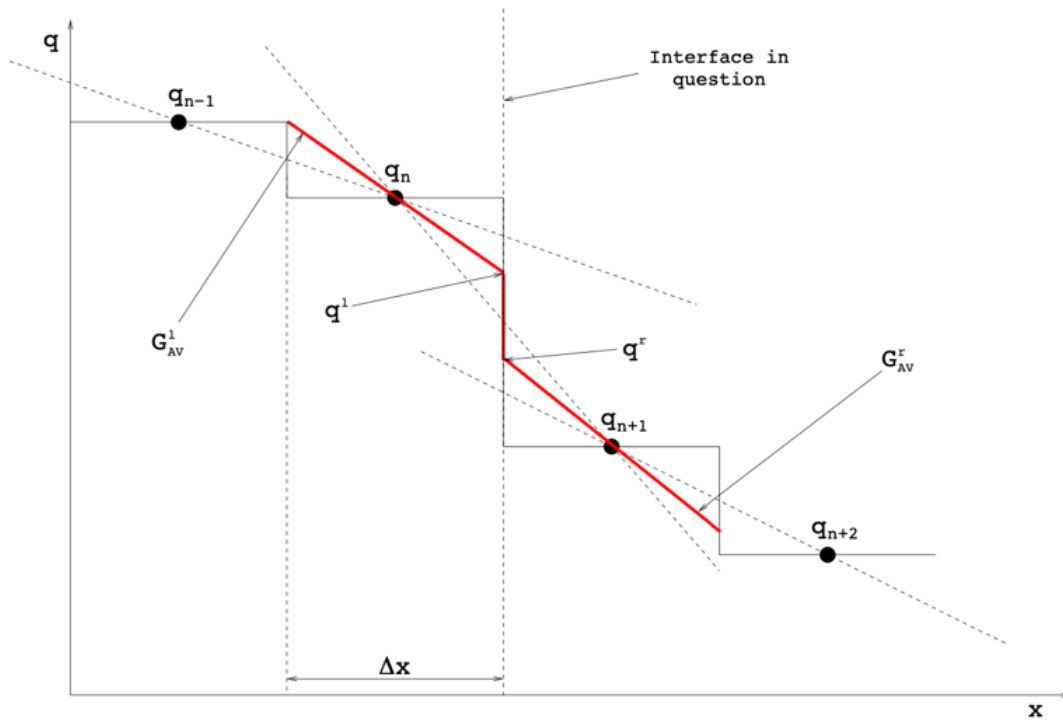


FIGURE A.1: A schematic of the second order Godunov scheme taken from Vaytet (2009). Here, q is a quantity, x is a spatial coordinate and Δx is the width of a cell. G_{AV}^l is the average of the two gradients between q_{n-1} and q_n , and q_n and q_{n+1} . The line G_{AV}^l is then used to find the value of q^l at the cell edge. Likewise, the line G_{AV}^r is used to find the value q^r . The red lines illustrate what the cells n and $n+1$ appear to be to the flux across the interface at $x = n \Delta x$.

to replicate the RS Oph eruption in Vaytet et al. (2007b). In this work, the parameter space of the simulations including the mass loss from the slow and fast wind, wind velocity, wind phase duration, outburst energy and ejected mass were explored to assess their impact on the end results (Vaytet et al., 2007b).

As described throughout this thesis, in a more recent study, Darnley et al. (2019a) utilised Morpheus to model identical recurrent nova eruptions from M 31N 2008-12a to test the viability of many previous outbursts creating the surrounding NSR. As Morpheus implements an Eulerian method of numerical modelling, this stationary linear grid is ideal for simulating multiple eruptions, unlike the Lagrangian approach which would be more suited to following one eruption along a certain trajectory. In conclusion, we know that this program is entirely suitable for modelling the ejecta of non-identical recurrent nova eruptions within a wide parameter space, in order to simulate a range of nova super-remnants.

Appendix B

Derivation of Strömgen sphere

In Section § 3.4 we explored the idea of the nova super-remnant surrounding M 31N 2008-12a being a fossil H II region by utilising the radius equation of a Strömgen sphere. Here we will derive this equation.

We will assume that the region around an ionising source is (i) fully ionised, (ii) exactly spherical, and (iii) composed of only hydrogen such that the number density of protons (n_p) is equal to the number density of electrons (n_e). The Strömgen radius around the ionising source can be defined as the region where the recombination rate is equal to the ionisation rate.

Firstly considering the recombination rate, N_R , of all energy levels ($n = 1$ has been omitted here because if an electron recombines directly to the ground state, a photon is released that is capable of ionising up from the ground state, as in Case B recombination):

$$N_R = \sum_{n=2}^{\infty} N_n, \quad (\text{B.1})$$

where N_n is the recombination rate of the n -th energy level given, with $n_e = n_p$, as:

$$N_n = n_e n_p \beta_n(T_e) = n_e^2 \beta_n(T_e). \quad (\text{B.2})$$

Here $\beta_n(T_e)$ is the recombination coefficient of the n -th energy level at a temperature, T_e (temperature of electrons in K), in a unitary volume. Substituting equation B.2 into equation B.1 and summing yields the following:

$$N_R = n_e^2 \beta_2(T_e), \quad (\text{B.3})$$

where $\beta_2(T_e)$ is the total recombination rate (Dyson & Williams, 1980):

$$\beta_2(T_e) \approx 2 \times 10^{-16} \times T_e^{-0.75} \text{ m}^3 \text{ s}^{-1}.$$

Letting n be the total number of protons ($n = n_p + n_H$), we can set $n_e = xn$ such that x defines the degree of ionisation ($0 \leq x \leq 1$). The number density of neutral hydrogen n_H is then the difference such that $n_H = (1 - x)n$. The ionisation rate N_I in a particular instance is then:

$$N_I = \alpha_0 n_H J,$$

where α_0 is the cross section and J is the ionising photon flux (number of ionising photons per unit area per second). If we simply consider the geometrical effects on J such that it is a function of radial distance r from the ionising source (with a flux S_*) then we have the following inverse square law:

$$N_I = \alpha_0 n_H J(r) = \frac{3S_*}{4\pi r^3}. \quad (\text{B.4})$$

As stated, the Strömgren radius (R_S) is the bordering region where recombination rate equals ionisation rate. This allows us to substitute the recombination rate (equation B.3) in place of the ionisation rate in equation B.4 when setting $r = R_s$ to give:

$$\begin{aligned} n_e^2 \beta_2 &= (nx)^2 \beta = \frac{3S_*}{4\pi R_s^3} \\ \implies R_s &= \left(\frac{3}{4\pi} \frac{S_*}{(nx)^2 \beta} \right)^{\frac{1}{3}}, \end{aligned}$$

and since we know that the region contained within the sphere is fully ionised such that $x = 1$, we arrive at the definition of the Strömgren radius:

$$R_s = \left(\frac{3}{4\pi} \frac{S_*}{n^2 \beta} \right)^{\frac{1}{3}}.$$

Appendix C

Determining boundary locations of the simulated NSRs

Throughout Chapter 4 and Chapter 5, we make extensive use of the radial growth curves of our suite of simulated nova super-remnants. Additionally, we wanted to know the exact boundary locations of our defined cavity, ejecta pile-up region, inner edge and outer edge of the remnant's shell. Here, I will outline the technique employed to find these boundaries from a simulation's output including a schematic in Figure C.1.

The outer edge of the NSR shell was defined from the density radial profile, working backward from the furthest boundary of the simulation box (**a** in Figure C.1), to the point at which the density rose by a small fraction (for example, 10%) above the surrounding ISM density (**b**). The inner edge was then similarly defined to be the

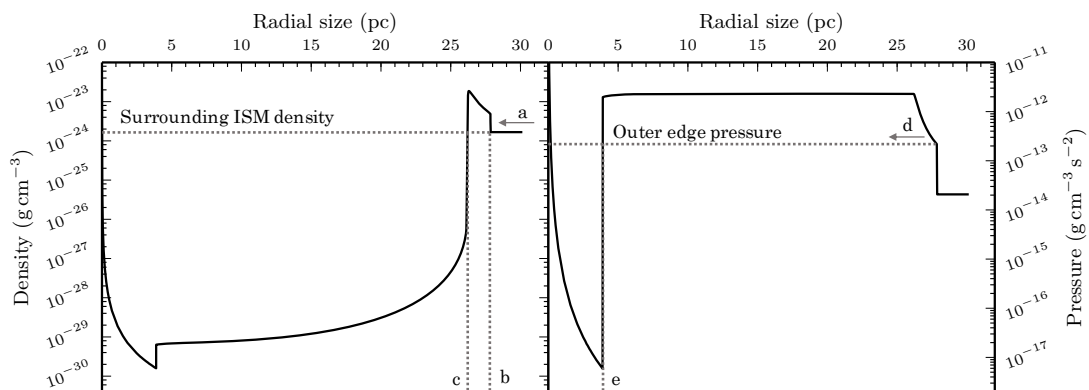


FIGURE C.1: A schematic to illustrate the technique employed to determine the boundary locations from the simulated nova super-remnants.

point at which the density dropped by a small fraction (again as an example, 10%) below the surrounding ISM density (**c**).

The ejecta pile-up boundary was determined from the pressure radial profile of the simulations. Similar to finding the outer edge of the remnant, we worked backward this time from the defined outer edge¹ of the shell (**d**) and set the ejecta pile-up boundary to be the point at which the pressure dropped by a small fraction (for example, 10%), below the pressure of the shell's outer edge (**e**).

Finally, the regions (as can be seen in Figure 4.1 of Chapter 4), were defined as follows: the nova super-remnant shell is the region between the defined inner and outer edge of the shell; the ejecta pile-up region lies between the ejecta pile-up boundary and the inner edge of the NSR shell, and the inner cavity is the zone between the origin (the edge of the nova system's Hill sphere) and the ejecta pile-up boundary.

¹We could have worked backward from the defined inner edge however choosing the outer edge had no impact on this.

Appendix D

Machines

In Chapter 4 we presented the suite of hydrodynamical simulations we ran of non-identical recurrent nova eruptions and in Chapter 6 we presented simulations of post-nova evolutionary scenarios. The simulations from both of these chapters were ran on the following high performance computers:

TABLE D.1: The six machines used for running hydrodynamical simulations. Note that COSMA is a small cluster of 10 identical machines.

Machine	Cores	RAM	CPU
Storm	64	256 GB	AMD Opteron 6380
Rogue	64	256 GB	AMD Opteron 6380
Sinister	32	512 GB	Xeon E5-2683 v4
Nova	6	64 GB	Intel Core i7-8700K
Trouble	6	64 GB	Intel Core i7-8700K
COSMA	10×12	10×60 GB	10x Intel Xeon X5650

Appendix E

Morpheus **code alteration**

In Section § 4.2.4 we described how a part of the Morpheus code was altered to address an issue with the timesteps within the simulations. Here we present the two pieces of code that were altered in the *extras* file:

```
!   write(*,*) 'Timedata',old_n,n,n+1,t, dt,tnrt(n),tnrt(n+1),t+dt

      if (t+dt.gt.tnrt(n+1)) then
!       write (*,*) 'Overrun',n,n+1,t, dt,tnrt(n),tnrt(n+1),t+dt
          dt=tnrt(n+1)-t
          dt_old=dt
!       write (*,*) 'Fix',n,n+1,t, dt,tnrt(n),tnrt(n+1),t+dt
      endif
```

```
      if(n.gt.old_n) then
          old_n=n
          dt=1.0
          dt_old=dt
!       write (*,*) 'dt reset'
      endif
```

Appendix F

Colouring Scheme

In Chapter 4 we presented the suite of hydrodynamical simulations we ran of non-identical recurrent nova eruptions, each with varying system parameters. As it was necessary in most instances to compare many of these simulations in one plot, we set up the colour scheme given in Figure F.1 with feedback from Prof Phil James, to maintain consistency throughout the thesis (as well as clarity, we hope!) These colours are for the runs without radiative cooling (see Section § 4.5) and for runs with radiative cooling included (see Section § 4.6), we simply increased the transparency of the lines.

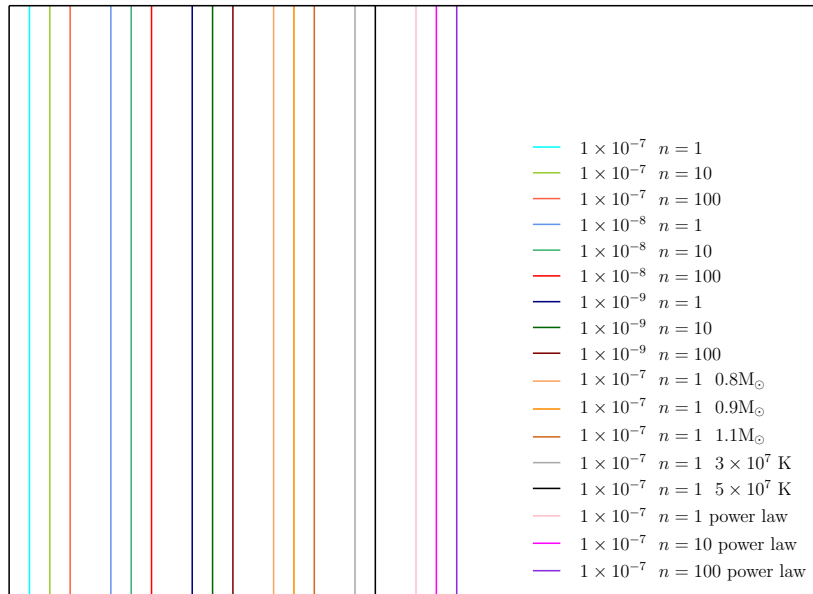


FIGURE F.1: The colour scheme we have adopted to present the results of each hydrodynamical simulation.

Bibliography

- Abdo A. A., et al., 2010, *Science*, 329, 817
- Ackermann M., et al., 2014, *Science*, 345, 554
- Adamakis S., Eyres S. P. S., Sarkar A., Walsh R. W., 2011, *MNRAS*, 414, 2195
- Anderson J., 2009, *Governing Equations of Fluid Dynamics*. Springer Berlin Heidelberg, Berlin, Heidelberg, pp 15–51, doi:10.1007/978-3-540-85056-4_2, https://doi.org/10.1007/978-3-540-85056-4_2
- Anderson L. D., Bania T. M., Jackson J. M., Clemens D. P., Heyer M., Simon R., Shah R. Y., Rathborne J. M., 2009, *ApJS*, 181, 255
- Anupama G. C., 2008, in Evans A., Bode M. F., O'Brien T. J., Darnley M. J., eds, *Astronomical Society of the Pacific Conference Series Vol. 401, RS Ophiuchi (2006) and the Recurrent Nova Phenomenon*. p. 31
- Arnaud K. A., 1996, in Jacoby G. H., Barnes J., eds, *Astronomical Society of the Pacific Conference Series Vol. 101, Astronomical Data Analysis Software and Systems V*. p. 17
- Arnould M., Norgaard H., 1975, *A&A*, 42, 55
- Arp H. C., 1956, *AJ*, 61, 15
- Aydi E., et al., 2018a, *MNRAS*, 474, 2679
- Aydi E., et al., 2018b, *MNRAS*, 480, 572
- Aydi E., et al., 2020a, *Nature Astronomy*, 4, 776
- Aydi E., et al., 2020b, *ApJ*, 905, 62
- Azimlu M., Marciniak R., Barmby P., 2011, *AJ*, 142, 139
- Bailer-Jones C. A. L., Rybizki J., Fouesneau M., Mantelet G., Andrae R., 2018, *AJ*, 156, 58

- Bakos G., PLANET Collaboration 1999, IAU Circ., 7211
- Balman Ş., Krautter J., Ögelman H., 1998, ApJ, 499, 395
- Banerjee D. P. K., et al., 2020, ApJ, 904, L23
- Barnard E. E., 1884, Astronomische Nachrichten, 110, 125
- Barry R. K., Mukai K., Sokoloski J. L., Danchi W. C., Hachisu I., Evans A., Gehrz R., Mikolajewska J., 2008, On the Distance of RS Ophiuchi. p. 52
- Barsukova E., Fabrika S., Hornoch K., Fatkhullin T., Sholukhova O., Pietsch W., 2011, The Astronomer's Telegram, 3725, 1
- Basu S., Antia H. M., 2004, ApJ, 606, L85
- Blackburn J. K., 1995, in Shaw R. A., Payne H. E., Hayes J. J. E., eds, Astronomical Society of the Pacific Conference Series Vol. 77, Astronomical Data Analysis Software and Systems IV. p. 367
- Bode M. F., 2010, Astronomische Nachrichten, 331, 160
- Bode M. F., Evans A., 1989, Science, 246, 136
- Bode M. F., Kahn F. D., 1985, MNRAS, 217, 205
- Bode M. F., O'Brien T. J., Simpson M., 2004, ApJ, 600, L63
- Bode M. F., et al., 2006, ApJ, 652, 629
- Bode M. F., Harman D. J., O'Brien T. J., Bond H. E., Starrfield S., Darnley M. J., Evans A., Eyres S. P. S., 2007, ApJ, 665, L63
- Bode M. F., Darnley M. J., Shafter A. W., Page K. L., Smirnova O., Anupama G. C., Hilton T., 2009, ApJ, 705, 1056
- Bowen I. S., 1934, PASP, 46, 146
- Bowen I. S., 1935, ApJ, 81, 1
- Boyd D., Hornoch K., Henze M., Darnley M. J., Shafter A. W., Kafka S., Kato M., et al. 2017, The Astronomer's Telegram, 11116
- Braun R., Walterbos R. A. M., 1993, A&AS, 98, 327
- Burrows D. N., et al., 2005, Space Sci. Rev., 120, 165
- Buscombe W., de Vaucouleurs G., 1955, The Observatory, 75, 170
- Cameron A. G. W., Fowler W. A., 1971, ApJ, 164, 111

- Campbell W. W., 1893, *Astronomische Nachrichten*, 133, 337
- Canterna R., Schwartz R. D., 1977, *ApJ*, 216, L91
- Canterna R., Thompson L. F., 1981, *PASP*, 93, 581
- Cardelli J. A., Clayton G. C., Mathis J. S., 1989, *ApJ*, 345, 245
- Casanova J., José J., García-Berro E., Shore S. N., 2016, *A&A*, 595, A28
- Chandrasekhar S., 1931, *ApJ*, 74, 81
- Cheung C. C., Donato D., Wallace E., Corbet R., Dubus G., Sokolovsky K., Takahashi H., 2010, *The Astronomer's Telegram*, 2487
- Clark D. H., Parkinson J. H., Stephenson F. R., 1977, *QJRAS*, 18, 443
- Coelho E. A., Shafter A. W., Misselt K. A., 2008, *ApJ*, 686, 1261
- Cohen J. G., 1985, *ApJ*, 292, 90
- Collins P., et al., 1992, *IAU Circ.*, 5454
- Curtin C., Shafter A. W., Pritchett C. J., Neill J. D., Kundu A., Maccarone T. J., 2015, *ApJ*, 811, 34
- Czekala I., et al., 2013, *ApJ*, 765, 57
- D'Antona F., Matteucci F., 1991, *A&A*, 248, 62
- Darnley M. J., 2021, in *The Golden Age of Cataclysmic Variables and Related Objects V*. p. 44 (arXiv:1912.13209)
- Darnley M. J., Henze M., 2020, *Advances in Space Research*, 66, 1147
- Darnley M. J., Page K. L., 2020, *The Astronomer's Telegram*, 14142, 1
- Darnley M. J., et al., 2006, *MNRAS*, 369, 257
- Darnley M. J., Ribeiro V. A. R. M., Bode M. F., Hounsell R. A., Williams R. P., 2012, *ApJ*, 746, 61
- Darnley M. J., Williams S. C., Bode M. F., Henze M., Ness J.-U., Shafter A. W., Hornoch K., Votruba V., 2014, *A&A*, 563, L9
- Darnley M. J., et al., 2015a, *A&A*, 580, A45
- Darnley M. J., Henze M., Shafter A. W., Kato M., 2015b, *ATel*, 7964, 1
- Darnley M. J., Henze M., Shafter A. W., Kato M., 2015c, *ATel*, 7965, 1

- Darnley M. J., et al., 2016, *ApJ*, 833, 149
- Darnley M. J., et al., 2017a, *ApJ*, 847, 35
- Darnley M. J., et al., 2017b, *ApJ*, 849, 96
- Darnley M. J., Healy M. W., Henze M., Williams S. C., 2018a, *The Astronomer's Telegram*, 11149
- Darnley M. J., Henze M., Shafter A. W., Kafka S., Kato M., et al. 2018b, *The Astronomer's Telegram*, 12177
- Darnley M. J., et al., 2019a, *Nature*, 565, 460
- Darnley M. J., Henze M., Hachisu I., Kato M., Osborne J. P., Ness J. U., Shafter A. W., 2019b, *The Astronomer's Telegram*, 13274, 1
- Darnley M. J., Henze M., Hachisu I., Kato M., Osborne J. P., Ness J. U., Shafter A. W., 2019c, *The Astronomer's Telegram*, 13290, 1
- Darnley M. J., Shafter A. W., Kafka S., Williams S., Henze M., 2020a, *The Astronomer's Telegram*, 14130, 1
- Darnley M. J., Page K. L., Henze M., 2020b, *The Astronomer's Telegram*, 14152, 1
- Della Valle M., Izzo L., 2020, *A&A Rev.*, 28, 3
- Della Valle M., Livio M., 1998, *ApJ*, 506, 818
- Della Valle M., Pasquini L., Daou D., Williams R. E., 2002, *A&A*, 390, 155
- Dodorico S., Dopita M. A., Benvenuti P., 1980, *A&AS*, 40, 67
- Dolphin A. E., 2000, *PASP*, 112, 1383
- Downes R. A., Duerbeck H. W., 2000, *AJ*, 120, 2007
- Drake J. J., Orlando S., 2010, *ApJ*, 720, L195
- Duerbeck H. W., 2008, *Novae: an historical perspective*, 2 edn. Cambridge University Press, pp 1–15, doi:10.1017/CBO9780511536168.003
- Duerbeck H. W., Pompei E., 2000, *IAU Circ.*, 7457
- Dyson J. E., Williams D. A., 1980, *Physics of the interstellar medium*
- ESA ed. 1997a, *The HIPPARCOS and TYCHO catalogues. Astrometric and photometric star catalogues derived from the ESA HIPPARCOS Space Astrometry Mission* ESA Special Publication Vol. 1200

- ESA 1997b, VizieR Online Data Catalog, 1239
- Evans A., et al., 2007, MNRAS, 374, L1
- Evans A., Bode M. F., O'Brien T. J., Darnley M. J., eds, 2008, RS Ophiuchi (2006) and the Recurrent Nova Phenomenon Astronomical Society of the Pacific Conference Series Vol. 401
- Evans P. A., et al., 2009, MNRAS, 397, 1177
- Eyres S. P. S., et al., 2018, MNRAS, 481, 4931
- Falle S. A. E. G., 1991, MNRAS, 250, 581
- Ferrarese L., Côté P., Jordán A., 2003, ApJ, 599, 1302
- Ferrière K. M., 2001, Reviews of Modern Physics, 73, 1031
- Figueira J., José J., García-Berro E., Campbell S. W., García-Senz D., Mohamed S., 2018, A&A, 613, A8
- Filippenko A. V., 1999, IAU Circ., 7220
- Filippenko A. V., Li W. D., Treffers R. R., Modjaz M., 2001, in Paczynski B., Chen W.-P., Lemme C., eds, Astronomical Society of the Pacific Conference Series Vol. 246, IAU Colloq. 183: Small Telescope Astronomy on Global Scales. p. 121
- Franck J. R., Shafter A. W., Hornoch K., Misselt K. A., 2012, ApJ, 760, 13
- Gaia Collaboration et al., 2018, A&A, 616, A1
- Gallart C., Aparicio A., Vilchez J. M., 1996, AJ, 112, 1928
- Ganeshalingam M., et al., 2010, ApJS, 190, 418
- Gehrels N., et al., 2004, ApJ, 611, 1005
- Gieren W., Pietrzyński G., Nalewajko K., Soszyński I., Bresolin F., Kudritzki R.-P., Minniti D., Romanowsky A., 2006, ApJ, 647, 1056
- Gill C. D., O'Brien T. J., 1998, MNRAS, 300, 221
- Gill C. D., O'Brien T. J., 1999, MNRAS, 307, 677
- Gill C. D., O'Brien T. J., 2000, MNRAS, 314, 175
- Ginzburg S., Quataert E., 2021, MNRAS, 507, 475
- Giraud K., Hart G., Peterson B., Nakata T., 2007, in APS Northwest Section Meeting Abstracts. p. C1.003

- Godunov S. K., 1959, *Mat. Sb., Nov. Ser.*, 47, 271
- Graczyk D., et al., 2014, *ApJ*, 780, 59
- Green G. M., et al., 2018, *MNRAS*, 478, 651
- Green G. M., Schlafly E., Zucker C., Speagle J. S., Finkbeiner D., 2019, *ApJ*, 887, 93
- Greiner J., Hasinger G., Kahabka P., 1991, *A&A*, 246, L17
- Greiner J., Orio M., Schartel N., 2003, *A&A*, 405, 703
- Gronow S., Collins C. E., Sim S. A., Röpke F. K., 2021, *A&A*, 649, A155
- Gutierrez J., Garcia-Berro E., Iben Icko J., Isern J., Labay J., Canal R., 1996, *ApJ*, 459, 701
- Güver T., Özel F., 2009, *MNRAS*, 400, 2050
- Hachisu I., Kato M., 2006, *ApJS*, 167, 59
- Hachisu I., Kato M., 2016, *ApJ*, 816, 26
- Hachisu I., Kato M., 2018, *ApJ*, 858, 108
- Hachisu I., Kato M., Nomoto K., Umeda H., 1999a, *ApJ*, 519, 314
- Hachisu I., Kato M., Nomoto K., 1999b, *ApJ*, 522, 487
- Hachisu I., Kato M., Kato T., Matsumoto K., 2000, *ApJ*, 528, L97
- Harvey E., Redman M. P., Boumis P., Akras S., 2016, *A&A*, 595, A64
- Harvey E. J., Redman M. P., Darnley M. J., Williams S. C., Berdyugin A., Piirola V. E., Fitzgerald K. P., O'Connor E. G. P., 2018, *A&A*, 611, A3
- Harvey E. J., et al., 2020, *MNRAS*, 499, 2959
- Healy M. W., et al., 2019, *MNRAS*, 486, 4334
- Hearnshaw J. B., Livingston C. M., Gilmore A. C., Kilmartin P. M., 2004, in Kurtz D. W., Pollard K. R., eds, *Astronomical Society of the Pacific Conference Series Vol. 310, IAU Colloq. 193: Variable Stars in the Local Group*. p. 103
- Heinze A. N., et al., 2018, *AJ*, 156, 241
- Henden A. A., Welch D. L., Terrell D., Levine S. E., 2009, in *American Astronomical Society Meeting Abstracts #214*. p. 669
- Henze M., et al., 2011, *A&A*, 533, A52

- Henze M., et al., 2014a, *A&A*, 563, A2
- Henze M., Ness J.-U., Darnley M. J., Bode M. F., Williams S. C., Shafter A. W., Kato M., Hachisu I., 2014b, *A&A*, 563, L8
- Henze M., et al., 2015a, *A&A*, 580, A46
- Henze M., Darnley M. J., Kabashima F., Nishiyama K., Itagaki K., Gao X., 2015b, *A&A*, 582, L8
- Henze M., et al., 2015c, *ATel*, 7984, 1
- Henze M., Darnley M. J., Shafter A. W., Kafka S., Kato M., 2016a, *ATel*, 9853
- Henze M., Darnley M. J., Shafter A. W., Kafka S., Kato M., 2016b, *ATel*, 9872
- Henze M., et al., 2018a, *ApJ*, 857, 68
- Henze M., Darnley M. J., Shafter A. W., Kafka S., Kato M., Williams S. C., et al. 2018b, *The Astronomer's Telegram*, 11121
- Henze M., Darnley M. J., Shafter A. W., Kafka S., Kato M., Williams S. C., et al. 2018c, *The Astronomer's Telegram*, 11130
- Henze M., Darnley M. J., Shafter A. W., Kafka S., Kato M., et al. 2018d, *The Astronomer's Telegram*, 12182
- Henze M., Darnley M. J., Shafter A. W., Kafka S., Kato M., Williams S. C., et al. 2018e, *The Astronomer's Telegram*, 12207
- Herbig G. H., Neubauer F. J., 1946, *PASP*, 58, 196
- Hestenes J. C., Zheng W., Filippenko A. V., 2017, *Transient Name Server Discovery Report*, 831
- Hillebrandt W., Niemeyer J. C., 2000, *ARA&A*, 38, 191
- Hillman Y., Prialnik D., Kovetz A., Shara M. M., 2015, *MNRAS*, 446, 1924
- Hillman Y., Prialnik D., Kovetz A., Shara M. M., 2016, *ApJ*, 819, 168
- Hillman Y., Shara M. M., Prialnik D., Kovetz A., 2020a, *Nature Astronomy*, 4, 886
- Hillman Y., Shara M., Prialnik D., Kovetz A., 2020b, *Advances in Space Research*, 66, 1072
- Hounsell R., et al., 2010, *ApJ*, 724, 480
- Hubble E. P., 1925, *ApJ*, 62

- Hutchings J. B., 1972, MNRAS, 158, 177
- Iben I. J., Tutukov A. V., 1984, ApJS, 54, 335
- Idan I., Shaviv N. J., Shaviv G., 2013, MNRAS, 433, 2884
- Iijima T., Esenoglu H. H., 2003, A&A, 404, 997
- Itagaki K., 2016, CBAT
- Itagaki K., Gao X., Darnley M. J., Henze M., Shafter A. W., Williams S. C., Kafka S., Kato M., 2016, ATel, 9848
- Izzo L., et al., 2015, ApJ, 808, L14
- Izzo L., et al., 2018, MNRAS, 478, 1601
- Jester S., et al., 2005, AJ, 130, 873
- Johnson L. C., et al., 2012, ApJ, 752, 95
- Kahn F. D., 1974, Symposium - International Astronomical Union, 60, 329
- Kalberla P. M. W., Burton W. B., Hartmann D., Arnal E. M., Bajaja E., Morras R., Pöppel W. G. L., 2005, A&A, 440, 775
- Karachentsev I. D., Makarov D. I., Kaisina E. I., 2013, AJ, 145, 101
- Kasliwal M. M., Cenko S. B., Kulkarni S. R., Ofek E. O., Quimby R., Rau A., 2011, ApJ, 735, 94
- Kasliwal M. M., et al., 2017, ApJ, 839, 88
- Kato M., Hachisu I., 2020, PASJ, 72, 82
- Kato M., Saio H., Hachisu I., Nomoto K., 2014, ApJ, 793, 136
- Kato M., Saio H., Hachisu I., 2015, ApJ, 808, 52
- Kawash A., et al., 2021, ApJ, 910, 120
- Kayser S. E., 1967, AJ, 72, 134
- King J. Y., Li W. D., 1999, IAU Circ., 7208
- Kniazev A. Y., Pustilnik S. A., Zucker D. B., 2008, MNRAS, 384, 1045
- Knigge C., King A. R., Patterson J., 2000, A&A, 364, L75
- Koribalski B. S., et al., 2004, AJ, 128, 16

- Korotkiy S., Elenin L., 2011, CBAT
- Kovetz A., Prialnik D., 1985, *ApJ*, 291, 812
- Kovetz A., Prialnik D., Shara M. M., 1988, *ApJ*, 325, 828
- Kraft R. P., 1964, *ApJ*, 139, 457
- Krautter J., 2008, X-ray emission from classical novae in outburst, 2 edn. Cambridge University Press, pp 232–251, doi:10.1017/CBO9780511536168.012
- Kuin N. P. M., et al., 2020, *MNRAS*, 491, 655
- Landsman W. B., 1993, in Hanisch R. J., Brissenden R. J. V., Barnes J., eds, *Astronomical Society of the Pacific Conference Series Vol. 52, Astronomical Data Analysis Software and Systems II*. p. 246
- Larsen S. S., Brodie J. P., Wasserman A., Strader J., 2018, *A&A*, 613, A56
- Li Q., 1988, in Börner G., ed., *High Energy Astrophysics*.
- Li K.-L., et al., 2017, *Nature Astronomy*, 1, 697
- Liller W., 1995, *IAU Circ.*, 6143
- Lloyd H. M., O'Brien T. J., Bode M. F., 1997, *MNRAS*, 284, 137
- Lodders K., 2019, arXiv e-prints, p. arXiv:1912.00844
- Long K. S., Blair W. P., Kirshner R. P., Winkler P. F., 1990, *ApJS*, 72, 61
- Marshall D. J., Robin A. C., Reylé C., Schultheis M., Picaud S., 2006, *A&A*, 453, 635
- Mason E., Brandeker A., Ederoclite A., Della Valle M., 2005a, *Central Bureau Electronic Telegrams*, 195
- Mason E., Della Valle M., Gilmozzi R., Lo Curto G., Williams R. E., 2005b, *A&A*, 435, 1031
- Mason E., Shore S. N., De Gennaro Aquino I., Izzo L., Page K., Schwarz G. J., 2018, *ApJ*, 853, 27
- Massey P., Armandroff T. E., Pyke R., Patel K., Wilson C. D., 1995, *AJ*, 110, 2715
- Massey P., Olsen K. A. G., Hodge P. W., Strong S. B., Jacoby G. H., Schlingman W., Smith R. C., 2006, *AJ*, 131, 2478
- Massey P., Olsen K. A. G., Hodge P. W., Jacoby G. H., McNeill R. T., Smith R. C., Strong S. B., 2007, *AJ*, 133, 2393

- Mateo M. L., 1998, *ARA&A*, 36, 435
- McAlary C. W., Madore B. F., McGonegal R., McLaren R. A., Welch D. L., 1983, *ApJ*, 273, 539
- McCray R., 1988, in Roger R. S., Landecker T. L., eds, *IAU Colloq. 101: Supernova Remnants and the Interstellar Medium*. p. 447
- McLaughlin D. B., 1939, *Popular Astronomy*, 47, 410
- McLaughlin D. B., 1960, *The Spectra of Novae*. p. 585
- McLaughlin D. B., 1945, *PASP*, 57, 69
- Metzger B. D., Hascoët R., Vurm I., Beloborodov A. M., Chomiuk L., Sokoloski J. L., Nelson T., 2014, *MNRAS*, 442, 713
- Mikołajewska J., Shara M. M., 2017, *ApJ*, 847, 99
- Molaro P., Izzo L., Mason E., Bonifacio P., Della Valle M., 2016, *MNRAS*, 463, L117
- Moore C. E., 1945, *Contributions from the Princeton University Observatory*, 21, 1
- Mróz P., et al., 2016, *ApJS*, 222, 9
- Nagakura T., Omukai K., 2005, *MNRAS*, 364, 1378
- Neill J. D., Shara M. M., 2004, *AJ*, 127, 816
- Neill J. D., Shara M. M., 2005, *AJ*, 129, 1873
- Ness J.-U., 2020, *Advances in Space Research*, 66, 1202
- Ness J.-U., et al., 2003, *ApJ*, 594, L127
- Nishiyama K., Kabashima F., 2008, *CBAT*
- Nishiyama K., Kabashima F., 2012, *CBAT*
- O'Brien T. J., 2008, *Resolved nebular remnants*, 2 edn. Cambridge University Press, pp 285–307, doi:10.1017/CBO9780511536168.014
- O'Brien T. J., Kahn F. D., 1987, *MNRAS*, 228, 277
- O'Brien T. J., Lloyd H. M., 1994, *Ap&SS*, 216, 167
- O'Brien T. J., Bode M. F., Kahn F. D., 1992, *MNRAS*, 255, 683
- O'Brien T. J., Lloyd H. M., Bode M. F., 1994, *MNRAS*, 271, 155
- O'Brien T. J., et al., 2006, *Nature*, 442, 279

- Oegelman H., Beuermann K., Krautter J., 1984, *ApJ*, 287, L31
- Oksanen A., Darnley M. J., Shafter A. W., Kafka S., Kato M., Henze M., 2019, *The Astronomer's Telegram*, 13269, 1
- Orio M., 2020, *Advances in Space Research*, 66, 1193
- Orio M., Greiner J., 1999, *A&A*, 344, L13
- Orlando S., Drake J. J., Laming J. M., 2009, *A&A*, 493, 1049
- Osborne J. P., 2015, *Journal of High Energy Astrophysics*, 7, 117
- Osborne J. P., et al., 2011, *ApJ*, 727, 124
- Osterbrock D. E., Ferland G. J., 2006, *Astrophysics of gaseous nebulae and active galactic nuclei*. CA: University Science Books
- Özdönmez A., Güver T., Cabrera-Lavers A., Ak T., 2016, *MNRAS*, 461, 1177
- Özdönmez A., Ege E., Güver T., Ak T., 2018, *MNRAS*, 476, 4162
- Pagnotta A., Schaefer B. E., 2014, *ApJ*, 788, 164
- Pagnotta A., Schaefer B. E., Xiao L., Collazzi A. C., Kroll P., 2009, *AJ*, 138, 1230
- Pagnotta A., et al., 2015, *ApJ*, 811, 32
- Payne-Gaposchkin C., 1957, *The Galactic Novae*. Amsterdam, North-Holland Pub. Co.
- Piasecik A. S., Steele I. A., Bates S. D., Mottram C. J., Smith R. J., Barnsley R. M., Bolton B., 2014, in *Ground-based and Airborne Instrumentation for Astronomy V*. p. 91478H
- Pietsch W., 2010, *Astronomische Nachrichten*, 331, 187
- Pietsch W., et al., 2007, *A&A*, 465, 375
- Popper D. M., 1940, *ApJ*, 92, 262
- Porter J. M., O'Brien T. J., Bode M. F., 1998, *MNRAS*, 296, 943
- Prentice S. J., et al., 2018, *ApJ*, 865, L3
- Prialnik D., Kovetz A., 1984, *ApJ*, 281, 367
- Prialnik D., Kovetz A., 1995, *ApJ*, 445, 789
- Raymond J. C., Cox D. P., Smith B. W., 1976, *ApJ*, 204, 290

- Ribeiro V. A. R. M., 2011, PhD thesis, Liverpool John Moores University
- Ribeiro V. A. R. M., et al., 2009, *ApJ*, 703, 1955
- Rich J. A., Persson S. E., Freedman W. L., Madore B. F., Monson A. J., Scowcroft V., Seibert M., 2014, *ApJ*, 794, 107
- Ritossa C., Garcia-Berro E., Iben Icko J., 1996, *ApJ*, 460, 489
- Roming P. W. A., et al., 2005, *Space Sci. Rev.*, 120, 95
- Santamaría E., Guerrero M. A., Ramos-Larios G., Toalá J. A., Sabin L., Rubio G., Quino-Mendoza J. A., 2020, *ApJ*, 892, 60
- Sasaki M., Pietsch W., Haberl F., Hatzidimitriou D., Stiele H., Williams B., Kong A., Kolb U., 2012, *A&A*, 544, A144
- Savage B. D., Mathis J. S., 1979, *ARA&A*, 17, 73
- Schaefer B. E., 2010, *ApJS*, 187, 275
- Schaefer B. E., 2018, *MNRAS*, 481, 3033
- Schaefer B. E., Pagnotta A., Shara M. M., 2010, *ApJ*, 708, 381
- Schwarz G. J., et al., 2011, *ApJS*, 197, 31
- Selvelli P., Gilmozzi R., 2019, *A&A*, 622, A186
- Shafter A. W., 2013, *AJ*, 145, 117
- Shafter A. W., 2017, *ApJ*, 834, 196
- Shafter A. W., Rau A., Quimby R. M., Kasliwal M. M., Bode M. F., Darnley M. J., Misselt K. A., 2009, *ApJ*, 690, 1148
- Shafter A. W., et al., 2011, *ApJ*, 734, 12
- Shafter A. W., Darnley M. J., Bode M. F., Ciardullo R., 2012a, *ApJ*, 752, 156
- Shafter A. W., Hornoch K., Ciardullo J. V. R., Darnley M. J., Bode M. F., 2012b, *ATel*, 4503, 1
- Shafter A. W., Curtin C., Pritchett C. J., Bode M. F., Darnley M. J., 2014, in Woudt P. A., Ribeiro V. A. R. M., eds, *Astronomical Society of the Pacific Conference Series Vol. 490, Stellar Novae: Past and Future Decades*. p. 77
- Shafter A. W., Kundu A., Henze M., 2017, *Research Notes of the American Astronomical Society*, 1, 11

- Shappee B. J., et al., 2014, *ApJ*, 788, 48
- Shara M. M., 1981, *ApJ*, 243, 926
- Shara M. M., 1989, *PASP*, 101, 5
- Shara M. M., Moffat A. F. J., Webbink R. F., 1985, *ApJ*, 294, 271
- Shara M. M., Zurek D. R., Williams R. E., Prialnik D., Gilmozzi R., Moffat A. F. J., 1997, *AJ*, 114, 258
- Shara M. M., et al., 2007, *Nature*, 446, 159
- Shara M. M., Yaron O., Prialnik D., Kovetz A., Zurek D., 2010, *ApJ*, 725, 831
- Shara M. M., Mizusawa T., Wehinger P., Zurek D., Martin C. D., Neill J. D., Forster K., Seibert M., 2012, *ApJ*, 758, 121
- Shara M. M., et al., 2016, *ApJS*, 227, 1
- Shara M. M., et al., 2017a, *Nature*, 548, 558
- Shara M. M., et al., 2017b, *ApJ*, 839, 109
- Shara M. M., et al., 2018, *MNRAS*, 474, 1746
- Shore S. N., 1992, *An introduction to astrophysical hydrodynamics*
- Shore S. N., 2012, *Bulletin of the Astronomical Society of India*, 40, 185
- Slavin A. J., O'Brien T. J., Dunlop J. S., 1995, *MNRAS*, 276, 353
- Sokoloski J. L., Luna G. J. M., Mukai K., Kenyon S. J., 2006, *Nature*, 442, 276
- Soraisam M. D., Gilfanov M., 2015, *A&A*, 583, A140
- Spite F., 1990, *Mem. Soc. Astron. Italiana*, 61, 663
- Stalder B., et al., 2017, *ApJ*, 850, 149
- Starrfield S., Truran J. W., Sparks W. M., Kutter G. S., 1972, *ApJ*, 176, 169
- Starrfield S., Sparks W. M., Truran J. W., 1976, in Eggleton P., Mitton S., Whelan J., eds, *IAU Symposium Vol. 73, Structure and Evolution of Close Binary Systems*. p. 155
- Starrfield S., Truran J. W., Sparks W. M., Arnould M., 1978, *ApJ*, 222, 600
- Starrfield S., Iliadis C., Hix W. R., 2016, *PASP*, 128, 051001

- Starrfield S., Bose M., Iliadis C., Hix W. R., Woodward C. E., Wagner R. M., 2020, *ApJ*, 895, 70
- Starrfield S., Bose M., Iliadis C., Hix W. R., Woodward C. E., Wagner R. M., 2021, in *The Golden Age of Cataclysmic Variables and Related Objects V.* p. 30 (arXiv:2006.01827)
- Steele I. A., et al., 2004, in Oschmann Jr. J. M., ed., *Proc. SPIE Vol. 5489, Ground-based Telescopes.* pp 679–692
- Steele I. A., Mottram C. J., Smith R. J., Barnsley R. M., 2014, in Holland A. D., Beletic J., eds, *Vol. 9154, High Energy, Optical, and Infrared Detectors for Astronomy VI. SPIE*, pp 725 – 730, doi:10.1117/12.2056602, <https://doi.org/10.1117/12.2056602>
- Stetson P. B., 1987, *PASP*, 99, 191
- Strömgren B., 1939, *ApJ*, 89, 526
- Strope R. J., Schaefer B. E., Henden A. A., 2010, *AJ*, 140, 34
- Tajitsu A., Sadakane K., Naito H., Arai A., Aoki W., 2015, *Nature*, 518, 381
- Tajitsu A., Sadakane K., Naito H., Arai A., Kawakita H., Aoki W., 2016, *ApJ*, 818, 191
- Tang S., Cao Y., Kasliwal M. M., 2013, *ATel*, 5607, 1
- Tang S., et al., 2014, *ApJ*, 786, 61
- Tomisaka K., Ikeuchi S., 1986, *PASJ*, 38, 697
- Tonry J. L., et al., 2018, *PASP*, 130, 064505
- Toraskar J., Mac Low M.-M., Shara M. M., Zurek D. R., 2013, *ApJ*, 768, 48
- Vaytet N. M. H., 2009, PhD thesis, <https://www.nbi.dk/~nvaytet/documents/thesis.pdf>
- Vaytet N. M. H., O'Brien T. J., Rushton A. P., 2007a, *MNRAS*, 380, 175
- Vaytet N. M. H., O'Brien T. J., Bode M. F., 2007b, *ApJ*, 665, 654
- Vaytet N. M. H., O'Brien T. J., Page K. L., Bode M. F., Lloyd M., Beardmore A. P., 2011, *ApJ*, 740, 5
- Walder R., Folini D., Shore S. N., 2008, *A&A*, 484, L9

- Walker M. F., 1954, *PASP*, 66, 230
- Walterbos R. A. M., Braun R., 1992, *A&AS*, 92, 625
- Wareing C. J., O'Brien T. J., Zijlstra A. A., Kwitter K. B., Irwin J., Wright N., Greimel R., Drew J. E., 2006, *MNRAS*, 366, 387
- Warner B., 1995, *Cambridge Astrophysics Series*, 28
- Webbink R. F., 1984, *ApJ*, 277, 355
- Wei J. Y., Xu D. W., Qiao Q. Y., Qiu Y. L., Hu J. Y., 1999, *IAU Circ.*, 7209
- Weldrake D. T. F., de Blok W. J. G., Walter F., 2003, *MNRAS*, 340, 12
- Whelan J., Iben Icko J., 1973, *ApJ*, 186, 1007
- White N. E., Giommi P., Heise J., Angelini L., Fantasia S., 1995, *ApJ*, 445, L125
- Williams R. E., 1992, *AJ*, 104, 725
- Williams R. E., 1994, *ApJ*, 426, 279
- Williams R., 2012, *AJ*, 144, 98
- Williams S. C., Darnley M. J., 2017a, *The Astronomer's Telegram*, 10042, 1
- Williams S. C., Darnley M. J., 2017b, *The Astronomer's Telegram*, 10630
- Williams S. J., Shafter A. W., 2004, *ApJ*, 612, 867
- Williams B. F., Garcia M. R., Kong A. K. H., Primini F. A., King A. R., Di Stefano R., Murray S. S., 2004, *ApJ*, 609, 735
- Williams S. C., Darnley M. J., Bode M. F., Keen A., Shafter A. W., 2014, *ApJS*, 213, 10
- Williams S. C., Darnley M. J., Bode M. F., Shafter A. W., 2016, *ApJ*, 817, 143
- Williams S. C., Darnley M. J., Henze M., 2017, *MNRAS*, 472, 1300
- Wilms J., Allen A., McCray R., 2000, *ApJ*, 542, 914
- Worters H. L., Eyres S. P. S., Bromage G. E., Osborne J. P., 2007, *MNRAS*, 379, 1557
- Wright W. H., 1940, *Publications of Lick Observatory*, 14, 27
- Yaron O., Prialnik D., Shara M. M., Kovetz A., 2005, *ApJ*, 623, 398
- Zwicky F., 1936, *Proceedings of the National Academy of Science*, 22, 457

di Mille F., Ciroi S., Botte V., Boschetti C. S., 2003, IAU Circ., 8231

van den Heuvel E. P. J., Bhattacharya D., Nomoto K., Rappaport S. A., 1992, A&A,
262, 97